ANDROGEN RECEPTOR ACTIVITY TUNES EFFECTOR AND MEMORY CD8 T CELL RESPONSES

Reed M. Hawkins

A DISSERTATION

Presented to the Cancer Biology Program and the
Oregon Health & Science University
School of Medicine
In partial fulfillment of the requirements for the degree of

Doctor of Philosophy

June 2025

Certificate of Approval

This is to certify that the PhD dissertation of
Reed M. Hawkins
has been approved

Advisor, Amy Moran, Ph.D.

Member & Chair, Melissa Wong, Ph.D.

Member, Julia Maxson, Ph.D.

Member, Megan Burger, Ph.D.

Outside Reader, Susan Murray, Ph.D.

Table of Contents

List of Figures

List of Abbreviations

Abbreviation	**Meaning**
AAI	Androgen axis inhibition
ACACA	Acetyl-CoA carboxylase alpha
ActA	Actin A
ADT	Androgen deprivation therapy
AIRE	Autoimmune regulator
AP-1	Activator protein 1
APC	Antigen presenting cell
AR	Androgen receptor
ARE	Androgen response element
AREG	Amphiregulin
ARG1	Arginase 1
ARID1A	AT-rich interactive domain containing protein 1A
ARKO	Androgen receptor knockout
ATAC	Assay for transposase accessible chromatin
BAF	BRG1-associated factors
BATF	Basic leucine zipper transcription factor, ATF-like
Bcl2	B cell lymphoma 2
BCR	B cell receptor
Blimp1	B lymphocytes-induced maturation protein 1
BRCA1/2	Breast cancer gene 1 and 2
CARM1	Coactivator-assocaiated arginine methyltransferase 1
CCR7	C-C chemokine receptor type 7
CD122	Interleukin 2 receptor β
CD127	Interleukin 7 receptor
CD25	Interleukin 2 receptor α
CD	Cluster of differentiation
CD49d	Integrin α4
CD62L	L-selectin
CDH1	Cadherin 1
cDNA	Comoplementary DNA
CEACAM	Carcinoembryonic antigen-related cell adhesion molecule 1
CFA	Complete Freund's adjuvant
CMV	Cytomegalo virus
CNV	Copy number variation
COVID-19	Coronavirus infectious disease 2019
CTL	Cytotoxic T lymphocyte
CTLA4	Ctytotoxic T lymphocyte associated protein 4
CTV	CellTrace violet
CX3CR1	C-X3-C motif chemokine receptor 1
CXCR5	C-X-C motif chemokine receptor 5
CYP17A1	Cytochrome p450 17A1

DC	Dendritic cell
DDR	DNA damage repair
DHEA	Dehydroepiandrosterone
dMMR	DNA mismatch repair
DNA	Deoxyribose nucleic acid
DP	Double positive thymocyte
e8i	Enhancer of CD8 I
EBV	Epstein-Barr virus
ECM	Extracellular matrix
EGF	Epidermal growth factor
Eomes	Eomesodermin
EP300	E1A binding protein p300
EPCAM	Epithelial cell adhesion molecule
ER	Estrogen receptor
FACS	Fluorescence activated cell sorting
FCG	Four core genotype
FoxA1	Forkhead box A1
FoxO1	Forkhead box O1
GAHT	Gender-affirming hormone therapy
GM-1	Monosialotetrahexosylganglioside
GNLY	Granulysin
GnRH	Gonadotropin releasing hormone
GSEA	Gene set enrichment analysis
GZM	Granzyme
H3K27Ac/Me3	Histone H3 lysine 27 acetylation and tri-methylation
HCV/HBV	Hepatitis C virus and Hepatitis B virus
HDAC	Histond deacetylase
HSP	Heat shock protein
HSV2	Herpes simplex virus 2
IAV	Influenza A virus
ICB	Immune checkpoint blockade
ICI	Immune checkpoint inhibition
ID2/ID3	Inhibitor of DNA binding 2 and 3
IFN	Interferon
IKZF2	Zinc finger protein Helios
IL-15R	Interleukin 15 receptor
IL-12R	Interleukin 12 receptor
IL-2	Interleukin 2 receptor
IL-7R	Interleukin 7 receptor
iMSC	Immature myeloid suppressor cell
IRF4	Interferon regulatory factor 4
JUNB	JunB proto-oncogene
Ki-67	Kiel 67
KLK	Kallikrein-related peptidase
KLRG1	Killer cell lectin-like receptor G1

KRT	Keratin
LAG3	Lymphocyte activation gene 3
LCMV	Lymphcotyic choriomeningitis virus
LM	Listeria monocytogenes
LTA/LTB	Lymphotoxin A and B
M2	Type 2 macrophage
MAPK	Mitogen-activated protein kinase
mCRPC	Metastatic castration resistant prostate cancer
MDSC	Myeloid-derived supressor cell
MHC	Major histocompatibility complex
MMP	Matrix metalloproteinase
MPEC	Memory precursor effector cell
MSI	Microsatellite instability
NFAT	Nuclear factor of activated T cells
NK cell	Natural killer cell
NF-κB	Nuclear factor κB
OVA	Ovalbumin
P4	Progesterone
PBS	Phosphate buffered saline
PD-1	Programmed cell death protein 1
PD-L1/PD-L2	Programmed cell death ligand 1 and 2
PFN	Perforin
PMA	Phorbol 12-myristate 13-acetate
pMHC	peptide-loaded MHC
PPSM	Pten- p53- SMAD4- prostate cancer cell line
PR	Progesterone receptor
PRC2	Polycomb repressive complex 2
PSA	Prostate specific antigen
R1881	Metribolone
RNA	Ribonucleic acid
ROS	Reactive oxygen species
RPMI	Roswell Park Memoria Institute cell culture media
RXRA/B	Retinoid X receptor alpha and beta
SARS-CoV2	Severe acute respiratory syndrome coronavirus 2
SDHA	Succinate dehydrogenase A
SHBG	Sex hormone binding globulin
SLEC	Short lived effector cell
SMARCA	Transcription activator BRG1 aka ATP-dependent chromatin remodeler
SPF	Specific pathogen free
STAT	Signal transducer and activator of transcription
TAM	Tumor-assocaited macrophage
T-bet	T-box expressed in T cells
TCF1/TCF7	T cell factor 1 (encoded by TCF7 gene)
Tcm	Central memory T cell

TCR	T cell receptor
Tem	Effector memory T cell
Tex	Exhausted T cell
Th	Helper T cell
Thy1	CD90
TIM3	T cell immunoglobulin and mucin domain-containing protein 3
TLR	Toll-like receptor
TME	Tumor microenvironment
TNF	Tumor necrosis factor
TNM	Tumor, lymph nodes, and metastasis staging
TOX	Thymocyte selection associated high mobility group box protein
Tpex	Progenitor exhausted T cell
Treg	Regulatory T cell
VEGF	Vascular endothelial growth factor
WT	Wild type

Acknowledgements

First, I would like to thank my mentor, Dr. Amy Moran, for her support of me on my personal and professional journey through graduate school. It has been a joy and an honor to work with Dr. Moran and the incredible team of scientists she has assembled around her. I thank Dr. Moran for having the patience and trust in me to give me agency in driving my project forward, and for offering me wisdom and guidance along the way. I believe I have developed into a better scientist in every way thanks to her mentorship. I truly appreciate her careful and deliberate approach to research and her willingness to go after difficult and meaningful questions. I am incredibly proud of what we have accomplished together and to have played a part in the incredible research community that Dr. Moran has built.

Secondly, I would like to thank the members of my dissertation advisory committee, Drs. Melissa Wong, Julia Maxson, Megan Burger, and former member Dr. Jeffery Nolz, for their advice and guidance as I navigated career decisions and moving a difficult project forward. They are an incredible team of scientists, and I am honored to have had the opportunity to learn from their expertise. Their dedication to my success was evident in every meeting and undoubtedly made me a better scientist. I would also like to thank Dr. Susan Murray, who is not only serving on my dissertation defense committee but has also worked closely with me as a collaborator in the Moran lab. Dr. Murray's enthusiasm for research and teaching are inspiring and her advice as I seek a career in teaching and mentoring has been invaluable.

There are many more incredible people at OHSU who have played large and small parts in contributing to my success. My project could not have progressed without the dedicated work of the support staff at OHSU, including the Department of Comparative Medicine, the flow cytometry core, and the massively-parallel sequencing shared resource.

I also want to acknowledge the cancer biology and immunology groups at OHSU for their valuable feedback on my research as my project progressed. I would also like to thank my fellow students who have been an incredible resource for camaraderie, support, and advice while navigating the difficulties of being a graduate student. I would like to thank my peers in the 2019 PMCB cohort who built an incredible community that endured throughout our years at OHSU and will endure long after. Particularly, I would like to thank Michelle Ozaki and Iván Rodriguez Siordia for their unwavering friendship.

Finally, I want to thank my friends and family, without whose support I could never have made it this far in pursuit of my goals. Thank you to my father, Gary Hawkins, who taught me the value of integrity and dedication and helped me pursue opportunities he never had. He always encouraged me to dream big and taught me to recognize the strength in myself that would empower me to achieve my goals. Most of all, thank you to my incredible fiancé, Kaia Thoreson, who not only invested greatly in my success, but has been the most enthusiastic in celebrating my successes and the greatest comfort during my failures. Kaia is truly the most incredible person I have ever met, and I cannot imagine making it through graduate school without her support.

Abstract

Sex differences in immune responses have long been observed across infectious diseases, autoimmunity, and cancer, yet the molecular underpinnings remain incompletely defined. Here, we examine the role of androgen receptor (AR) signaling in regulating CD8 T cell differentiation and function during homeostasis and infection and investigate its therapeutic relevance in prostate cancer treatment with neoadjuvant androgen axis inhibition and anti-PD1 immune checkpoint blockade. Using a model of CD8 T cell-specific AR knockout (ARKO) in mice, we demonstrate that AR expression is dynamically induced upon TCR engagement. AR-deficient CD8 T cells exhibit enhanced expansion, cytokine production, and effector subset formation in response to bacterial and viral infection. Following acute infection, AR activity favors central memory (Tcm) differentiation and limits memory recall protection. These findings suggest that AR tempers early effector responses limits the potential for long-term immunity. Ultimately, we associate mechanisms of AR regulation of CD8 T cell responses to sex differences in CD8 T cell responses, which may be instrumental in understanding the underlying mechanisms behind sex differences in disease susceptibility.

Complementing these mechanistic studies, single-cell RNA sequencing of prostate tumors from patients treated with neoadjuvant androgen axis inhibition (AAI), which includes androgen deprivation therapy (ADT) and AR inhibition, and anti-PD-1 immunotherapy reveals therapy-induced changes in the prostate tumor environment. Neoadjuvant therapy is associated with reduced AR activity and cancer cell frequency in post-treatment biopsies compared to pre-treatment, increased antigen presentation by neoplastic epithelial cells, and enhanced infiltration of cytotoxic effector T cells (CD8 Teff). Notably, AR inhibition in tumors mimics some of the CD8 T cell phenotypes observed in

ARKO mice, including a shift toward effector differentiation. However, the persistence of stromal and myeloid cells with immunosuppressive features highlights the complexity of the tumor microenvironment and the need for combinatorial approaches.

Together, these findings establish AR as a key transcriptional brake on CD8 T cell effector function and memory fate decisions. They reveal a convergence between AR-regulated immune mechanisms in infection and cancer, with important implications for understanding sex differences in disease susceptibility and optimizing AR-targeted therapies and immunotherapies.

Chapter 1: Background and Introduction

1.1 Background and Context

1.1.1 Scope

This dissertation is principally concerned with CD8 T cells and describing the role of sex hormones, particularly androgens, in shaping their response to viruses, intracellular bacteria, and cancer. The remainder of **Chapter 1** provides an overview of the development, function, and maintenance of CD8 T cells in immune responses; the influence of sex and sex hormones on immune responses; and the use of anti-androgen therapies in prostate cancer and their effects on the immune response. **Chapter 2** describes investigations into the role of the androgen receptor (AR) in regulating CD8 T cell immune responses using *in vitro* models and *in vivo* bacterial and viral infections. **Chapter 3** leverages data from a clinical trial of high-risk prostate cancer patients to describe the impact of systemic androgen deprivation therapy, AR small molecule inhibitors, and immunotherapy on the epithelial, stromal, and immune cells of the tumor microenvironment. The culmination of this work is discussed in **Chapter 4**, followed by a discussion of remaining questions to be addressed and suggested approaches to do so.

1.1.2 Overview of the immune system and the role of T cells in adaptive immunity

The immune system is tasked with maintaining the health of hosts by preventing disease. To achieve this, the complex network of cells and molecules that comprise the immune system work together to surveil the body, identify potential threats, and mount a coordinated response to eliminate them. Each of these processes is tightly regulated by molecular signals that ensure that immune cells respond appropriately to eliminate the threat while preserving the health of the host. To that end, local, long-range, and systemic cues are integrated by immune cells to discern whether the environmental context warrants an immune response. When this information is properly relayed and received, the immune system efficiently recognizes and eliminates threats posed by external or internal sources. This process can be conceptually divided into three phases: 1) recognition of the threat by innate immune cells, which act to limit pathogen spread and recruit additional immune cells through inflammatory cues, 2) presentation of pathogenic antigens to adaptive immune cells, which subsequently gain the ability to specifically target and eliminate the pathogen, and 3) resolution of the threat, contraction of responding immune cell populations, and repair of damaged tissue (**Figure 1.1**). Some cells, chiefly T and B lymphocytes of the adaptive immune system, survive long after the contraction phase and retain the capacity to respond quickly and protect the host from re-challenge by the same threat, a phenomenon termed immune memory.

T and B lymphocytes (i.e., T and B cells) are both cell types of the adaptive immune system, which express antigen receptors that can bind to specific epitopes from target cells or pathogens and stimulate their recognition and destruction. The B cell receptor (BCR) generally recognizes extracellular antigen epitopes in their natural conformation (i.e., non-denatured) and is produced and released by B cells in a soluble form called antibodies (humoral immunity). In contrast, the T cell receptor (TCR) is a membrane-bound receptor which recognizes short antigen structures processed and presented on major histocompatibility complex (MHC) proteins on the target cell surface. T cell mediated immunity is therefore called cellular immunity because of the requirement for antigens to be processed and presented on the surface of other host cells. Both BCRs and TCRs are derived from DNA recombination which generates high variability in the sequence of the antigen receptors on a cell-by-cell basis. This high variability produces a repertoire of billions of adaptive immune cells with billions of unique antigen receptor specificities collectively, able to respond to virtually any antigen epitope.

T cells can be generally divided into two main sub-types based on the specificity for their TCR for antigens presented on MHC class I (MHCI) or MHC class II (MHCII), with concomitant expression of the TCR co-receptors, CD8 and CD4, respectively. MHCI is expressed by all nucleated cells in the body, and the main function of CD8-expressing T cells (i.e., CD8 T cells) is to recognize antigens presented on MHCI and effectuate the death of the cells presenting them. MHCII is mainly expressed by cells of the innate immune system which present antigens to CD4 T cells, which in turn release signals that help amplify and support the immune response. Therefore, CD8 T cells are also called cytotoxic T lymphocytes (CTLs) and CD4 T cells are also called T helper cells (Th).

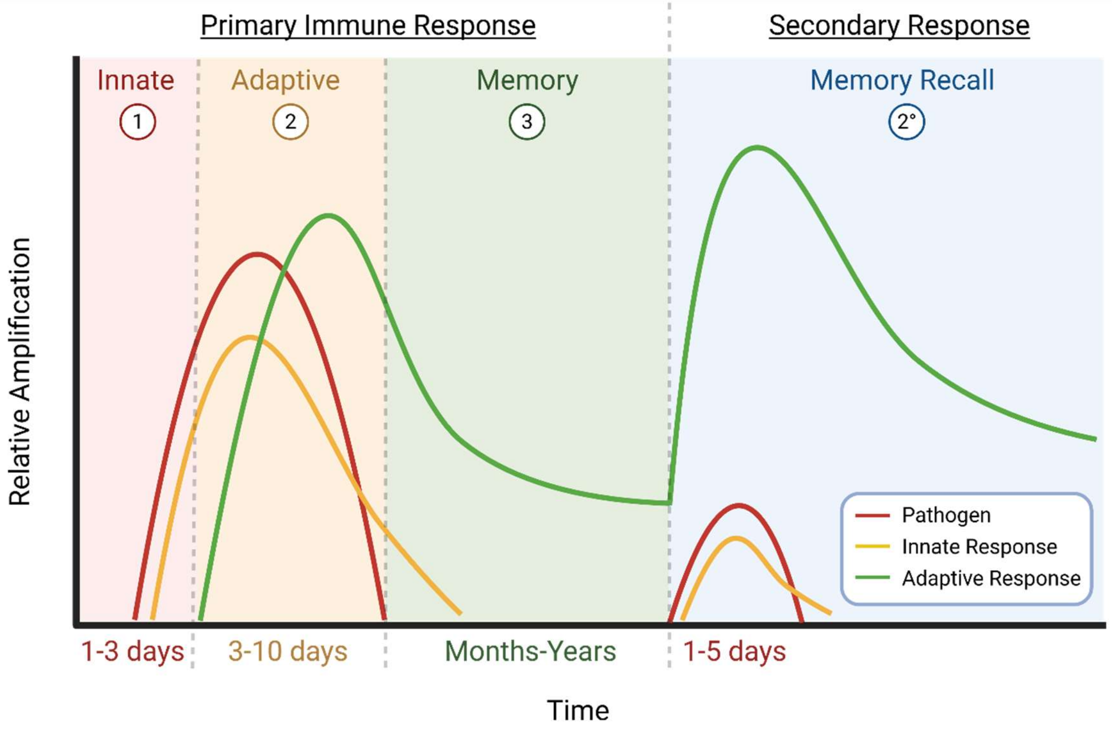

Figure 1.1 Phases of immune responses

When a pathogen establishes an infection, the primary immune response to that pathogen can be divided into three phases: 1) Innate immune cell recognition of the threat, recruitment of other immune cells to the infection site, and containment of the threat, 2) presentation of pathogen-derived antigens by antigen presenting cells (APCs) to adaptive immune cells which, along with co-stimulatory receptor engagement ant cytokine signaling, initiates priming, activation, and differentiation of naïve T cells into effector and memory populations, and 3) programmed apoptosis of terminally-differentiated effector cells and survival of T cells with the capacity to differentiate into memory populations. The initial response by innate immune cells is typically short before adaptive immune cells begin to be activated. By 7-14 days post-infection, most infections are efficiently cleared by adaptive immune cells, some of which survive for months to years as memory cells. In the case of a secondary challenge by the same pathogen, memory adaptive immune cells are capable of rapidly re-expanding and releasing effector molecules to efficiently eliminate the infection. Created with biorender.com

1.2 Mechanisms of CD8 T cell Immune Responses

1.2.1 Naïve T cell development and homeostasis

The pool of naïve conventional αβ T cells poised to respond to pathogenic challenge is generated through the maturation of lymphoid progenitors in the thymus. During this process, immature, CD4 and CD8 double-positive (DP) lymphocytes are queried for reactivity against self-peptide-MHC (self-pMHC) complexes presented by thymic epithelial cells (1). T cell receptor (TCR) interaction with pMHC is a critical signal to promote the survival of T lymphocytes, but most immature DP cells exhibit little or no reactivity to self-peptide-MHC and therefore die by neglect. The cells that react strongly (i.e., have a TCR with high affinity for self-pMHC) are programmed to die to prevent the production of mature T cells capable of targeting healthy host tissues. Those cells that exhibit low, but sufficient affinity for self-pMHC survive selection in the thymus and become mature CD4 or CD8 single-positive T cells, depending on their reaction to MHC class II or MHC class I, respectively.

In the periphery, mature, naïve T cells are long-lived, relatively quiescent cells, that exhibit low levels of transcription, cellular respiration, and proliferation (2). These cells are phenotypically defined by expression of L-selectin (CD62L), CCR7, and CD27, while lacking CD44 expression (3). During this time, the survival of naïve T cells relies on signals received through tonic, low-level TCR engagement and cytokines such as IL-2, IL-7 and IL-15 in the environment (4-7). Peripheral CD5 expression correlates with CD8 T cell responsiveness to homeostatic cytokines, including IL-2, IL-7 and IL-15, but not responsiveness to TCR ligation by anti-CD3 antibody stimulation (8). This hyperresponsiveness of CD5hi cells is dependent on continued self-pMHC engagement and enhanced formation of GM-1-containing lipid rafts that enhance signal transduction (9). Thus, the developmental and environmental experience of CD8 T cells dictates their homeostatic maintenance and the magnitude of their response to proliferative signals.

The TCR and cytokine signals received by naïve T cells are usually weak enough to promote their survival while maintaining the cells in a resting state, just below the threshold required to induce activation and entry into the cell cycle (10). However, exposure to higher concentrations of homeostatic cytokines or heightened responsiveness to self-pMHC can induce homeostatic proliferation of naïve T cells and acquisition of features normally associated with memory T cells (**Figure 1.2**). Naïve T cells that acquire this memory-like phenotype in the absence of cognate antigen encounter have been called “virtual memory” cells and are defined by the expression of CD44, the IL-2 receptor β chain (CD122), and the absence of α4 integrin (CD49d) expression (11, 12). Functionally, virtual memory CD8 T cells retain many characteristics associated with conventional memory CD8 T cells, including the ability to quickly proliferate, acquire effector function, and control pathogen burden in response to infection (13, 14). Therefore, the differentiation of virtual memory CD8 T cells represents an alternative pathway of memory differentiation that does not require recognition of foreign pMHC and inflammatory cues produced during infection.

During homeostasis, T cells that have not yet encountered their cognate antigen recirculate through blood and secondary lymphoid organs such as the lymphatic vessels, lymph nodes, and spleen. At this stage, gene expression, particularly expression of genes involved in the T cell effector response, is relatively low (15-17). In order to respond to infection and differentiate into effector and true memory cells, naïve T cells must encounter foreign pMHC on APCs and inflammatory cues that strongly drive their proliferation and differentiation.

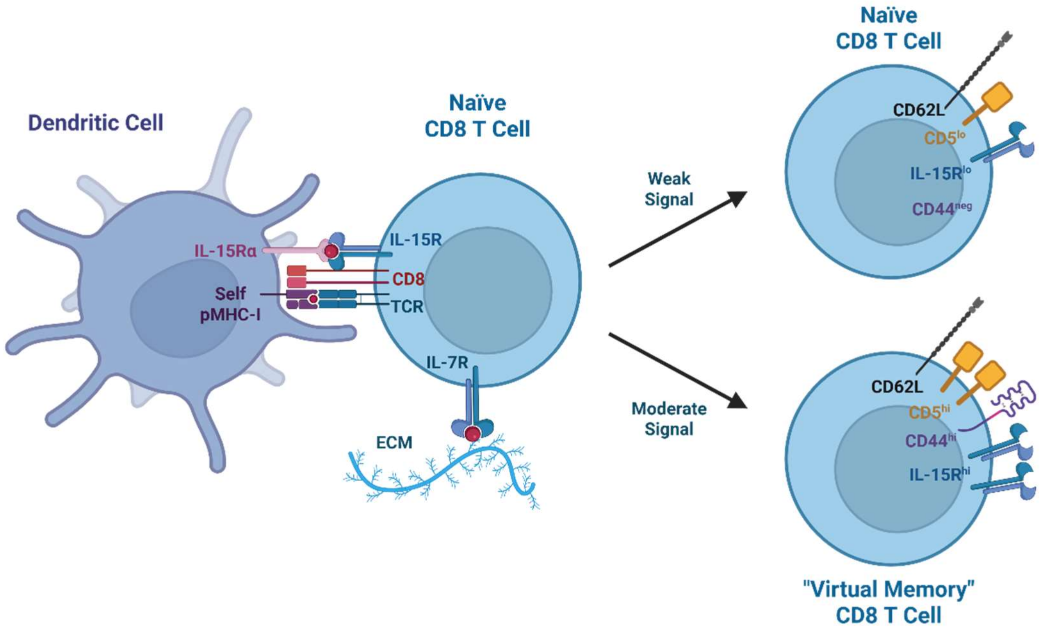

Figure 1.2 Generation of virtual memory T cells

The engagement of low-affinity self-pMHC complexes as well as low-level cytokine signals from APCs or the environment are critical for the survival of naïve CD8 T cells. When these signals remain low, naïve CD8 T cells remain in a quiescent state and maintain their naïve characteristics. However, when these signals are moderate to strong, they may stimulate proliferation of naïve CD8 T cells and the expression of memory-associated markers such as elevated IL-15R, elevated CD5, and CD44 expression. ECM = extracellular matrix. Created with biorender.com

1.2.2 T cell activation, expansion, and acquisition of effector characteristics

Upon pathogenic challenge, naïve CD8 T cells differentiate into effector and memory cells through a complex and highly regulated process stimulated by TCR-mediated recognition of antigens presented on MHCI, co-stimulatory interactions, and cytokine engagement, which act together to initiate epigenetic and transcriptional changes that control CD8 T cell fate (18-22). Upon encounter with mature antigen presenting cells

(APCs)—primarily dendritic cells (DCs)—presenting cognate antigens in secondary lymphoid organs, naïve CD8 T cells initiate a program of proliferation and differentiation into effector CTLs. The signals required to initiate that program can be broadly split into three categories: signals received through direct TCR:pMHCI interactions (signal 1), co-stimulatory receptor engagement (signal 2), and environmental cues such as inflammatory cytokines (signal 3) produced by APCs, CD4 helper T cells, or other environmental sources **(Figure 1.3)** (23, 24). If one of these environmental cues is not present, naïve CD8 T cells that receive a signal through TCR:pMHCI interactions may undergo programmed cell death rather than differentiate into effector CTLs (25).

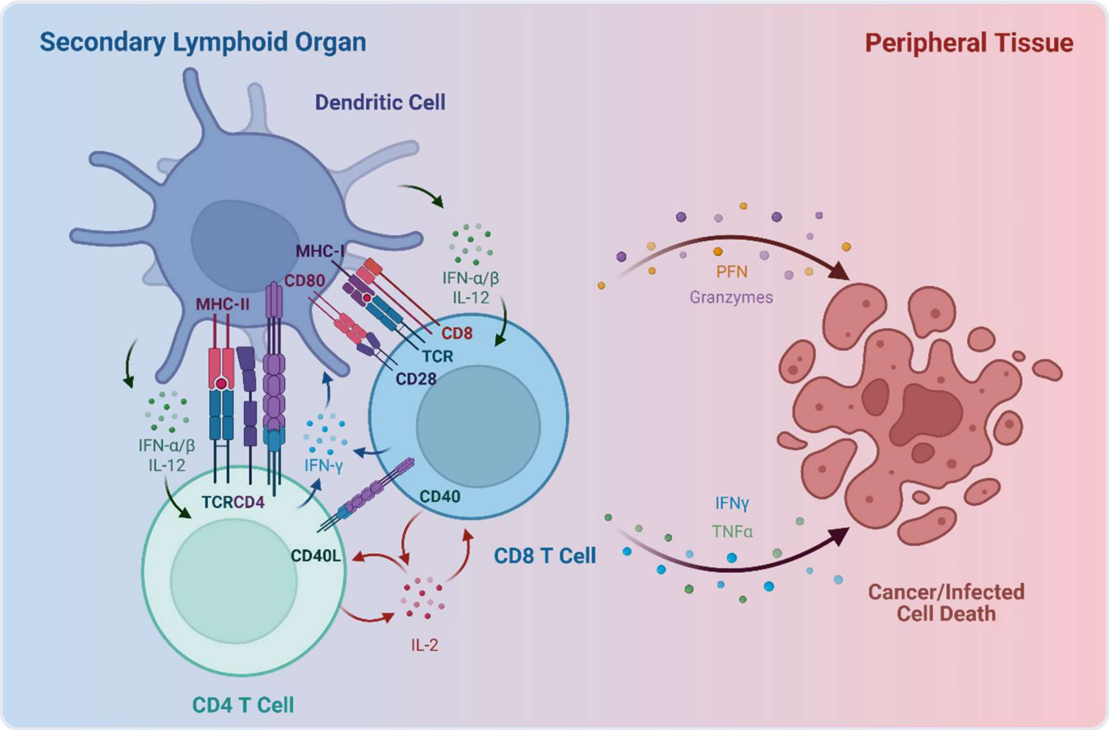

Figure 1.3 T cell priming and activation

Naïve CD8 T cells are primed to differentiate into effector and memory populations in secondary lymphoid organs by APCs which present pathogen-derived antigens on MHC complexes on their surface. This process involves the cooperation of APCs, CD4 Th, and CD8 T cells. These cells provide important co-stimulatory cues and release cytokines, such as interferons and IL-12, which support the survival, differentiation, and function of each other. Once primed and activated, CD8 T cells gain the capacity to produce and release cytotoxic molecules such as perforins (PFNs), granzymes, and TNFα to induce the death of infected or malignant cells. Created with biorender.com

When all three signals are present, a cascade of signal transduction and transcription factor activation initiates cytoskeleton reorganization, metabolic shifts, and changes in gene expression that endow CD8 T cells with the ability to rapidly proliferate, migrate to sites of inflammation, and produce and release effector molecules such as perforins, granzymes, and interferons. The main pathways activated downstream of TCR and co-stimulatory receptor engagement (signals 1 and 2) converge on mitogen-activated protein kinase (MAPK) phosphorylation, calcium flux, and nuclear translocation of transcription factors, including nuclear factor κ B (NF- κB), nuclear factor of activated T cells (NFAT), and activator protein 1 (AP-1), which work together to initiate the expression of genes involved in CD8 T cell effector and memory differentiation and function (26, 27). Additionally, critical transcription factors that are induced by these signaling cascades include T-box expressed in T cells (T-bet), forkhead box O1 (FoxO1), inhibitor of DNA binding 2 (ID2), ID3, B lymphocyte-induced maturation protein-1 (Blimp1), and eomesodermin (Eomes), which are active at varying levels depending on the strength and nature of signals received by CD8 T cells and ultimately dictate CD8 T cell phenotypic fate (21, 22). The differentiation of CD8 T cells into effector CTLs is favored by the activity of T-bet, ID2, Eomes, and signal transducer and activator of transcription (STAT) proteins, the latter of which can be activated downstream of signal 3 provided by IL-12, type I interferons such as interferon α (IFNα) or IFNβ, or other cytokines (22, 28-31).

The cytokines produced and released into the environment vary by the type of pathogen encountered, and therefore the exact STAT molecules that are active in responding CD8 T cells also vary by infection. For example, IL-12 activates STAT 4 in CD8 T cells and is produced by antigen presenting cells in response to interactions with T helper cells and Toll-like receptor 3 (TLR3) and TLR4 activation by bacterial lipopolysaccharide or viral dsRNA, respectively (32, 33). By contrast, type I interferons induce STAT1 and STAT2 (and sometimes STAT4) activation in CD8 T cells and are produced primarily by plasmacytoid dendritic cells and to a lesser extent by other immune cells when they sense intracellular foreign genetic material (28, 31, 34). Therefore, distinct kinds of pathogens can elicit disparate responses by CD8 T cells through the induction and release of different cytokines into the environment.

1.2.3 Heterogeneity of the CD8 T cell effector response

Early during priming and activation, CD8 T cells acquire the ability to differentiate into distinct populations of effector cells called short-lived effector cells (SLECs) and memory precursor effector cells (MPECs; **Figure 1.4**) (35). SLECs generally exhibit a high capacity for effector function, but do not survive following infection clearance, whereas MPEC exhibit relatively lower effector capacity, but are able to survive and give rise to memory populations following pathogen clearance (36). These populations of effector cells can be discriminated by expression of surface markers killer cell lectin-like receptor subfamily G member 1 (KLRG1) and IL-7 receptor α (IL-7Rα a.k.a. CD127), such that SLECs express high KLRG1 and low CD127 and MPECs express low KLRG1 and high CD127 (36-

38). In adoptive transfer experiments, transfer of sorted CD8 SLECs and MPECs from infected mouse donors into infection-matched recipients demonstrated that SLEC and MPEC phenotypes are generally stable early during infection, with most transferred cells retaining their phenotypic expression of KLRG1 and CD127 two days after transfer (39). Notably, transferred MPECs were able to survive up to 35 days post-infection and seed the pool of memory cells, whereas very few SLECs were detected following pathogen clearance. These data demonstrate a differential capacity for SLECs and MPECs to survive contraction and persist as memory populations following the resolution of infection. However, the phenotypic division of SLECs and MPECs by expression of KLRG1 and CD127 does not perfectly divide cells by their capacity to generate memory. Some KLRG1highCD127low cells persist long after infection resolution and some effector and memory populations express both KLRG1 and CD127 (36, 37).

The molecular influences that control differentiation of effector CD8 T cells into SLEC and terminal effector cells or MPEC and memory cells are established early during priming. For example, early after infection, Tbet and the zinc finger transcription factor Blimp1 are expressed at higher levels in SLECs than MPECs and are required for the development of KLRG1^{+}CD127^{-} SLECs (36, 40, 41). Mechanistically, T-bet supports SLECs by promoting IFNγ expression, repressing CD127 expression, and supporting CD122 (IL-2/IL-15β receptor) expression and supporting SLEC survival in the late stages of the effector response (42). Blimp1 expression supports high expression of effector molecules, including granzyme B (GZMB) and perforin while repressing expression of receptors involved in T cell homing to secondary lymphoid organs, including CCR7 and CD62L (40, 41). Blimp1 also inhibits the expression of ID3 and TCF1, both of which are required for the long-term survival of MPEC cells (43). In turn, TCF1 supports the expression of Eomes, a transcription factor that promotes expression of CD122 and supports survival of MPECs and later memory cells through IL-15 signaling (42). Finally, FoxO1 expression promotes MPEC fate by both inhibiting expression of SLEC-associated Tbet and promoting Eomes, CD127, and CD62L expression (44). Expression of FoxO1 in early effector CD8 T cells supports expression of memory-associated genes by shielding the gene loci from the deposition of repressive histone modifications by the polycomb repressive complex 2 (PRC2) (45). Taken together, these findings demonstrate that distinct gene expression programs in SLECs and MPECs are driven by the opposing functions of transcription factors that ultimately dictate effector cell fate during differentiation.

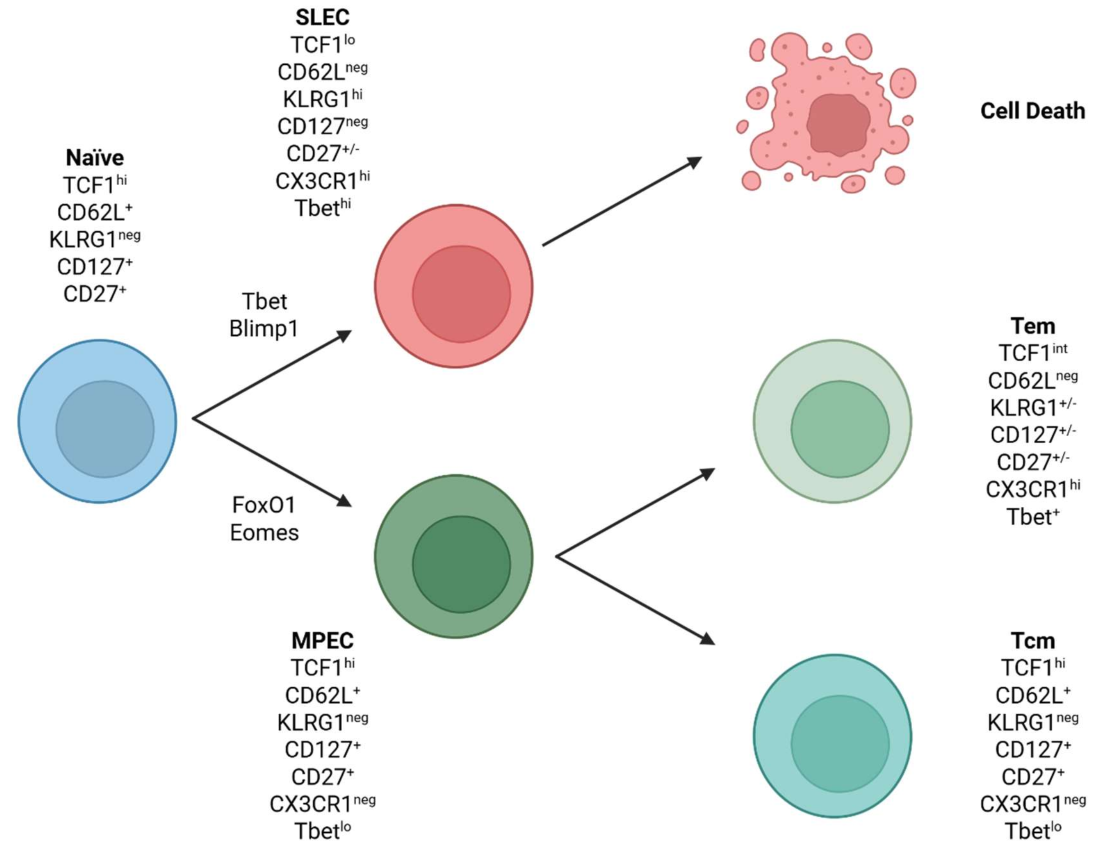

Figure 1.4 T cell effector and memory differentiation

Early during priming, CD8 T cells begin to acquire phenotypic characteristics associated with effector function and differentiate into two distinct populations with disparate propensity to survive and differentiate into memory populations following pathogen clearance. Short lived effector cells (SLECs) are phenotypically marked by low expression of TCF1, CD62L, and IL-7R (CD127), high expression of KLRG1, CX3CR1, and Tbet, and high capacity for effector function. SLECs eventually give rise to terminally differentiated effector cells which generally do not survive following pathogen clearance. Memory precursor effector cells (MPECs) are phenotypically marked by high expression of TCF1, CD62L, IL-7R (CD127), and CD27 and low expression of KLRG1, CX3CR1, and Tbet, and give rise to effector memory (Tem) and central memory (Tcm) T cells that survive contraction and contribute to the pool of memory cells that protect from re-infection.

1.2.4 Memory T cell homeostasis

Unlike naïve T cell homeostasis, the homeostatic survival of memory T cells is MHC-independent but remains dependent on IL-7 and IL-15 (7, 46). Studies of IL-15 deficient mice confirmed the requirement of IL-15 produced by non-T cells for the survival of memory CD8 T cells (47-49). The contribution of IL-7 to memory T cell homeostasis was discovered in IL-15 deficient mice, where it was found that endogenous levels of IL-7 were insufficient to support memory survival without IL-15, but overexpression of IL-7 could do so (50). Mechanistically, both IL-15 and IL-7 stimulate STAT5 phosphorylation and B cell lymphoma 2 (Bcl2) expression, an anti-apoptotic protein that to suppresses pro-apoptotic protein activity (51-54).

Although the survival of memory CD4 T cells does not depend on MHCII, in the absence of MHCII engagement, the functional capacity for memory CD4 T cells to respond to rechallenge is impaired (55). By contrast, memory CD8 T cell survival and maintenance of recall capacity does not depend on MHCI. However, although the generation of memory CD8 T cells does not require CD4 T cell help, without CD4 T cells memory CD8 T cells gradually decline in abundance over time and lose their protective capacity (56-60). Studies of CD4 T cell deficient mice demonstrated reduced expression of the IL-7 and IL-15 receptors on CD8 T cells in the absence of CD4 T cell help (61, 62). Additionally, without CD4 T cell help, memory CD8 T cells rapidly induce expression of tumor-necrosis factor-related apoptosis-induced ligand (TRAIL) and undergo activation-induced cell death (14, 63). However, TRAIL deficiency does not fully restore the capacity for memory CD8 T cell protection (64). Therefore, the survival and protective capacity of memory CD8 T cells is mediated through IL-7 and IL-15 signaling and is supported by CD4 T cell help.

1.2.5 T cell differentiation and function in chronic disease

When the immune response is unable to clear an inflammatory challenge as in chronic viral infections and persistent cancer, it becomes advantageous to dampen the immune response to limit off-target toxicity caused by prolonged inflammation (65, 66). T cells adapt to the persistent challenge by limiting their effector activity through a process called exhaustion, which develops at the expense of memory differentiation. Exhaustion is induced by the induction of exhaustion-associated transcription factors such as TOX, BATF, and IRF4 and upregulation of immune checkpoint receptor expression, including programmed cell death protein 1 (PD1), lymphocyte activation gene 3 (LAG3), and T cell immunoglobulin domain and mucin domain protein 3 (TIM3) (28, 67, 68). T cell exhaustion has also been associated with transcriptional, epigenetic, and metabolic shifts which enforce the exhausted cell state in the face of persistent antigen encounter. These adaptations act together to reduce TCR and co-stimulatory signal transduction, the expression of CD8 T cell effector genes, including IFNγ, TNFα, perforins, and granzymes, and oppose the acquisition of memory-associated features (69-71).

T cell exhaustion was first characterized in detail in mouse models of chronic lymphocytic choriomeningitis virus (LCMV) infection, which is unable to be cleared before day 40+ post-infection (72, 73). Since then, other studies have extended those findings and described T cell exhaustion in other chronic viral infections, including HIV (74-77), HCV (78, 79), and HBV (80); autoimmune diseases (81, 82); and cancer (83, 84), including melanoma (85), non-small cell carcinoma (86), and chronic myeloid leukemia (87). T cells in the prostate tumor microenvironment also resemble exhausted cells and express PD-1, TIM3, CTLA4, and TIGIT (88, 89). Thus, T cell exhaustion likely contributes to prostate cancer treatment resistance and progression.

There are several immunosuppressive cell types with roles in promoting T cell exhaustion in both infection and cancer settings. The major types of suppressive immune cells that limit T cell responses are suppressive cells of the myeloid lineage, myeloid-derived suppressor cells (MDSC) and tumor-associated macrophages (TAMs), as well as regulatory T cells (Tregs). These cell populations are best defined by their functional capacity to limit the function of other cell types, which includes inhibition of effector T cell function through production of inhibitory mediators such as IL-10, tumor growth factor β (TGFβ), reactive oxygen species (ROS), and L-arginine depletion through activity of arginase 1 (ARG1) (90, 91). Therefore, it is important to uncover the mechanisms of T cell exhaustion in chronic disease so we can rationally design treatments to prevent and reverse exhaustion and renew the T cell anti-viral and anti-tumor immune response.

1.2.6 T cell responses to immune checkpoint blockade (ICB)

When T cell exhaustion was first described, it was unclear whether it is a cell state that is irreversible like terminal differentiation, or whether it could be reversed to replenish the immune response (66). Barber et al. discovered that blocking interactions between PD-1 and its ligand PD-L1 could rejuvenate the anti-LMCV immune response in chronic infection and could simulate the clearance of viral load. Similar findings were made for T cell exhaustion in cancer (92-94). Later studies revealed that a specific exhausted cell subset is responsible for re-invigorating and sustaining anti-tumor T cell effector responses (95). This subset of PD-1-expressing Tex cells was found to express features of memory or stem-like T cells (CXCR5 and TCF1) while lacking expression of markers of terminal exhaustion (TIM3, LAG3 and others). In response to anti-PD-1 or anti-PD-L1 immune checkpoint blockade, this subset, called progenitor exhausted T cells (Tpex), proliferates and produces cells with the capacity to release effector molecules and migrate to the tumor or infection site.

Since the discovery that blocking PD-1 could reinvigorate T cell responses, antibody drugs targeting immune inhibitory protein, PD-1, PD-L1, and CTLA4 have been clinically tested and approved to treat several cancer types. The first antibody to achieve FDA approval, ipilimumab, targets CTLA4. CTLA4 is upregulated on activated T cells and inhibits T cell responses by outcompeting CD28 for ligand binding and recruiting inhibitory intracellular signaling molecules to the immune synapse (96-98). Additionally, CTLA4 is expressed by regulatory T cells (Tregs) and supports their suppressive function (99). Blockade of CTLA4 enhances antitumor immunity and was first validated in murine models before achieving clinical success in metastatic melanoma (100-103). PD-1, expressed predominantly on exhausted T cells, inhibits TCR signaling through SHP-2-mediated dephosphorylation (104). Blocking PD-1 or its ligand PD-L1 with antibodies like pembrolizumab, nivolumab, and atezolizumab has demonstrated efficacy in various cancers, including melanoma and non-small cell lung cancer (NSCLC), leading to FDA approvals (105-108). These therapies have been approved for a range of cancers, often in combination with chemotherapy or other immunotherapies. Despite their success, only a subset of patients respond and resistance can emerge. For example, although melanoma typically has one of the highest response rates to ICB, about 60-70% of patients do not respond to ICB treatment, and approximately 20-30% of responders eventually relapse (109, 110). Ongoing clinical trials are exploring new combinations and therapeutic strategies to overcome these challenges and expand the clinical benefit of ICB.

Although immune checkpoint blockade (ICB) has been shown to elicit robust immune responses and durable remission for many patients of diverse cancer types, the clinical response rate is highly variable between different cancer types and most patients do not achieve durable remission (111). Therefore, identification of factors associated with ICB resistance is an area of intense research. Several factors associated with resistance have been identified to date, including lack of target expression within the tumor, low tumor mutational and neoantigen burden, low T cell infiltration into the tumor, and the presence of immunosuppressive cell types within the tumor environment (111). Furthermore, despite initial responses to ICB, many patients acquire therapy resistance, which occurs through mechanisms such as expression of alternative immune checkpoints, treatment-associated influx of immunosuppressive cells, and loss of antigen presentation on cancer cells (111). Notably, the presence of immunosuppressive cells within the tumor environment can lead to both primary and acquired resistance to ICB. Therefore, there have been many efforts to understand and therapeutically reverse the mechanisms of immunosuppression in the tumor environment to reduce ICB resistance.

Immunosuppressive cell types identified within the tumor environment of many tumor types include Tregs, myeloid-derived suppressor cells (MDSCs), and tumor-associated macrophages (TAMs). Tregs suppress effector T cell and antigen-presenting cell activity via immunosuppressive cytokines (IL-10, IL-35, TGF-β) (112). Although ICI treatment can reduce Treg levels and improve the effector T cell/Treg ratio, incomplete depletion and compensatory upregulation of other checkpoints may sustain immunosuppression (28, 113-117). TGF-β and adenosine production by Tregs have been specifically linked to resistance. MDSCs similarly suppress immune responses by releasing immunosuppressive cytokines and producing enzymes such nitrous oxide synthase, arginase-1, and indoleamine 2,3-dioxygenase, which produce suppressive nitrogen species and deplete arginine and tryptophan in the tumor environment (118-121). The presence of MDSCs in the TME correlates with poor ICI efficacy (122-126). Moreover, blocking MDSC recruitment can enhance responses, indicating their role in both primary and acquired resistance (127, 128). TAMs, particularly those polarized to the M2 phenotype, also drive resistance through multiple mechanisms: releasing immunosuppressive cytokines into the tumor environment, upregulating PD-L1 on tumor cells, and physically impeding $CD8^+$ T cell infiltration (129, 130). Studies show that depleting M2 TAMs or reprogramming them toward the M1 phenotype improves ICI outcomes (131-134). Additional mechanisms of resistance include $PD\text{-}1^-$ TAMs capturing anti-PD-1 antibodies from $PD\text{-}1^+$ T cells, blunting therapeutic efficacy (135). Overall, the immunosuppressive TME is a major barrier to successful ICI therapy. Strategies that reprogram the tumor immune environment through combination therapies or disrupting harmful immune cell interactions have shown promise in overcoming resistance and improving treatment outcomes.

1.3 Sex Differences in Immune Responses

1.3.1 Sex as a biological variable

Biological sex generally refers to males and females as defined by sex chromosome composition (i.e., XX or XY), development and maintenance of reproductive tissues (i.e., testes and ovaries), and the concentrations of circulating sex hormones, including androgens and estrogens. Each of the aspects that govern biological sex work together to support development and maintenance of sex characteristics, including sex differences in the function of non-reproductive tissues and cells. Although most human individuals can be categorized into XY male or XX female sex identities, many individuals cannot, including those with uncommon sex chromosome composition (for example XXY), transgender individuals receiving gender-affirming hormone therapy (GAHT), and individuals with differences in sexual development. Nonetheless, many of the factors that influence sex differences, including sex hormones, influence the biology of an individual regardless of their sexual development. For example, although estrogen is predominantly responsible for supporting female sexual development, androgens are also present in females and influence many aspects of their biology. In fact, while the circulating concentration of estrogen in normal adult females is ~200 pg/mL, the concentration of circulating testosterone in normal adult females is ~1000 pg/mL, or about 5x higher than estrogen, suggesting that androgens have important biological functions beyond supporting male sexual development (136). Therefore, understanding the function of sex hormones and their receptors on tissues and cells outside of the reproductive tract is important in understanding how sex hormones contribute to sex differences across organ systems.

1.3.2 Introduction to androgen hormones and mechanisms of AR activity

Steroid hormones are a class of cholesterol-derived hormones produced by the enzymatic conversion of cholesterol derivatives in various tissues, including adrenal glands, salivary gland, kidney, testes, ovaries, breast, and adipose tissue (137). Steroid hormones that are critical for the development and maintenance of sex-specific biology are classified by the receptors they bind to and are found at varying circulating concentrations based on the individual's sex. Generally, androgen hormones bind to the androgen receptor (AR) and are found at higher concentrations in males, whereas estrogen and progesterone hormones bind to the estrogen (ER) and progesterone (PR) receptors, respectively, and are found at higher concentrations in females.

AR, ER, and PR are classes of nuclear hormone receptors that exert ligand-dependent and ligand-independent control over signaling cascades and gene transcription. In the absence of its ligand, AR is normally sequestered in an inactive form in the cytoplasm by heat shock proteins, including heat shock proteins (HSPs, **Figure 1.5**). Upon binding to androgens, AR is released from cytoplasmic chaperones, homodimerizes, and translocates to the nucleus where it can bind DNA at specific motifs called androgen response elements (AREs), recruit cofactors, and regulate target gene expression (138). The class of androgen hormones includes testosterone, 5α-dihydrotestosterone (DHT), androstenedione, dehydroepiandrosterone (DHEA) and its sulfated form, DHEA-S, which vary by their molecular structure, enzymatic derivation, and affinity for AR (139). Following their synthesis, androgens are secreted into blood and circulate throughout the body in blood vessels. The predominant form of androgens in blood is testosterone, which has a high affinity for sex hormone-binding globulin (SHBG), which binds to the majority of circulating testosterone (>97%) (138). Upon entering cells, testosterone can be converted into DHT by

5α-reductase, although this dynamic is based on studies of male reproductive organs and may not be present in all cells. DHT is a higher-affinity ligand for AR than testosterone or other androgens and therefore more potently induces AR activity (139). Additionally, testosterone and other sex hormones can be interconverted by enzymatic activity. For example, testosterone is converted into estradiol by the enzyme aromatase, which frequently occurs in adipose tissue, the hypothalamus, and hematopoietic tissue (140). It is therefore important to consider the complexity of the synthesis and enzymatic interconversion of steroid hormones when studying their effects on physiology. In many cases, as in the approaches described herein, a more definitive approach to uncovering the cell-intrinsic impacts of sex steroid hormones is to manipulate the hormone receptor of interest rather than the systemic, circulating concentrations of the hormones themselves. The work described herein does not attempt to determine whether the activity of other steroid hormone receptors in the absence of AR contributes to the observed phenotypes when AR activity is altered, but the potential implications of such mechanisms will be discussed in **Chapter 4**.

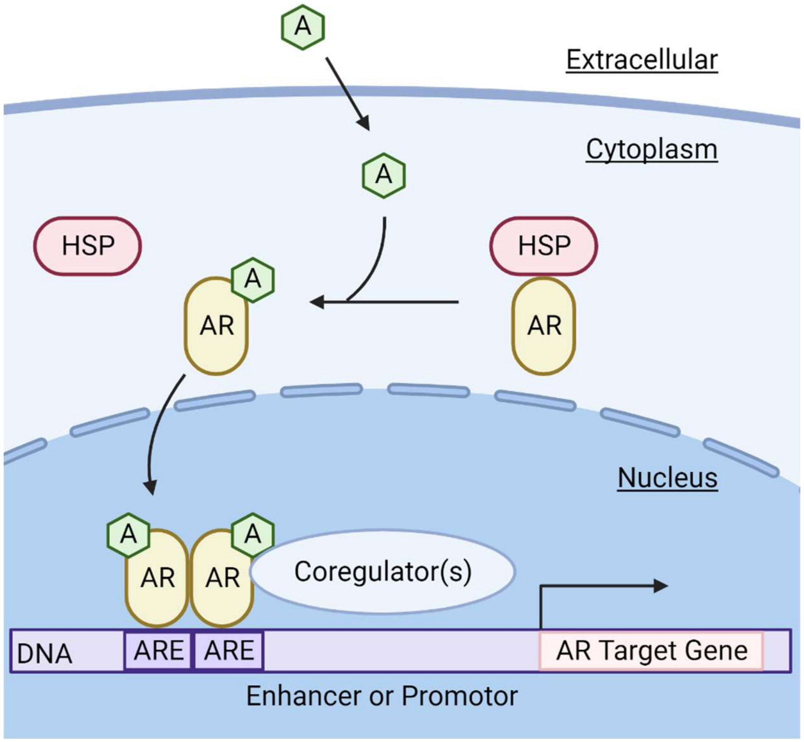

Figure 1.5 Overview of androgen receptor regulation of transcription

AR is a member of a class of nuclear hormone receptors which bind to small, cholesterol-derived ligands to initiate their function. AR is normally sequestered in the cytoplasm bound to heat shock proteins (HSPs) in an inactive form when ligands are not present. When androgen hormones pass into the cytoplasm, they bind to AR and stimulate its release from HSPs, homodimerization with another AR molecule, and translocation to the nucleus. In the nucleus, AR binds to specific DNA sequence motifs called androgen response elements (AREs), recruits other coregulators, and ultimately controls transcription of nearby AR target genes. Created with biorender.com

1.3.3 Sex differences in disease susceptibility and immune responses

Sex differences in the incidence and mortality from myriad diseases, including infections, cancer, and autoimmunity, have been characterized, with females generally more susceptible to autoimmunity and males more susceptible to many infections and non-reproductive organ cancers, including leukemia, lung cancer and melanoma (141-143). For example, males experience increased hospitalization, intensive care admission, and mortality due to COVID-19 infection (141, 144-148). Additionally, incidence of infection with Dengue virus, hantaviruses, and hepatitis B and C viruses (HBV and HCV) are greater in males than females, and disease outcomes are more severe in males than females infected with Epstein-Barr virus (EBV), HBV, HCV, and West Nile virus (149, 150). Conversely, females experience increased susceptibility to many autoimmune diseases, representing approximately 80% of individuals diagnosed with autoimmunity (143).

Although overall susceptibility to viral infection tends to be greater in males, females experience a higher incidence or severity of infection with some viruses, including more prevalent cytomegalovirus and herpes simplex virus infections and more severe infection with HSV2, human immunodeficiency virus (HIV), and measles virus (150). Interestingly, females also experience increased susceptibility to influenza A virus (IAV). In studies of mice and humans, females exhibit increased lung inflammation and worse outcomes following IAV infection even with similar viral burden (150-153). Several studies have aimed to uncover the roles of sex hormones in contributing to sex differences in IAV susceptibility. In mice, treatment with P4 or synthetic progestin reduced lung inflammation and increased tissue repair after IAV infection (154, 155), and higher concentrations of 17β-estradiol in females protects them during IAV infection by reducing inflammation and promoting the recruitment of neutrophils and CD8 T cells into the lungs (156). On the other hand, testosterone or DHT signaling through AR limits severe IAV in male mice (157). Therefore, sex hormones seem to be protective against IAV in both male and females. This paradox might be explained by the observation that sex hormone production is reduced in females during infection, but further studies are needed to assess that possibility (158, 159).

In general, men are also more susceptible to bacterial infections, including tuberculosis and pneumococcal infection (160-162). However, females tend to be more susceptible to some bacterial infections, including infection with Escherichia coli, Bordetella pertussis, and Listeria monocytogenes (163, 164). The causes of such differential infection susceptibility are multi-faceted. The fact that females are more susceptible to some infections suggests that the mechanisms of differential susceptibility are varied, complex, and dependent on the specific pathogenic challenge.

Among the factors that are associated with sex differences in disease susceptibility are sex differences in immune responses. In general, females are believed to mount stronger immune responses than males which contributes to better disease control in females. Indeed, many studies have described sex differences in the abundance and function of immune cells (143, 165-168). In humans, the number of circulating CD4 T cells and the ratio of CD4 to CD8 T cells are higher in females while the number of circulating CD8 T cells and the abundance of regulatory T cells are higher in men (143). As central components of the adaptive immune response, reduced T cell responses in males could explain why males more often fail to clear infections and tumors. Indeed, studies have demonstrated that T cells from female mice proliferate more and produce more IFNγ in response to stimulation with complete Freund’s adjuvant (CFA) and protein antigens (169, 170). Additionally, female mice mount a stronger T cell response compared to males when vaccinated with malaria sporozoites or infected with HIV (171, 172). In humans, females mount a stronger T cell response to HCV and SARS-CoV2 infection and measles vaccination (173-175). To unravel the relative contribution of sex chromosome composition versus sex hormones in influencing sex differences in T cell responses, some studies have turned to the “four core genotype” (FCG) model (170). The FCG utilizes four genotypes of mice in which sex chromosome composition is uncoupled from gonadal development by knocking out expression of the *Sry* gene, which controls testes development, from the Y chromosome and expressing it on chromosome 3 via a transgenic cassette. Thus, the four genotypes of this model produce XX females and XY males with normal gonadal development as well as $XX^{Sry\text{-}tg}$ males and $XY^{Sry\text{-}}$ females (176). In the FCG model, gonadal females (XX and $XY^{Sry\text{-}}$ mice) exhibit stronger T cell responses than gonadal males (XY and $XX^{Sry\text{-}tg}$ mice) after vaccination with myelin basic protein antigens and CFA, including greater T cell proliferation and IFNγ. These findings demonstrate that sex hormones influence T cell responses regardless of sex chromosome composition. Further investigation revealed that orchiectomy of gonadal males reduced the sex difference in the vaccine response whereas ovariectomy of gonadal females did not, demonstrating that androgen hormones are largely responsible for the observed sex difference. However, because the FCG model alters gonadal development and therefore alters systemic circulating sex hormone concentrations, it is unclear in this model to what extent these differences are due to a direct effect of androgen hormones on T cells or an indirect effect through other cell type like APCs.

In models of autoimmunity, sex differences in disease susceptibility have been linked to sex hormone-mediated sex differences in T cell function. In mouse models of experimental autoimmune encephalomyelitis (EAE), androgen-treated T cells from proteolipid protein-immunized mice produced less IFNγ and more IL-10 than in the absence of exogenous androgens (177). When transferred into recipient mice, T cells from female proteolipid protein-immunized mice induced more severe EAE than T cells from male donors. Interestingly, the impacts of androgens during acute stimulation on the production of cytokines was not reversed by the absence of androgen, suggesting that androgen exposure during activation and differentiation of effector T cells programs their later fate (177). Interestingly, treatment with low-dose estrogen elicited a similar, but modest, Th2 to Th1 bias, but estrogen pretreatment was not able to reduce EAE severity induced by T cell transfer (178). Therefore, the sex bias in autoimmune disease susceptibility may be mediated by the anti-inflammatory protective effects of androgens on T cells in males rather than through the impacts of estrogens on T cells in females.

In humans, microarray analysis reveals T cells from females express more of the proliferation marker, antigen Kiel 67 (Ki-67) at homeostasis and produce more IFNγ, lymphotoxin β (LTB), granzyme A (GZMA), granulysin (GLNY), and IL-12 receptor β2 (IL12RB2) than male T cells when cultured in vitro with phytohaemagglutinin, which induces TCR and co-receptor stimulation (179). Mechanistically, sex differences in IFNγ expression have been linked to androgen- and AR-induced epigenetic control of chromatin at control elements of the *Ifng* locus in mice and the *IFNG* locus in humans. In mice, AR knockdown increases IFNγ production in CD8 T cells in response to chronic infection and AR can bind to an enhancer in the *Ifng* locus, which is reduced by treatment with an AR small molecule inhibitor, enzalutamide (88). Additionally, studies have demonstrated androgen-regulated expression of peroxisome proliferator-activated receptor-α (PPARα) in human T cells, which regulates chromatin modifications and gene expression at the *IFNG* locus (168, 180). Taken together, these studies demonstrate a role for androgen hormones in regulating the effector gene expression of T cells and limiting their response to vaccination and *in vitro* stimulation.

Sex is also associated with response to checkpoint blockade immunotherapy. In meta-analyses of clinical trials for multiple tumor types, sex was associated with response to multiple immunotherapy modalities (181-185). Although the findings in these analyses are mixed regarding which biological sex generally benefits more from immunotherapy, the varying design, therapeutic approaches, objective endpoints, and exclusion criteria between trials included in the meta-analyses are likely confounding factors. Further investigation of the association between sex and immunotherapy will require careful study design and consideration of these factors. Therefore, it is important to understand the specific mechanisms that may impact the response to checkpoint blockade immunotherapy in a sex-specific manner.

1.3.4 Clinical opportunities to understand the role for androgen hormones and AR signaling on immune responses

Prostate cancer is a disease setting which offers a unique opportunity to investigate the impact of androgen hormones on T cell anti-cancer responses and responses to immunotherapy. By nature, prostate cancer only affects people with male sexual development and as part of the male reproductive system, prostate epithelial cells rely on androgen hormones and AR signaling for differentiation and survival. Because prostate cancer almost always presents as androgen-sensitive disease, the standard of care for prostate cancer includes therapies that disrupt AR activity either by reducing circulating levels of androgen hormones or by directly inhibiting AR activity through small molecule drugs. Therefore, it is critical to understand the impacts of systemic anti-androgen therapy on immune cells involved in the anti-cancer response and how anti-androgen therapies interact with immunotherapies. The administration of anti-androgen therapy in prostate cancer patients provides an opportunity to study the consequences of androgen hormones in a more controlled manner than in other disease settings. Indeed, a previous investigation by the Moran lab revealed a role for AR signaling in CD8 T cells in limiting the response to anti-PD-1 immunotherapy in a clinical trial of metastatic castration-resistant prostate cancer (mCRPC) patients. A deeper understanding of this phenomenon may reveal mechanisms that influence sex differences in immunotherapy responses in other disease settings and inform rational design and administration of immunotherapies. **Chapter 3** of this dissertation leverages single cell RNA sequencing data from prostate tumor biopsies from a cohort of high-risk prostate cancer patients before and after co-administration of anti-androgen and anti-PD-1 immunotherapy to understand the influence of these therapies on the anti-tumor immune response.

1.4 Overview of prostate cancer biology and clinical management

1.4.1 Incidence and mortality of prostate cancer

Prostate cancer is the most diagnosed cancer in males in the United States, accounting for approximately 30% of new cases per year, with over 300,000 cases expected to be diagnosed in the US in 2025. Although prostate cancer is the most common cancer type in males, it is the second most deadly cancer in males, accounting for approximately ~11% of cancer deaths (18.7 per 100,000) among males in 2022 (186). Risk factors associated with prostate cancer include age, certain genetic aberrations like *BRCA1* and *BRCA2* mutations, family history, and West African ancestry, with Black men in the US experiencing approximately 70% greater incidence of prostate cancer compared to White men.

The 5-year survival rate of newly diagnosed prostate cancer is approximately 97% but depends on cancer stage at diagnosis. Patients diagnosed with localized and regionally confined prostate cancer almost all survive 5 years post-diagnosis while approximately 36%

of patients diagnosed with distant metastatic disease survive 5 years (cdc.gov, U.S. cancer statistics prostate cancer bite). Of all prostate cancer cases diagnosed in the US, ~70% present as localized disease, ~14% are regionally confined, ~8% are distant metastatic disease, and ~8% are of unknown stage. Prostate cancer staging utilizes the recommendations from the American Joint Committee on Cancer for tumor, nodes, and metastasis (TNM) staging (187). Along with TNM staging, clinicians utilize measurements of circulating prostate specific antigen (PSA) concentrations, which correlates with cancer burden, as well as pathological analysis of prostate biopsies (Gleason score) to assess disease grade. Gleason scores are determined by pathological analysis of multiple prostate biopsies and is a combination of the scores (from 1-5) from two biopsies with the highest (most advanced) scores. Based on this information, patients may be stratified into different stages (ranging from I through IV), which ultimately guides treatment recommendations.

1.4.2 Standard of care treatment for prostate cancer

Prostate cancer treatment decisions are informed by risk of progression as determined by the level of PSA elevation in blood, assessment of tumor size by digital rectal evaluation, and Gleason grade (188). Treatments may range from active surveillance for very low risk patients to radiotherapy, prostatectomy, and/or androgen deprivation therapy (ADT). For local disease or locally-advanced disease, radiotherapy and radical prostatectomy are the most common first-line therapies, which may be administered with or without ADT depending on progression risk. ADT is achieved by orchiectomy or pharmacologic inhibition of pathways involved in androgen hormone synthesis, including gonadotropin-releasing hormone (GnRH) agonists (e.g. leuprolide), GnRH antagonists (e.g. degarelix), or cytochrome P450 17A1 (CYP17A1) inhibitors (e.g. abiraterone), which inhibit adrenal conversion of androgen precursors (**Figure 1.6**). For patients who are diagnosed with metastatic disease, standard treatment usually includes ADT and active surveillance of disease until disease progression, at which time docetaxel chemotherapy plus prednisone may be added to the treatment regimen.

The goal of ADT is to reduce the concentration of circulating testosterone to castrate or near-castrate levels to deprive AR-dependent prostate cancer cells of AR ligands. However, despite achieving low levels of circulating testosterone, many patients on ADT eventually develop resistance to the therapy and their tumors progress. ADT resistance can be caused by mutations in AR which render it constitutively active despite paucity of available ligands, upregulation of AR expression, and intratumoral conversion of precursor steroids into androgens by stromal or epithelial cells (189-191). To overcome these mechanisms of resistance, AR inhibitors were developed (e.g. bicalutamide and enzalutamide) to directly inhibit the activity of AR by competing for ligand binding, preventing nuclear translocation, and preventing DNA binding by AR (192). Despite initial success of these therapies, most patients eventually develop resistance to ADT and progress to castration-resistant prostate cancer (CRPC), characterized by rising circulating PSA concentrations while on ADT (193). After developing CRPC, treatment options are relatively limited and survival ranges from 9-30 months (194). Therefore, there is a great need for the development of novel therapies that can overcome castration resistance.

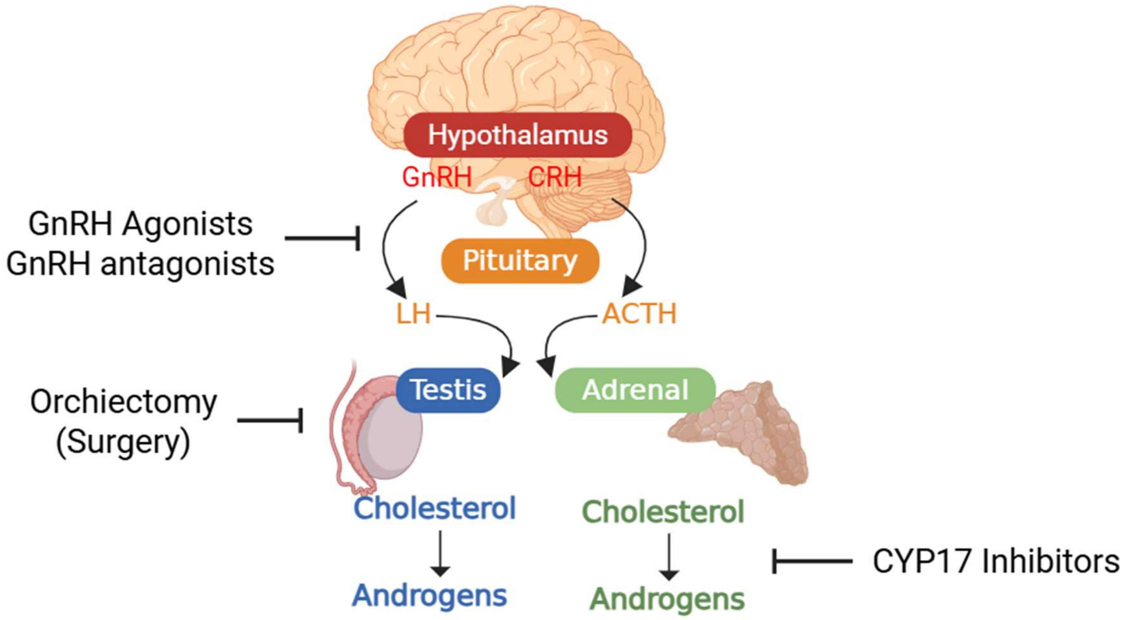

Figure 1.6 Mechanisms of androgen deprivation therapy

The hypothalamus-pituitary axis controls steroid synthesis through GnRH-induced release of luteinizing hormone (LH). Clinical methods of androgen deprivation therapy include blockade of this axis by treatment with GnRH agonists or antagonists. CYP17 inhibitors are used to block conversion of the androgen precursor, pregnenolone, into DHEA by the enzyme CYP17A1 in the adrenal gland. Surgery (orchiectomy) is often used in mouse models but is less commonly used in humans to remove testes, the major source of androgen hormones. Created with biorender.com.

1.4.3 Immunotherapy for prostate cancer

Despite recent therapeutic advances in cancer immunotherapy that have led to dramatic improvements in survival for many types of cancer, responses to immunotherapy vary widely by cancer type, patient characteristics, and immunotherapy modalities. Factors associated with favorable response to immunotherapy, discussed in **Section 1.2.6**, include the infiltration of the tumor by immune cells, particularly T cells, the mutational burden of the tumor, which influences the abundance of neoantigens that can be recognized by adaptive immune cells, and the expression of targetable immune checkpoint molecules in the tumor environment (111). Additionally, several factors are associated with resistance to ICB, including low infiltration of T cells into the tumor, high infiltration of immunosuppressive cell types such as MDSCs and TAMs, and low tumor mutational and neoantigen burden. Tumors with the presence of such resistance factors are considered immunologically “cold” and tend to display low response rates and reduced survival following ICB treatment.

PC has often been categorized as a "cold" tumor type that is generally poorly infiltrated by immune cells or contains immunosuppressive features that dampen anti-tumor immune responses (195, 196). However, single cell profiling of the primary prostate tumor environment by Hirz et al. revealed a substantial presence of CD8 T cells in the prostate tumor environment, representing the largest population of immune cells in the prostate environment (196). These data suggest that poor infiltration of T cells into the prostate is not likely a major limiting factor for ICB response and other factors likely contribute to the “cold” environment. Indeed, T cells expressed features of terminal exhaustion and were accompanied by suppressive myeloid and Treg cells (196). Therefore, even when anti-tumor immune cells are present within the prostate tumor environment, the anti-tumor immune response appears to be largely impaired. Several studies have pointed to immunosuppressive immune populations in the prostate TME as the drivers of low immune activity (197-199). Additional mechanisms are also likely important in limiting the anti-tumor immune response in PC, including a recently revealed role for AR activity in inhibiting antigen presentation by PC cells, and direct suppression of T cells by androgens as described in this dissertation (200). These findings reveal the necessity to develop novel therapeutic approaches that can effectively stimulate anti-tumor immunity and overcome the mechanisms of immunosuppression. However, when immunotherapies have been employed in prostate cancer treatment in hopes of overcoming such immunosuppression, responses have been largely underwhelming (201).

Immunotherapy has been tested as a treatment for prostate cancer both as a therapy for CRPC and as a first-line therapy for hormone sensitive disease. However, PC has often proved to be resistant to immunotherapy approaches. For example, CTLA4 ICB demonstrated no overall survival benefit in phase III trials in mCRPC patients (202, 203). Similarly low rates of response were observed in trials of PD-1 and PD-L1 targeted ICB in PC patients as well (204-206). Therefore, there are currently few approved immunotherapy treatments for prostate cancer, which includes a DC vaccine, Sipuleucel-T and anti-PD-L1 immune checkpoint inhibitors (207-217). However, these therapies have achieved only limited success, which has limited their approved uses to patients with tumors most likely to respond to ICB such as sub-types with microsatellite instability and defects in DNA mismatch repair (dMMR), both of which are associated with stronger pre-treatment immune responses and response to ICB due to the increased abundance of neoantigens (Vareki JIC 2018). For example, while the IMbassador 250 phase III trial failed to show a survival advantage for atezolizumab plus enzalutamide, some subgroup analyses indicated potential benefit in patients with high PD-L1 expression and pre-existing immunity (211). However, the patients with such mutational landscapes are rare in PC, which generally presents with a relatively low mutation burden compared to other cancers (218). In contrast to PC, ICB has demonstrated greater success in treating other cancer types, including non-small-cell lung cancer, renal cell carcinoma, urothelial cancer, and melanoma (207).

Therefore, there are significant hurdles to overcome in developing more widely effective immunotherapies for prostate cancer, but great opportunity to do so if the mechanisms that limit immune responses and ICB efficacy in prostate tumors can be uncovered and effectively targeted.

1.5 Overview of research approaches

Despite the heterogeneity of sex and gender identities and the complexities of the interaction between those variables, the work described in this dissertation takes a narrow approach toward understanding how one variable that largely distinguishes XX and XY individuals, the activity of androgen hormones through AR, shapes CD8 T cell responses. **Chapter 2** first aims to utilize mouse models of disease to understand mechanisms and functional consequences AR activity in regulating CD8 T cell immune responses in male mice, in which androgen hormones are most abundant (219). Following that comparison, **Chapter 2** further investigates whether the mechanisms by which AR regulates CD8 T cells in male mice also occur in female mice and whether they contribute to sex differences in CD8 T cell mediated immune responses. Finally, **Chapter 3** leverages clinical data from prostate cancer patients, a disease setting in which anti-androgen therapy is standard-of-care, to investigate the role of androgen hormones and immunotherapy in shaping the immune response to prostate cancer. Together, these findings reveal mechanisms of androgen hormone regulation of immune responses in mice and humans and may be critical to guide further investigation of mechanisms of sex differences in immune responses.

Chapter 2: Androgen receptor skews CD8$^+$ T cell effector and memory responses to acute infection

Contributing authors: Reed M. Hawkins[1, 2, 3, 4], Fanny Polesso[2], Aaron Ko[2], John Cheney[3], Rachel Huynh[2], Mark Flory[4], Hisham Mohammed[4], Amy Moran[5, 6]

Author Contributions:

1: Manuscript preparation

2: Experimental design and execution

3: Computational analysis

4: Immunoprecipitation and mass spectrometry execution and analysis

5: Experimental design

6: Funding support

2.1 Abstract

As a critical driver of sexual dimorphism, our group and others have described a role for the androgen receptor (AR) in limiting CD8 T cell anti-tumor activity by inhibiting IFNγ production and responses to immune checkpoint blockade. However, the mechanisms by which AR regulates CD8 T cell differentiation and function are unknown. To define the AR regulatory network in T cells, we overexpressed AR in T cells and revealed AR-mediated epigenetic and transcriptional regulation of effector- and memory-associated genes. AR protein interactions with epigenetic regulators from the BAF complex and histone deacetylases were identified, underscoring epigenetic remodeling enforced by androgens. In mouse models of infection, we demonstrate that genetic deletion of *Ar* in CD8 T cells enhances the effector response by increasing proliferation, function, and effector differentiation. Furthermore, deletion of *Ar* in CD8 T cells skews effector memory differentiation and improves recall protection. Interestingly, AR expression rapidly increases in CD8 T cells during priming, which is associated with AR-induced changes in chromatin accessibility. Importantly, the observations made in AR-deficient CD8 T cells are phenocopied in female CD8 T cells when compared to males. These data suggest that AR regulates epigenetic and transcriptional changes induced during T cell activation and differentiation, thereby tuning CD8 T cell effector and memory responses.

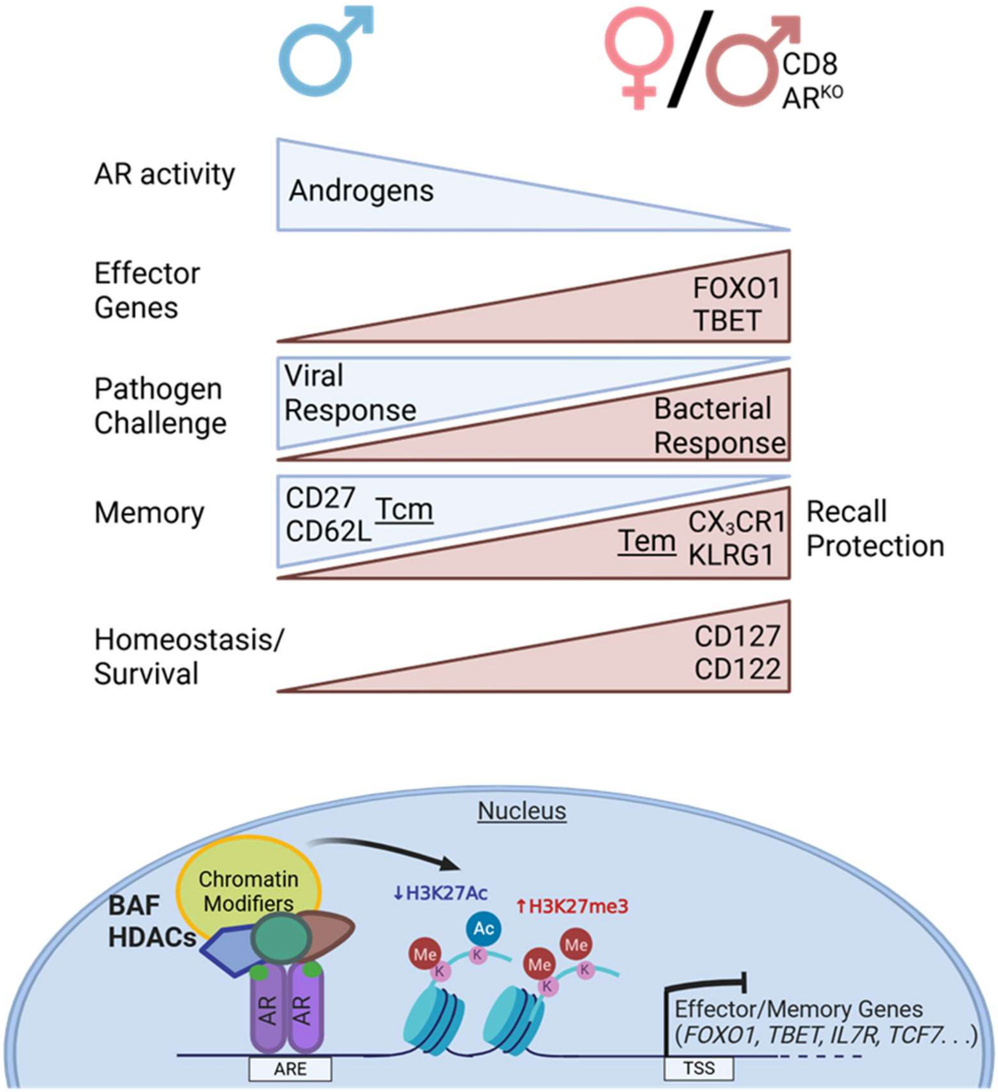

Figure 2.0 Graphical abstract

AR and androgen hormones are expressed in both males and females, but circulating androgen hormones are higher in males, generally leading to heightened AR activity in males. We reveal that AR activity in male CD8 T cells limits their capacity to differentiate into effector cells and limits expression of effector-associated genes. AR expression supports expansion of male CD8 T cells in a response to viral infections whereas it inhibits the bacterial effector response. Following pathogen clearance, AR expression favors central memory differentiation in CD8 T cells rather than effector memory cells. Moreover, knockout of AR confers superior protective capacity to memory cells.

Mechanistically, in vitro models reveal AR cooperation with epigenetic modifying proteins, AR regulation of T cell epigenetic state, and repression of the expression of effector- and memory-associated genes.

2.2 Introduction

Increasing emphasis on understanding how biological sex contributes to health and disease has revealed underappreciated sex differences in immune responses and disease susceptibility. For example, males experience increased susceptibility to many non-reproductive cancers and infectious diseases, including SARS-CoV2 infection, and females experience increased susceptibility to autoimmunity (141-143, 220-222). While the causes of such differential susceptibility are multi-faceted and still poorly understood, sex differences in immune responses may be important contributing factors.

Indeed, T cells are critical components of the adaptive immune response in infection, cancer, and autoimmunity, and several studies have described sex differences in the abundance, phenotype, and function of multiple T cell subsets. For example, androgen deprivation in male mice inhibits IL-12-mediated STAT4 phosphorylation thereby enhancing Th1 differentiation and function (223). However, to date, most studies investigating the role of androgen hormones in influencing T cells relied on altering circulating hormone levels by androgen deprivation therapy and androgen supplementation or bone marrow transplantation from germline AR knockout donors. Such approaches may confound the direct impacts of androgens on T cells due to the influence of androgens on other cell types. In fact, our group and others have described roles for androgen hormones in suppressing antigen presentation by target cells, suppressing inflammatory cytokine secretion by macrophages and dendritic cells, and promoting immune-inhibitory cells such as myeloid-derived suppressor cells (MDSCs) and regulatory T cells (Tregs) (169, 200, 224, 225).

Recent evidence has demonstrated a role for CD8 T cell intrinsic androgen receptor (AR) signaling in regulating the functional capacity of CD8 T cells to control cancer growth and respond to immunotherapy (88, 226, 227). These studies established that CD8 T cells express androgen receptor (AR) and that AR activity regulates the expression of effector molecules IFNγ and GZMB and the stemness-associated transcription factor, TCF-1. These findings demonstrate that AR suppresses CD8 T cell anti-tumor responses, but the mechanisms of such suppression and whether AR similarly suppresses CD8 T cell function in other disease settings remain unknown.

In this study, we demonstrate that naïve, effector, and memory CD8 T cells express AR during the response to infection. Using a mouse model of cre-mediated deletion specifically in mature CD8 T cells, we demonstrate that AR suppresses the effector response of CD8 T cells, skews the memory phenotype, and impairs the memory recall protective capacity. We further utilize a model of AR overexpression in a human T cell line to reveal AR cooperation with epigenetic regulators in T cells and demonstrate AR-mediated epigenetic and transcriptional regulation of T cell effector- and memory-associated genes.

2.3 Results

2.3.1 CD8 T cell AR expression is dynamically regulated following TCR engagement

To determine whether AR may regulate CD8 T cell responses to acute infection, we first determined whether CD8 T cells express AR during acute infection. We adoptively transferred CD8+ TCR-transgenic, LCMV GP$^{33\text{-}41}$-specific (P14) T cells from Thy1.1+ C57BL/6 donors into congenic C57BL/6 Thy1.2+ recipients, then infected recipient mice one day later with LCMV Armstrong to induce acute infection (Figure 2.1A). On day 7 and day 30 post-infection, Thy1.1+ P14 cells were magnetically sorted from recipient splenocytes and RNA extracted for measurement of *Ar* mRNA expression by qPCR in effector and memory CD8 T cells, respectively. Compared to prostate cancer cells as a positive control, naïve (pre-transfer) P14 cells expressed a moderate amount of *Ar* mRNA, which was similar in effector and memory P14 cells (Figure 2.1B). Considering our previously published evidence that human lymphocytes express AR at varying levels in tissue and secondary lymphoid organs (88), we hypothesized that Ar mRNA expression may be dependent on environmental or stimulatory cues. To test this hypothesis, we sorted naïve CD8 T cells from WT mouse splenocytes and provided T cell receptor (TCR) and costimulatory receptor engagement in vitro via plate-bound anti-CD3 and anti-CD28 antibodies for three days. At 0-, 0.5-, 1, 2-, 4-, 8-, 24-, 48-, and 72-hours post-stimulation, qPCR analysis of *Ar* mRNA expression revealed that relative to naïve, unstimulated cells, *Ar* expression rapidly increased between 2 and 8h post-stimulation, then returned to baseline levels by 24 hours before increasing again at 72h (Figure 2.1C). These data suggest that *Ar* expression by antigen-specific CD8 T cells remains stable at the bulk population level during acute infection but is dynamically regulated in response to TCR and co-stimulation receptor engagement. Therefore, AR is poised to regulate CD8 T cells throughout the response to acute infection, but may be most active shortly after antigen encounter.

2.3.2 AR inhibits CD8 T cell homeostatic memory-like phenotype

To investigate whether AR expression impacts CD8 T cell phenotype and function at steady state and during infection, we developed a model of CD8 T cell specific *Ar* knockout by crossing mice bearing a floxed *Ar* allele with mice bearing a cre recombinase transgene under the control of the CD8 T cell specific e8i enhancer (228, 229). We validated CD8 T cell *Ar* knockdown by qPCR analysis of CD8 T cells from splenocytes of Ar-WT/Y; e8i-cre+ (ARWT)and Ar-fl/Y; e8i-cre+ (ARKO) mice (Figure 2.1D). Cre expression under the control of the e8i enhancer is expected to be restricted to mature CD8 T cells and therefore have no impact on T cell development. Indeed, we observed no differences in the frequency of immature T cell subsets and other lymphocyte subsets in the thymi of ARWT and ARKO mice (Supplemental Fig. 1A). Additionally, we observed no difference in the frequency of CD8α$^+$ cells among TCRβ$^+$ cells in ARKO mouse lymph nodes and spleens compared to WT mice (Supplemental Fig. 1B). Given that naïve CD8 T cells express *Ar*, we next determined whether *Ar* knockdown impacts the homeostatic maintenance of CD8 T cells in specific pathogen free (SPF) mice. We found a significant increase of CD44+CD122+CD49d- memory-like CD8 T cells in the lymph nodes, but not spleens of ARKO versus ARWT mice (Figure 2.1E). Previous evidence suggests that memory-like CD8 T cells in SPF mice are maintained by homeostatic cytokine engagement, including IL-7 and IL-15, and by engagement with MHC-presented self-antigens. Compared to CD44-CD122- naïve T cells, CD44+CD122+ CD8 T cells expressed more CD127 (IL-7R) and markers of TCR-engagement, including increased CD5 and decreased TCRb expression, suggesting that CD44+CD122+ cells receive stronger baseline TCR stimulation and may be more responsive to IL-7 (Supplemental Figure 1C). However, CD127 and CD5 expression were not substantially changed on ARKO versus ARWT CD8 T cells, indicating that the mechanisms by which AR regulates this population may be distinct from or downstream of these markers of cytokine and TCR engagement (Figure 2.1F-G).

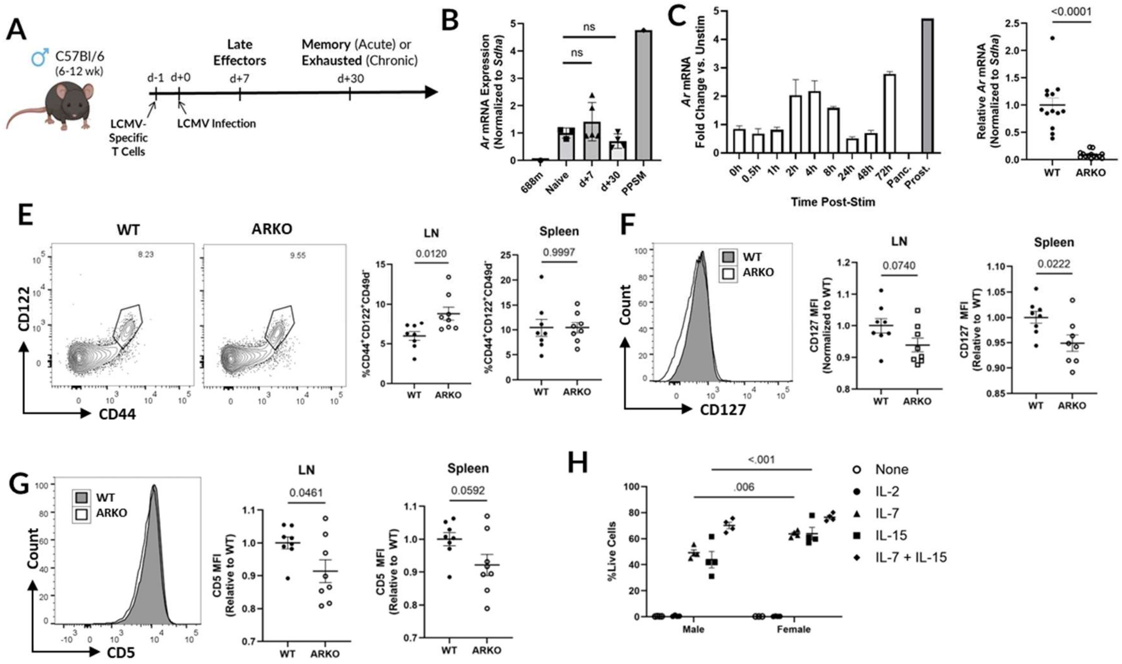

Figure 2.1 AR limits CD8 T cell homeostatic memory-like phenotype

(A) Experiment outline for adoptive transfer of P14; Thy1.1 CD8+ T cells and infection of wild type mice. (B) Ar mRNA expression measured by qPCR in naïve (pre-transfer), effector (day+7) and memory (day+30) P14 CD8 T cells sorted from mice in A at the indicated timepoints. PPSM = mouse prostate cancer cell line positive control. 688m = mouse pancreatic cancer cell line negative control. (C) Ar mRNA expression measured by qPCR at the indicated timepoints in magnetically sorted mouse CD8+ T cells stimulated in vitro with anti-CD3 and anti-CD28. Panc. = mouse pancreatic cancer cell line negative control. Prost. = mouse prostate cancer cell line positive control. (D) Ar mRNA expression measured by qPCR in purified CD8 T cells from splenocytes of Ar-WT/Y; e8i-cre+ (WT control) and AR-flox/Y; e8i-cre+ (CD8 ARKO) mice. (E) Example flow cytometry measurement of CD4 and CD8 expression among TCRb+ T cells and CD44 and CD122 co-expression on CD8 T cells (left) and summary of the frequency of CD8+ cells and CD8+CD44+CD122+CD49d- cells among T cells in the lymph nodes and spleens of WT control and CD8 ARKO mice. (F) Flow cytometric measurement of CD127 expression on CD8a+TCRb+ cells in the lymph nodes and spleens of WT control and CD8 ARKO mice. (G) Flow cytometric measurement of CD5 expression on CD8a+TCRb+ cells in the lymph nodes and spleens of WT control and CD8 ARKO mice. (H) Flow cytometric measurement of IFNγ expression by WT control and ARKO CD8 T cells following 3 days of anti-CD3 and anti-CD28 stimulation in vitro. (I) GSEA of GSE15930 in ranked differentially-expressed genes between Jurkat-AR + R1881 versus Jurkat-EV + R1881 from Figure 2.1A.

2.3.3 AR inhibits CD8 T cell IFNγ production in response to acute stimulation

Given that *Ar* expression rapidly fluctuates early following TCR engagement, we sought to determine whether AR regulates the acquisition of effector phenotype and function in CD8 T cells during the first 24 hours of priming. Magnetically sorted naïve CD8 T cells from ARWT and ARKO mice were stimulated in vitro with plate-bound anti-CD3 and anti-CD28 antibodies and 25 Units/mL IL-2 for 24 hours before RNA extraction and assessment of gene expression by RNA sequencing. Interestingly, we found few differentially expressed genes between WT and ARKO naïve CD8 T cells (before stimulation) and after 24 hours of priming (Supplemental Figure 2A). These data reveal that although *Ar* expression is relatively high early following TCR engagement, it ultimately has little impact on gene expression at that time.

We next assessed whether Ar expression alters the acquisition of effector phenotype and function later during the priming phase. Magnetically sorted naïve CD8 T cells from ARWT and ARKO mice were stimulated in vitro with plate-bound anti-CD3 and anti-CD28 and IL-2 for 72 hours before by intracellular cytokine staining and flow cytometry (Supplemental Figure 2B). We detected a modest increase in the frequency of IFNγ-producing cells among ARKO cells on day 3 post-stimulation, but similar production of TNFα and GZMB. When comparing male and female WT and ARKO CD8 T cells under similar stimulation conditions, we found a similar modest increase in IFNγ production in both male and female ARKO cells compared to WT, but no sex difference was observed (Supplemental

Figure 2C). These data corroborate our previously published findings that AR regulates CD8 T cell IFNγ production, but do not indicate a role for AR in regulating the acquisition of activation markers during acute stimulation.

2.3.4 AR inhibits CD8 T cell effector differentiation and expansion in response to Listeria monocytogenes infection

We next sought to determine whether AR expression in CD8 T cells regulates effector differentiation and expansion in response to acute infection. To test this, we crossed Ar-fl and e8i-cre mice with OTI TCR transgenic mice carrying the CD45.1 allele to generate Ar-fl/Y; e8i-cre+; OTI+; Thy1.2+/+; CD45.1+/+ (ARKO OTI) mice. Naïve CD8+ splenocytes (CD8+/CD44-) were sorted from ARKO OTI mice and co-transferred at a 1:1 ratio with sorted naive Ar-wt/Y; OTI+; Thy1.1+/+; CD45.2+/+ (ARWT OTI) CD8 T cells into Thy1.2+/+; CD45.2+/+ wild type recipients (Figure 2.2A and Supplemental Figure 3). One day following adoptive co-transfer, recipient mice were infected with 5x10^6 CFU *ActA-Listeria monocytogenes* expressing the OVA antigen. On day 5 post-infection, lymph nodes and spleens from recipient mice were assessed for transferred OTI T cell abundance, phenotype, and function upon re-stimulation. Transferred ARKO OTIs were found at a higher frequency than WT OTIs among CD8 T cells in both lymph nodes and spleens (Figure 2.2B). A higher frequency of ARKO OTIs lost expression of CD62L and TCF1, indicating fewer ARKO OTIs remained naïve 5 days post-infection compared to ARWT OTIs (Figure 2.2C). Additionally, a higher frequency of ARKO OTIs were $CD27^{lo}CX3CR1^{+}$ and $KLRG1^{+}$, indicating enhanced differentiation into terminal-effector-like cells on day 5 post-infection (Figure 2.2D). Interestingly, a higher frequency of ARKO OTIs expressed markers of memory precursor effector cells (MPEC; $CD127^{+}KLRG1^{-}$) and short-lived effector cells (SLEC;

$CD127^{-}KLRG1^{+}$), indicating that AR may influence the balance of both subsets of effector cells (Figure 2.2E). Interestingly, the SLEC subset was the largest subset in both WT and ARKO mice, indicating that overall SLEC is favored. However, we found that ARKO OTI cells expressed significantly more Tbet, a transcription factor that is critical for effector differentiation (Figure 2.2F). Upon ex-vivo re-stimulation with SIINFEKL OVA peptide, in both lymph nodes and spleens a higher frequency responding CD8+ T cells that produced IFNγ and TNFα were ARKO OTIs (Figure 2.2G). These data indicate that in the early effector response, AR inhibits CD8 T cell differentiation into effector cells, including MPEC, SLEC, and terminal effector subsets, and inhibits their ability to produce effector cytokines in response to antigen stimulation.

In the competitive co-transfer model, the higher frequency of ARKO OTIs recovered compared to WT OTIs suggests AR inhibits CD8 T cell proliferation or survival following activation and priming. To address this question, we crossed Ar-fl; e8i-cre mice with P14 TCR transgenic mice carrying the Thy1.1 congenic allele to generate Ar-fl/Y; e8i-cre+; P14+; Thy1.1+/- (P14 ARKO) and Ar-WT/Y; e8i-cre+; P14+; Thy1.1+/+ (P14 WT). Naïve CD8 T cells from P14 WT and P14 ARKO mice were labeled with cell trace violet proliferation dye, mixed at a 1:1 ratio (Supplemental Figure 3), and adoptively transferred into wild type recipient mice one day before LCMV Armstrong infection. On day 2.5 post-infection, splenocytes were isolated from recipient for assessment of proliferation by CTV dilution. P14 ARKO cells were recovered at a higher frequency than P14 WT cells, corroborating our findings with ARKO OTI versus WT OTI cells after ActA-LM-OVA infection (Figure 2.2H). However, there was only a modest difference in the dilution of the CTV dye (Figure 2.2I). The modest difference in early proliferation may partially explain the difference in ARWT versus ARKO OTI recovery at day 5 post-infection, however other mechanisms, including potential differences in cell survival and trafficking, may also be involved. These data suggest that AR does not have a substantial impact on the early proliferation of CD8 T cells in response to infection.

Finally, we asked whether the enhanced effector differentiation in ARKO CD8 T cells confers an increased capacity to control the early persistence of LM. On day 5 post-infection, LM burden in the liver and spleen of male and female ARWT and ARKO mice was similar, indicating that AR does not inhibit the capacity for CD8 T cells to control early LM infection (Figure 2.2J). Taken together, these data demonstrate that AR limits the expansion and differentiation of early effector CD8 T cells in males, including differentiation into both SLECs and MPECs, but ultimately does not alter their capacity to control LM burden up to day 5 after infection.

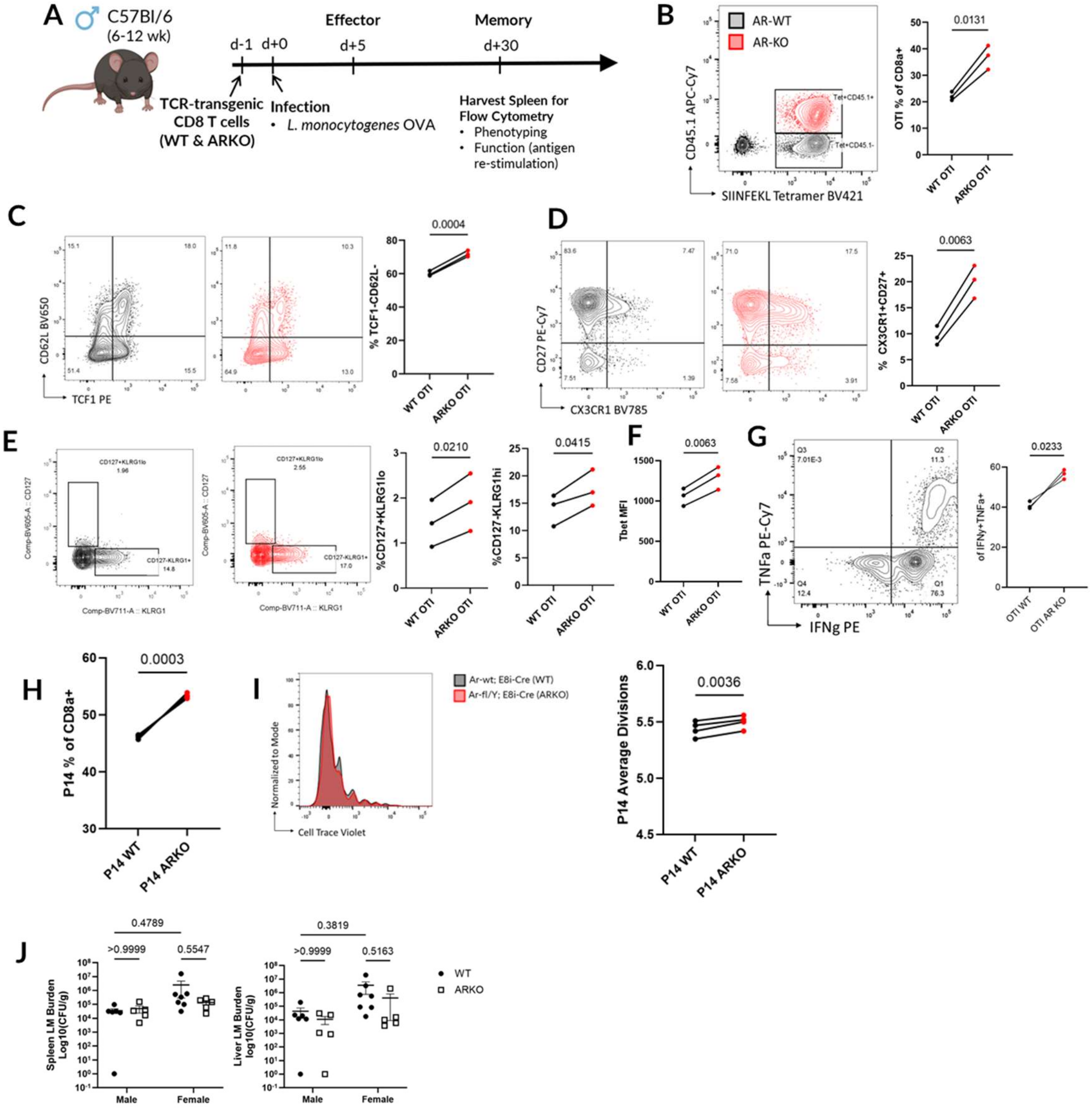

Figure 2.2 AR inhibits CD8 T cell effector differentiation and expansion in response to acute infection

(A) Experiment outline for adoptive transfer of WT and ARKO OTI CD8+ T cells co-transferred into wild type mice one day before infection with 5x10^6 CFU ActA- LM-OVA. (B) Frequency of transferred WT and ARKO OTI T cells among all CD8+ T cells in the spleen of recipient mice from D on day 5 post-infection measured by flow cytometry. (C) Frequency of TCF1-/CD62L- cells among transferred WT and ARKO OTI CD8 T cells in splenocytes from mice on day 5 post-infection as in A. (D) Frequency of CX3CR1+/CD27low cells among transferred WT and ARKO OTI CD8 T cells in splenocytes from mice on day 5 post-infection as in A. (E) Frequency of CD127+KLRG1- (MPEC) and

CD127-KLRG1+ (SLEC) cells among transferred WT and ARKO OTI CD8 T cells in splenocytes from mice on day 5 post-infection as in A. (F) TBET mean fluorescence intensity (MFI) of transferred WT and ARKO OTI CD8 T cells. (G) Frequency of transferred WT and ARKO OTI CD8+ T cells among all IFNγ and TNFα co-producing CD8+ T cells in splenocytes from mice on day 5 post-infection as in A, re-stimulated in vitro with 100 nM SIINFEKL peptide and brefeldin A for (4-6h, check time). (H) Relative abundance of P14 WT and ARKO following co-transfer into recipient mice and infection with LCMV Armstrong (I) Representative histogram (left) and summary statistics (right) of the CTV intensity of cells from (H) on day 3 post-infection. (J) Spleen (left) and liver (right) Listeria monocytogenes CFU burden on day 5 post-infection with 5x10^4 CFU LM-GP33 in male and female WT and ARKO mice.

2.3.5 AR skews CD8 T cell memory differentiation and limits memory protection

Our finding that AR controls the balance of effector CD8 T cell subsets suggests that AR may influence the later fate of effector CD8 T cells during memory formation. Using the same model of co-transfer of WT and ARKO OTI cells and LM-OVA infection as previously described (Figure 2.2A), we determined whether the skewed effector phenotype observed early during infection conferred disparate memory differentiation and survival capacity after infection clearance, and whether expression of AR impacts the phenotype and persistence of memory CD8 T cells. The frequency of ARKO OTI cells compared to WT after pathogen clearance (day 21 early memory and day 60 late memory) was increased in splenocytes on day 21, but similar in lymph nodes and splenocytes on day 60, indicating that there is to no preferential persistence of ARKO OTI cells compared to ARWT OTI cells following pathogen clearance (Figure 2.3A). Consistent with that finding, the expression of CD127, which supports memory CD8 survival after contraction (discussed in Chapter 1), only remained moderately elevated in ARKO CD8 T cells on day 21 (Figure 2.3B).

Like our findings on day 5 post-infection, fewer ARKO OTI cells co-expressed CD62L and TCF1 on day 21 and 60 in both lymph nodes and spleens, suggesting that AR expression supports the differentiation and persistence of central memory CD8 T cells (Tcm; Figure 2.3B). Additionally, we observed that a higher frequency of ARKO OTIs retained expression of CX3CR1 on day 21 and day 60, indicating that AR expression inhibits the persistence of long-lived effector cells (Figure 2.3D). Taken together, these findings indicate that AR controls the balance between CD8 T cells memory subsets that persist following contraction. Interestingly, we also measured moderate decreases in ARKO CD8 T cells in the expression of transcription factors that control memory CD8 T cell differentiation, TCF1, Eomes, and Blimp1, which suggests that AR may skew the phenotype of CD8 T cells by altering the expression of these key differentiation factors (Figure 2.3E-H). Finally, we assessed memory WT and ARKO OTIs ex-vivo for the capacity to produce effector cytokines and again found that a higher frequency of cytokine-producing cells were ARKO as opposed to WT (Figure 2.3I)

Previous studies established that the memory CD8 T cell subsets differ in their capacity to re-expand and control pathogen burden upon re-infection, with Tcm generally more capable of re-expansion and pathogen control than Tem subsets. We therefore asked whether the altered phenotype of ARKO CD8 T cells is associated with an altered capacity for protection upon antigen-specific re-challenge. To test this, we crossed Ar-fl/Y; e8i-cre+ and Ar-wt/Y; e8i-cre mice onto a P14 TCR transgenic background expressing the Thy1.1 congenic marker to generate ARWT and ARKO CD8 T cells specific for the dominant LCMV antigen, GP33-41. Naïve Ar-fl/Y; e8i-cre+; P14+; Thy1.1+/Thy1.2+ (ARKO P14) and Ar-wt/Y; e8i-cre+; P14+; Thy1.1+/Thy1.1+ (ARKO P14) were magnetically sorted by negative selection, mixed at a 1:1 ratio, and adoptively transferred into WT Thy1.2+/Thy1.2+ recipient mice (Figure 2.3J). One day after adoptive transfer, recipient mice were infected with 5x10^6 CFU *ActA*- LM expressing GP33-41. On day 60 post-infection, memory CD8a+CD44+Thy1.1+Thy1.2- ARWT P14s and CD8a+CD44+Thy1.1+Thy1.2+ ARKO P14s were FACS sorted from the spleens of recipient mice and 33k cells of each genotype were adoptively transferred separately into naïve recipient mice, which were infected with 1x10^5 CFU virulent LM-GP33 one day later. On day 3 post-infection, spleens and livers were harvested from recipient mice for evaluation of LM-GP33 burden by CFU assay. We observed a significant reduction in LM-GP33 burden in the spleens of ARKO P14 recipient mice compared to those that received ARWT P14s, but no significant difference in pathogen burden in the liver (Figure 2.3K).

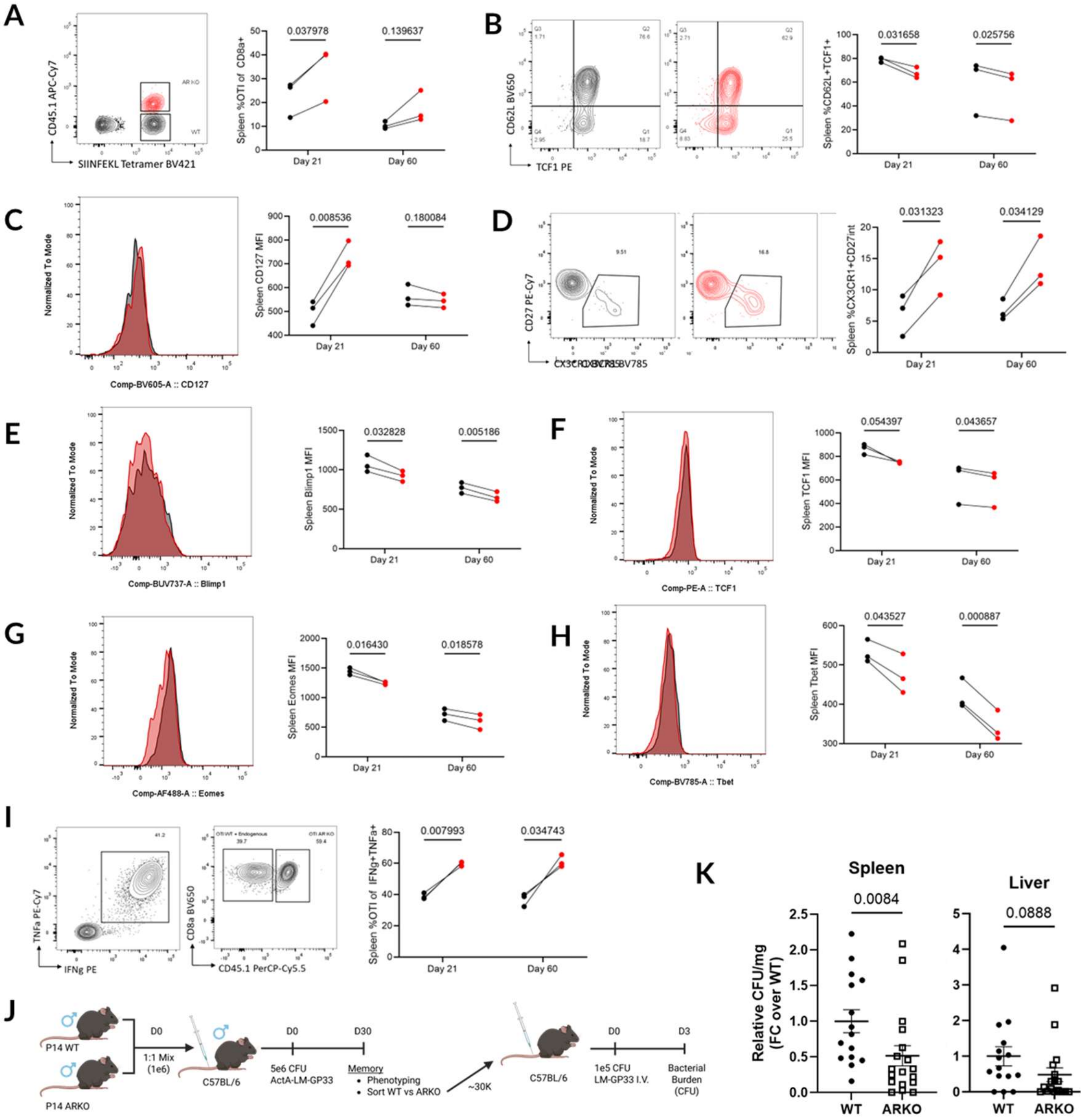

Figure 2.3 AR skews CD8 T cell memory differentiation and limits protection

(A) Frequency of transferred WT and ARKO OTI T cells among all CD8+ T cells in the spleen and lymph nodes of recipient mice from Fig2A on day 21 and day 60 post-infection measured by flow cytometry. (B-D) MFI of CD127 (B), frequency of TCF1+/CD62L+ (C), and CX3CR1+CD27int (D) cells among transferred WT and ARKO OTI CD8 T cells in the spleen and lymph nodes from mice on day 21 and 60 post-infection as in Fig. 2.2A. (E-H) Mean fluorescence intensity of transcription factors Blimp1 (E), TCF1 (F), Eomes (G), and Tbet (H) in WT and ARKO OTIs measured by flow cytometry in the spleen and lymph nodes. (I) Frequency of transferred WT and ARKO OTI CD8+ T cells among all IFNγ and

TNFα co-producing CD8+ T cells in splenocytes from mice on day 21 post-infection as in Fig. 2.2D re-stimulated in vitro with 100 nM SIINFEKL peptide and brefeldin A for (4-6h, check time). (J) Experiment outline for ARKO and WT P14 primary infection, sort, adoptive transfer, and re-challenge with 1x10^6 CFU virulent LM-GP33 (right). (K) Relative LM-GP33 burden (CFU/mg) in spleen (left) and liver (right) LM-GP33 burden from receipient mice on day 3 post-rechallenge (left). Data combined from three independent experiments normalized to the mean of WT.

2.3.6 Sex differences in CD8 T cell memory

The fact that AR expression skews effector and memory CD8 T cell differentiation and function in male mice raised the possibility that differential androgen hormone availability may also lead to differential AR activity in CD8 T cells between male and female mice, thereby contributing to sex differences in CD8 T cell responses. To compare memory CD8 T cell responses between male and female mice, we infected WT C57Bl/6 mice with $2x10^5$ PFU LCMV Armstrong to induce acute infection and memory CD8 T cell differentiation. Ninety days later, previously infected mice and naive male mice were challenged with $1x10^5$ CFU LM-GP33. On Day 3 post-challenge, spleens and livers were harvested and assessed for bacterial burden and splenic CD8 T cell phenotype. We found similar abundance of GP^{33-41}-tetramer$^+$ memory CD8 T cells in male and female mice (Figure 2.4A). Phenotypically, a higher frequency of female GP^{33-41}-tetramer$^+$ memory CD8 T cells expressed Tem markers, including a higher frequency of KLRG1$^+$ and CD44$^+$CD62L$^-$ cells, but not CX3CR1$^+$CD27^{lo} or Tcm (CD44$^+$CD62L$^+$) cells (Figure 2.4B-D). Additionally, female GP33-41-specific memory CD8 T cells expressed more of the IL-2 receptor subunits, CD122 and CD25 (Figure 2.4E-F) These data demonstrate that female memory CD8 T cells responding to re-challenge resemble effector cells more than male memory cells, and suggest that there may be a sex difference in the pre-challenge memory phenotype or the post-rechallenge reacquisition of effector characteristics. Given that sexual dimorphism in the concentration of circulating hormones is a key difference between sexes, along with the AR-mediated regulation of transcription factor expression detected in male mice in Figures 2.2 and 2.3, these sex differences in memory CD8 T cell phenotype may similarly be associated with differences in transcription factor expression. Indeed, we detected lower expression of TBET and Eomes and higher expression of TCF1 in male memory cells compared to female cells (Figure 2.4G). Together, these data suggest that mechanisms similar to those that control effector and Tem differentiation in male mice may also contribute to sex differences in CD8 T cell memory. Ultimately, however, these differences did not lead to a significant difference in the persistence of LM-GP33 in the livers of male and female mice on day 3 post-rechallenge, and most of the mice had cleared the pathogen from that tissue by that time (Figure 2.4H).

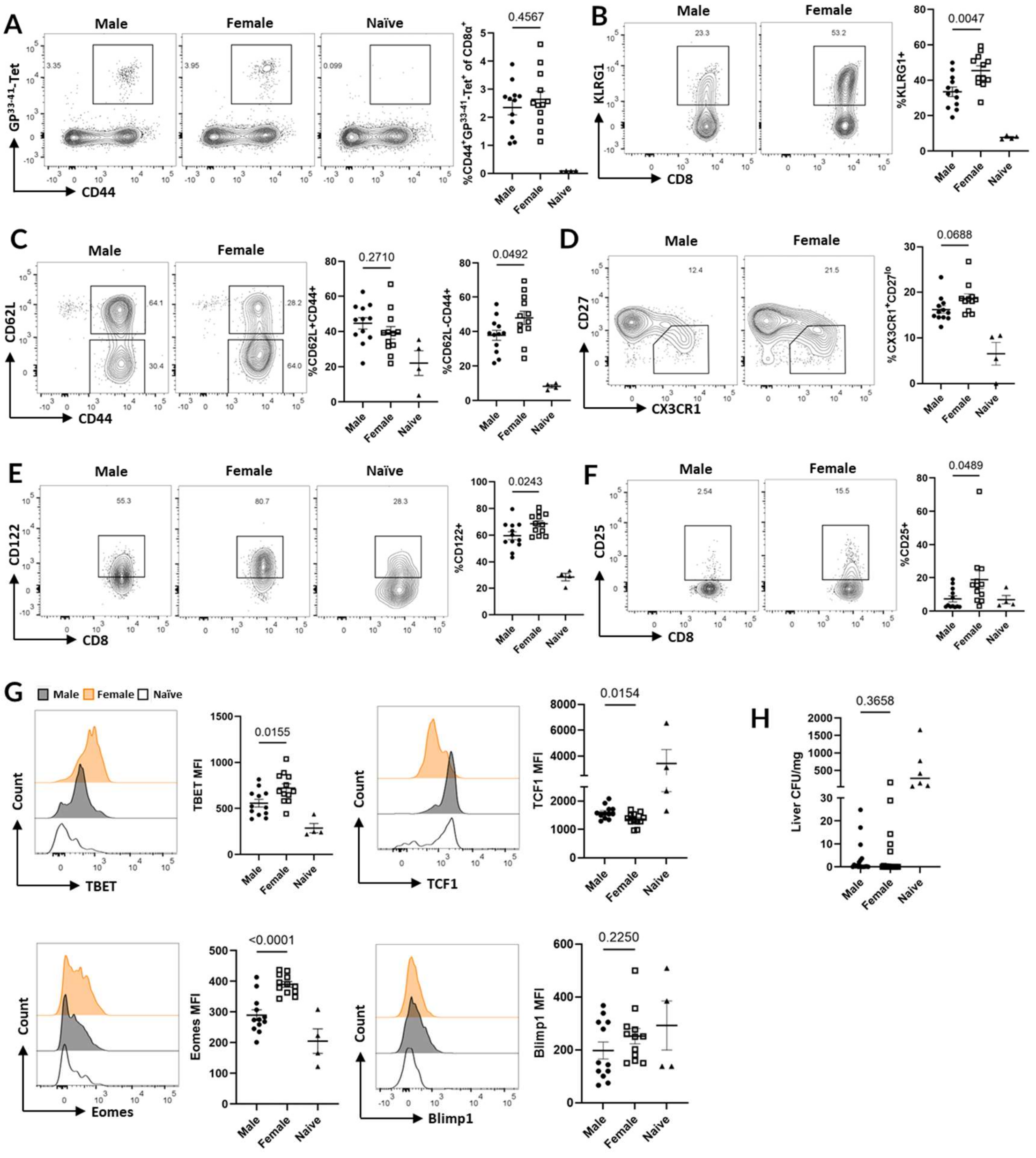

Figure 2.4 Sex differences in CD8 T cell memory to LCMV infection

Wild type male and female mice were infected with 2x10^5 PFU LMCV Armstrong and challenged with 1x10^5 CFU LM-GP33 on day 90 post-LCMV infection. (A) Frequency of CD8a+GP33-tetramer+ cells of live splenocytes compared to naïve male mice on day 3 after LM-GP33 challenge. (B) Frequency of KLRG1+, (C) CD62L+CD44+, (D) CX3CR1+CD27low, (E) CD122+ and (F) CD25+ among WT and ARKO GP33-Tetramer+ cells. (G) TCF1, Eomes, and TBET MFI of CD8a+GP33-tetramer+ splenocytes on day 3 after LM-GP33 challenge. (H) Liver bacterial burden in mice on day 3 after LM-GP33 challenge.

2.3.7 AR contributes to sexual dimorphism in CD8 T cell memory

We next sought to determine whether AR expression by CD8 T cells contributes to sexual dimorphism in CD8 T cell memory following acute infection. We adoptively transferred CD8+ P14 cells from male or female WT and ARKO mice into male or female recipients then infected with LCMV Armstrong. On day 35-42 post-infection, the frequency of adoptively transferred male WT P14 cells among CD8a+ splenocytes was higher than female WT P14s (Figure 2.5A). In contrast to bacterial challenge, ARKO in antigen-specific CD8 T cells reduced the frequency of male WT P14 memory cells and abrogated the difference observed between WT male and female P14s (Figure 2.5A). We also evaluated the impact of AR expression on the expression of memory differentiation markers in both male and female memory P14s (Figure 2.5B-C). We found that WT female P14 cells exhibited an increased frequency of CX3CR1+CD27lo (Figure 2.5B) and KLRG1-CD127+ (Figure 2.5C) cells compared to WT male P14 cells. Consistent with our observations of male WT and ARKO memory CD8 T cells following bacterial infection, ARKO in male P14 cells following LCMV Armstrong infection increased the frequency of CX3CR1+CD27lo and KLRG1+CD127- Tem cells in male mice, but this effect was not observed in female mice. Additionally, we observed a male-specific decrease in CD122 expression, suggesting that AR may control the sensitivity of male CD8 T cells to homeostatic signals received through IL-15 (Figure 2.5D). Overall, expression of Eomes was higher in P14 cells in female mice compared to male mice, but ARKO in male CD8 T cells induced expression of Eomes at a similar level to female cells (Figure 2.5E). There were relatively small differences observed in the expression of other transcription factors, TCF1, Blimp1, and Tbet (Figure 2.5F-H). Upon ex-vivo stimulation with GP33-41 peptide, there was no sex difference in the capacity of P14 memory cells to produce IFNγ and TNFα, but a higher frequency of female WT P14 cells produced GZMB compared to WT male cells (Figure 2.5I-J). Interestingly, the frequency of P14s that produced GZMB was reduced by ARKO in both male and female mice, indicating that the mechanism by which AR regulates GZMB expression may be conserved between male and female mice. Together, these data indicate that male and female mice exhibit sexual dimorphism in memory CD8 T cell differentiation and persistence following acute viral infection, which is at least partially mediated by AR expression.

We next investigated the mechanism by which AR enhances the persistence of memory CD8 T cells following acute viral infection. Previous literature has defined a role for homeostatic cytokines, IL-7 and IL-15, in supporting the long-term survival of memory CD8 T cells (discussed in Chapter 1). Given our observation that ARKO reduces the expression of the IL-7 and IL-2/IL-15 receptors (CD127 and CD122) in memory CD8 T cells in male mice (Figure 2.5C-D), and that AR expression does not substantially impact antigen-driven proliferation of CD8 T cells (Figure 2.2H), we reasoned that AR-mediated differential sensitivity to homeostatic cytokines may contribute to the sexual dimorphism in memory CD8 T cell persistence. To test this, we stained splenocytes from Figure 5A-E with CTV and stimulated them for three days in vitro with 10 nM GP33-41 peptide or 25 ng/mL of IL-7 and IL-15. Consistent with our findings during early activation of naïve cells, we observed no difference in peptide-induced proliferation of memory P14 cells based on sex or AR expression (Figure 2.5K). However, male WT P14 cells proliferated significantly more in response to IL-7 and IL-15 compared to female and ARKO male P14 cells. These data suggest that persistence of memory CD8 T cells is regulated in male mice through AR-mediated control over homeostatic cytokine sensitivity.

Previous studies have also demonstrated that the expansion and persistence of CD8 T cells in response to LCMV infection depends on type I IFN signaling (230). We therefore asked whether AR may control the persistence of memory CD8 T cells in male mice by influencing type I IFN signaling. To assess this possibility, we adoptively transferred WT and ARKO P14 CD8 T cells at a 1:1 ratio into congenic recipient mice and infected recipient mice one day later with LCMV. On day 4 post-infection, spleens were harvested from recipient mice and $CD8^+$ splenocytes were assessed by flow cytometry for expression of the type I IFN receptor, IFNα receptor 1 (IFNAR1). We found that ARKO P14 T cells expressed less IFNAR1 than co-transferred WT P14 cells in 3 out of 4 mice, but found no overall statistical difference in expression (Figure 2.5L). Thus, AR does not substantially alter the expression of IFNAR1 on effector CD8 T cells early following LCMV infection and whether AR controls effector CD8 T cell responses by supporting type I IFN sensitivity remains unclear.

Finally, we asked whether the influence of AR in memory phenotype and persistence may also relate to differences memory CD8 T cell protection. To test this, we pooled all splenocytes from replicate mice described in Figure 2.5A, then magnetically sorted memory P14 T cells by Thy1.1-PE^+ selection. The purity of P14 T cells in selected samples was determined by flow cytometry, then used to normalize P14 cell concentrations across samples before injecting 30K cells per mouse into sex-matched WT recipient mice by i.v. injection. One day later, recipient mice were challenged with $2x10^5$ CFU LM-GP33. Three days after challenge, spleens were harvested from recipient mice and assessed for bacterial burden. We found that male mice had significantly lower splenic LM-GP33 burden than female mice (Figure 2.5M). However, there was no significant boost in protection with ARKO memory P14s compared to WT P14s in both male and female mice, suggesting that AR expression does not contribute to the differential capacity for male and female LMCV-specific memory CD8 T cells to protect against re-infection with pathogens expressing their cognate antigen.

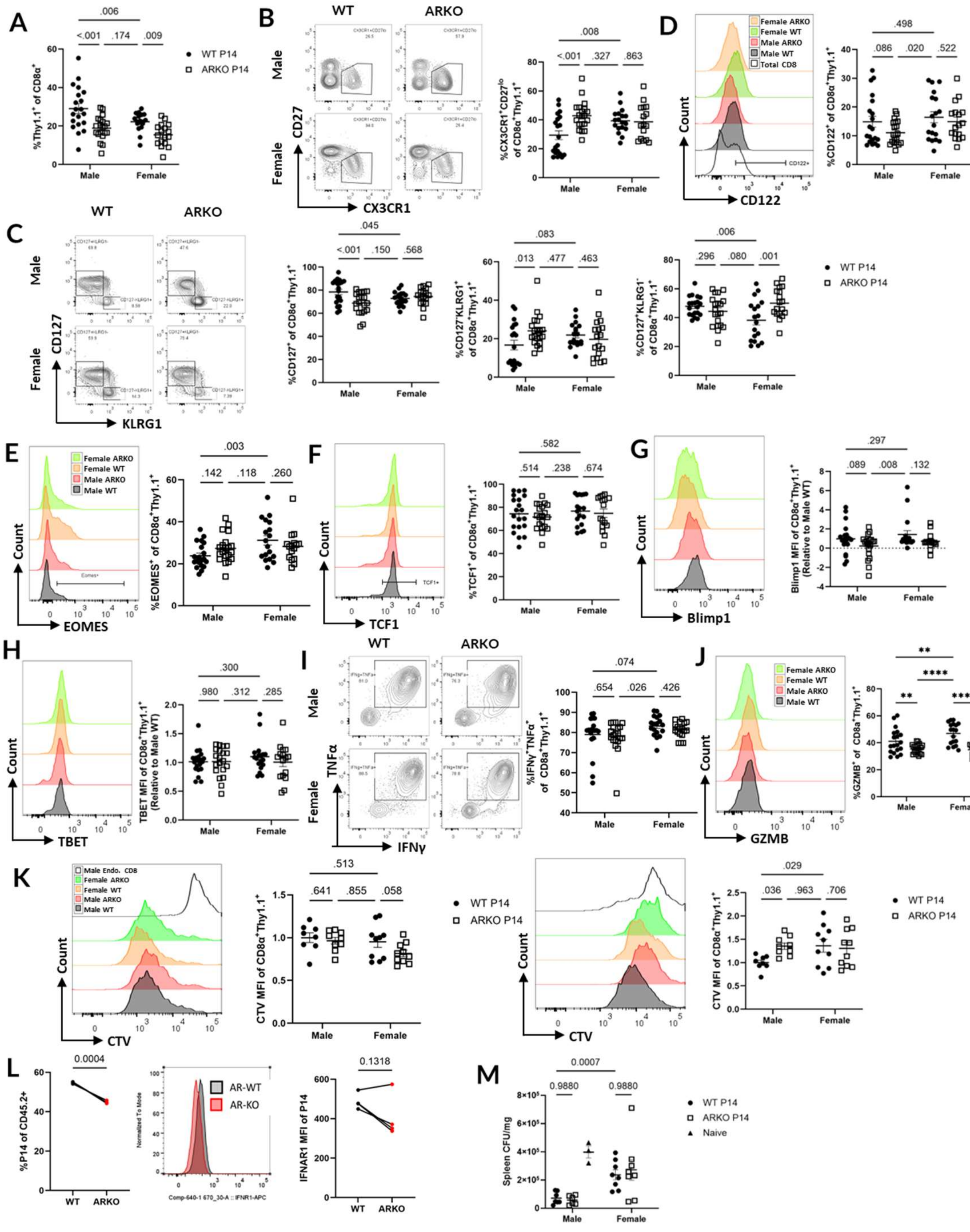

Figure 2.5 AR contributes to sexual dimorphism in CD8 T cell memory to LCMV infection

WT control P14s and ARKO P14s were transferred to WT recipient mice and recipient mice before infection with 2x10^5 PFU LCMV Armstrong. On day 30-45 post-infection, spleens were harvested from recipient mice and analyzed by flow cytometry for (A) frequency and abundance of Thy1.1+ P14 cells, (B) frequency of CX3CR1+CD27low, CD122+, CD127+, CD127-KLRG1+, and CD127+KLRG1- cells. (C) frequency of CD127+KLRG1-, CD127-KLRG1+ among transferred P14s (D) frequency of CD122+ cells among transferred P14s. (E)-(H) frequency of EOMES+ (E) and TCF1+ (F) cells and MFI of Blimp1 (G) and TBET (H) among transferred P14s. (I)-(J) frequency of IFNγ+TNFα+ (I) and GZMB+ (J) cells among transferred P14s following ex-vivo stimulation of splenocytes with $GP^{33\text{-}41}$ peptide for 4 hours followed by intracellular cytokine staining. (K) Mean cell trace violet (CTV) fluorescence intensity of CTV labeled splenocytes from A-D cultured in vitro for three days with GP33 peptide + 25 U/mL IL-2 (left) or 25 ng/mL IL-7 + 25 ng/mL IL-15 (right) measured by flow cytometry. (L) Frequency (left) and mean IFNAR1 expression (right) of WT control and ARKO P14s in the spleens of recipient mice four days after P14 co-transfer at a 1:1 ratio followed by LCMV Armstrong infection. (M) Thy1.1+ memory P14 cells magnetically sorted from (A) were adoptively transferred into sex-matched naïve recipient mice that were infected with 2×10^5 CFU LM-GP33 one day later. On day 3 post-infection, spleens were collected from recipient mice and LM-GP33 CFU/mg spleens was determined.

2.3.8 *AR cooperates with epigenetic regulators to control expression of T cell effector- and memory-associated genes*

As a nuclear hormone receptor, AR is poised to tune CD8 T cell responses through both epigenetic and transcriptional control of gene expression. To uncover the mechanisms by which AR controls T cells effector and memory differentiation and define the targets of AR transcriptional regulation in T cells, we utilized an in vitro model of AR overexpression. To express AR in human T cells, we transfected an immortalized T cell line, Jurkats, with a pcDNA3.1 vector containing a human AR cDNA sequence under the control of a CMV promotor (Jurkat-AR) or empty vector as a control (Jurkat-EV). We confirmed overexpression of AR in Jurkat-AR and no expression of AR in Jurkat-EV by flow cytometry (Supplemental

Figure 4). To determine whether AR activity regulates T cell gene expression in response to stimulation, we stimulated Jurkat-AR and Jurkat-EV cells in vitro with PMA and ionomycin for 24 hours in charcoal-stripped serum with or without addition of synthetic AR ligand, R1881 (Figure 2.6A). At 24 hours post-stimulation, cells were harvested for bulk RNAseq and ATACseq analysis. Dimensionality reduction and principal component analysis of the RNAseq data revealed both ligand-dependent and -independent changes in gene expression induced by AR expression (Figure 2.6B and Supplemental Figure 5). Interestingly, in principal component analysis, PC1 accounts for ~67% of the gene expression variance and mostly separates samples by AR expression, regardless of ligand exposure (Figure 2.6B). In contrast, PC2 accounts for ~13% of the variance and largely separates AR-expressing cells by addition of R1881 or vehicle control. The fact that AR expression alone has a larger impact on gene expression in our system may reflect ligand-independent roles for AR in T cells. Alternatively, this phenomenon may reflect lasting impacts of long-term culture with AR expression in androgen-containing culture media (via fetal bovine serum addition) prior to assay initiation, which may not be reversed by 24 hours of hormone deprivation in charcoal-stripped serum culture media at the beginning of the assay.

Genes significantly inhibited by AR activity include T cell effector- and memory-associated genes, *TBX21, GZMK, LTA, LTB, SELL,* and *FOXO1* (Figure 2.6C). Previous literature has defined the role of FoxO1 in supporting memory CD8 T cell differentiation by shielding of memory-associated genes from epigenetic silencing in memory precursor effector cells (45). To test whether AR may cooperate in that process, we performed gene set enrichment analysis to determine whether genes up- and down-regulated in *Foxo1*-knockout effector CD8 T cells are enriched in Jurkat-AR cells (Figure 2.6D). We found that genes up-regulated in Foxo1-KO effector CD8 T cells were significantly enriched in Jurkat-AR cells compared to Jurkat-EV and genes down-regulated by Foxo1-KO were conversely enriched in Jurkat-EV cells, indicating that AR may regulate T cell effector and memory gene expression through mechanisms dependent on FoxO1. To determine what other cellular processes may be regulated by AR in T cells, we performed further GSEA using Hallmark and gene ontology (GO) gene sets (Figure 2.6 E-F, respectively). Gene sets suppressed in Jurkat-AR cells included several immune effector gene sets, including Hallmark gene sets, IL2_STAT5_SIGNALING, INTERFERON_GAMMA_RESPONSE, and INTERFERON_ALPHA_RESPONSE, and GO gene sets, response to interferon-gamma, regulation of leukocyte activation, adaptive immune response, and regulation of immune effector process. These findings are consistent with our earlier observations in mouse models that AR skews CD8 T cell effector and memory differentiation and inhibits CD8 T cell effector responses.

Evidence from the relatively well-defined role of AR in prostate epithelial cells demonstrates that AR is capable of cooperating with epigenetic regulators to control target gene expression. To test whether AR may utilize similar mechanisms of epigenetic regulation in T cells, we profiled the chromatin accessibility landscape of Jurkat-EV and Jurkat-AR by assay for transposase-accessible chromatin (ATAC) sequencing. Following in vitro stimulation and R1881 treatment as outlined above (Figure 2.6A), overall chromatin accessibility in R1881-treated Jurkat-AR cells was reduced compared to Jurkat-EV and vehicle-control Jurkat-AR cells (Figure 2.6G). However, ligand-induced chromatin accessibility changes in Jurkat-AR cells included both regions of increased and decreased accessibility. This suggests that AR plays a role predominantly in epigenetic repression in T cells. Indeed, among all differentially accessible ATACseq peaks (DAPs), most peaks exhibited reduced accessibility in Jurkat-AR cells compared to Jurkat-EV (Figure 2.6G). We next utilized the putative AREs identified by the Jaspar database to filter DAPs to those that contain putative AREs and reveal chromatin accessibility changes in peaks that could be directly bound by AR (Figure 2.6H). ARE-containing DAPs included peaks that were both more and less accessible between Jurkat-AR and Jurkat-EV cells and between R1881-treated and vehicle-treated Jurkat-AR cells. When looking across the whole genome, we observed approximately twice as much chromatin closing as opening between Jurkat-AR with and without R1881 (Figure 2.6I). These findings demonstrate that open chromatin regions in T cells contain putative AREs and that many of these regions exhibit AR-induced changes in chromatin accessibility. Among loci that exhibited differential accessibility and contain putative AREs were T cell effector- and memory-associated genes, including *CX3CR1, TBX21, IFNG, GZMK, SELL, TCF7,* and *FOXO1* (Supplemental Figure 6). Taken together, these data suggest that AR coordinates changes in chromatin accessibility and is poised to regulate expression of T cell effector and memory genes through the cooperation of chromatin-modifying enzymes.

Given that AR activity altered Jurkat transcription and epigenetic state, we sought to determine whether AR cooperates with other transcription factors and chromatin-modifying enzymes. To reveal AR protein interactions, we applied rapid immunoprecipitation and mass spectrometry of endogenous protein (RIME) to Jurkat-AR and Jurkat-EV cells following the same stimulation conditions outlined in Figure 2.6A. Mass spectrometry of proteins pulled down by anti-AR and IgG control antibodies in both Jurkat-EV and Jurkat-AR cells detected 1528 proteins. After subtracting background intensity values of proteins detected in the IgG and Jurkat-EV controls, 152 proteins were detected with > 0 intensity in two independent clones of Jurkat-AR cells (Figure 2.6J). AR-interacting proteins included proteins previously known to associate with AR in prostate epithelial cells, BAF complex members (SMARCA4, SMARCA2, and SMARCC2), HDAC3, HDAC1, and EP300. Additionally, several other transcription factors and chromatin modifiers with known roles in controlling T cell differentiation and function immunoprecipitated with AR, including JUNB, SETB1, IKZF2, RXRA, RXRB, ACACA, CARM1, and ARID1A. Notably, ARID1A is a member of the canonical BAF (cBAF) complex and not PBAF and non-canonical BAF, suggesting AR preferentially associates with cBAF in T cells. To validate this finding, we performed AR immunoprecipitation and immunoblot for common BAF member, BRG1/SMARCA4, and cBAF and pBAF members ARID1A and ARID2, respectively, from Jurkat-EV and Jurkat-AR cells stimulated and treated with R1881 as described above. We found that BRG1/SMARCA4 and ARID1A, but not ARID2, co-immunoprecipitated with AR, corroborating our mass spectrometry analysis (Figure 2.6K).

AR's association with histone-modifying enzymes such as HDACs and SWI/SNF members, along with the evidence of AR-mediated regulation of chromatin accessibility suggest that AR may regulate the deposition or maintenance of histone post-translational modifications. To test this, we stimulated Jurkat-EV and Jurkat-AR cells for 24 hours as previously described, then assessed the abundance of histone modifications, histone 3 lysine 4 tri-methylation (H3K4me3), H3 lysine 27 tri-methylation (H3K27Me3), and H3 lysine 27 acetylation (H3K27Ac), relative to total H3 abundance by intranuclear staining and flow cytometry (Figure 2.6L). AR expression did not alter total H3 or H3K4Me3, but significantly decreased H3K27Ac abundance and increased H3K27Me3 abundance in Jurkat-AR cells compared to Jurkat-EV. These data are consistent with the finding that AR activity resulted in an overall decrease in chromatin accessibility in Jurkat-AR versus Jurkat-EV cells (Figure 6H) and the well-defined dichotomy of H3K27Ac and H3K27Me3 in marking active and repressed chromatin regions, respectively. Further, these data suggest that AR regulates the deposition or maintenance of histone modifications in T cells, and predominantly favors transcriptionally repressive H3K27Me3 over permissive H3K27Ac. This finding is consistent with our previously published evidence that AR acts to transcriptionally repress IFNγ production through direct binding to IFNγ enhancer (88). However, given that we identified ARE-containing ATACseq peaks that both increased and decreased in accessibility with AR activity, the general reduction in chromatin accessibility observed in Jurkat-AR cells compared to Jurkat-EV may occur through AR-mediated control of the transcription or activity of other epigenetic regulators, and not only through direct cooperation.

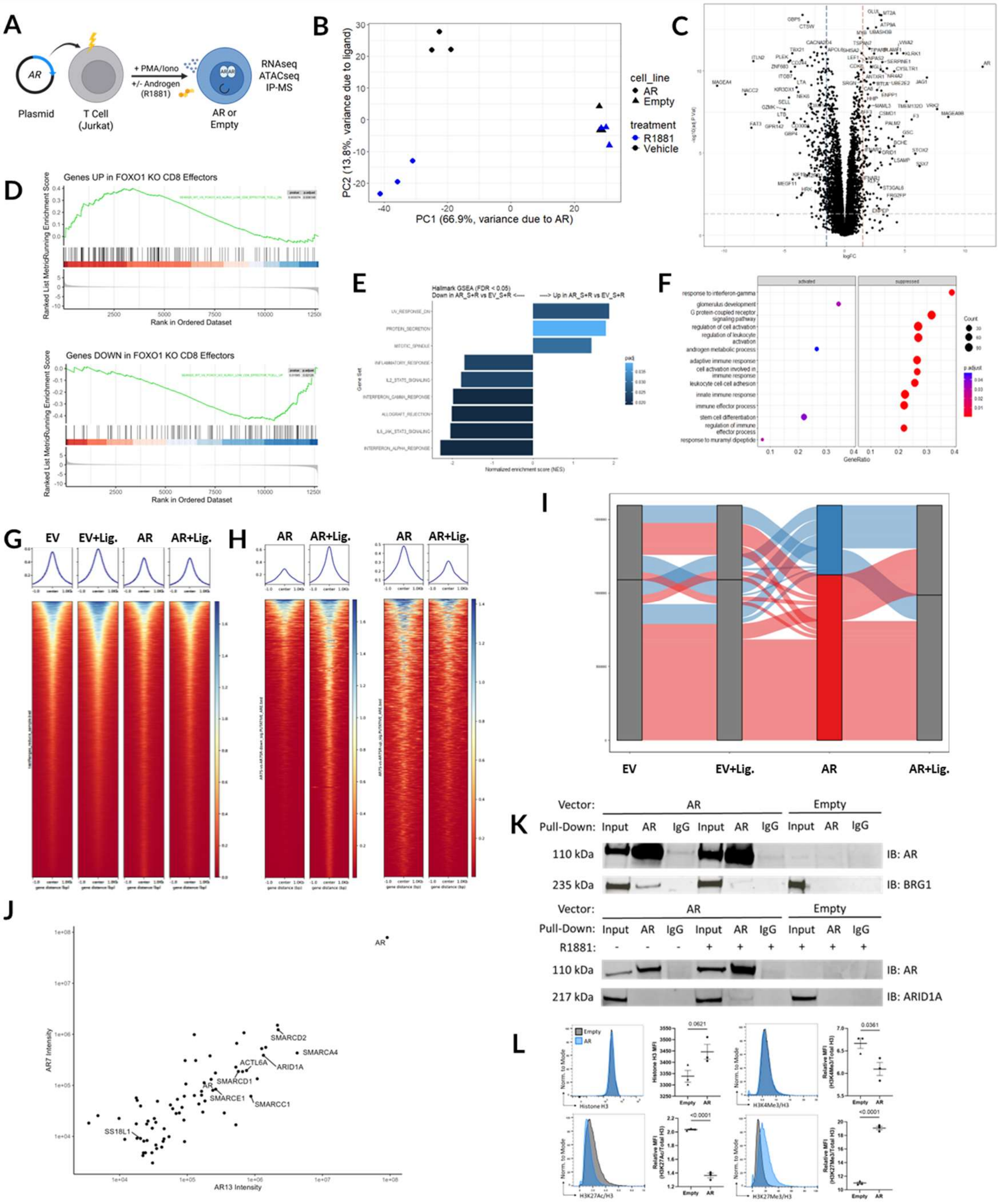

Figure 2.6 AR cooperates with epigenetic regulators to control CD8 T cell effector- and memory-associated genes

(A) Graphical overview of experimental methods. Jurkat T cells were electroporated with empty pcDNA3.1 or AR overexpression vectors and single-cell clones were cultured with PMA + ionomycin stimulation with synthetic androgen stimulation (R1881) or vehicle control. (B) Principal component analysis (PCA) of RNA expression in Jurkat-AR and

Jurkat-EV stimulated with PMA and ionomycin for 24 hours in charcoal stripped serum media with and without 100 nM R1881. (C) Volcano plot of differentially expressed genes between Jurkat-AR + R1881 and Jurkat-EV + R1881 as in A. (D) Gene set enrichment analysis (GSEA) of GSE46025 in Jurkat-AR + R1881 versus Jurkat-EV + R1881. (E) Hallmark pathway enrichment analysis in Jurkat-AR + R1881 versus Jurkat-EV + R1881. (F) Gene ontology enrichment analysis in Jurkat-AR + R1881 versus Jurkat-EV + R1881. (G) Heatmap of accessibility of differentially accessible chromatin regions assessed by ATACseq. (H) Differentially-accessible chromatin regions from F, filtered for peaks containing putative androgen response elements predicted by the Jaspar database. (I) Alluvial plot depicting overall chromatin accessibility changes between Jurkat-EV and Jurkat-AR cells with and without ligand. Bars represent closed (top, blue) and closed (bottom, red) chromatin regions within each condition. Lines connecting the bars show changes in chromatin accessibility in 100 bp regions between each condition. (J) Net intensity of proteins pulled-down with AR and detected by LC-MS in RIME analysis in two separate Jurkat-AR clones minus respective IgG control Jurkat-EV control intensities. (K) AR Immunoprecipitation and immunoblot for indicated proteins in Jurkat-EV and Jurkat-AR cells stimulated for 24 hours with PMA + ionomycin +/- 100 nM R1881. (L) Flow cytometry measurement of total histone H3 expression and H3K4Me3, H3K27Ac, and H3K27Me3 expression normalized to total H3 fluorescence in Jurkat-EV and Jurkat-AR cells stimulated with PMA/ionomycin + R1881.

2.4 Discussion

In this study, we uncover a role for AR in influencing the effector and memory responses of CD8 T cells to acute infection. Although CD8 T cell expression of AR in mice and humans has been previously reported (88), the role of AR in CD8 T cells in acute infections and the mechanisms by which AR controls CD8 T cell function remained largely undefined. Here, we show that AR limits the effector response of CD8 T cells to acute infections and limits the capacity for memory CD8 T cells to protect against re-challenge.

Further, we utilize an *in vitro* model of AR overexpression to profile the targets of AR-mediated gene expression in T cells, associate changes in gene expression with AR-mediated changes in chromatin accessibility and reveal cofactors that associate with AR in T cells.

Our data demonstrate that while AR expression is relatively stable during acute viral infection in vivo, it is highly dynamic in response to acute TCR stimulation in vitro. This suggests that AR activity is tightly linked to antigen encounter and co-stimulatory signals and warrants further investigation into the mechanisms that control AR expression in T cells. Using a conditional knockout model, we show that AR limits the homeostatic expansion and differentiation of memory-like $CD8^+$ T cells under steady-state conditions. This likely reflects a role for AR in restraining tonic TCR signaling and responsiveness to homeostatic cytokines such as IL-7 and IL-15, signals that are required both for the survival of naïve T cells and for the conversion into "virtual memory" cells (11, 12). The role for AR in limiting these signals may prevent aberrant activation in the absence of infection. Further investigation into how AR expression limits homeostatic signaling in T cells should investigate the intersection between AR activity and the strength of homeostatic signaling T cells receive at steady state.

Most consistently, we demonstrate that AR expression limits the expression of markers of CD8 T cells with high effector capacity, including CX3CR1 and KLRG1, in both the acute and memory phases of infection. These data suggest that AR-expressing CD8 T cells may have less cytotoxic activity, though that possibility is not directly addressed in this work. During the memory phase, the heightened expression of CX3CR1 and KLRG1, along with reduced expression of CD27 and CD62L suggest that AR-deficient CD8 T cells most closely resemble effector memory rather than central memory T cells. Previous studies of memory subsets of CD8 T cells demonstrated that Tcm CD8 T cells exhibit a superior capacity to control re-challenge compared to Tem cells (231). Paradoxically, although AR-deficient memory CD8 T cells exhibited increased Tem-like differentiation, they also exhibited an increased capacity to control re-challenge compared to WT CD8 T cells. This finding suggests that the mechanisms by which AR regulates CD8 T cell responses act to influence both the phenotypic and functional characteristics of memory cells, but the influence of AR on limiting Tem features is not entirely coupled with protective capacity in this context.

Interestingly, we revealed seemingly contradictory effects of AR activity on CD8 T cells in the context of bacterial versus viral infections. While some impacts of AR activity, such as limiting the differentiation of antigen-specific CD8 T cells into CX3CR1+CD27lo terminal effector or Tem for example, remain consistent between the two disease models, the impact of AR on other aspects, such as the expansion and persistence of antigen specific CD8 T cells, are disparate. These findings suggest that the mechanisms by which AR integrates with other regulators of CD8 T cell responses include those that are common between disparate pathogens, but also mechanisms that are dependent on pathogen-specific signals. Earlier reports that investigated the signaling requirements for optimal CD8 T cell responses to bacterial and viral infections revealed different dependencies for optimal expansion and persistence of CD8 T cells depending on the nature of the infection. For example, bacterial models of infection with Listeria monocytogenes have demonstrated a dependence of Listeria-specific CD8 T cells on IL-12 for optimal expansion and memory persistence (232, 233). On the other hand, virus-specific CD8 T cell expansion and memory persistence are more reliant on type I IFN signaling and less dependent on IL-12 (230). This raises the possibility that AR differentially regulates signaling through the IL-12 and type I

IFN receptors, thereby supporting expansion of CD8 T cells in viral infections while limiting the expansion of bacteria-specific cells. To determine whether that is true, further work should directly compare responses of ARWT and ARKO CD8 T cells to both bacterial and viral infections and assess whether AR expression influences the dependence of CD8 T cells on IL-12 and type I IFN in those models.

Mechanistically, we demonstrate that AR interacts with epigenetic regulators in T cells, alters T cell chromatin accessibility, and controls expression of effector- and memory-associated genes, including genes critical for T cell function such as *TBX21, FOXO1, GZMK, LTA, LTB, SELL, TCF7, RUNX2,* and *KLF2*. The important role for expression of many of these genes in effector and memory T cell differentiation has been demonstrated (21, 22). Additionally, proteins found to interact with AR, cBAF complex members and HDACs for example, are known to play important roles in regulating the differentiation and function of CD8 T cells (234, 235). It is therefore unsurprising that AR was found to interact with those proteins in controlling gene expression in T cells in our model. Interestingly, as a whole, AR expression was found to be repressive for chromatin accessibility in T cells, revealing an overall repressive role for AR in controlling T cell gene expression. However, when the ATACseq analysis was limited to peaks that contained AREs, there were similar numbers of peaks that opened and closed in AR-expressing Jurkat cells with the addition of synthetic androgens (Figure 2.6H). This disparity shows that AR is capable of coordinating both the opening and closing of chromatin in T cells, but suggests that regions opened by AR and genes induced by AR may overall be genes that inhibit effector and memory differentiation. Further work is needed to unequivocally identify the genetic loci that are directly bound by AR in T cells, especially in primary CD8 T cells, which was not addressed in this work. Additionally, because we identified AR interactions with chromatin-modifying factors, investigations into the AR-mediated epigenetic histone modifications, including H3K27Ac and H3K27Me3, may reveal which epigenetic modifications are associated with AR activity and potentiate targeted interventions to disrupt those changes.

Overall, the findings of this work have important implications for understanding the mechanisms that drive sex differences in immune responses and disease susceptibility. The importance of understanding what drives sexual dimorphism in immune responses is no more apparent than in the observed sex disparities in infection, severity, and mortality during the recent COVID-19 pandemic, where men were more likely to be infected, require hospitalization to manage severe symptoms, and eventually succumb to the disease (236). Our findings may provide a mechanistic basis for observed sex differences in T cell immunity. Given that AR is activated by androgens—present at higher levels in males—AR-mediated signaling may contribute to the generally reduced $CD8^+$ T cell activation and memory formation observed in male subjects across multiple species. This raises the possibility that physiological differences in AR activity contribute to sex-specific immune responses to infection, vaccination, and immunotherapy.

Finally, the potential to therapeutically modulate AR signaling in T cells warrants investigation. AR antagonists and agonists are already in clinical use for prostate cancer and could be repurposed or optimized to enhance T cell immunity in settings such as vaccination, chronic infection, or cancer immunotherapy. However, careful evaluation of the systemic effects and immune-specific consequences of such interventions will be necessary to balance efficacy and safety. For example, several other immune cell types are known to be regulated by androgen signaling, including suppressive regulatory T cell and myeloid cell types which are supported by AR activity (237). Together, these results position AR as a critical node in the regulation of $CD8^+$ T cell responses, integrating hormonal cues with antigenic and inflammatory signals to modulate T cell fate. This work lays the groundwork for future studies examining AR as a potential immunomodulatory target in both infectious and non-infectious disease settings.

2.5 Methods

2.5.1 Mice

B6 (C57BL/6J) and e8i-cre (C57BL/6-Tg(Cd8a-cre)1Itan/J) mice were purchased from the Jackson Laboratory. $Ar^{fl/fl}$ mice were a kind gift from the Golnick lab (229). P14 TCR transgenic mice were obtained from Dr. Jeffrey Nolz. OTI TCR-transgenic mice were obtained from the Dr. Amanda Lund. All mice were housed under specific-pathogen-free conditions at Oregon Health & Science University. All experimental procedures performed were approved by the Oregon Health & Science University Animal Care and Use Committee.

2.5.2 Single cell isolation from mouse tissues

To isolate single-cell suspensions of mouse splenocytes, lymphocytes and thymocytes, mouse spleens, lymph nodes, or thymi were disrupted by grinding between frosted glass slides or mashing through a 70 μM mesh filter (Falcon, 352350) using the end of a 1 mL syringe plunger (BD cat # 309659). Suspensions were then washed in 10 mL 1x PBS and pelleted at 350 x g for 5 minutes. Pellets were then resuspended in 3 mL ACK lysis buffer (Gibco, A1049201) and incubated at room temperature for 3 minutes before washing with 12 mL 1x PBS and filtering through a 70 μM mesh filter.

2.5.3 Adoptive T cell transfers

For adoptive transfer of TCR transgenic CD8 T cells, splenocytes were collected from donor mice as described above. CD8 T cells were isolated from splenocytes by magnetic sorting using the Mouse CD8 T Cell Positive Selection Kit (StemCell, 19853) or the Mouse Naïve CD8 T Cell Positive Selection Kit (StemCell, 19858). Sorted CD8 T cells were washed and resuspended at 1-10x10^6 cells/mL in 1x PBS and 100 μL of the cell suspension was injected into recipient mice by retroorbital intravenous injection.

2.5.4 Mouse infections

LCMV Armstrong virus was provided by Dr. Mark Slifka Lab. Viral stocks were diluted to 1x10^6 PFU/mL in 1x PBS and 200 μL injected into recipient mice via retroorbital intravenous (i.v.) injection for a total infectious dose of 2x10^5 PFU.

Virulent and ActA-attenuated L. monocytogenes expressing GP33-41 were gifts from the Nolz lab and ActA-attenuated L. monocytogenes expressing OVA was received from Amanda Lund Lab, OHSU, CDCB. For infection of mice with ActA-attenuated L. monocytogenes, bacteria were grown in tryptic soy broth (Sigma-Aldrich, 22091-500G) containing 50 μg/mL streptomycin sulfate (Gibco, 11860038) by shaking at 37 °C to optical density at 600 nm of 0.1 (~10^8 CFU/mL). Bacteria were diluted to 2.5x10^7 CFU/mL in 1x PBS and 200 μL injected into recipient mice by retroorbital intravenous injection. For infection of mice with virulent LM-GP33 for CFU assays, LM-GP33 were grown to OD = 0.1 as described above. LM-GP33 were diluted 1:100 in 1x PBS for a final concentration of ~1x10^6 CFU/mL and 100 μL was injected into recipient mice by retroorbital i.v. injection for a total infectious dose of ~1x10^5 CFU.

2.5.5 Colony forming unit assays

For measurement of bacterial burden, spleens and liver lobes were collected from LM-GP33-infected mice on day 3 post-infection and placed in 0.1% IGEPAL (Sigma-Aldrich, I3021) in 1x PBS. Tissues were weighed and homogenized using a tissue homogenizer (FisherScientific, 15-340-167). Homogenized samples were incubated on ice for 30 minutes before serial dilutions were plated on tryptic soy agar supplemented with 50 μg/mL streptomycin. Plates were incubated at 37 °C overnight and colony forming units were counted the next day for calculation of bacterial burden.

2.5.6 In vitro T cell stimulation

T cells were stimulated in vitro using plate-bound anti-CD3 and anti-CD28 antibodies. Flat-bottom tissue culture plates were coated with 5 μg/mL anti-mouse CD3 and 2.5 μg/mL anti-mouse CD28 antibodies in 1x PBS for 4 hours at 37 °C or overnight at 4 °C and washed with 1x PBS. Mouse T cells were plated on antibody-coated plates at a density of 1-2x10^6 cells/mL in complete RPMI (see above for recipe) supplemented with 25 Units/mL recombinant mouse IL-2 (Peprotech 212-12-20UG) then cultured at 37 °C and 5% CO_2 for varying times depending on experimental endpoint.

2.5.7 Proliferation assays

Magnetically-sorted mouse bulk $CD8^+$ or naïve $CD8^+$ T cells were stained for 20 minutes at 37 °C with CellTrace Violet (ThermoFisher C34557) in pre-warmed 1x PBS at a density of $10x10^6$ cells/mL. Pre-warmed complete RPMI was added at 5x the CTV staining volume and cells were incubated for an additional 5 minutes at 37 °C before washing with 1x PBS. CTV-stained cells were stimulated in vitro with anti-CD3 and anti-CD28 or adoptively transferred into recipient mice before infection as outlined above.

2.5.8 Ar qPCR

For ex-vivo mouse T cell Ar mRNA measurement, CD8+ T cells were sorted from week-old male Thy1.1+/+ P14 TCR transgenic mouse spleens using the EasySep Mouse CD8+ T cell isolation kit (StemCell 19853). 1,000,000 sorted CD8+ P14 cells were preserved in 700 µL QIAazol (Qiagen, 79306) for pre-infection Ar mRNA measurement. 100,000 CD8+ T cells were transferred into male C57Bl/6J recipient mice by retroorbital i.v. injection in 100 µL 1x PBS. One day later, mice were infected with $2x10^5$ PFU LCMV Armstrong by retroorbital intravenous injection. On day 7 or day 30 post-infection, spleens were harvested from recipient mice and processed into single-cell suspensions as outlined above. P14 T cells were sorted from splenocytes using the EasySep PE Release Positive Selection Kit II (StemCell, 17684) with PE-conjugated anti-mouse CD90.1 (Invitrogen, 12-0900-83) according to the manufacturer's instructions. Sorted PE+ cells were then resuspended in 700 µL QIAzol and preserved at -80 °C for batched RNA extraction. RNA was extracted using the Qiagen miRNeasy Mini kit (Qiagen, 217004) and 500 ng of isolated RNA were used for cDNA synthesis using the High-Capacity cDNA Reverse Transcriptase kit (ThermoFisher, 4374966). 1/100th of the cDNA was used per qPCR reaction using the TaqMan Universal PCR Master Mix (ThermoFisher, 4304437) with TaqMan assays for *Ar* (ThermoFisher, Mm00442688_m1), *Gapdh* (ThermoFisher, Mm99999915_g1), *Sdha* (ThermoFisher, Mm01352366_m1), and *18S* (Hs99999901_s1) using a QuantStudio 3 qPCR machine with the following protocol: 2 minutes at 50 °C and 10 minutes at 95 °C followed by 40 cycles of 15 seconds at 95 °C and 1 minute at 60 °C. Data analysis was performed using QuantStudio Design & Analysis Software (version 1.5.2).

5 µg of extracted RNA per sample was used for qPCR analysis using the GoTaq 1-Step RT-qPCR kit (Promega, A6020) and primers for *Ar* (forward: GGA GAA CTA CTC CGG TTA T, reverse GGG TGG AAA GTA ATA GTC GAT GG:) and *Sdha* (forward: GAG ATA CGC ACC TGT TGC CAA G, reverse: GGT AGA CGT GAT CCT TCT CAG GG).

2.5.9 Flow Cytometry

1-10x10^6 cells from single cell suspensions were first stained with 1:1000 diluted Live/Dead Fixable Aqua (Molecular Probes, L34966) or Live/Dead Fixable Blue (Molecular Probes, L34962) stain in 1x PBS for 15 minutes at 4 °C in the dark. For cell surface marker staining, samples were stained in 100 µL antibody cocktails containing 50 µL Brilliant Stain Buffer (BD Horizon, BD566349), fluorochrome-conjugated antibodies at defined dilutions (see below), and the remaining volume of FACS buffer (1x PBS + 1% FBS + 0.1% sodium azide). Cells were incubated with cell surface staining cocktails for 0.5-1 hours and washed twice before analysis. For intracellular transcription factor staining, cell suspensions were fixed and permeabilized using the eBioscience Foxp3 Transcription Factor Staining Kit (Invitrogen, 00552300) following cell surface staining. Fixed and permeabilized cell suspensions were then stained in 100 µL perm/wash buffer containing fluorochrome-conjugated anti-transcription factor antibodies at defined dilutions (see below) and incubated for 1 hour at 4 °C in the dark. Cell suspensions were then washed twice in 250 µL permeabilization buffer before resuspension in FACS buffer for analysis. Data were collected on a BD FACS Symphony A5 or a BD LSRFortessa and analyzed using FlowJo version 10.

2.5.10 Fluorescence activated cell sorting

All cell sorting was performed on a BD FACS Symphony S6 cell sorter. For naïve OTI CD8 T cell transfer described in Figures 2.2-2.3 and memory P14 CD8 T cells adoptive transfer described in Figure 2.3, cells were sorted from bulk splenocytes by FACS prior to adoptive transfer. Naïve cells were sorted by staining splenocytes with anti-mouse CD8-FITC, anti-mouse CD4 BV650 and anti-mouse CD44-PE. $CD8^+$ $CD4^-$ $CD44^{low}$ cells were sorted into complete RPMI media, washed and resuspended in 1x PBS prior to adoptive transfer. To sort memory P14 cells, splenocytes from LCMV-immune mice were stained with anti-mouse CD8-FITC, anti-mouse Thy1.1-PE and anti-mouse CD44 AF700. $CD8^+$ $CD44^+$ $Thy1.1^+$ cells were sorted into complete RPMI then washed with 1x PBS prior to adoptive transfer.

2.5.11 Jurkat AR overexpression

Jurkat cells were a generous gift from Dr. Evan Lind. Parental Jurkat cells were maintained in culture with stock 500mL RPMI media supplemented with 1% 100X penicillin/streptomycin (Cytiva HyClone, SV30010), 5% 100X non-essential amino acids (Cytiva HyClone, SH3023801), 1% 1M HEPES buffer (Corning, 25060CI), 1% 100mM sodium pyruvate (Gibco, 11360070), and 10% fetal bovine serum (Cytiva HyClone, SH30396.03). Parental Jurkat cells were transfected with pcDNA3.1 plasmids either containing a human AR cDNA expression cassette or the empty vector only using the Neon™ Transfection System (Invitrogen) using the manufacturer's recommended settings for Jurkat cells. Plasmids were a generous gift from the Alumkal Lab (University of Michigan Medicine) Transfected plasmid-expressing cells were selected using 800 ng/mL G418 sulfate antibiotic selection (Abcam, ab144261) in RPMI media supplemented as above without penicillin and streptomycin. AR expression in Jurkat-AR cells, and lack thereof in Jurkat-EV cells, was confirmed by flow cytometry (supplemental Fig1). Individual clones of Jurkat-AR and Jurkat-EV cells were then derived by limiting dilution plating to expand single-cell-derived clones. AR expression in Jurkat-AR clones, and lack thereof in Jurkat-EV clones, was again confirmed by flow cytometry following clonal expansion (Supplemental Figure 13).

2.5.12 Immunoprecipitation and immunoblot

Cells were harvested on ice, pooled by condition, and washed with ice-cold 1x PBS. Cell suspensions were then fixed for five minutes with ice-cold 1% formaldehyde (Thermo Scientific, 28906) in 1x PBS and fixation was quenched by the addition of glycine to a final concentration of 0.1M (Sigma-Aldrich, G7126) for 3 minutes on ice. Cell pellets were then resuspended in immunoprecipitation buffer containing 50 mM TrisHCl (Promega, H5121), 1% Triton X-100 (ThermoFisher, HFH10), 150 mM NaCl (FisherScientific, BP358-1), and Roche cOmplete protease inhibitor (Millipore, 11697498001, 1 tablet/50mL buffer). Cells were then disrupted by sonication using the Fisherbrand Model 50 Sonic Dismembrator (FisherScientific, FB50) at amplitude 30 for five cycles of 10 seconds on/10 seconds off, and lysates cleared by centrifugation at 12,000 x g for 15 minutes at 4 °C. 10% of cleared lysate was reserved for input control before splitting the remaining volume for incubation with anti-AR (1:50, Sigma-Aldrich, 06-680) and rabbit IgG (1:250, Sigma-Aldrich, 12-370) isotype control antibodies rotating at 4 °C overnight. The following day, 50 µL protein A microbeads were added to each lysate, then lysates were rotated for 3 hours at 4 °C. Lysates were then cleared by magnetic separation on ice and the microbead pellet reserved for Western blot analysis.

For Western blot analysis, microbead pellets and 10% input samples were incubated for 20 minutes at 95 °C in immunoprecipitation buffer supplemented with 1x fluorescent-compatible protein loading dye and 1x sample reducing buffer. Samples were then cleared by magnetic separation and loaded onto a NuPAGE 3-8% Tris-Acetate gel (Invitrogen, EA0375) for size separation by denaturing electrophoresis before transfer to a PVDF membrane (Invitrogen, LC2002). Membranes were then blocked using PBS Intercept Blocking Buffer (LiCOR, 927-70001), stained with primary antibodies against AR (Sigma-Aldrich, 06-680), BRG1 (ThermoFisher, MA5-31550), ARID1A (Cell Signaling Technology, 12354S) or ARID2 (Boster Bio, A05064) overnight at 4 °C, and stained with fluorescently-labeled anti-goat (LiCOR, 926-68070?) or anti-rabbit (LiCOR, 926-68071) secondary antibodies for 2 hours at RT. Membranes were then imaged using a LiCOR Odyssey CLx.

2.5.13 Immunoprecipitation and mass spectrometry

Samples were prepared for immunoprecipitation and mass spectrometry according to the protocol outlined by Mohammed et al. (238). Cells were harvested on ice and washed with ice-cold 1x PBS. Cells were fixed for 8 minutes in ice-cold 1% formaldehyde in 1x PBS and incubated for an additional 5 minutes on ice after adding glycine to a final concentration of 0.1 M. Cells were then resuspended in 10 mL ice-cold nuclei extraction buffer (LB1) and rotated for 10 minutes at 4 °C. Nuclei were pelleted at 2000 x g and 4 °C, resuspended in 10 mL ice-cold lysis buffer 2 (LB2), and rotated for 10 minutes at 4 °C. Nuclei were then resuspended in 300 µL ice-cold lysis buffer 3 (LB3), transferred to 1.5 mL Bioruptor microtubes (Diagenode C30010016) and sonicated in a Diagenode Bioruptor Pico sonicator for 10 cycles of 30 seconds on and 30 seconds off. 30 µL of 10% Triton X-100 was added to each lysate and lysates were cleared by centrifugation at 20,000 x g. Immunoprecipitation antibodies against AR (Sigma-Aldrich, 06-680) and rabbit IgG control (Sigma-Aldrich, 12-370) were conjugated to Protein A dynabeads (ThermoFisher 10002D) overnight in 5% BSA in 1x PBS. Cell lysates were incubated with antibody-conjugated dynabeads overnight, washed 4x with ice-cold RIPA buffer by magnetic separation, then washed twice with ice-cold 100 mM ammonium hydrogen carbon (AMBIC). Pellets were then digested overnight at 37 °C with 10 µL of 10 ng/µL trypsin (Worthington Biochem. LS003741) in AMBIC and again for 4 hours at 37 °C by adding another 10 µL of the trypsin solution. Following digestion, 100% formic acid (Sigma-Aldrich, F0507) was added to a final concentration of 5% (vol/vol) formic acid. Peptide desalting was performed using the Phoenix Peptide Cleanup Kit (PreOmics P.O.00023). Dry peptides were reconstituted in 20 µL LCMS-grade water and 15 µL of a 3% acetonitrile and 5% formic acid solution in LCMS-grade water prior to LCMS analysis.

2.5.14 RNA sequencing

Jurkat-EV and Jurkat-AR cells were cultured for 24 hours in CSS-RPMI media containing 10% charcoal stripped serum (Biowest USA, S162C), 1% non-essential amino acids Cytiva HyClone, SH3023801), 1% 1M HEPES buffer (Corning, 25060CI), 1% 100mM sodium pyruvate (Gibco, 11360070), and 800 ng/mL G418 sulfate (Abcam, ab144261) before being cultured for an additional 24 hours in CSS-RPMI with or without eBioscience cell stimulation cocktail (Invitrogen, 00497093) and with or without 100 nM R1881 (Sigma-Aldrich, R0908) or DMSO vehicle control. Cells were then harvested on ice and resuspended in buffer RLT for storage at -80 °C before batched RNA extraction using the miRNeasy Micro RNA extraction kit (Qiagen, 217084). RNA sequencing libraries were constructed using the TruSeq Stranded mRNA Library Prep kit (Illumina, 20020594) and libraries were sequenced on an Illumina NovaSeq 6000 by paired-end, 2x150 bp sequencing.

2.5.15 ATAC sequencing

Jurkat-EV and Jurkat-AR cells were cultured as described above for RNA sequencing. 50,000 cells per condition were reserved for ATACseq library preparation using the ActiveMotif ATACseq library preparation kit (Active Motif, 53150). Libraries were sequenced on an Illumina NovaSeq by paired-end, 2x150 bp sequencing.

2.5.16 RNA sequencing data analysis

Raw fastq files were assessed for quality using FASTQC. Sequencing reads were aligned to the hg38 reference transcriptome (EnsemblDB Hsapiens v86) using kallisto. Gene-level counts per million (cpm) were derived from transcript-level abundance using length-scaled TPM via tximport and edgeR. Genes with read counts of <1 cpm in half or more of the samples were removed from the analysis before normalizing read counts between samples using the trimmed mean of m-values method.

2.5.17 ATAC sequencing data analysis

Raw sequencing data quality were assessed using fastqc (version 0.12.1), followed by duplicate removal and adapter trimming by fastp (version 0.23.4, --dup_calc_accuracy level 3). Sequencing alignment was conducted using bowtie2 (version 2.5.4)to hg38 with the following flags: --local, --no-mixed, --nodiscordant, --very-sensitive-local, -I 25 and -X 700. Chromatin accessibility peaks were called using macs2 (version 2.2.9.1) using the callpeak command with --gsize "hs" flag. Consensus peaks were defined as any accessible chromatin region present in at least 2 or more sample replicates within a single sample condition. Differential peak accessibility analysis was conducted with the DESeq2 package (version 1.46.0, R version 4.4.2) applied to a matrix of sample replicate consensus peaks counts via the DESeq() command with an adjusted pvalue cutoff of 0.05. Motif enrichment of differentially accessible peaks were conducted with the HOMER (version 4.11) annotatePeaks.pl script. Bam alignment files were converted to bigwig files for visualization using bamCoverage (deeptools version 3.5.5) with the flag --normalizeUsing CPM. Putative Androgen Response Element bedfiles were obtained from the JASPAR database. Differentially accessible peak bedfiles were overlapped using the bedtools intersect command (version 2.31.1). Accessibility heatmaps were created using deeptools computeMatrix command. Alluvial plots were generated by binning the entire genome into 100 basepair bins, then identifying changes in chromatin accessibility across sample conditions, collapsing the genome-wide matrix into a frequency table and applying the ggalluvial R package (version 0.12.5, ggplot version 3.5.1).

2.5.18 Statistical analysis

Statistical tests were performed in Graphpad Prism v. Data shown are either representative data from one of two or three replicate experiments or a combination of data from replicate experiments. Strudent's t-test was used for statistical tests between two groups except when normality was not assumed, in which case a non-parametric Mann-Whitney test was performed. Where appropriate in co-transfer models, paired samples t-tests were performed. In experiments with two factors (i.e., WT and ARKO males and females), two-way ANOVAs followed by Bonferroni-corrected multiple t-tests were performed. The robust regression and outlier removal (ROUT) method was used to identify outliers in CFU data with Q = 1%. All statistical tests were assessed for significance at α = 0.05.

Interchapter: Leveraging human prostate cancer clinical trial data to investigate the impact of androgen deprivation therapy on primary human T cells

An open question not addressed by our previous published work or the work described in **Chapter 2** is what role AR plays in regulating the responses of primary human T cells. Our previous work established an association between AR signaling in CD8 T cells and poor response of metastatic CRPC (mCRPC) patients to anti-PD-1 checkpoint blockade therapy (88). In that study, mouse models of prostate cancer and chronic infection demonstrated that AR expression in CD8 T cells limits IFNγ production and anti-PD-1 response. These findings highlight an important role for T cell intrinsic AR expression in controlling the anti-tumor response in prostate cancer. However, the patients on that study were treated with long-term ADT prior to study enrollment and had developed resistance to treatment. Therefore, it was not possible to compare the tumor microenvironment pre- and post-ADT to elucidate the effects of ADT on the anti-tumor immune response. The following chapter describes the results of single cell RNA sequencing profiling of treatment-naïve patient prostate tumor biopsies before and after treatment with neoadjuvant androgen axis inhibition (AAI) and anti-PD-1 checkpoint blockade. This clinical trial provides a powerful setting to study the impact of AAI on the tumor immune response in humans and provides an important context against which to compare our findings from acute mouse models of infection.

Chapter 3: Deciphering the prostate tumor microenvironment: transcriptional insights into therapy response following androgen axis inhibition and immune checkpoint blockade

Contributing authors: Reed Hawkins[1, 2], Benjamin Weeder[1, 3], Sushil Kumar[4], Ryan Kopp[5], Mark Garzotto[5, 6], Reid Thompson[7], Amy Moran[7]

Author Contributions:

1: Manuscript preparation, data interpretation, analysis planning

2: Biopsy processing and single cell library preparation

3: Computational analysis

4: Analysis and interpretation of myeloid cell gene expression

5: Clinical research support

6: Clinical trial principal investigator

7: Funding support, data interpretation, analysis planning

Abstract

Aggressive prostate cancers often exhibit progression and recurrence, including evolving resistance to therapy. Unfortunately, we lack a detailed understanding of the cellular composition and cell-cell interactions within high-risk prostate tumor microenvironments, and in particular, how populations change in response to therapy. In this study we perform single-cell transcriptomic profiling of paired temporal samples from subjects receiving androgen axis inhibition in combination with immune checkpoint inhibition. By leveraging single cell approaches, we show how treatment leads to a significant reduction in malignant cells and results in concurrent reduction in AR activity and upregulation of antigen presentation machinery within the malignant population, even in the absence of IFNγ response. We also highlight how mast cells and other components in the tumor microenvironment contribute to tissue dysregulation through angiogenic and immune-suppressive signaling.

3.1 Introduction

Many prostate cancer patients have lower risk disease that can be managed through active surveillance or local therapies, however patients with more aggressive disease have a higher risk of progression even after standard treatment options. Approaches such as androgen deprivation therapy (ADT) are often met with initial success but may result in eventual hormonal resistance and continued disease progression (239). The treatment-refractory nature of prostate cancer in some cases highlights the need for novel solutions.

Immune checkpoint inhibition (ICI) therapy has been considered as one potential option for patients with aggressive disease, however clinical trials using ICI in prostate cancer have shown minimal success in the metastatic setting (207). It is hypothesized that this may be due to the generally immune “cold” environment of prostatic tissue. Studies have shown that prostate tumors have generally low T-cell infiltration and often harbor pro-inflammatory and pro-tumorigenic immune populations such as myeloid derived suppressor cells and M2-like macrophages, especially after long periods of ADT therapy (240, 241). In addition to a suppressive tumor microenvironment, late-stage prostate cancers are also characterized by high levels of T-cell exhaustion, a mechanism by which cytotoxic cells lose their cytokine expression and upregulate key checkpoint molecules such as PD-1 and CTLA4 (242)[5]. Although ICI therapy is aimed at preventing T-cell exhaustion and reinvigorating partially exhausted cells, the lack of response in many patients who have received ICI suggests that exhaustion may not be the sole barrier to ICI response in prostate cancer patients.

This highlights the fundamental need for a better understanding of the prostate tumor landscape and how its intrinsic properties and cellular interactions may support resistance to current therapy options. Unfortunately, the dynamics of the prostate tumor microenvironment (TME) and its changes in response to treatment remain incompletely characterized, with previous single cell RNA-sequencing studies often limited by a lack of temporal sampling. Understanding how prostate cancer responds, adapts, and develops resistance to therapy remains a critical area of research with implications for therapy design and selection and ultimately patient outcomes.

Here, we analyze both tumor and non-tumor specimens from subjects with localized but aggressive prostate cancer, both prior to and after initial course of treatment. This gives a unique look into the naïve tumor landscape and how prostatic tumors fundamentally change after androgen axis blockade alongside the anti-PD-1 immune checkpoint inhibitor pembrolizumab. Transcriptional analysis, in conjunction with inference of structural variations has allowed us to confidently annotate malignant cells and better understand the direct effects of treatment on the tumor epithelium. Unenriched transcriptional profiling in conjunction with receptor-ligand cross-talk analysis also provides fundamental insight into broader interactions within the TME and their potential implications in therapeutic response or resistance.

3.2 Results

3.2.1 Subject sampling and overview

We recently demonstrated that T cell intrinsic androgen receptor (AR) activity correlates with poor response to PD-1 targeted immunotherapy in metastatic castration resistant prostate cancer patients (88). To gain insight into the effects of AR on the prostate cancer immune landscape, we performed single cell RNA sequencing (scRNA-seq) on cells isolated from both tumor and non-tumor specimens from subjects enrolled in a Phase II single-arm, open label, neoadjuvant hormonal plus immunotherapy clinical trial for high-risk localized prostate cancer (NCT03753243).

Longitudinal specimens were collected prior to the initiation of androgen axis inhibition (GNRH agonist therapy plus AR inhibition) and pembrolizumab, and at the time of prostatectomy after sixteen weeks of treatment (Fig. 3.1A). In total, 47 prostate specimens were collected across 18 individuals (Fig. 3.1B). After scRNA-seq and processing of these specimens, we successfully recovered single cell transcriptomes for 158,838 cells with 108,317 cells (69.5%) passing all filtering criteria.

Integration of subject samples and unsupervised clustering revealed 27 distinct groups of cells. These clusters were merged into 8 super groups shared broadly across samples and annotated using canonical markers and top differentially expressed genes, with resulting cell type identities including: fibroblasts, mast cells, B-cells & plasma cells, endothelial cells, epithelial cells, myeloid cells, and T-cells & NK cells (Fig. 3.1C, 1D). Notably, epithelial cells also sub-clustered distinctly based on prostate specific antigen (PSA) expression status giving distinct PSA-high and PSA-low subsets of epithelial cells (Fig. 3.1C, 1D).

Across samples, epithelial, myeloid, and NK & T cells were consistently the most abundant cell types captured, however we also observed high variability in cell type abundance between subjects, and even for samples within the same subject (Fig. 3.1E).

3.2.2 Neoadjuvant androgen axis inhibition with αPD1 therapy changes both tumor and non-tumor cellular compositions

Previous work analyzing the effects of androgen deprivation therapy has highlighted the immunosuppressive characteristics of androgen and characterized increases in both T-cell abundance and transient proliferative ability under androgen suppression (243). Other reports have also described associations between ADT response and tumor-associated myeloid cells. Tumor-associated macrophages and T-regulatory cells are observed in biopsies from subjects on androgen deprivation therapy (ADT), and lower TAM infiltration is associated with longer overall survival (244). Further, loss androgen and AR signaling in MDSCs promotes tumor progression by enhancing the immunosuppressive capacity of MDSCs (245). Therefore, response to ADT and ICB may be associated with the impacts of androgens on the immune cells within the tumor environment.

To assess the effect of androgen axis inhibition alongside aPD-1 therapy, we assessed relative abundance of each cell type between tumor and non-tumor labeled specimens, and across pre- and post-treatment timepoints. Surprisingly, the baseline proportion of each cell group was largely consistent between tumor and non-tumor tissues, with no significant differences in overall proportions between locations (Supplemental Figure 7). In contrast, the administration of neoadjuvant androgen axis inhibition with aPD-1 was associated with multiple changes in the cellular landscape of the prostate, including a significant drop in PSA-high epithelial cells, consistent with previous reports showing tissue atrophy in androgen sensitive tumor and non-tumor tissues (Fig. 3.1F) (246). Notably, PSA-low epithelial cells did not change significantly with treatment and remained consistent in both tumor and non-tumor locations (Fig. 3.1F). We also observed an increase in myeloid cells across all tissues, consistent with previous findings that also show infiltration of myeloid populations such as tumor associated macrophages (Fig. 3.1F). In addition, we observed a tumor sample specific increase in NK & T-cells following treatment (Fig. 3.1F).

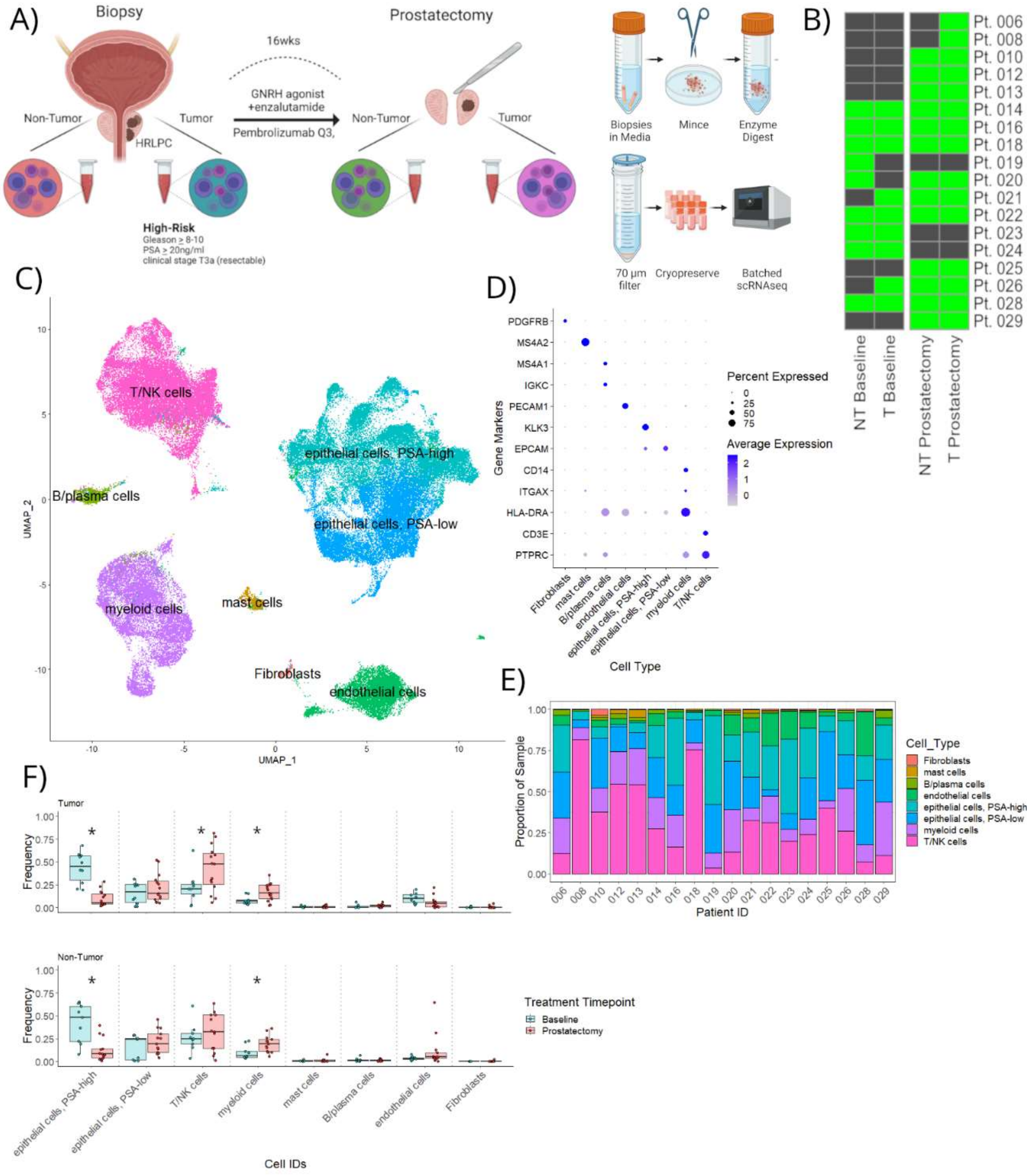

Figure 3.1 Sampling overview and heterogeneity of prostate samples

A) Tumor and non-tumor biopsies were taken from treatment naïve tissues for subjects with stage IIIA high-risk localized prostate cancer (HRLPC), Gleason score ≥ 8 and PSA ≥20 ng/mL. Subjects underwent 16 weeks of androgen axis inhibition (GNRH agonist + enzalutamide) with concurrent aPD-1 therapy (Pembrolizumab). After drug course, subjects underwent radical prostatectomy where both tumor and non-tumor tissues were again sampled. Single cell suspensions were generated from biopsy and radical prostatectomy samples and sc-RNAseq was performed using an Illumna NovaSeq 6000. B) Heatmap representing the presence or absence of a subjects' samples (y-axis) by timepoint and location (x-axis). Green squares represent subject samples that were successfully collected, processed and sequenced. C) UMAP projection of clustered and annotated cell types: B/plasma cells, T/NK cells, myeloid cells, mast cells, fibroblasts, endothelial cells, epithelial cells (PSA-high and PSA-low). D) Expression of 12 canonical markers (y-axis) was used to annotate each of eight cell types (x-axis). PSA-high and PSA-low cells were categorized based on shared expression of EPCAM with differential KLK3 (PSA) expression. E) Relative cellular composition (y-axis) for each subject (x-axis) is shown as a series of stacked bars, with each color representing an annotated cell type according to the key as shown. F) Baseline versus post-treatment proportions of each cell population within tumor (top) and non-tumor (bottom) specimens are shown as a series of boxplots, where each pair of boxplots corresponds to a specific cell type along the x-axis. Proportions are reported as the relative quantity of each cell type across all cells from a given specimen. Asterisks (*) indicate significant difference (Wilcoxon rank-sum test, $p<0.05$) in cell composition between baseline and post-treatment timepoints.

3.2.3 Malignant epithelial cells show responsiveness to androgen deprivation

Given that the goal of androgen deprivation therapy (ADT) is to starve androgen dependent tumor cells of a necessary hormone, we sought to confirm the 'on target' drug effect of androgen blockade. We focused on the epithelial cell population, interrogating nuances among five distinct sub-populations including: two different luminal cell clusters (high *KLK2*, *KLK3*, and *KLK4)*, basal cells (*KRT5*, *KRT14*, and *TP63 positive)*, and two other epithelial cells (OE1 and OE2) with less defined cellular characteristics but clear pan-epithelial marker expression (*EPCAM*, *CDH1*, and *CEACAM1 positive)* (Fig. 3.2A, 3.2B). To clarify the cell identities of both the OE1 and OE2 clusters, all epithelial subsets were scored using gene signatures for club cells; a population previously identified in normal prostatic as well as lung tissues (247, 248). The OE1 subset had a significantly higher club signature score than all other identified subsets, suggesting this cluster may consist of predominantly club-like epithelial cells (Fig. 4.2C). OE2 cells expressed genes associated with neuroendocrine cells but could not be confidently annotated.

To identify a malignant subset within the tumor-specific epithelial cell population, we interrogated expression of a malignancy signature constructed from genes previously defined in literature (see methods) (196). One subset of luminal cells, denoted as luminal (1), expressed a high malignancy signature (Fig. 3.2D) compared to the second subset, subsequently referred to as luminal (2) cells. (Fig. 3.2D). Moreover, the prevalence of luminal (1) cells was heavily enriched in subject tumor samples compared to non-tumor samples and similarly enriched at baseline prior to treatment when compared to samples taken post-treatment at time of prostatectomy (Fig. 3.2E). In contrast, luminal (2) cells did not show significant changes in prevalence across tissues or sampling timepoints, suggesting that changes in luminal cell proportions are specific to cells expressing high malignancy signature. We also observed a significant increase in the proportion of club-like OE1 cells with treatment (Fig. 3.2E). We further confirmed the malignant nature of luminal (1) cells via copy number variation (CNV) analysis using inferCNV. Inferred aberrations for subjects with paired tumor and non-tumor biopsies, demonstrated that luminal (1) populations harbored unique subject-specific aberrations, while other epithelial populations did not.

The specific decrease in the proportion of malignant epithelial cells after treatment suggests on-target therapeutic effects. Indeed, hallmark gene set enrichment analysis revealed a marked decrease in androgen pathway gene expression in post-treatment epithelial cells (Figure 3.2F). We also investigated the effects of androgen axis inhibition directly on epithelial cell androgen pathway signaling. Average androgen response scores for each subject showed a notable reduction in AR signaling with treatment, primarily driven by luminal populations (Supplemental Figure 8) and reflecting on-target androgen axis inhibition (Fig. 3.2G). This result was consistent across tumor and non-tumor tissues with no significant difference in response signatures between sampling locations. Repeating this analysis specifically for malignant epithelial cells confirmed downregulation of androgen response signature (Fig. 3.2G). Taken in conjunction with proportional differences, this suggests that all luminal populations are responding to androgen axis inhibition, however population loss is preferentially occurring in malignant luminal cells.

3.2.4 Antigen presentation machinery is upregulated with treatment and correlated with androgen axis inhibition

Previous literature has also shown that inhibition of AR activity in prostate tumors is associated with increased antigen presentation and may aid with improved immune-driven tumor clearance (249). To investigate whether we see similar responses in our data we scored all epithelial cells using an antigen processing and presentation score using genes defined in the Reactome database (250). Pseudobulk comparisons of antigen presentation scores showed significant increases in antigen processing and presentation across subjects following treatment (Fig. 3.2G). This upregulation of antigen presentation signature with treatment was also seen in malignant cells, suggesting this a common treatment response across both malignant and non-malignant epithelial cells. Additional analysis also demonstrated a significant inverse correlation between androgen pathway score and antigen presentation score across subjects (r=-0.49, p=0.013).

Although AR activity has been shown to directly modulate antigen pathway expression *in vitro,* one alternative explanation for increased antigen presentation *in vivo* is through intrinsic IFNγ response (251). We therefore assessed an IFNγ response score using a signature constructed from epithelial response to exogenous IFNγ application in epithelial cells from previous literature (Calistri et al. in press). Although we see indications of IFNγ response in pseudobulk data, IFNγ response scores in malignant cells alone do not change significantly with treatment (Fig. 3.2G). Notably we also see higher levels of FOXA1 expression in malignant epithelial cells compared to combined non-malignant epithelial sub-populations, a gene associated with inhibition of IFN response in previous literature (log2FC=0.37, $p<1e-16$) (252). This suggests that while IFNγ may play a role in the overall upregulation of antigen presentation in bulk epithelial cells, it may not contribute to the same antigen upregulation in malignant subsets.

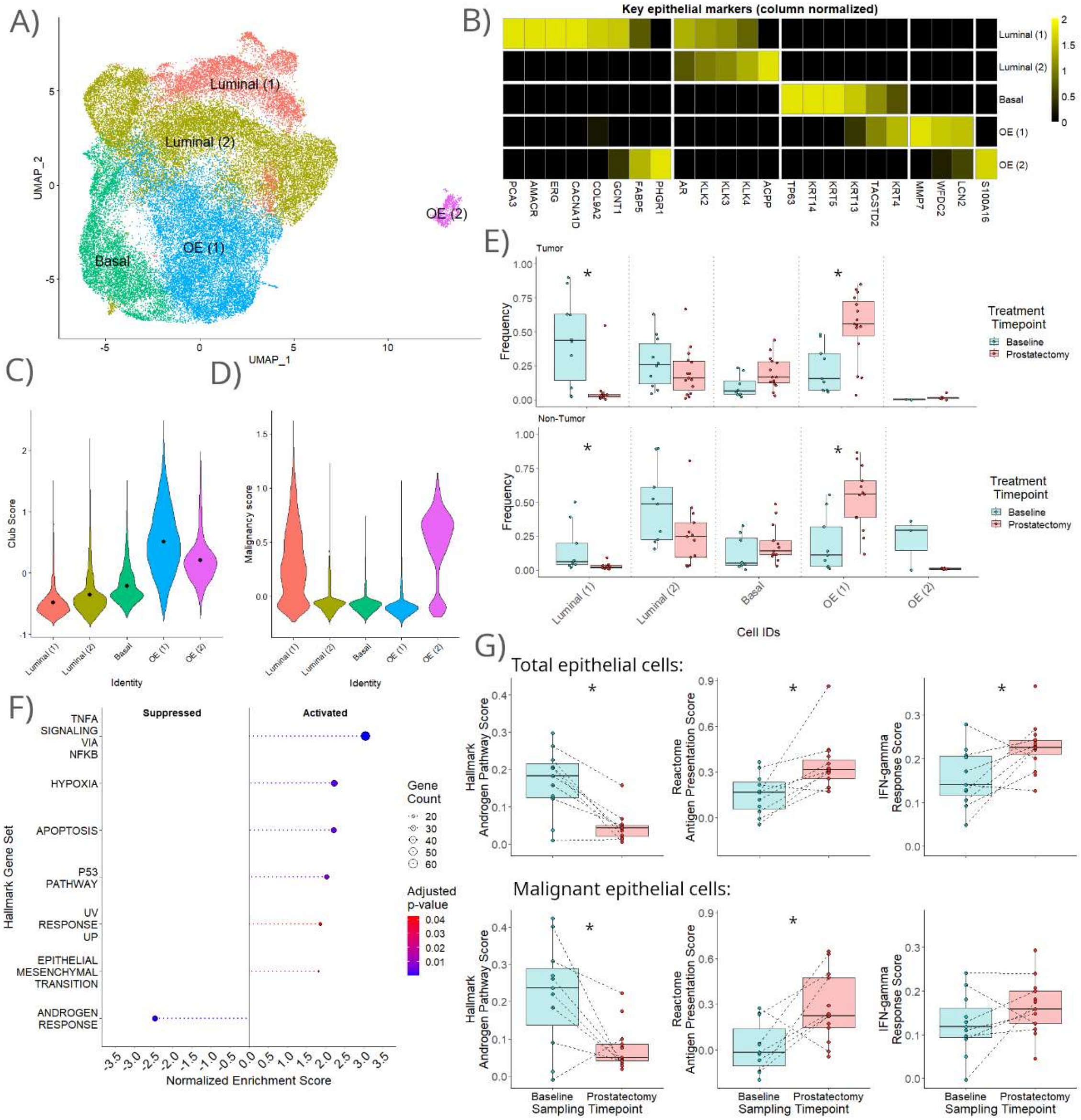

Figure 3.2 Epithelial cell identities and responses to treatment

A) Identified epithelial cells were re-clustered into five subtypes (two luminal, one basal, and two other epithelial cells [OE]) and projected into UMAP space. B) Heatmap demonstrates relative expression of malignancy associated genes (PCA3, AMACR, ERG, CACNA1D, COL9A2, GCNT1, GABP5, PHGR1) and other canonical markers (x-axis) among each of the five epithelial sub-populations (y-axis). C) Violin plot demonstrating the distributions of relative club cell signature expression[12] (y-axis) among epithelial subpopulations as labeled (x-axis). D) Violin plot demonstrating the distributions of relative malignancy signature expression (y-axis; see methods) among epithelial subpopulations as labeled (x-axis). E) Baseline versus post-treatment (prostatectomy) proportions of each epithelial cell subpopulation within tumor (top) and non-tumor (bottom) specimens are shown as a series of boxplots, where each pair of boxplots corresponds to a specific cell type along the x-axis. Proportions are reported as the relative quantity of each cell type across all epithelial cells from a given specimen. Asterisks (*) indicate significant difference (Wilcoxon rank-sum test, $p<0.05$) in cell composition between baseline and post-treatment timepoints. F) Hallmark gene set enrichment analysis (GSEA), with normalized GSEA enrichment score (x-axis) depicted for each of seven hallmark gene sets (y-axis). Size of points represents the number of genes differentially expressed within an altered gene set. All presented gene sets are significantly altered (Wilcoxon rank-sum test, adj. $p < 0.05$). G) Androgen pathway, antigen presentation, and IFNγ response scores (see methods) are plotted as aggregate values, either across total epithelial cells or identified malignant cells per subject sample. Dotted lines connect subjects with paired baseline and prostatectomy samples. Asterisks (*) indicate significant changes in the proportion of a given cellular population between baseline and prostatectomy (Wilcoxon rank-sum test, $p < 0.05$).

3.2.5 Evidence of activated CD8 T cell influx after neoadjuvant androgen axis inhibition with αPD1 therapy

In previous studies investigating T-cell exhaustion, ICI therapy has been shown to increase the expression of proliferative markers such as Ki67 and is matched with restoration of cytotoxic signaling through re-invigoration of T-cells (66). Since subjects received treatment that also includes aPD-1 therapy, we sought to investigate exhaustion and potential aPD-1 response among the T-cell populations present in tumor samples.

Upon re-clustering CD3+ NK and T cells into distinct subtypes (Fig. 3.3A, 3.3B), we identified multiple CD8 T-cell populations at varying stages in the activation spectrum according to relative expression of early effector genes (*IFNG, IL2, TNF*) compared to activated cytokine expression (*GZM* family genes); these cell types included: naïve CD8 T-cells, recently activated CD8 effector cells, cytotoxic T-cells, and terminally differentiated T-cells (Fig. 3.3D). Other populations were also characterized and annotated in detail (see methods).

Interestingly, we saw a significant increase in what we defined as recently activated CD8-effector cell populations across both tumor and non-tumor tissues with response to treatment (Fig. 3.3C). In tumor, CD8-effector changes were in conjunction with a proportional decrease in CD4-naïve and γδ T-cell populations. In non-tumor tissues, we saw a similar loss of naïve and γδ populations, as well as an increase in terminally differentiated CD8 T-cells and Tregs (Fig. 3.3C).

With the abundance of literature highlighting the relevance of T-cell exhaustion in the context of aPD-1 treatment, we also wanted to assess any signs of functional exhaustion in our data. Interestingly, we found negligible expression of PD-1, LAG3, and TIGIT (Supplemental Figure 9), all markers generally associated T-cell exhaustion (81). Only one cluster, annotated as CD8-cytotoxic-2, expressed high levels of exhaustion associated markers, however these cells retained expression of *IFNG, FASLG*, and multiple *GZM* family genes normally lost in functional exhaustion phenotypes (Fig 3.3D). While PD-1, LAG3, and TIGIT are associated with exhaustion in T-cells, they are also important markers of cognate antigen encounter. Unfortunately, we are unable to differentiate early exhaustion from antigen encounter in CD8-cytotoxic-2 cells given the available data.

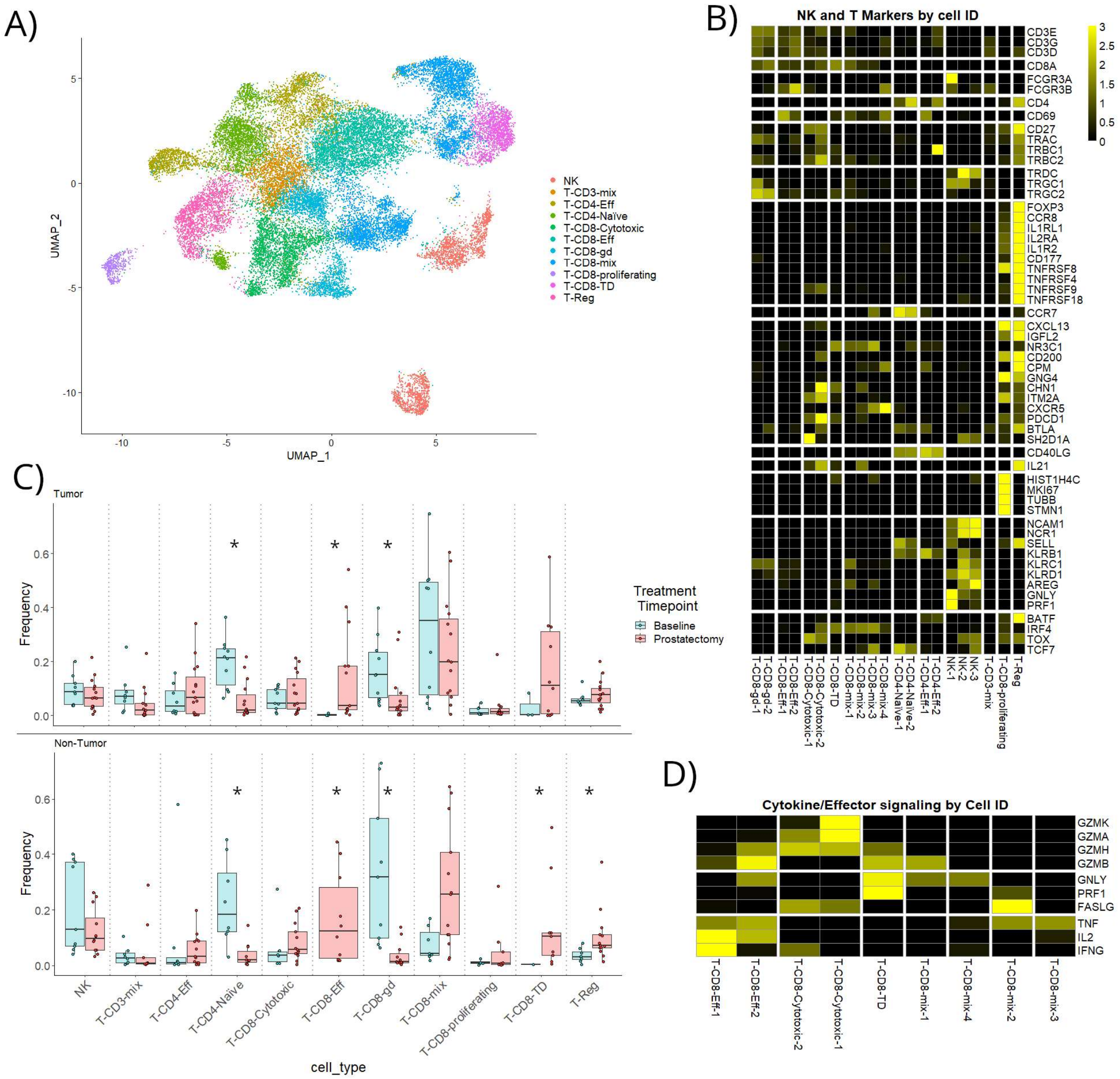

Figure 3.3 Neoadjuvant androgen axis inhibition with aPD1 therapy results in an influx of recently activated T cells

A) UMAP projection of 11 broadly annotated NK and T-cell clusters as labeled. B) Row-normalized heatmap showing expression of canonical and functional T-cell markers (y-axis) by annotated high-resolution cluster identities merged for broad cell annotations (x-axis). C) Boxplot of proportional changes in annotated NK & T cell sub-types across tumor (top) and non-tumor (bottom) with treatment. Baseline versus post-treatment (prostatectomy) proportions of NK&T cell subpopulations, grouped by broader cell type, within tumor (top) and non-tumor (bottom) specimens are shown as a series of boxplots, where each pair of boxplots corresponds to a specific cell type along the x-axis. Proportions are reported as the relative quantity of each cell type across all NK&T cells from a given specimen. Asterisks (*)

indicate significant difference (Wilcoxon rank-sum test, $p<0.05$) in cell composition between baseline and post-treatment timepoints. D) Row-normalized heatmap showing expression of cytokine and effector genes (y-axis) in identified CD8 T-cell populations (x-axis).

3.2.6 Myeloid sub-population proportions remain constant across treatment

Not considered canonical aPD1 targets, myeloid cells nonetheless have a complex and important role in both suppressing and assisting with tumor growth and metastasis. Previous studies have shown that M2-like macrophages and MDSC's can alter the balance of pro- vs. anti- tumorigenic signaling and assist in tumor resistance to therapy (244, 245). We therefore investigated the distribution of distinct myeloid subpopulations across our samples, including immature myeloid suppressor-like cells (iMSCs), dendritic cells, innate lymphocytic cells (ILC's), patrolling monocytes, resident macrophages, and tumor associated macrophage (TAM)-like cells with high expression of APOE (*APOC1, APOE high*) and alternately with low expression of APOE (Fig. 3.4A, Fig. 3.4B).

While the global proportion of myeloid cells across subject samples increases with treatment, we do not observe significant proportional changes in the vast majority of myeloid subsets, with the exception of non-tumor APOE-high TAM-like cells (Fig. 3.4C). This suggests that treatment stimulated influx of myeloid populations occurs in a non-specific manner and not through recruitment of specific sub-populations. Notably, we see relatively stable proportions of iMSCs across treatment in both tumor and non-tumor tissues, a population characterized by high their expression of genes associated with MDSC's (Fig. 3.4D). These cells are often associated with resistance to therapy and tumor metastasis in late-stage disease, however we observe their presence even in treatment naïve biopsy samples, consistent with previous treatment naïve observations from single cell prostate cancer biopsies (196).

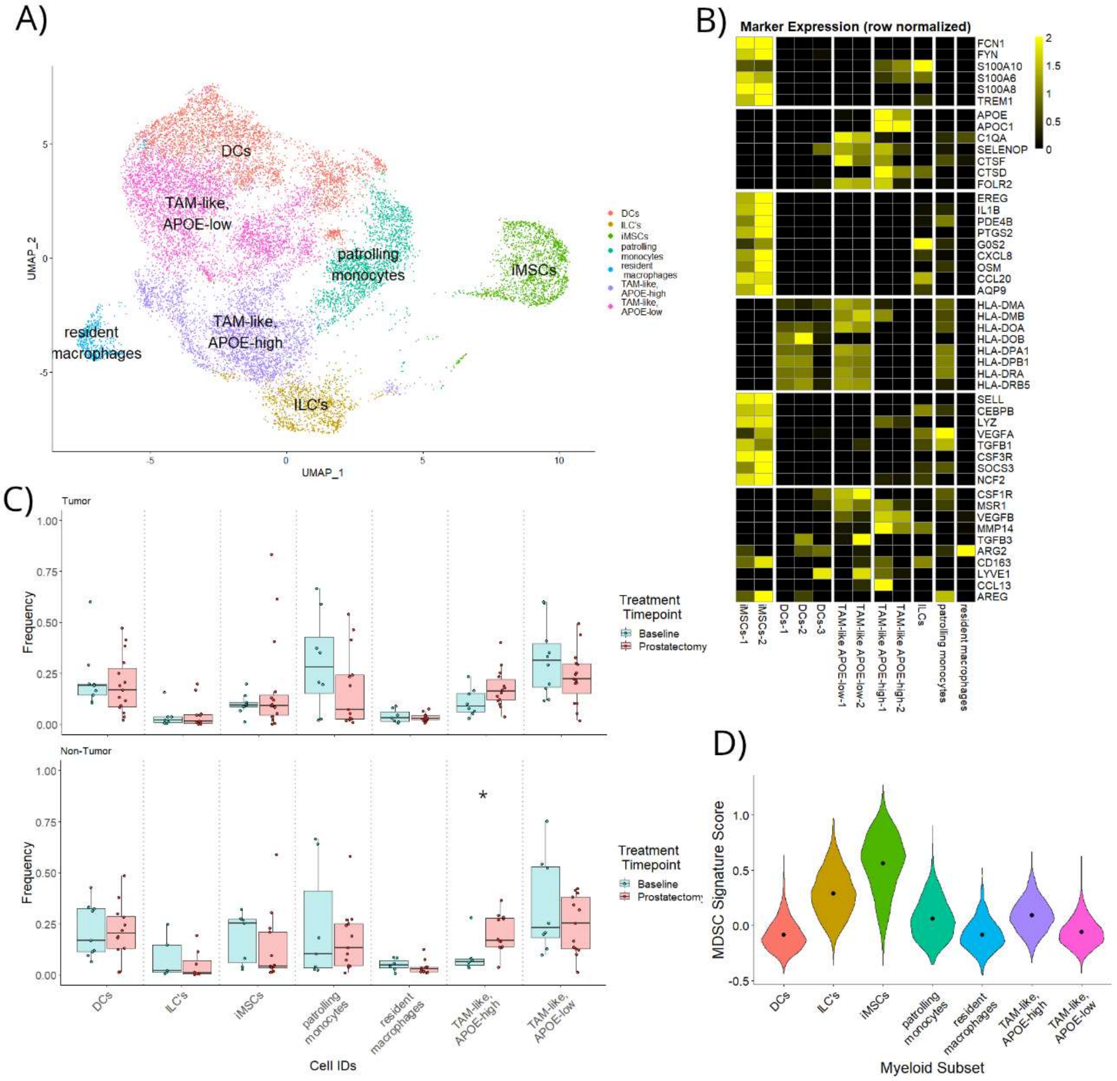

Figure 3.4 Inflammatory myeloid subsets are present in treatment naïve tissues and remain constant with treatment

A) UMAP projection of re-clustered myeloid populations with broad annotations. B) Heatmap represents expression of common myeloid markers (y-axis) across 12 high-resolution myeloid cell clusters ultimately merged for broad annotations (x-axis). C) Baseline versus post-treatment (prostatectomy) proportions, after grouping by broader myeloid cell type, of 7 myeloid subpopulations within tumor (top) and non-tumor (bottom) specimens are shown as a series of boxplots, where each pair of boxplots corresponds to a specific cell type along the x-axis. Proportions are reported as the relative quantity of each cell type across all myeloid cells from a given specimen. D) Gene signature score for MDSC-like phenotype was constructed and applied to cells aggregated by sub-population annotation (see methods). iMSCs had significantly higher levels of MDSC-score than other myeloid populations (Wilcoxon rank-sum test, adj. $p < 0.05$).

3.2.7 Angiogenesis, inflammation and wound healing are upregulated with treatment

Cellular processes such as angiogenesis and inflammation have been well described in the context of various cancers, including prostate cancer (253-256). In particular, inflammatory signaling has been emphasized as a key driver of immunosuppression and dysregulated angiogenesis has been linked with tumor growth and metastasis (257). In prostate cancer specifically, androgen deprivation therapy has been associated with increased angiogenesis and studies have suggested a role for anti-angiogenic targeting in conjunction with aPD1 therapy as a potential treatment for further investigation (258, 259).

Leveraging gene set enrichment analysis (GSEA) of pre- versus post-treatment pseudobulk samples, we identified suppression of androgen response and activation of apoptotic signaling, in keeping with our prior observations among isolated epithelial cells. Additionally, we saw activation of signals associated with inflammation and tissue dysregulation (i.e., TNFα signaling, hypoxia, and IFNγ response), all consistent with previous reports (Supplemental Figure 10) (260, 261).

To further investigate how specific cell types might be driving tissue dysregulation in the tumor microenvironment we scored each using an inflammatory signaling score, as well as an angiogenic signaling score through the application of gene sets previously defined in

Hirz et al. (196). Although myeloid cells contributed the most to overall inflammatory signaling, consistent with our identification of pro-inflammatory myeloid populations, we did not observe an increase in myeloid inflammatory signature after treatment. In contrast, PSA-high epithelial cells, endothelial cells, B/plasma cells, mast cells, and T&NK cells all showed relatively low levels of baseline inflammation but signs of increased inflammatory signaling at time of prostatectomy, indicating broad upregulation of inflammatory signaling across the majority of cell types with treatment (Fig. 3.5A). Similarly, we observed broad upregulation of angiogenic signaling with treatment across a variety of cell types including both PSA-high and PSA-low epithelial cells, myeloid cells, T&NK cells, and mast cells (Fig. 3.5B). Importantly, these phenomena were highly consistent across all subjects (Fig. 3.5A-B).

Alongside upregulation of angiogenic and inflammatory signaling pathways, we also saw upregulation of multiple genes associated with growth factor signaling and wound healing responses (*VEGF, EGF, S100 family genes, MMP family genes*) (262). To investigate the contributions among different cell populations, we next analyzed inferred receptor-ligand interactions via CellChat (263). Most notably, cross-talk inference highlighted mast cells as a key contributor of VEGF signaling to endothelial cells and EGF signaling to epithelial cells at time of prostatectomy (Fig. 3.5E, 3.5F). In particular, EGF signaling was primarily driven by interactions between EGFR and AREG (Supplemental Figure 11). Notably, AREG expression has been previously associated with cancer migration and metastasis and is also upregulated in other cell populations including myeloid cells and B/plasma cells at time of prostatectomy (264). Although we do not see signs of strong cross-talk between AREG expressing cells and T-cells, expression of AREG in literature has also been shown to upregulate Treg activity and further facilitates their suppressive function

(265). For mast cells specifically, their presence and expression of VEGF has also been associated with increased micro vessel density and resistance to anti-angiogenic therapies, as well as resistance to aPD-1 therapies (266, 267).

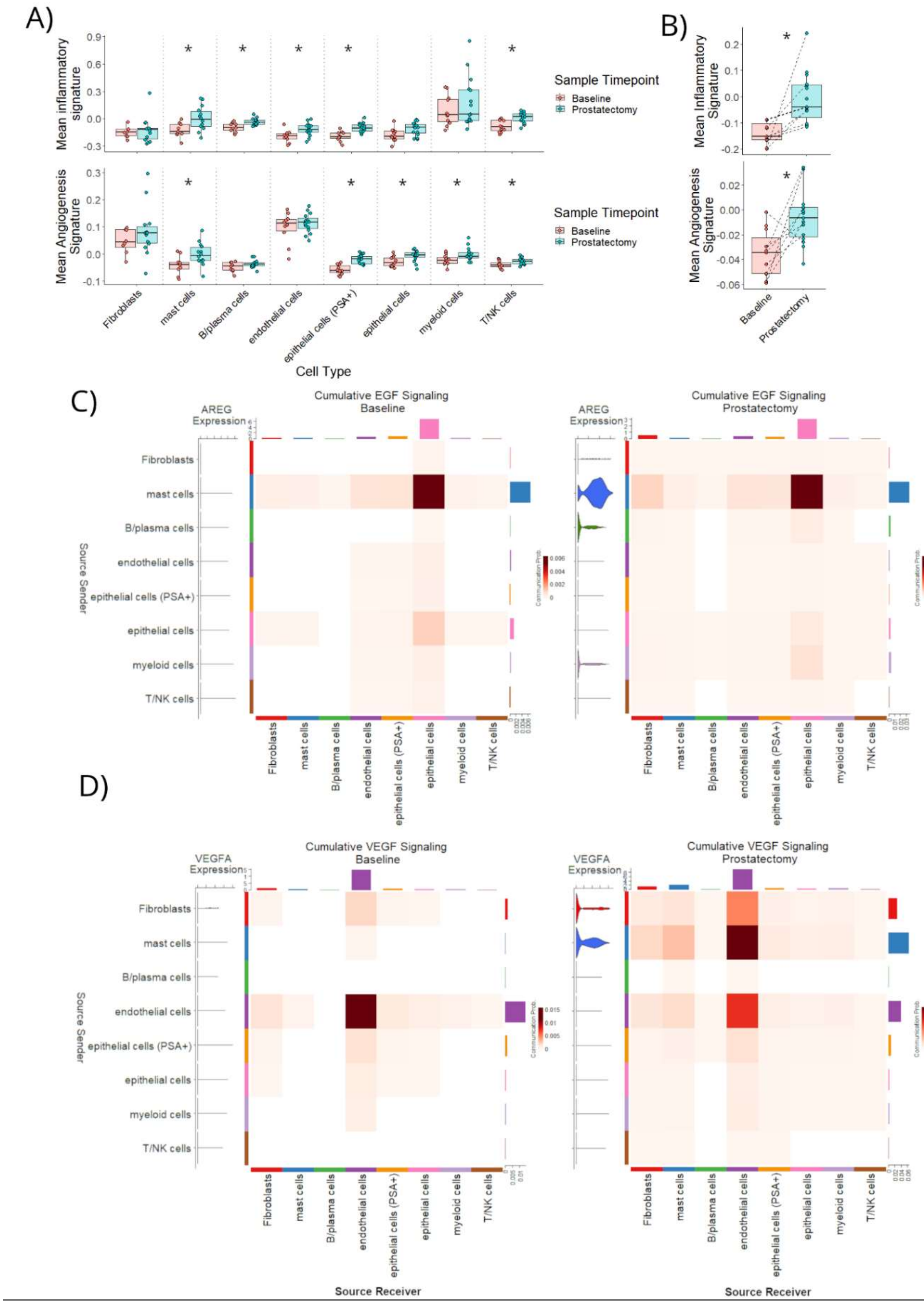
A)
Mean inflammatory signature
Mean Angiogenesis Signature
Sample Timepoint
Baseline
Prostatectomy
Fibroblasts
mast cells
B/plasma cells
endothelial cells
epithelial cells (PSA+)
epithelial cells
myeloid cells
T/NK cells
Cell Type
B)
Mean Inflammatory Signature
Mean Angiogenesis Signature
Baseline
Prostatectomy
C)
AREG Expression
Cumulative EGF Signaling Baseline
Cumulative EGF Signaling Prostatectomy
Source Sender
Communication Prob.
D)
VEGFA Expression
Cumulative VEGF Signaling Baseline
Cumulative VEGF Signaling Prostatectomy
Source Receiver

Figure 3.5 Receptor-ligand interaction inference highlights mast cells as key drivers of growth factor signaling

A) Baseline versus prostatectomy inflammatory (top) and angiogenesis (bottom) signatures adapted from Hirz et al.[12] are shown as a series of boxplots, where each pair of boxplots corresponds to a specific cell type along the x-axis. B) Inflammatory (top) and angiogenesis (bottom) signatures (see methods) are plotted as aggregate values across all cells per subject sample. Dotted lines connect subjects with paired baseline and prostatectomy samples. Epidermal growth factor (EGF) signaling (C) and vascular endothelial growth factor (VEGF) signaling (D) were assessed through receptor-ligand interactions using CellChat[31]. Cell types initiating pathway signaling are represented on the left-hand side of each plot (y-axis), while cell types receiving pathway signal are represented on the bottom of each plot (x-axis). Within the heatmap, each value represents the relative pathway signaling strength of each sender-receiver pairing. Bars on the right and top of each plot represent the cumulative signal sent and cumulative signal received for each cell type, respectively. For both EGF and VEGF, plots on the left side represent baseline receptor-ligand interactions while the right hand represents receptor-ligand interactions at prostatectomy.

3.3 Discussion

To the best of our knowledge, this represents the first single-cell transcriptomic study to report on temporal sampling of paired naïve and post-treatment samples in prostate cancer. We characterize compositional and transcriptional changes throughout the prostate cancer cellular landscape, including malignant epithelial cells and key immune cell populations.

Across subjects, we were able to identify a sharp and consistent decrease in PSA-high epithelial cells consistent with on-target treatment response. While proportional changes suggest a response to therapy, re-clustering of epithelial cells allowed for the identification of malignant cells and direct analysis of treatment response in both malignant cells and psuedobulk epithelial cells. Using this approach, we were able to identify a significant drop in androgen pathway activity indicative of androgen axis inhibition and a correlated increase in expression of antigen presentation machinery. The observed correlation between low AR activity and increased antigen presentation is consistent with previous *in vitro* findings that show androgen receptor activity can directly modulate the expression of genes related to antigen processing and presentation through upstream androgen response elements (200) . While there are other known mechanisms that upregulate antigen presentation, such as response to IFNγ, malignant epithelial cells in our dataset do not show signs of increased IFNγ response with treatment and subsequently show increased expression of FOXA1, a gene linked with IFNγ resistance in previous literature (252). Thus, the mechanism(s) AR-associated repression of antigen presentation machinery expression in epithelial cells may be independent of the impact of AR on IFNγ in the tumor environment.

Within the tumor, we also see an increase in NK & T-cells with treatment, primarily driven by CD8 T-cells with an effector like phenotype. While NK & T cell proportions increased in tumor tissue specifically, we saw a much broader influx of myeloid cells across both tumor and non-tumor tissues. Unlike with NK & T-cell populations this shift appeared to be driven by a broad influx across a variety of cell types already present in baseline samples. While myeloid populations remained proportionally stable with treatment, we observed the presence of both iMSC's and TAM-like populations, both of which have also been identified in previous single-cell prostate cancer analyses and associated with poor prognosis in bulk tumor analyses (244, 245).

Although our analysis of T-cell populations indicates signs of activation, the presence of multiple immune-suppressive myeloid populations highlights the importance of the tumor microenvironment and complex interplay between immune populations therein. This is further emphasized by post-treatment upregulation of both inflammatory and angiogenic signaling across a variety of different cell types. In particular, mast cell expression of both VEGF and AREG highlights the broad ability for immune cells in the TME to influence other cell populations. VEGF is perhaps the best known regulator of endothelial growth and associated with both normal and tumor-associated angiogenesis (268). Similarly, under normal conditions AREG is associated with wound healing and tissue normalization, however in tumor contexts increased AREG expression has also been associated with tumor migration and resistance to therapy (264, 269). The association of AREG and VEGF expression with poor disease prognosis in other studies, and the treatment-related upregulation of cross-talk related to both receptor-ligand pathways in our data warrants further investigation.

Our study has several limitations. Given additional time is needed to reach study endpoints, we are unable at this time to report on clinical outcomes or other subject-level clinical details. This unfortunately limits our ability to link observed proportional and transcriptional changes with clinical response. In addition, we are blinded to measurable tumor burden, potentially reducing our power to detect differences between tumor and non-tumor specimens, as some subjects were reported to have diffuse prostatic disease which may have impacted the ability to take purely non-tumor biopsies. In addition, while we attempted to use objective clustering approaches with minimal bias, single cell annotations are inherently subjective and clustering itself may misattribute cell identities for intermediate or outlier cell states. Our interpretations of results are based on a mix of both canonical and differential genes, but ultimately constrained by gaps in current biological knowledge. Our results are further constrained by the current limits of scRNA-seq, including limited per-cell sampling depth, transcriptional dropout, and variance in read quality, among other phenomena. In future studies we plan to link clinical outcomes with transcriptional biomarkers to identify potential prognostic markers of response or early indicators of resistance.

3.4 Methods

3.4.1 Subject samples

Treatment-naïve, high-risk prostate cancer subjects with Gleason grade > 8-10 enrolled on clinical trial NCT03753243 underwent biopsy of a primary tumor lesion and non-tumor tissue prior to treatment. Following 14 to 16 weeks of treatment with neoadjuvant pembrolizumab (QW3) with anti-androgen therapy (enzalutamide plus GNRH inhibitor), subjects received a radical prostatectomy procedure. At the time of prostatectomy, biopsies from tumor lesions and paired non-tumor tissue were obtained.

3.4.2 Biopsy processing

Fresh biopsy specimens were collected immediately following the biopsy or prostatectomy procedure and processed same-day. Biopsies were mechanically dissociated using forceps and scissors into pieces that could be pipetted in phosphate buffered saline (PBS, Hyclone #SH30028FS) using a serological pipette. Biopsies were further dissociated by shaking at 300 rpm for 30 minutes at 37 °C in PBS containing 30 U/mL DNAase I (Roche #04536282001), hyaluronidase (Sigma # H6254-500MG), and 1 mg/mL collagenase IV (Sigma #C5138-1G). Tissue digests were then filtered through 70 μm mesh filters (BD

Biosciences ##352350) to obtain single cell suspensions. Samples were then cryopreserved in 90% FBS + 10% DMSO for later batch processing.

3.4.3 Single cell RNA library preparation and sequencing

Single cell capturing and library preparation were performed using the Chromium Next GEM Single Cell 3' v3.1 kit (10X Genomics, PN-1000128) according to the manufacturer's instructions. Cryopreserved single cell suspensions of biopsies were thawed and filtered through a 30 μm filter prior to loading up to 30,000 cells per sample onto the Next GEM chip. Libraries were pooled and sequenced using an Illumina NovaSeq 6000 with 2 x 100 bp paired-end sequencing. Raw sequencing reads were aligned to the human reference genome GRCh38 and quantified using CellRanger (10x Genomics, v6.2.1).

3.4.4 Sample pre-processing and integration

Unless otherwise specified, all single cell analysis was performed using R v.4.2.2 and Seurat v.4.3.0 (270). Initial samples were filtered to remove ambient RNA contamination using SoupX (271) (https://github.com/constantAmateur/SoupX) with default recommended settings. After ambient de-contamination, individual samples were filtered to keep only cells with greater than 500 features and less than 25% of reads aligning to mitochondrial genes. Filtered samples next underwent doublet identification and prediction using DoubletFinder (272) (https://github.com/chris-mcginnis-ucsf/DoubletFinder) with default settings and an expected doublet formation rate of 7.5%, filtering out all droplets with a high doublet likelihood. Samples were then merged and normalized by batch based on the 2000 most variable genes using the Seurat ScaleData() function. Merged data was then integrated across batches by performing principal component analysis and using Harmony (273) v0.1 on the first 30 principal components (PC's).

3.4.5 Initial clustering and cell identification

Clustering was performed using the Louvain algorithm after calculating nearest neighbors using the first 10 Harmony components as input to the FindNeighbors function. A clustering resolution of 0.68 was selected after optimizing to reduce the average root mean square deviation (RMSD) of clusters, then fine tuning resolution for cluster stability using the Clustree package v0.5.0, ultimately identifying 27 clusters. Positive differentially expressed markers for each of the identified clusters were determined using Seurat's FindAllMarkers function and manual cell type annotation was performed based on the top markers for each cluster as well as canonical markers. Ultimately, clusters with shared canonical markers were merged to into 8 broad supergroups. Gene set enrichment analysis (GSEA) was performed using the GSEA() function from cluster profiler to compare psuedobulk baseline to prostatectomy samples. Only genes with a log2FC threshold of at least +/- 0.5 between baseline and prostatectomy were used and all hallmark gene sets were queried for enrichment.

3.4.6 Epithelial re-clustering and identification

Identified epithelial cells from the initial clustering step were re-normalized and re-clustered using the same approach as above, but instead using the 5000 most variable features during normalization and re-integration. A clustering resolution of 0.35 was ultimately selected, again based on RMSD minimization and clustering stability. Positive differentially expressed markers for each of the identified clusters were determined using

Seurat’s FindAllMarkers function and manual cell type annotation was performed based on the top markers for each of 15 graph based clusters, as well as using key genes from previous literature (196, 274). Grouping based on shared gene signatures resulted in 5 broader epithelial groups including two subsets of luminal cells, one subset of basal cells, and two subsets of other epithelial cells that did not directly fit pre-defined cell identities. Luminal subsets were differentiated based on a shared luminal gene signature including (*KLK2*, *KLK3*, and *KLK4, AR)*, in conjunction with expression of defined malignancy genes including (*PCA3, AMACR, ERG, CACNA1D, COL9A2, GCNT1, FABP5, and PHGR1)* that were consistently expressed in the luminal (1) subset but not luminal (2) cells. Scores used to assess club and malignancy phenotype in epithelial cells were defined using the genes defined in Hirz et al. (196) and scoring cells using the AddModuleScore function in seurat. Gene set enrichment analysis (GSEA) was performed using the GSEA() function from clusterProfiler to compare psuedobulk baseline to prostatectomy samples. Only genes with a logFC threshold of at least +/- 0.5 between baseline and prostatectomy were used and all hallmark gene sets were queried for enrichment.

3.4.7 Inference of chromosomal aberrations in epithelial subsets

For subjects with paired tumor and non-tumor samples, chromosomal aberrations were inferred using inferCNV v1.3.3 (Trinity CTAT Project, https://github.com/broadinstitute/inferCNV). For each subject, non-tumor epithelial cells, excluding luminal (1) cells, were used as background reference while all tumor epithelial cells were assessed for chromosomal aberrations. Copy number variants were inferred using the inferCNV “subcluster” mode with a cutoff of 0.1 as recommended for 10X derived data and use of HMM for inference smoothing. After inference and smoothing, CNV's were compared visually for regional amplifications/deletions.

3.4.8 Quantification of androgen response, antigen presentation, and IFNγ response in epithelial subsets

Epithelial cells were scored for antigen presentation and androgen pathway expression using the AddModuleScore function in Seurat, and the "REACTOME_ANTIGEN_PRESENTATION_FOLDING_ASSEMBLY_AND_PEPTIDE_LOADING_OF_CLASS_I_MHC " and "HALLMARK_ANDROGEN_RESPONSE " gene sets from the Molecular Signatures Database (MSigDB) respectively. To aggregate scores on a per sample basis, mean expression was calculated across all scored cells, sub-setting by cell type and time point where relevant. Wilcoxon ranked sum tests were used to compare mean scores at baseline and prostatectomy in order to incorporate both paired and unpaired samples. IFNγ response signature in epithelial cells was again calculated using Seurat's AddModuleScore(), using a list of 453 genes differentially upregulated (Log2FC > 0.5, FDR < 0.01) in HCC1143 cells treated with 10ng/mL of IFNγ for 72 hours compared to PBS vehicle control (Calistri, in press).

3.4.9 NK and T cell re-clustering and identification

Identified NK and T cells were further analyzed through re-normalization and re-clustering using the approach previously described for epithelial re-clustering with the 5000 most variable features and a cluster resolution of 0.99. Using the same graph-based clustering approach and RMSD minimization, we identified 3 NK and 18 T-cell clusters. Each cluster was identified using a mix of top differentially expressed genes and relative expression of canonical markers. Cells annotated based on activation spectrum including naïve, early/recently activated effector, cytotoxic, and terminally differentiated T-cells were all characterized based on their position on a spectrum of early effector signal expression (*IFNG, IL2, and TNF*) compared to cytotoxic gene expression (*GZMA, GZMB, GZMH, and GZMK*).

3.4.10 Myeloid re-clustering and identification

As with epithelial and NK&T cell subsets, myeloid populations were re-normalized and re-clustered using the same approach RMSD based approach and a clustering resolution of 0.56. In total, we identified 14 myeloid clusters. Using canonical marker expression we identified two clusters of immature myeloid suppressor-like cells (iMSC's) (*S100A8, TREM1, CSF3R positive*), three clusters of dendritic cells, two tumor associated macrophage (TAM)-like clusters with high expression of APOE (*MSR1, APOC1, APOE positive*), and two TAM-like clusters characterized by low expression of APOE. In addition, we identified clusters including innate lymphocytic cells (ILC's), patrolling monocytes (high levels of *CXCL* markers), and resident macrophages. MDSC signature was defined using genes previously detailed in Hirz et al.[12] and applied using the AddModuleScore() function.

3.4.11 Cell-cell communication inference

Cell to Cell communication analysis between initially identified cell types was performed using CellChat with the default receptor-ligand database. The integrated single-cell dataset was split into baseline and prostatectomy subsets and receptor-ligand interactions were estimated using the identifyOverExpressedInteractions() function on each respectively. Cell to cell communication probabilities were assessed using the computeCommunProb()

function. Baseline and prostatectomy communication inference objects were then merged, and interactions upregulated with treatment were identified using the rankNet() function with statistical estimation.

Chapter 4: Conclusions and Future Directions

4.1 Conclusions

Together, the studies described herein demonstrate a role for AR in regulating the response of CD8 T cells to infections and the prostate tumor microenvironment. In both cases, disrupting androgen signaling leads to the increase in markers of CD8 T cell effector function, suggesting that AR activity limits effector differentiation and function in both mice and humans. These findings have major implications for understanding sex differences in immune responses and for improving immunotherapeutic strategies, particularly in male-biased diseases.

In **Chapter 2**, AR is shown to be dynamically regulated upon TCR engagement, with peaks during early activation and directly post-priming. Functionally, AR dampens effector CD8$^+$ T cell expansion and cytokine production (especially IFNγ), while simultaneously skewing the formation of memory phenotypes. Loss of AR leads to heightened effector responses and enhanced acute expansion during infection and results in memory cells that are skewed toward an effector-like, CX3CR1$^+$ phenotype with enhanced recall capacity. These findings suggest that AR tempers initial CD8 T cell activation and is required for memory fitness and long-term protection.

In **Chapter 3**, AR inhibition via ADT and small molecule inhibitors combined with anti-PD-1 therapy reduced tumor AR activity and malignant cell burden while increasing antigen presentation gene expression in epithelial cells. Notably, this occurred in the absence of increased IFNγ signaling in epithelial cells, implicating AR in the repression of antigen presentation pathways independent of IFNγ. Furthermore, treatment facilitated CD8$^+$ T cell infiltration and activation, without overt signs of exhaustion. These data mirror the T cell-intrinsic findings—where AR loss enhances CD8$^+$ effector function—and extend them to a tumor context, showing that AR activity in epithelial cells also regulates immunogenicity.

Both studies converge on the idea that AR is a critical immunoregulatory node, not only within CD8$^+$ T cells but also in tumor epithelial cells. The T cell study shows that AR dampens effector and memory potential, while the human prostate tumor study demonstrates that its inhibition is associated with enhanced antigen presentation, a prerequisite for effective T cell priming. These findings provide mechanistic insight into why men, who have higher androgen levels, may exhibit weaker responses to infection and immunotherapy compared to women—a phenomenon well-documented in clinical epidemiology. The data support a model in which AR enforces immune restraint in both immune and non-immune cells, contributing to male-biased susceptibility to certain infections and reduced efficacy of immune checkpoint inhibitors (ICIs).

These studies also suggest therapeutic opportunities. In prostate cancer, combining AAI with ICIs improved immune infiltration and tumor antigenicity. The CD8$^+$ T cell data indicate that timing AR inhibition to coincide with early activation may optimize T cell expansion and effector function. However, chronic or prolonged AR inhibition may compromise memory formation, potentially limiting long-term immunologic protection—an important consideration for vaccine strategies and adoptive T cell therapies.

The research highlights AR as a molecular mediator of sex differences in immune responses. Men generally exhibit lower CD8$^+$ T cell activation and memory formation, consistent with the suppressive role of AR. In infections like COVID-19 or influenza, males have higher mortality, and sex hormones have been implicated in these disparities. The findings support targeting AR (or downstream effectors) as a strategy to boost immunity in male patients, particularly in settings where robust CD8$^+$ responses are required. Interestingly, the ARKO model recapitulates features of female-like immunity in male mice—enhanced effector function but reduced memory persistence—underscoring the plasticity of sex hormone regulation in immunity. Future studies might explore whether modulating AR during specific stages of infection or therapy (e.g., early effector versus memory maintenance phases) can fine-tune immunity without inducing exhaustion or loss of recall potential.

4.2 Limitations of the applicability of conclusions

The investigations described in **Chapter 2** of this dissertation are primarily concerned with understanding how androgen hormones and AR activity interact with sex as a biological variable to influence immune responses and disease susceptibility, but does so primarily by comparing XY males and XX females with normal sexual development and circulating hormone concentrations. Although this approach does not consider the full diversity of biological sex, nor does it consider the contribution of sex chromosome linked gene expression, the findings herein contain important implications for those that do not fall into the usual XY male and XX female categories, as discussed in **Chapter 1**.

Additionally, **Chapter 3** of this dissertation addresses the impact of systemic androgen hormone ablation and its intersection with ICB in prostate cancer patients. By nature, this study does not address the impact of sex hormones on sex differences in immune cells but rather addresses such mechanisms in only XY individuals. While **Chapter 3** does not directly describe sex differences in immune cells and ICB response, the findings therein may resemble mechanisms that are also involved in driving sex differences in immune cell phenotype, function, and immunotherapy response across cancer and disease types. However, addressing such questions is outside of the scope of this work.

Further, while sex chromosome composition and gender identify are strongly linked, with XX individuals generally self-identifying as women and XY individuals generally as men, the former biologically based classification does not unequivocally divide individuals by gender identity. In fact, just as the biological classification of sex is not binary, nor is the spectrum of gender identity, and each undoubtedly influences immunity and disease susceptibility through independent mechanisms. For example, a person's gender identity may influence their environmental exposures, lived experience in the structure of society, and access to and participation in healthcare systems (275). Nonetheless, sex and gender are strongly correlated and interact to influence disease susceptibility and treatment outcomes. However, the investigations herein do not consider how gender identity interacts with biological sex to influence the mechanisms of sex hormone action, disease susceptibility, and immune responses.

4.3 Future research directions

The findings presented so far lay the ground work for further work elucidating the role of AR in T cells and the mechanisms by which AR influences responses to acute infection and cancer. Several open questions are outlined below, with suggested approaches to address them.

4.3.1 The influence of AR on CD8 T cell homeostatic maintenance

As discussed earlier in **Chapter 2**, AR influences the abundance of memory-like CD8 T cells present at steady state in male mice. However, the mechanism by which AR suppresses differentiation of memory-like CD8 T cells at steady state is still unclear. We reveal that CD127 (IL-7R) and CD5 expression are both mildly reduced on ARKO CD8 T cells compared to WT in male mice. CD5 expression is directly related with the strength of TCR signal a T cell experiences during development or during homeostasis, so the mild reduction in CD5 expression on ARKO CD8 T cells may reflect slightly lower TCR signal strength received by those cells at steady state. Thus, CD5 expression does not support TCR signaling as the mechanism that drives enhanced virtual memory differentiation in ARKO cells. On the other hand, the amount of CD127 expressed on the cell surface controls the sensitivity of CD8 T cells to IL-7 signaling (276). Therefore, the reduced expression of CD127 on the surface of ARKO cells may reflect a reduced sensitivity to IL-7 signaling. However, surface expression of CD127 is controlled by a negative feedback loop downstream of signaling through CD127. Thus, the reduced CD127 on ARKO cells could be a reflection of increased signaling through CD127 experience *in vivo* and may explain the increase in memory-like differentiation. Additionally, signaling through the IL-15R (CD122) is known to reduce the surface expression of CD127, so sensitivity to IL-15 signaling may also be involved. To test whether these mechanisms might be involved in the observed phenotype, further studies should test the sensitivity of WT and ARKO CD8 T cells to IL-7 and IL-15 signaling by treating cells with those cytokines and assessing 1) whether adding exogenous IL-7 and/or IL-15 is able to induce memory-like differentiation of naïve WT and ARKO cells and 2) the relative activation of the phosphorylation cascade downstream of each of the cytokine receptors.

4.3.2 Mechanisms of AR-mediated regulation of thymocyte development

One of the known mechanisms by which AR influences sex differences in T cells is through their development in the thymus. In the thymus, thymic epithelial cells express the transcription factor, autoimmune regulator (AIRE), which controls expression of endogenous genes to be presented to developing T cells to query for TCR reactivity to self-antigens (277). Therefore, AIRE is a critical component of T cell development and influences developing T cell survival or rejection. *Aire* is expressed at higher levels in thymic epithelial cells (TECs) of males compared to females, and is induced by androgen hormones and repressed by estrogens (278, 279). Therefore, male and female TECs may present disparate antigens to query TCR reactivity during development. With heightened AIRE expression, which is critical for negative selection of developing thymocytes, male mice may more efficiently reject self-reactive T cells, which could at least partially explain the female bias in autoimmune diseases. In fact, previous studies demonstrated that *Aire* knockout mice which develop experimental autoimmune encephalopathy are resistant to the protective effects of androgens on EAE severity (278).

Other mechanisms, including costimulatory receptor and cytokine engagement, are also important to properly support thymocyte development and may influence peripheral T cell self-reactivity (280). The work described in this dissertation suggests a role for AR in controlling sensitivity to homeostatic cytokines, including IL-7, by modulating the expression of cytokine receptors. Therefore, future work should seek to determine whether there are AR-influenced mechanisms that skew thymocyte development other than AIRE expression. Comparing the peripheral TCR diversity between males and females may provide a clue as to whether the biological differences in sex influence T cell selection. If that is true, I would expect to observe increased TCR diversity among females, reflecting an increased diversity of TCRs that survive negative selection, potentially due to relatively lower AIRE expression. Indeed, in humans T cells in the gut of female exhibit increased signs of activation, including CD69 and Ki67 (167, 281), suggesting sex differences in the sensitivity to steady state tonic signals received by T cells.

4.3.3 Mechanisms of AR expression in CD8 T cells

In **Chapter 2**, *Ar* mRNA expression is shown to be dynamically changed following TCR and co-stimulatory receptor engagement. This rapid induction and contraction of *Ar* expression in close proximity to TCR stimulation strongly suggests that signals downstream of TCR and co-receptor stimulation induce the expression of *Ar* and that AR may play an important role in the fate decisions made early in CD8 T cell activation. Future studies should attempt to elucidate which factors downstream of TCR and co-receptor signaling may be involved in regulating *Ar* expression, including NFAT, AP1, and NF-κB.

4.3.4 Detecting AR expression in primary T cells

A significant limitation of the study of AR activity in CD8 T cells to date has been the limited evidence of AR protein expression in primary CD8 T cells from mice and humans. In our previous publication, the Moran Lab showed AR protein expression in human lymphocytes in prostate tissue and secondary lymphoid organs using immunohistochemistry (IHC) (88). However, these data were not able to discriminate whether AR-expressing lymphocytes were CD8 T cells or another subset of lymphoid cells. A similar histology approach that includes AR staining along with CD3, CD4, and CD8 counter stains would be able to discriminate between the two major lineages of T cells and determine which subset(s) express high levels of AR in human tissues. Additionally, developing a method to specifically detect AR expression in CD8 T cells may empower other methods to study AR in CD8 T cells in more detail. For example, if AR could be stained for flow cytometry, we could determine whether there is variety in the amount of AR expressed in CD8 T cells and whether varying levels of expression correlate with specific phenotypes, functions, or signals received by CD8 T cells.

4.3.5 Profiling the AR target genes, cistrome, and interactome in primary CD8 T cells

A significant challenge of this project has been attempting to elucidate the target genes of AR in primary CD8 T cells. RNA sequencing of bulk antigen-specific T cells at baseline, 24-hours post-stimulation, at the peak of acute infection, and in memory CD8 T cells revealed few differentially-expressed genes between ARKO and WT cells (**Chapter 2,** some data not shown). It is possible that due to low expression in primary cells, the influence of AR on gene expression is relatively small and to have the power required to detect difference in expression of AR-target genes would require larger sample sizes. Additionally, it is possible that like the expression of *Ar* itself, the influence of AR on the expression of its target genes is dynamic and transient, requiring precise timing to observe the influence of AR.

Another significant challenge has been finding a commercially-available AR antibody that can reliably detect AR in primary CD8 T cells, discussed above. If an AR-reactive antibody that works well on CD8 T cell AR is found or developed, it would be a valuable tool in investigating the mechanisms of AR regulation in CD8 T cells. In **Chapter 2**, we profiled target genes of AR in T cells, but resorted to a model of AR overexpression in an immortalized T cell line, which is relatively decoupled from direct physiological relevance. It will be important to validate our findings through similar approaches in primary CD8 T cells using ATACseq and immunoprecipitation and mass spectrometry to profile the epigenetic changes induced by AR in primary T cells and assocaiate those changes with interactions with chromatin-modifying enzymes. Additionally, targeted sequencing approaches like chromatin immunoprecipitation sequencing (ChIPseq) could more definitively profile the AR cistrome in primary cells.

4.3.6 Elucidating the role of AR in bacterial versus viral infections

One of the most intriguing findings of **Chapter 2** is the finding that AR expression differentially influences the persistence of memory CD8 T cells in bacterial versus viral infections. We find that AR expression limits the persistence of memory CD8 T cells following bacterial infection while it supports the persistence of virus-specific memory cells. This context-dependent role for AR is supported by epidemiological evidence from human disease, which shows that males are generally more susceptible than females to various viruses, but not all viruses. For example, females tend to be more susceptible to HIV and IAV, which is consistent with our findings that female memory CD8 T cells do not persist as well as male cells following LCMV infection. To determine whether the sex difference in disease susceptibility and memory persistence observed in mice is similarly dependent on the type of virus encountered, studies of WT and ARKO CD8 T cell responses to other viral infections, including vaccinia virus (VacV) and IAV, in mice should be performed.

4.3.7 The role of AR in prostate tumor mast cells and endothelial growth factor production

The most striking inferred cell interaction revealed by our analysis of prostate tumor cells post-treatment was the endothelial growth factor production by mast cells. As early as 1891, mast cells were observed in the prostate tumor environment in close proximity to prostate cancer cells (282). High infiltration of mast cells into the prostate tumor environment has been associated with lower Gleason score and positive prognosis (283) Within the tumor environment in multiple cancer types, mast cells are known to influence type 2 immunity, angiogenesis, and wound healing responses (282). Vascular normalization has increasingly been appreciated as a mechanism to mitigate the hypoxic tumor environment and improve circulation in the tumor, thereby alleviating two important barriers to immune responses to cancer (284). Therefore, mast cells may be an important factor that contributes to the enhanced infiltration of T and NK cells into the prostate tumor environment following neoadjuvant ADT + anti-PD1 therapy. This possibility warrants further investigation, which may reveal targetable mechanisms by which mast cells support the immune response and response to immunotherapy in prostate cancer.

4.3.8 Assessment of 5-year survival in prostate cancer patients treated with combination ADT and anti-PD1

So far, we have only been able to describe the cellular landscape of prostate tumors before and after treatment with ADT and anti-PD1 therapy and have not been able to associate changes in the microenvironment composition with patient outcomes. When the clinical trial endpoint of 5-year radiographic progression-free survival is reached, there will be an opportunity to add survival outcomes as a predictor in our models of the tumor environment and associate specific features with response to therapy. The findings of such an analysis could be valuable in determining appropriate parameters for patient stratification into groups more and less likely to respond to treatment. If we can predict with high confidence which patients are more likely to respond to treatment, we can prioritize those patients to receive the combination treatment while allowing likely non-responders to consider other treatment modalities. We will further be able to compare the outcomes of this novel neoadjuvant therapy strategy to current standard-of-care, which could provide rationale to continue to study this combination as a new first-line therapy for high-risk patients.

4.3.9 Determining whether the increased activated CD8 T cells in combination treated prostate cancer patients participate in the anti-tumor reaction

In **Chapter 3**, we demonstrate an increase in the frequency of activated CD8 T cells in the tumor environment following combination treatment as well as an increase in antigen presentation in prostate epithelial cells. These findings together provide evidence that CD8 T cells in the tumor environment may respond to antigens presented by prostate epithelial cells thereby receiving an activating signal allowing them to participate in the anti-tumor response. However, further work is required to determine whether that is the case. An approach that would provide more evidence of activated CD8 T cells responding specifically to prostate epithelial cells would be histological analysis of prostate cancer tissues to spatially profile the landscape of cells of the tumor environment before and after treatment. If CD8 T cells respond directly to antigens presented by prostate cancer cells following treatment, we should expect to observe a significant co-localization of activated ($CD69^+$) CD8 T cells alongside antigen-presenting ($MHCI^{hi}$) prostate cancer cells.

4.3.10 Elucidating the mechanism(s) of the synergy between ADT and anti-PD1 blockade in prostate cancer

In our previous publication, the Moran Lab demonstrated that low AR activity in CD8 T cells prior to anti-PD1 ICB was associated with treatment response in metastatic prostate cancer patients (88). In mouse models of chronic LCMV infection, we demonstrated that knockdown in CD8 T cells alone, rather than systemic ADT, was able to enhance CD8 T cell anti-viral responses and prevent functional exhaustion. Interestingly, in the context of chronic infection as opposed to cancer challenge, anti-PD1 therapy was not necessary to restore CD8 T cell function. This finding reveals the possibility that there are fundamental differences in the functional exhaustion induced by chronic infection as opposed to cancer challenge, such that exhaustion induced during prostate cancer challenge is resistant to anti-PD1 therapy. Previous studies have demonstrated that terminally-exhausted CD8 T cells in the tumor microenvironment exhibit a unique epigenetic state that is not reversed by ICB or clearance of chronic antigen persistence (285). Therefore, I propose that the requirement for both ADT and anti-PD1 blockade to induce an immunotherapy response in prostate cancer patients hinges on the influence of ADT on the epigenetic plasticity of exhausted CD8 T cells. Epigenetic profiling of exhausted CD8 T cells in the context of prostate cancer, with or without ADT and/or anti-PD1 ICB could shed light on the epigenetic changes induced by these two therapies and determine whether the epigenetic state associated with terminal exhaustion is reversed by ADT.

References

1. Klein L, Kyewski B, Allen PM, Hogquist KA. Positive and negative selection of the T cell repertoire: what thymocytes see (and don't see). Nat Rev Immunol. 2014;14(6):377-91. Epub 20140516. doi: 10.1038/nri3667. PubMed PMID: 24830344; PubMed Central PMCID: PMC4757912.
2. Hamilton SE, Jameson SC. CD8 T cell quiescence revisited. Trends Immunol. 2012;33(5):224-30. Epub 20120221. doi: 10.1016/j.it.2012.01.007. PubMed PMID: 22361353; PubMed Central PMCID: PMC3348359.
3. Berard M, Tough DF. Qualitative differences between naïve and memory T cells. Immunology. 2002;106(2):127-38. doi: 10.1046/j.1365-2567.2002.01447.x. PubMed PMID: 12047742; PubMed Central PMCID: PMC1782715.
4. Takeda S, Rodewald HR, Arakawa H, Bluethmann H, Shimizu T. MHC class II molecules are not required for survival of newly generated CD4+ T cells, but affect their long-term life span. Immunity. 1996;5(3):217-28. doi: 10.1016/s1074-7613(00)80317-9. PubMed PMID: 8808677.
5. Tanchot C, Lemonnier FA, Pérarnau B, Freitas AA, Rocha B. Differential requirements for survival and proliferation of CD8 naïve or memory T cells. Science. 1997;276(5321):2057-62. doi: 10.1126/science.276.5321.2057. PubMed PMID: 9197272.
6. Dorfman JR, Stefanová I, Yasutomo K, Germain RN. CD4+ T cell survival is not directly linked to self-MHC-induced TCR signaling. Nat Immunol. 2000;1(4):329-35. doi: 10.1038/79783. PubMed PMID: 11017105.
7. Surh CD, Sprent J. Homeostasis of naive and memory T cells. Immunity. 2008;29(6):848-62. doi: 10.1016/j.immuni.2008.11.002. PubMed PMID: 19100699.
8. Cho JH, Kim HO, Surh CD, Sprent J. T cell receptor-dependent regulation of lipid rafts controls naive CD8+ T cell homeostasis. Immunity. 2010;32(2):214-26. Epub 20100204. doi: 10.1016/j.immuni.2009.11.014. PubMed PMID: 20137986; PubMed Central PMCID: PMC2830358.
9. Simons K, Toomre D. Lipid rafts and signal transduction. Nat Rev Mol Cell Biol. 2000;1(1):31-9. doi: 10.1038/35036052. PubMed PMID: 11413487.
10. Sprent J, Surh CD. Normal T cell homeostasis: the conversion of naive cells into memory-phenotype cells. Nat Immunol. 2011;12(6):478-84. doi: 10.1038/ni.2018. PubMed PMID: 21739670; PubMed Central PMCID: PMC3434123.
11. Haluszczak C, Akue AD, Hamilton SE, Johnson LD, Pujanauski L, Teodorovic L, et al. The antigen-specific CD8+ T cell repertoire in unimmunized mice includes memory phenotype cells bearing markers of homeostatic expansion. J Exp Med. 2009;206(2):435-48. Epub 20090202. doi: 10.1084/jem.20081829. PubMed PMID: 19188498; PubMed Central PMCID: PMC2646575.
12. Akue AD, Lee JY, Jameson SC. Derivation and maintenance of virtual memory CD8 T cells. J Immunol. 2012;188(6):2516-23. Epub 20120203. doi: 10.4049/jimmunol.1102213. PubMed PMID: 22308307; PubMed Central PMCID: PMC3294185.
13. Hamilton SE, Jameson SC. The nature of the lymphopenic environment dictates protective function of homeostatic-memory CD8+ T cells. Proc Natl Acad Sci U S A. 2008;105(47):18484-9. PubMed PMID: 19020089.
14. Hamilton SE, Wolkers MC, Schoenberger SP, Jameson SC. The generation of protective memory-like CD8+ T cells during homeostatic proliferation requires CD4+ T cells. Nat Immunol. 2006;7(5):475-81. doi: 10.1038/ni1326.

15. Berkley AM, Fink PJ. Cutting edge: CD8+ recent thymic emigrants exhibit increased responses to low-affinity ligands and improved access to peripheral sites of inflammation. J Immunol. 2014;193(7):3262-6. Epub 20140829. doi: 10.4049/jimmunol.1401870. PubMed PMID: 25172492; PubMed Central PMCID: PMC4170019.
16. Cunningham CA, Bergsbaken T, Fink PJ. Cutting Edge: Defective Aerobic Glycolysis Defines the Distinct Effector Function in Antigen-Activated CD8(+) Recent Thymic Emigrants. J Immunol. 2017;198(12):4575-80. Epub 20170515. doi: 10.4049/jimmunol.1700465. PubMed PMID: 28507025; PubMed Central PMCID: PMC5499662.
17. Moskowitz DM, Zhang DW, Hu B, Le Saux S, Yanes RE, Ye Z, et al. Epigenomics of human CD8 T cell differentiation and aging. Sci Immunol. 2017;2(8). Epub 20170217. doi: 10.1126/sciimmunol.aag0192. PubMed PMID: 28439570; PubMed Central PMCID: PMC5399889.
18. Croft M. Activation of naive, memory and effector T cells. Curr Opin Immunol. 1994;6(3):431-7. doi: 10.1016/0952-7915(94)90123-6. PubMed PMID: 7917111.
19. Gray SM, Kaech SM, Staron MM. The interface between transcriptional and epigenetic control of effector and memory CD8$^+$ T-cell differentiation. Immunol Rev. 2014;261(1):157-68. doi: 10.1111/imr.12205. PubMed PMID: 25123283; PubMed Central PMCID: PMC4267690.
20. Kaech SM, Cui W. Transcriptional control of effector and memory CD8+ T cell differentiation. Nat Rev Immunol. 2012;12(11):749-61. Epub 20121019. doi: 10.1038/nri3307. PubMed PMID: 23080391; PubMed Central PMCID: PMC4137483.
21. Chang JT, Wherry EJ, Goldrath AW. Molecular regulation of effector and memory T cell differentiation. Nat Immunol. 2014;15(12):1104-15. doi: 10.1038/ni.3031. PubMed PMID: 25396352; PubMed Central PMCID: PMC4386685.
22. Chen Y, Zander R, Khatun A, Schauder DM, Cui W. Transcriptional and Epigenetic Regulation of Effector and Memory CD8 T Cell Differentiation. Front Immunol. 2018;9:2826. Epub 20181207. doi: 10.3389/fimmu.2018.02826. PubMed PMID: 30581433; PubMed Central PMCID: PMC6292868.
23. Prlic M, Williams MA, Bevan MJ. Requirements for CD8 T-cell priming, memory generation and maintenance. Curr Opin Immunol. 2007;19(3):315-9. Epub 20070412. doi: 10.1016/j.coi.2007.04.010. PubMed PMID: 17433873.
24. Bevan MJ. Helping the CD8(+) T-cell response. Nat Rev Immunol. 2004;4(8):595-602. doi: 10.1038/nri1413. PubMed PMID: 15286726.
25. Jiang J, Lau LL, Shen H. Selective depletion of nonspecific T cells during the early stage of immune responses to infection. J Immunol. 2003;171(8):4352-8. doi: 10.4049/jimmunol.171.8.4352. PubMed PMID: 14530360.
26. Chan AC, Desai DM, Weiss A. The role of protein tyrosine kinases and protein tyrosine phosphatases in T cell antigen receptor signal transduction. Annu Rev Immunol. 1994;12:555-92. doi: 10.1146/annurev.iy.12.040194.003011. PubMed PMID: 8011291.
27. Brownlie RJ, Zamoyska R. T cell receptor signalling networks: branched, diversified and bounded. Nat Rev Immunol. 2013;13(4):257-69. doi: 10.1038/nri3403. PubMed PMID: 23524462.
28. Koh CH, Lee S, Kwak M, Kim BS, Chung Y. CD8 T-cell subsets: heterogeneity, functions, and therapeutic potential. Exp Mol Med. 2023;55(11):2287-99. Epub 20231101. doi: 10.1038/s12276-023-01105-x. PubMed PMID: 37907738; PubMed Central PMCID: PMC10689838.

29. St Paul M, Ohashi PS. The Roles of CD8(+) T Cell Subsets in Antitumor Immunity. Trends Cell Biol. 2020;30(9):695-704. Epub 20200702. doi: 10.1016/j.tcb.2020.06.003. PubMed PMID: 32624246.

30. Mittrücker HW, Visekruna A, Huber M. Heterogeneity in the differentiation and function of CD8$^+$ T cells. Arch Immunol Ther Exp (Warsz). 2014;62(6):449-58. Epub 20140531. doi: 10.1007/s00005-014-0293-y. PubMed PMID: 24879097.

31. Newby BN, Brusko TM, Zou B, Atkinson MA, Clare-Salzler M, Mathews CE. Type 1 Interferons Potentiate Human CD8(+) T-Cell Cytotoxicity Through a STAT4- and Granzyme B-Dependent Pathway. Diabetes. 2017;66(12):3061-71. Epub 20170906. doi: 10.2337/db17-0106. PubMed PMID: 28877912; PubMed Central PMCID: PMC5697952.

32. Goriely S, Demonté D, Nizet S, De Wit D, Willems F, Goldman M, et al. Human IL-12(p35) gene activation involves selective remodeling of a single nucleosome within a region of the promoter containing critical Sp1-binding sites. Blood. 2003;101(12):4894-902. Epub 20030206. doi: 10.1182/blood-2002-09-2851. PubMed PMID: 12576336.

33. Goriely S, Molle C, Nguyen M, Albarani V, Haddou NO, Lin R, et al. Interferon regulatory factor 3 is involved in Toll-like receptor 4 (TLR4)- and TLR3-induced IL-12p35 gene activation. Blood. 2006;107(3):1078-84. Epub 20051011. doi: 10.1182/blood-2005-06-2416. PubMed PMID: 16219795.

34. Rauch I, Müller M, Decker T. The regulation of inflammation by interferons and their STATs. Jakstat. 2013;2(1):e23820. doi: 10.4161/jkst.23820. PubMed PMID: 24058799; PubMed Central PMCID: PMC3670275.

35. Joshi NS, Kaech SM. Effector CD8 T cell development: a balancing act between memory cell potential and terminal differentiation. J Immunol. 2008;180(3):1309-15. doi: 10.4049/jimmunol.180.3.1309. PubMed PMID: 18209024.

36. Joshi NS, Cui W, Chandele A, Lee HK, Urso DR, Hagman J, et al. Inflammation directs memory precursor and short-lived effector CD8(+) T cell fates via the graded expression of T-bet transcription factor. Immunity. 2007;27(2):281-95. doi: 10.1016/j.immuni.2007.07.010. PubMed PMID: 17723218; PubMed Central PMCID: PMC2034442.

37. Kaech SM, Tan JT, Wherry EJ, Konieczny BT, Surh CD, Ahmed R. Selective expression of the interleukin 7 receptor identifies effector CD8 T cells that give rise to long-lived memory cells. Nat Immunol. 2003;4(12):1191-8. Epub 20031116. doi: 10.1038/ni1009. PubMed PMID: 14625547.

38. Huster KM, Busch V, Schiemann M, Linkemann K, Kerksiek KM, Wagner H, et al. Selective expression of IL-7 receptor on memory T cells identifies early CD40L-dependent generation of distinct CD8+ memory T cell subsets. Proc Natl Acad Sci U S A. 2004;101(15):5610-5. Epub 20040325. doi: 10.1073/pnas.0308054101. PubMed PMID: 15044705; PubMed Central PMCID: PMC397444.

39. Obar JJ, Jellison ER, Sheridan BS, Blair DA, Pham QM, Zickovich JM, et al. Pathogen-induced inflammatory environment controls effector and memory CD8+ T cell differentiation. J Immunol. 2011;187(10):4967-78. Epub 20111010. doi: 10.4049/jimmunol.1102335. PubMed PMID: 21987662; PubMed Central PMCID: PMC3208080.

40. Rutishauser RL, Martins GA, Kalachikov S, Chandele A, Parish IA, Meffre E, et al. Transcriptional repressor Blimp-1 promotes CD8(+) T cell terminal differentiation and represses the acquisition of central memory T cell properties. Immunity. 2009;31(2):296-308. Epub 20090806. doi: 10.1016/j.immuni.2009.05.014. PubMed PMID: 19664941; PubMed Central PMCID: PMC2783637.

41. Kallies A, Xin A, Belz GT, Nutt SL. Blimp-1 transcription factor is required for the differentiation of effector CD8(+) T cells and memory responses. Immunity. 2009;31(2):283-95. Epub 20090806. doi: 10.1016/j.immuni.2009.06.021. PubMed PMID: 19664942.
42. Intlekofer AM, Takemoto N, Wherry EJ, Longworth SA, Northrup JT, Palanivel VR, et al. Effector and memory CD8+ T cell fate coupled by T-bet and eomesodermin. Nat Immunol. 2005;6(12):1236-44. Epub 20051106. doi: 10.1038/ni1268. PubMed PMID: 16273099.
43. Zhou X, Yu S, Zhao DM, Harty JT, Badovinac VP, Xue HH. Differentiation and persistence of memory CD8(+) T cells depend on T cell factor 1. Immunity. 2010;33(2):229-40. doi: 10.1016/j.immuni.2010.08.002. PubMed PMID: 20727791; PubMed Central PMCID: PMC2928475.
44. Rao RR, Li Q, Gubbels Bupp MR, Shrikant PA. Transcription factor Foxo1 represses T-bet-mediated effector functions and promotes memory CD8(+) T cell differentiation. Immunity. 2012;36(3):374-87. Epub 20120315. doi: 10.1016/j.immuni.2012.01.015. PubMed PMID: 22425248; PubMed Central PMCID: PMC3314246.
45. Gray SM, Amezquita RA, Guan T, Kleinstein SH, Kaech SM. Polycomb Repressive Complex 2-Mediated Chromatin Repression Guides Effector CD8(+) T Cell Terminal Differentiation and Loss of Multipotency. Immunity. 2017;46(4):596-608. Epub 20170411. doi: 10.1016/j.immuni.2017.03.012. PubMed PMID: 28410989; PubMed Central PMCID: PMC5457165.
46. Jameson SC. Maintaining the norm: T-cell homeostasis. Nat Rev Immunol. 2002;2(8):547-56. doi: 10.1038/nri853. PubMed PMID: 12154374.
47. Tough DF, Sun S, Sprent J. T cell stimulation in vivo by lipopolysaccharide (LPS). J Exp Med. 1997;185(12):2089-94. doi: 10.1084/jem.185.12.2089. PubMed PMID: 9182680; PubMed Central PMCID: PMC2196347.
48. Zhang X, Sun S, Hwang I, Tough DF, Sprent J. Potent and selective stimulation of memory-phenotype CD8+ T cells in vivo by IL-15. Immunity. 1998;8(5):591-9. doi: 10.1016/s1074-7613(00)80564-6. PubMed PMID: 9620680.
49. Kennedy MK, Glaccum M, Brown SN, Butz EA, Viney JL, Embers M, et al. Reversible defects in natural killer and memory CD8 T cell lineages in interleukin 15-deficient mice. J Exp Med. 2000;191(5):771-80. doi: 10.1084/jem.191.5.771. PubMed PMID: 10704459; PubMed Central PMCID: PMC2195858.
50. Tan JT, Ernst B, Kieper WC, LeRoy E, Sprent J, Surh CD. Interleukin (IL)-15 and IL-7 jointly regulate homeostatic proliferation of memory phenotype CD8+ cells but are not required for memory phenotype CD4+ cells. J Exp Med. 2002;195(12):1523-32. doi: 10.1084/jem.20020066. PubMed PMID: 12070280; PubMed Central PMCID: PMC2193564.
51. Buentke E, Mathiot A, Tolaini M, Di Santo J, Zamoyska R, Seddon B. Do CD8 effector cells need IL-7R expression to become resting memory cells? Blood. 2006;108(6):1949-56. Epub 20060516. doi: 10.1182/blood-2006-04-016857. PubMed PMID: 16705084.
52. Carrio R, Rolle CE, Malek TR. Non-redundant role for IL-7R signaling for the survival of CD8+ memory T cells. Eur J Immunol. 2007;37(11):3078-88. doi: 10.1002/eji.200737585. PubMed PMID: 17935075.
53. Osborne LC, Dhanji S, Snow JW, Priatel JJ, Ma MC, Miners MJ, et al. Impaired CD8 T cell memory and CD4 T cell primary responses in IL-7R alpha mutant mice. J Exp Med. 2007;204(3):619-31. Epub 20070226. doi: 10.1084/jem.20061871. PubMed PMID: 17325202; PubMed Central PMCID: PMC2137912.

54. Youle RJ, Strasser A. The BCL-2 protein family: opposing activities that mediate cell death. Nat Rev Mol Cell Biol. 2008;9(1):47-59. doi: 10.1038/nrm2308. PubMed PMID: 18097445.
55. Kassiotis G, Garcia S, Simpson E, Stockinger B. Impairment of immunological memory in the absence of MHC despite survival of memory T cells. Nat Immunol. 2002;3(3):244-50. Epub 20020211. doi: 10.1038/ni766. PubMed PMID: 11836529.
56. Williams MA, Holmes BJ, Sun JC, Bevan MJ. Developing and maintaining protective CD8+ memory T cells. Immunol Rev. 2006;211:146-53. doi: 10.1111/j.0105-2896.2006.00389.x. PubMed PMID: 16824124.
57. Sun JC, Bevan MJ. Defective CD8 T cell memory following acute infection without CD4 T cell help. Science. 2003;300(5617):339-42. doi: 10.1126/science.1083317. PubMed PMID: 12690202; PubMed Central PMCID: PMC2778341.
58. Bourgeois C, Rocha B, Tanchot C. A role for CD40 expression on CD8+ T cells in the generation of CD8+ T cell memory. Science. 2002;297(5589):2060-3. doi: 10.1126/science.1072615. PubMed PMID: 12242444.
59. Janssen EM, Lemmens EE, Wolfe T, Christen U, von Herrath MG, Schoenberger SP. CD4+ T cells are required for secondary expansion and memory in CD8+ T lymphocytes. Nature. 2003;421(6925):852-6. Epub 20030209. doi: 10.1038/nature01441. PubMed PMID: 12594515.
60. Shedlock DJ, Shen H. Requirement for CD4 T cell help in generating functional CD8 T cell memory. Science. 2003;300(5617):337-9. doi: 10.1126/science.1082305. PubMed PMID: 12690201.
61. Sun JC, Williams MA, Bevan MJ. CD4+ T cells are required for the maintenance, not programming, of memory CD8+ T cells after acute infection. Nat Immunol. 2004;5(9):927-33. Epub 20040808. doi: 10.1038/ni1105. PubMed PMID: 15300249; PubMed Central PMCID: PMC2776074.
62. Sun JC, Bevan MJ. Cutting edge: long-lived CD8 memory and protective immunity in the absence of CD40 expression on CD8 T cells. J Immunol. 2004;172(6):3385-9. doi: 10.4049/jimmunol.172.6.3385. PubMed PMID: 15004136.
63. Janssen EM, Droin NM, Lemmens EE, Pinkoski MJ, Bensinger SJ, Ehst BD, et al. CD4+ T-cell help controls CD8+ T-cell memory via TRAIL-mediated activation-induced cell death. Nature. 2005;434(7029):88-93. doi: 10.1038/nature03337. PubMed PMID: 15744305.
64. Sacks JA, Bevan MJ. TRAIL deficiency does not rescue impaired CD8+ T cell memory generated in the absence of CD4+ T cell help. J Immunol. 2008;180(7):4570-6. doi: 10.4049/jimmunol.180.7.4570. PubMed PMID: 18354179; PubMed Central PMCID: PMC2776088.
65. Virgin HW, Wherry EJ, Ahmed R. Redefining chronic viral infection. Cell. 2009;138(1):30-50. doi: 10.1016/j.cell.2009.06.036. PubMed PMID: 19596234.
66. Barber DL, Wherry EJ, Masopust D, Zhu B, Allison JP, Sharpe AH, et al. Restoring function in exhausted CD8 T cells during chronic viral infection. Nature. 2006;439(7077):682-7. Epub 2005/12/31. doi: 10.1038/nature04444. PubMed PMID: 16382236.
67. Philip M, Schietinger A. CD8(+) T cell differentiation and dysfunction in cancer. Nat Rev Immunol. 2022;22(4):209-23. Epub 20210712. doi: 10.1038/s41577-021-00574-3. PubMed PMID: 34253904; PubMed Central PMCID: PMC9792152.
68. Speiser DE, Utzschneider DT, Oberle SG, Münz C, Romero P, Zehn D. T cell differentiation in chronic infection and cancer: functional adaptation or exhaustion? Nat

Rev Immunol. 2014;14(11):768-74. Epub 20140926. doi: 10.1038/nri3740. PubMed PMID: 25257362.
69. Wherry EJ. T cell exhaustion. Nat Immunol. 2011;12(6):492-9. doi: 10.1038/ni.2035. PubMed PMID: 21739672.
70. Doering TA, Crawford A, Angelosanto JM, Paley MA, Ziegler CG, Wherry EJ. Network analysis reveals centrally connected genes and pathways involved in CD8+ T cell exhaustion versus memory. Immunity. 2012;37(6):1130-44. Epub 20121115. doi: 10.1016/j.immuni.2012.08.021. PubMed PMID: 23159438; PubMed Central PMCID: PMC3749234.
71. Schietinger A, Greenberg PD. Tolerance and exhaustion: defining mechanisms of T cell dysfunction. Trends Immunol. 2014;35(2):51-60. Epub 20131106. doi: 10.1016/j.it.2013.10.001. PubMed PMID: 24210163; PubMed Central PMCID: PMC3946600.
72. Zajac AJ, Blattman JN, Murali-Krishna K, Sourdive DJ, Suresh M, Altman JD, et al. Viral immune evasion due to persistence of activated T cells without effector function. J Exp Med. 1998;188(12):2205-13. Epub 1998/12/22. doi: 10.1084/jem.188.12.2205. PubMed PMID: 9858507; PubMed Central PMCID: PMC2212420.
73. Gallimore A, Glithero A, Godkin A, Tissot AC, Plückthun A, Elliott T, et al. Induction and exhaustion of lymphocytic choriomeningitis virus-specific cytotoxic T lymphocytes visualized using soluble tetrameric major histocompatibility complex class I-peptide complexes. J Exp Med. 1998;187(9):1383-93. doi: 10.1084/jem.187.9.1383. PubMed PMID: 9565631; PubMed Central PMCID: PMC2212278.
74. Goepfert PA, Bansal A, Edwards BH, Ritter GD, Jr., Tellez I, McPherson SA, et al. A significant number of human immunodeficiency virus epitope-specific cytotoxic T lymphocytes detected by tetramer binding do not produce gamma interferon. J Virol. 2000;74(21):10249-55. doi: 10.1128/jvi.74.21.10249-10255.2000. PubMed PMID: 11024158; PubMed Central PMCID: PMC102068.
75. Shankar P, Russo M, Harnisch B, Patterson M, Skolnik P, Lieberman J. Impaired function of circulating HIV-specific CD8(+) T cells in chronic human immunodeficiency virus infection. Blood. 2000;96(9):3094-101. PubMed PMID: 11049989.
76. Kostense S, Ogg GS, Manting EH, Gillespie G, Joling J, Vandenberghe K, et al. High viral burden in the presence of major HIV-specific CD8(+) T cell expansions: evidence for impaired CTL effector function. Eur J Immunol. 2001;31(3):677-86. doi: 10.1002/1521-4141(200103)31:3<677::aid-immu677>3.0.co;2-m. PubMed PMID: 11241270.
77. Day CL, Kaufmann DE, Kiepiela P, Brown JA, Moodley ES, Reddy S, et al. PD-1 expression on HIV-specific T cells is associated with T-cell exhaustion and disease progression. Nature. 2006;443(7109):350-4. Epub 20060820. doi: 10.1038/nature05115. PubMed PMID: 16921384.
78. Lechner F, Wong DK, Dunbar PR, Chapman R, Chung RT, Dohrenwend P, et al. Analysis of successful immune responses in persons infected with hepatitis C virus. J Exp Med. 2000;191(9):1499-512. doi: 10.1084/jem.191.9.1499. PubMed PMID: 10790425; PubMed Central PMCID: PMC2213430.
79. Gruener NH, Lechner F, Jung MC, Diepolder H, Gerlach T, Lauer G, et al. Sustained dysfunction of antiviral CD8+ T lymphocytes after infection with hepatitis C virus. J Virol. 2001;75(12):5550-8. doi: 10.1128/jvi.75.12.5550-5558.2001. PubMed PMID: 11356962; PubMed Central PMCID: PMC114267.
80. Ye B, Liu X, Li X, Kong H, Tian L, Chen Y. T-cell exhaustion in chronic hepatitis B infection: current knowledge and clinical significance. Cell Death Dis. 2015;6(3):e1694.

Epub 20150319. doi: 10.1038/cddis.2015.42. PubMed PMID: 25789969; PubMed Central PMCID: PMC4385920.
81. Wherry EJ, Kurachi M. Molecular and cellular insights into T cell exhaustion. Nat Rev Immunol. 2015;15(8):486-99. Epub 2015/07/25. doi: 10.1038/nri3862. PubMed PMID: 26205583; PubMed Central PMCID: PMC4889009.
82. Sharpe AH, Wherry EJ, Ahmed R, Freeman GJ. The function of programmed cell death 1 and its ligands in regulating autoimmunity and infection. Nat Immunol. 2007;8(3):239-45. doi: 10.1038/ni1443. PubMed PMID: 17304234.
83. Pauken KE, Wherry EJ. Overcoming T cell exhaustion in infection and cancer. Trends Immunol. 2015;36(4):265-76. Epub 20150318. doi: 10.1016/j.it.2015.02.008. PubMed PMID: 25797516; PubMed Central PMCID: PMC4393798.
84. Zarour HM. Reversing T-cell Dysfunction and Exhaustion in Cancer. Clin Cancer Res. 2016;22(8):1856-64. doi: 10.1158/1078-0432.Ccr-15-1849. PubMed PMID: 27084739; PubMed Central PMCID: PMC4872712.
85. Huang AC, Postow MA, Orlowski RJ, Mick R, Bengsch B, Manne S, et al. T-cell invigoration to tumour burden ratio associated with anti-PD-1 response. Nature. 2017;545(7652):60-5. Epub 20170410. doi: 10.1038/nature22079. PubMed PMID: 28397821; PubMed Central PMCID: PMC5554367.
86. Zhang H, Xie Y, Li W, Chibbar R, Xiong S, Xiang J. CD4+ T cell-released exosomes inhibit CD8+ cytotoxic T-lymphocyte responses and antitumor immunity. Cell Mol Immunol. 2011;8(1):23-30. doi: 10.1038/cmi.2010.59.
87. Mumprecht S, Claus C, Schürch C, Pavelic V, Matter MS, Ochsenbein AF. Defective homing and impaired induction of cytotoxic T cells by BCR/ABL-expressing dendritic cells. Blood. 2009;113(19):4681-9. Epub 20090227. doi: 10.1182/blood-2008-05-156471. PubMed PMID: 19252140.
88. Guan X, Polesso F, Wang C, Sehrawat A, Hawkins RM, Murray SE, et al. Androgen receptor activity in T cells limits checkpoint blockade efficacy. Nature. 2022. Epub 2022/03/25. doi: 10.1038/s41586-022-04522-6. PubMed PMID: 35322234.
89. Tuong ZK, Loudon KW, Berry B, Richoz N, Jones J, Tan X, et al. Resolving the immune landscape of human prostate at a single-cell level in health and cancer. Cell Rep. 2021;37(12):110132. doi: 10.1016/j.celrep.2021.110132. PubMed PMID: 34936871; PubMed Central PMCID: PMC8721283.
90. Yang Z, Guo J, Weng L, Tang W, Jin S, Ma W. Myeloid-derived suppressor cells-new and exciting players in lung cancer. J Hematol Oncol. 2020;13(1):10. Epub 20200131. doi: 10.1186/s13045-020-0843-1. PubMed PMID: 32005273; PubMed Central PMCID: PMC6995114.
91. Karpisheh V, Mousavi SM, Naghavi Sheykholeslami P, Fathi M, Mohammadpour Saray M, Aghebati-Maleki L, et al. The role of regulatory T cells in the pathogenesis and treatment of prostate cancer. Life Sci. 2021;284:119132. Epub 20210126. doi: 10.1016/j.lfs.2021.119132. PubMed PMID: 33513396.
92. Iwai Y, Ishida M, Tanaka Y, Okazaki T, Honjo T, Minato N. Involvement of PD-L1 on tumor cells in the escape from host immune system and tumor immunotherapy by PD-L1 blockade. Proc Natl Acad Sci U S A. 2002;99(19):12293-7. Epub 20020906. doi: 10.1073/pnas.192461099. PubMed PMID: 12218188; PubMed Central PMCID: PMC129438.
93. Hirano F, Kaneko K, Tamura H, Dong H, Wang S, Ichikawa M, et al. Blockade of B7-H1 and PD-1 by monoclonal antibodies potentiates cancer therapeutic immunity. Cancer Res. 2005;65(3):1089-96. PubMed PMID: 15705911.

94. Keir ME, Butte MJ, Freeman GJ, Sharpe AH. PD-1 and its ligands in tolerance and immunity. Annu Rev Immunol. 2008;26:677-704. doi: 10.1146/annurev.immunol.26.021607.090331. PubMed PMID: 18173375; PubMed Central PMCID: PMC10637733.
95. Im SJ, Hashimoto M, Gerner MY, Lee J, Kissick HT, Burger MC, et al. Defining CD8+ T cells that provide the proliferative burst after PD-1 therapy. Nature. 2016;537(7620):417-21. Epub 20160802. doi: 10.1038/nature19330. PubMed PMID: 27501248; PubMed Central PMCID: PMC5297183.
96. Valk E, Rudd CE, Schneider H. CTLA-4 trafficking and surface expression. Trends Immunol. 2008;29(6):272-9. Epub 20080509. doi: 10.1016/j.it.2008.02.011. PubMed PMID: 18468488; PubMed Central PMCID: PMC4186961.
97. Walunas TL, Lenschow DJ, Bakker CY, Linsley PS, Freeman GJ, Green JM, et al. CTLA-4 can function as a negative regulator of T cell activation. Immunity. 1994;1(5):405-13. doi: 10.1016/1074-7613(94)90071-x. PubMed PMID: 7882171.
98. Krummel MF, Allison JP. CD28 and CTLA-4 have opposing effects on the response of T cells to stimulation. J Exp Med. 1995;182(2):459-65. doi: 10.1084/jem.182.2.459. PubMed PMID: 7543139; PubMed Central PMCID: PMC2192127.
99. Walker LS. Treg and CTLA-4: two intertwining pathways to immune tolerance. J Autoimmun. 2013;45(100):49-57. Epub 20130710. doi: 10.1016/j.jaut.2013.06.006. PubMed PMID: 23849743; PubMed Central PMCID: PMC3989116.
100. Leach DR, Krummel MF, Allison JP. Enhancement of antitumor immunity by CTLA-4 blockade. Science. 1996;271(5256):1734-6. doi: 10.1126/science.271.5256.1734. PubMed PMID: 8596936.
101. Kwon ED, Hurwitz AA, Foster BA, Madias C, Feldhaus AL, Greenberg NM, et al. Manipulation of T cell costimulatory and inhibitory signals for immunotherapy of prostate cancer. Proc Natl Acad Sci U S A. 1997;94(15):8099-103. doi: 10.1073/pnas.94.15.8099. PubMed PMID: 9223321; PubMed Central PMCID: PMC21563.
102. Yang YF, Zou JP, Mu J, Wijesuriya R, Ono S, Walunas T, et al. Enhanced induction of antitumor T-cell responses by cytotoxic T lymphocyte-associated molecule-4 blockade: the effect is manifested only at the restricted tumor-bearing stages. Cancer Res. 1997;57(18):4036-41. PubMed PMID: 9307290.
103. Hodi FS, O'Day SJ, McDermott DF, Weber RW, Sosman JA, Haanen JB, et al. Improved survival with ipilimumab in patients with metastatic melanoma. N Engl J Med. 2010;363(8):711-23. Epub 20100605. doi: 10.1056/NEJMoa1003466. PubMed PMID: 20525992; PubMed Central PMCID: PMC3549297.
104. Okazaki T, Maeda A, Nishimura H, Kurosaki T, Honjo T. PD-1 immunoreceptor inhibits B cell receptor-mediated signaling by recruiting src homology 2-domain-containing tyrosine phosphatase 2 to phosphotyrosine. Proc Natl Acad Sci U S A. 2001;98(24):13866-71. Epub 20011106. doi: 10.1073/pnas.231486598. PubMed PMID: 11698646; PubMed Central PMCID: PMC61133.
105. Reck M, Rodríguez-Abreu D, Robinson AG, Hui R, Csőszi T, Fülöp A, et al. Pembrolizumab versus Chemotherapy for PD-L1-Positive Non-Small-Cell Lung Cancer. N Engl J Med. 2016;375(19):1823-33. Epub 20161008. doi: 10.1056/NEJMoa1606774. PubMed PMID: 27718847.
106. Larkin J, Chiarion-Sileni V, Gonzalez R, Grob JJ, Cowey CL, Lao CD, et al. Combined Nivolumab and Ipilimumab or Monotherapy in Untreated Melanoma. N Engl J Med. 2015;373(1):23-34. Epub 20150531. doi: 10.1056/NEJMoa1504030. PubMed PMID: 26027431; PubMed Central PMCID: PMC5698905.

107. Robert C, Ribas A, Wolchok JD, Hodi FS, Hamid O, Kefford R, et al. Anti-programmed-death-receptor-1 treatment with pembrolizumab in ipilimumab-refractory advanced melanoma: a randomised dose-comparison cohort of a phase 1 trial. Lancet. 2014;384(9948):1109-17. Epub 20140715. doi: 10.1016/s0140-6736(14)60958-2. PubMed PMID: 25034862.
108. Robert C, Schachter J, Long GV, Arance A, Grob JJ, Mortier L, et al. Pembrolizumab versus Ipilimumab in Advanced Melanoma. N Engl J Med. 2015;372(26):2521-32. Epub 20150419. doi: 10.1056/NEJMoa1503093. PubMed PMID: 25891173.
109. Garon EB, Rizvi NA, Hui R, Leighl N, Balmanoukian AS, Eder JP, et al. Pembrolizumab for the treatment of non-small-cell lung cancer. N Engl J Med. 2015;372(21):2018-28. Epub 20150419. doi: 10.1056/NEJMoa1501824. PubMed PMID: 25891174.
110. Ott PA, Bang YJ, Piha-Paul SA, Razak ARA, Bennouna J, Soria JC, et al. T-Cell-Inflamed Gene-Expression Profile, Programmed Death Ligand 1 Expression, and Tumor Mutational Burden Predict Efficacy in Patients Treated With Pembrolizumab Across 20 Cancers: KEYNOTE-028. J Clin Oncol. 2019;37(4):318-27. Epub 20181213. doi: 10.1200/jco.2018.78.2276. PubMed PMID: 30557521.
111. Bagchi S, Yuan R, Engleman EG. Immune Checkpoint Inhibitors for the Treatment of Cancer: Clinical Impact and Mechanisms of Response and Resistance. Annu Rev Pathol. 2021;16:223-49. Epub 20201116. doi: 10.1146/annurev-pathol-042020-042741. PubMed PMID: 33197221.
112. Saleh R, Elkord E. Treg-mediated acquired resistance to immune checkpoint inhibitors. Cancer Lett. 2019;457:168-79. Epub 20190509. doi: 10.1016/j.canlet.2019.05.003. PubMed PMID: 31078738.
113. Quezada SA, Simpson TR, Peggs KS, Merghoub T, Vider J, Fan X, et al. Tumor-reactive CD4(+) T cells develop cytotoxic activity and eradicate large established melanoma after transfer into lymphopenic hosts. J Exp Med. 2010;207(3):637-50. Epub 20100215. doi: 10.1084/jem.20091918. PubMed PMID: 20156971; PubMed Central PMCID: PMC2839156.
114. Curran MA, Montalvo W, Yagita H, Allison JP. PD-1 and CTLA-4 combination blockade expands infiltrating T cells and reduces regulatory T and myeloid cells within B16 melanoma tumors. Proc Natl Acad Sci U S A. 2010;107(9):4275-80. Epub 20100216. doi: 10.1073/pnas.0915174107. PubMed PMID: 20160101; PubMed Central PMCID: PMC2840093.
115. Ma Q, Liu J, Wu G, Teng M, Wang S, Cui M, et al. Co-expression of LAG3 and TIM3 identifies a potent Treg population that suppresses macrophage functions in colorectal cancer patients. Clin Exp Pharmacol Physiol. 2018;45(10):1002-9. Epub 20180726. doi: 10.1111/1440-1681.12992. PubMed PMID: 29905955.
116. Kavanagh B, O'Brien S, Lee D, Hou Y, Weinberg V, Rini B, et al. CTLA4 blockade expands FoxP3+ regulatory and activated effector CD4+ T cells in a dose-dependent fashion. Blood. 2008;112(4):1175-83. Epub 20080603. doi: 10.1182/blood-2007-11-125435. PubMed PMID: 18523152; PubMed Central PMCID: PMC2515138.
117. Saleh R, Toor SM, Khalaf S, Elkord E. Breast Cancer Cells and PD-1/PD-L1 Blockade Upregulate the Expression of PD-1, CTLA-4, TIM-3 and LAG-3 Immune Checkpoints in CD4(+) T Cells. Vaccines (Basel). 2019;7(4). Epub 20191012. doi: 10.3390/vaccines7040149. PubMed PMID: 31614877; PubMed Central PMCID: PMC6963740.
118. Rodriguez PC, Quiceno DG, Zabaleta J, Ortiz B, Zea AH, Piazuelo MB, et al. Arginase I production in the tumor microenvironment by mature myeloid cells inhibits T-cell receptor

expression and antigen-specific T-cell responses. Cancer Res. 2004;64(16):5839-49. doi: 10.1158/0008-5472.Can-04-0465. PubMed PMID: 15313928.

119. Rodriguez PC, Quiceno DG, Ochoa AC. L-arginine availability regulates T-lymphocyte cell-cycle progression. Blood. 2007;109(4):1568-73. Epub 20061005. doi: 10.1182/blood-2006-06-031856. PubMed PMID: 17023580; PubMed Central PMCID: PMC1794048.

120. Baniyash M. TCR zeta-chain downregulation: curtailing an excessive inflammatory immune response. Nat Rev Immunol. 2004;4(9):675-87. doi: 10.1038/nri1434. PubMed PMID: 15343367.

121. Parker KH, Beury DW, Ostrand-Rosenberg S. Myeloid-Derived Suppressor Cells: Critical Cells Driving Immune Suppression in the Tumor Microenvironment. Adv Cancer Res. 2015;128:95-139. Epub 20150512. doi: 10.1016/bs.acr.2015.04.002. PubMed PMID: 26216631; PubMed Central PMCID: PMC4662416.

122. Li K, Shi H, Zhang B, Ou X, Ma Q, Chen Y, et al. Myeloid-derived suppressor cells as immunosuppressive regulators and therapeutic targets in cancer. Signal Transduct Target Ther. 2021;6(1):362. Epub 20211007. doi: 10.1038/s41392-021-00670-9. PubMed PMID: 34620838; PubMed Central PMCID: PMC8497485.

123. Liu D, Wang L, Guo Y. Advances in and prospects of immunotherapy for prostate cancer. Cancer Lett. 2024;601:217155. Epub 20240808. doi: 10.1016/j.canlet.2024.217155. PubMed PMID: 39127338.

124. Koh J, Kim Y, Lee KY, Hur JY, Kim MS, Kim B, et al. MDSC subtypes and CD39 expression on CD8(+) T cells predict the efficacy of anti-PD-1 immunotherapy in patients with advanced NSCLC. Eur J Immunol. 2020;50(11):1810-9. Epub 20200709. doi: 10.1002/eji.202048534. PubMed PMID: 32510574; PubMed Central PMCID: PMC7689686.

125. Limagne E, Richard C, Thibaudin M, Fumet JD, Truntzer C, Lagrange A, et al. Tim-3/galectin-9 pathway and mMDSC control primary and secondary resistances to PD-1 blockade in lung cancer patients. Oncoimmunology. 2019;8(4):e1564505. Epub 20190122. doi: 10.1080/2162402x.2018.1564505. PubMed PMID: 30906658; PubMed Central PMCID: PMC6422400.

126. Youn JI, Park SM, Park S, Kim G, Lee HJ, Son J, et al. Peripheral natural killer cells and myeloid-derived suppressor cells correlate with anti-PD-1 responses in non-small cell lung cancer. Sci Rep. 2020;10(1):9050. Epub 20200603. doi: 10.1038/s41598-020-65666-x. PubMed PMID: 32493990; PubMed Central PMCID: PMC7270107.

127. Liao W, Overman MJ, Boutin AT, Shang X, Zhao D, Dey P, et al. KRAS-IRF2 Axis Drives Immune Suppression and Immune Therapy Resistance in Colorectal Cancer. Cancer Cell. 2019;35(4):559-72.e7. Epub 20190321. doi: 10.1016/j.ccell.2019.02.008. PubMed PMID: 30905761; PubMed Central PMCID: PMC6467776.

128. Ghonim MA, Ibba SV, Tarhuni AF, Errami Y, Luu HH, Dean MJ, et al. Targeting PARP-1 with metronomic therapy modulates MDSC suppressive function and enhances anti-PD-1 immunotherapy in colon cancer. J Immunother Cancer. 2021;9(1). doi: 10.1136/jitc-2020-001643. PubMed PMID: 33495297; PubMed Central PMCID: PMC7839867.

129. Boutilier AJ, Elsawa SF. Macrophage Polarization States in the Tumor Microenvironment. Int J Mol Sci. 2021;22(13). Epub 20210629. doi: 10.3390/ijms22136995. PubMed PMID: 34209703; PubMed Central PMCID: PMC8268869.

130. Zhang H, Liu L, Liu J, Dang P, Hu S, Yuan W, et al. Roles of tumor-associated macrophages in anti-PD-1/PD-L1 immunotherapy for solid cancers. Mol Cancer. 2023;22(1):58. Epub 20230321. doi: 10.1186/s12943-023-01725-x. PubMed PMID: 36941614; PubMed Central PMCID: PMC10029244.

131. Peranzoni E, Lemoine J, Vimeux L, Feuillet V, Barrin S, Kantari-Mimoun C, et al. Macrophages impede CD8 T cells from reaching tumor cells and limit the efficacy of anti-PD-1 treatment. Proc Natl Acad Sci U S A. 2018;115(17):E4041-e50. Epub 20180409. doi: 10.1073/pnas.1720948115. PubMed PMID: 29632196; PubMed Central PMCID: PMC5924916.
132. Zhu Y, Yang J, Xu D, Gao XM, Zhang Z, Hsu JL, et al. Disruption of tumour-associated macrophage trafficking by the osteopontin-induced colony-stimulating factor-1 signalling sensitises hepatocellular carcinoma to anti-PD-L1 blockade. Gut. 2019;68(9):1653-66. Epub 20190322. doi: 10.1136/gutjnl-2019-318419. PubMed PMID: 30902885.
133. Zhu Y, Knolhoff BL, Meyer MA, Nywening TM, West BL, Luo J, et al. CSF1/CSF1R blockade reprograms tumor-infiltrating macrophages and improves response to T-cell checkpoint immunotherapy in pancreatic cancer models. Cancer Res. 2014;74(18):5057-69. Epub 20140731. doi: 10.1158/0008-5472.Can-13-3723. PubMed PMID: 25082815; PubMed Central PMCID: PMC4182950.
134. Rodell CB, Arlauckas SP, Cuccarese MF, Garris CS, Li R, Ahmed MS, et al. TLR7/8-agonist-loaded nanoparticles promote the polarization of tumour-associated macrophages to enhance cancer immunotherapy. Nat Biomed Eng. 2018;2(8):578-88. Epub 20180521. doi: 10.1038/s41551-018-0236-8. PubMed PMID: 31015631; PubMed Central PMCID: PMC6192054.
135. Arlauckas SP, Garris CS, Kohler RH, Kitaoka M, Cuccarese MF, Yang KS, et al. In vivo imaging reveals a tumor-associated macrophage-mediated resistance pathway in anti-PD-1 therapy. Sci Transl Med. 2017;9(389). doi: 10.1126/scitranslmed.aal3604. PubMed PMID: 28490665; PubMed Central PMCID: PMC5734617.
136. Decaroli MC, De Vincentis S, Rochira V. Aging and sex hormones in males. Vitam Horm. 2021;115:333-66. Epub 20210213. doi: 10.1016/bs.vh.2020.12.014. PubMed PMID: 33706953.
137. Schiffer L, Arlt W, Storbeck KH. Intracrine androgen biosynthesis, metabolism and action revisited. Mol Cell Endocrinol. 2018;465:4-26. Epub 20170901. doi: 10.1016/j.mce.2017.08.016. PubMed PMID: 28865807; PubMed Central PMCID: PMC6565845.
138. Mizushima T, Miyamoto H. The Role of Androgen Receptor Signaling in Ovarian Cancer. Cells. 2019;8(2). Epub 20190219. doi: 10.3390/cells8020176. PubMed PMID: 30791431; PubMed Central PMCID: PMC6406955.
139. Wilson JD. The role of 5alpha-reduction in steroid hormone physiology. Reprod Fertil Dev. 2001;13(7-8):673-8. doi: 10.1071/rd01074. PubMed PMID: 11999320.
140. Simpson E, Rubin G, Clyne C, Robertson K, O'Donnell L, Davis S, et al. Local estrogen biosynthesis in males and females. Endocr Relat Cancer. 1999;6(2):131-7. doi: 10.1677/erc.0.0060131. PubMed PMID: 10731101.
141. Takahashi T, Ellingson MK, Wong P, Israelow B, Lucas C, Klein J, et al. Sex differences in immune responses that underlie COVID-19 disease outcomes. Nature. 2020;588(7837):315-20. Epub 2020/08/28. doi: 10.1038/s41586-020-2700-3. PubMed PMID: 32846427; PubMed Central PMCID: PMC7725931.
142. Márquez EJ, Chung CH, Marches R, Rossi RJ, Nehar-Belaid D, Eroglu A, et al. Sexual-dimorphism in human immune system aging. Nat Commun. 2020;11(1):751. Epub 2020/02/08. doi: 10.1038/s41467-020-14396-9. PubMed PMID: 32029736; PubMed Central PMCID: PMC7005316.
143. Klein SL, Flanagan KL. Sex differences in immune responses. Nat Rev Immunol. 2016;16(10):626-38. Epub 2016/08/23. doi: 10.1038/nri.2016.90. PubMed PMID: 27546235.

144. Scully EP, Haverfield J, Ursin RL, Tannenbaum C, Klein SL. Considering how biological sex impacts immune responses and COVID-19 outcomes. Nat Rev Immunol. 2020;20(7):442-7. Epub 20200611. doi: 10.1038/s41577-020-0348-8. PubMed PMID: 32528136; PubMed Central PMCID: PMC7288618.
145. Scully EP, Schumock G, Fu M, Massaccesi G, Muschelli J, Betz J, et al. Sex and Gender Differences in Testing, Hospital Admission, Clinical Presentation, and Drivers of Severe Outcomes From COVID-19. Open Forum Infect Dis. 2021;8(9):ofab448. Epub 20210831. doi: 10.1093/ofid/ofab448. PubMed PMID: 34584899; PubMed Central PMCID: PMC8465334.
146. Kharroubi SA, Diab-El-Harake M. Sex-differences in COVID-19 diagnosis, risk factors and disease comorbidities: A large US-based cohort study. Front Public Health. 2022;10:1029190. Epub 20221117. doi: 10.3389/fpubh.2022.1029190. PubMed PMID: 36466473; PubMed Central PMCID: PMC9714345.
147. Moreno-Torres V, Martínez-Urbistondo M, Calderón-Parra J, de Mendoza C, Soriano V. COVID-19 mortality amongst the immunosuppresed. J Infect. 2024;88(4):106137. Epub 20240311. doi: 10.1016/j.jinf.2024.106137. PubMed PMID: 38479495.
148. Gebhard C, Regitz-Zagrosek V, Neuhauser HK, Morgan R, Klein SL. Impact of sex and gender on COVID-19 outcomes in Europe. Biol Sex Differ. 2020;11(1):29. Epub 20200525. doi: 10.1186/s13293-020-00304-9. PubMed PMID: 32450906; PubMed Central PMCID: PMC7247289.
149. Klein SL. Sex influences immune responses to viruses, and efficacy of prophylaxis and treatments for viral diseases. Bioessays. 2012;34(12):1050-9. Epub 20120926. doi: 10.1002/bies.201200099. PubMed PMID: 23012250; PubMed Central PMCID: PMC4120666.
150. vom Steeg LG, Klein SL. SeXX Matters in Infectious Disease Pathogenesis. PLoS Pathog. 2016;12(2):e1005374. Epub 20160218. doi: 10.1371/journal.ppat.1005374. PubMed PMID: 26891052; PubMed Central PMCID: PMC4759457.
151. Lorenzo ME, Hodgson A, Robinson DP, Kaplan JB, Pekosz A, Klein SL. Antibody responses and cross protection against lethal influenza A viruses differ between the sexes in C57BL/6 mice. Vaccine. 2011;29(49):9246-55. Epub 20111006. doi: 10.1016/j.vaccine.2011.09.110. PubMed PMID: 21983155; PubMed Central PMCID: PMC3206291.
152. Larcombe AN, Foong RE, Bozanich EM, Berry LJ, Garratt LW, Gualano RC, et al. Sexual dimorphism in lung function responses to acute influenza A infection. Influenza Other Respir Viruses. 2011;5(5):334-42. Epub 20110321. doi: 10.1111/j.1750-2659.2011.00236.x. PubMed PMID: 21668688; PubMed Central PMCID: PMC4942045.
153. Giurgea LT, Cervantes-Medina A, Walters KA, Scherler K, Han A, Czajkowski LM, et al. Sex Differences in Influenza: The Challenge Study Experience. J Infect Dis. 2022;225(4):715-22. doi: 10.1093/infdis/jiab422. PubMed PMID: 34423369; PubMed Central PMCID: PMC8844587.
154. Hall OJ, Limjunyawong N, Vermillion MS, Robinson DP, Wohlgemuth N, Pekosz A, et al. Progesterone-Based Therapy Protects Against Influenza by Promoting Lung Repair and Recovery in Females. PLoS Pathog. 2016;12(9):e1005840. Epub 20160915. doi: 10.1371/journal.ppat.1005840. PubMed PMID: 27631986; PubMed Central PMCID: PMC5025002.
155. Hall OJ, Nachbagauer R, Vermillion MS, Fink AL, Phuong V, Krammer F, et al. Progesterone-Based Contraceptives Reduce Adaptive Immune Responses and Protection against Sequential Influenza A Virus Infections. J Virol. 2017;91(8). Epub 20170329. doi: 10.1128/jvi.02160-16. PubMed PMID: 28179523; PubMed Central PMCID: PMC5375688.

156. Robinson KM, McHugh KJ, Mandalapu S, Clay ME, Lee B, Scheller EV, et al. Influenza A virus exacerbates Staphylococcus aureus pneumonia in mice by attenuating antimicrobial peptide production. J Infect Dis. 2014;209(6):865-75. Epub 20130926. doi: 10.1093/infdis/jit527. PubMed PMID: 24072844; PubMed Central PMCID: PMC3935471.
157. Vom Steeg LG, Dhakal S, Woldetsadik YA, Park HS, Mulka KR, Reilly EC, et al. Androgen receptor signaling in the lungs mitigates inflammation and improves the outcome of influenza in mice. PLoS Pathog. 2020;16(7):e1008506. Epub 20200709. doi: 10.1371/journal.ppat.1008506. PubMed PMID: 32645119; PubMed Central PMCID: PMC7373319.
158. Robinson DP, Lorenzo ME, Jian W, Klein SL. Elevated 17β-estradiol protects females from influenza A virus pathogenesis by suppressing inflammatory responses. PLoS Pathog. 2011;7(7):e1002149. Epub 20110728. doi: 10.1371/journal.ppat.1002149. PubMed PMID: 21829352; PubMed Central PMCID: PMC3145801.
159. Vermillion MS, Ursin RL, Attreed SE, Klein SL. Estriol Reduces Pulmonary Immune Cell Recruitment and Inflammation to Protect Female Mice From Severe Influenza. Endocrinology. 2018;159(9):3306-20. doi: 10.1210/en.2018-00486. PubMed PMID: 30032246; PubMed Central PMCID: PMC6109301.
160. Narasimhan P, Wood J, Macintyre CR, Mathai D. Risk factors for tuberculosis. Pulm Med. 2013;2013:828939. Epub 20130212. doi: 10.1155/2013/828939. PubMed PMID: 23476764; PubMed Central PMCID: PMC3583136.
161. Sleeman K, Knox K, George R, Miller E, Waight P, Griffiths D, et al. Invasive pneumococcal disease in England and Wales: vaccination implications. J Infect Dis. 2001;183(2):239-46. Epub 20001221. doi: 10.1086/317924. PubMed PMID: 11120930.
162. Gannon CJ, Pasquale M, Tracy JK, McCarter RJ, Napolitano LM. Male gender is associated with increased risk for postinjury pneumonia. Shock. 2004;21(5):410-4. doi: 10.1097/00024382-200405000-00003. PubMed PMID: 15087816.
163. Dias SP, Brouwer MC, van de Beek D. Sex and Gender Differences in Bacterial Infections. Infect Immun. 2022;90(10):e0028322. Epub 20220919. doi: 10.1128/iai.00283-22. PubMed PMID: 36121220; PubMed Central PMCID: PMC9584217.
164. Pasche B, Kalaydjiev S, Franz TJ, Kremmer E, Gailus-Durner V, Fuchs H, et al. Sex-dependent susceptibility to Listeria monocytogenes infection is mediated by differential interleukin-10 production. Infect Immun. 2005;73(9):5952-60. doi: 10.1128/iai.73.9.5952-5960.2005. PubMed PMID: 16113316; PubMed Central PMCID: PMC1231091.
165. Leposavić G, Karapetrović B, Obradović S, Vidiíc Dandović B, Kosec D. Differential effects of gonadectomy on the thymocyte phenotypic profile in male and female rats. Pharmacol Biochem Behav. 1996;54(1):269-76. Epub 1996/05/01. doi: 10.1016/0091-3057(95)02165-5. PubMed PMID: 8728568.
166. Abdullah M, Chai PS, Chong MY, Tohit ER, Ramasamy R, Pei CP, et al. Gender effect on in vitro lymphocyte subset levels of healthy individuals. Cell Immunol. 2012;272(2):214-9. Epub 2011/11/15. doi: 10.1016/j.cellimm.2011.10.009. PubMed PMID: 22078320.
167. Sankaran-Walters S, Macal M, Grishina I, Nagy L, Goulart L, Coolidge K, et al. Sex differences matter in the gut: effect on mucosal immune activation and inflammation. Biol Sex Differ. 2013;4(1):10. Epub 2013/05/09. doi: 10.1186/2042-6410-4-10. PubMed PMID: 23651648; PubMed Central PMCID: PMC3652739.
168. Zhang MA, Rego D, Moshkova M, Kebir H, Chruscinski A, Nguyen H, et al. Peroxisome proliferator-activated receptor (PPAR)α and -γ regulate IFNγ and IL-17A production by human T cells in a sex-specific way. Proc Natl Acad Sci U S A.

2012;109(24):9505-10. Epub 2012/06/01. doi: 10.1073/pnas.1118458109. PubMed PMID: 22647601; PubMed Central PMCID: PMC3386070.

169. Weinstein Y, Ran S, Segal S. Sex-associated differences in the regulation of immune responses controlled by the MHC of the mouse. J Immunol. 1984;132(2):656-61. PubMed PMID: 6228595.

170. Palaszynski KM, Smith DL, Kamrava S, Burgoyne PS, Arnold AP, Voskuhl RR. A yin-yang effect between sex chromosome complement and sex hormones on the immune response. Endocrinology. 2005;146(8):3280-5. Epub 20050519. doi: 10.1210/en.2005-0284. PubMed PMID: 15905317.

171. Vom Steeg LG, Flores-Garcia Y, Zavala F, Klein SL. Irradiated sporozoite vaccination induces sex-specific immune responses and protection against malaria in mice. Vaccine. 2019;37(32):4468-76. Epub 20190628. doi: 10.1016/j.vaccine.2019.06.075. PubMed PMID: 31262583; PubMed Central PMCID: PMC7862922.

172. Peacock JW, Nordone SK, Jackson SS, Liao HX, Letvin NL, Yafal AG, et al. Gender differences in human immunodeficiency virus type 1-specific CD8 responses in the reproductive tract and colon following nasal peptide priming and modified vaccinia virus Ankara boosting. J Virol. 2004;78(23):13163-72. doi: 10.1128/jvi.78.23.13163-13172.2004. PubMed PMID: 15542668; PubMed Central PMCID: PMC524967.

173. Kondo H, Kageyama T, Tanaka S, Otsuka K, Tsukumo SI, Mashimo Y, et al. Markers of Memory CD8 T Cells Depicting the Effect of the BNT162b2 mRNA COVID-19 Vaccine in Japan. Front Immunol. 2022;13:836923. Epub 20220428. doi: 10.3389/fimmu.2022.836923. PubMed PMID: 35572546; PubMed Central PMCID: PMC9096866.

174. Stanberry LR, Spruance SL, Cunningham AL, Bernstein DI, Mindel A, Sacks S, et al. Glycoprotein-D-adjuvant vaccine to prevent genital herpes. N Engl J Med. 2002;347(21):1652-61. doi: 10.1056/NEJMoa011915. PubMed PMID: 12444179.

175. Umlauf BJ, Haralambieva IH, Ovsyannikova IG, Kennedy RB, Pankratz VS, Jacobson RM, et al. Associations between demographic variables and multiple measles-specific innate and cell-mediated immune responses after measles vaccination. Viral Immunol. 2012;25(1):29-36. Epub 20120112. doi: 10.1089/vim.2011.0051. PubMed PMID: 22239234; PubMed Central PMCID: PMC3271368.

176. Arnold AP, Chen X. What does the "four core genotypes" mouse model tell us about sex differences in the brain and other tissues? Front Neuroendocrinol. 2009;30(1):1-9. Epub 20081111. doi: 10.1016/j.yfrne.2008.11.001. PubMed PMID: 19028515; PubMed Central PMCID: PMC3282561.

177. Bebo BF, Jr., Schuster JC, Vandenbark AA, Offner H. Androgens alter the cytokine profile and reduce encephalitogenicity of myelin-reactive T cells. J Immunol. 1999;162(1):35-40. Epub 1999/01/14. PubMed PMID: 9886367.

178. Bebo BF, Jr., Fyfe-Johnson A, Adlard K, Beam AG, Vandenbark AA, Offner H. Low-dose estrogen therapy ameliorates experimental autoimmune encephalomyelitis in two different inbred mouse strains. J Immunol. 2001;166(3):2080-9. doi: 10.4049/jimmunol.166.3.2080. PubMed PMID: 11160259.

179. Hewagama A, Patel D, Yarlagadda S, Strickland FM, Richardson BC. Stronger inflammatory/cytotoxic T-cell response in women identified by microarray analysis. Genes Immun. 2009;10(5):509-16. Epub 2009/03/13. doi: 10.1038/gene.2009.12. PubMed PMID: 19279650; PubMed Central PMCID: PMC2735332.

180. Park HJ, Park HS, Lee JU, Bothwell AL, Choi JM. Gender-specific differences in PPARγ regulation of follicular helper T cell responses with estrogen. Sci Rep. 2016;6:28495. Epub

20160623. doi: 10.1038/srep28495. PubMed PMID: 27335315; PubMed Central PMCID: PMC4917844.

181. Conforti F, Pala L, Bagnardi V, De Pas T, Martinetti M, Viale G, et al. Cancer immunotherapy efficacy and patients' sex: a systematic review and meta-analysis. Lancet Oncol. 2018;19(6):737-46. Epub 2018/05/21. doi: 10.1016/s1470-2045(18)30261-4. PubMed PMID: 29778737.

182. Wang PF, Song HF, Zhang Q, Yan CX. Pan-cancer immunogenomic analyses reveal sex disparity in the efficacy of cancer immunotherapy. Eur J Cancer. 2020;126:136-8. Epub 2020/01/14. doi: 10.1016/j.ejca.2019.12.008. PubMed PMID: 31927214.

183. Botticelli A, Onesti CE, Zizzari I, Cerbelli B, Sciattella P, Occhipinti M, et al. The sexist behaviour of immune checkpoint inhibitors in cancer therapy? Oncotarget. 2017;8(59):99336-46. Epub 2017/12/17. doi: 10.18632/oncotarget.22242. PubMed PMID: 29245905; PubMed Central PMCID: PMC5725096.

184. Klein SL, Morgan R. The impact of sex and gender on immunotherapy outcomes. Biol Sex Differ. 2020;11(1):24. Epub 2020/05/06. doi: 10.1186/s13293-020-00301-y. PubMed PMID: 32366281; PubMed Central PMCID: PMC7197158.

185. Wallis CJD, Butaney M, Satkunasivam R, Freedland SJ, Patel SP, Hamid O, et al. Association of Patient Sex With Efficacy of Immune Checkpoint Inhibitors and Overall Survival in Advanced Cancers: A Systematic Review and Meta-analysis. JAMA Oncol. 2019;5(4):529-36. Epub 2019/01/04. doi: 10.1001/jamaoncol.2018.5904. PubMed PMID: 30605213; PubMed Central PMCID: PMC6459215 outside of the submitted work. Dr Patel reported receiving scientific advisory income from AstraZeneca, BMS, Illumina, Tempus, and Novartis. Dr Patel's university receives research funding from Bristol-Myers Squibb, Eli Lilly, Fate, Incyte, AstraZeneca/MedImmune, Merck, Pfizer, Roche/Genentech, Xcovery, Fate Therapeutics, Genocea, and Iovance. Dr Pal reported receiving personal fees from Genentech, Pfizer, and BMS outside of the submitted work. No other disclosures were reported.

186. Siegel RL, Miller KD, Fuchs HE, Jemal A. Cancer Statistics, 2021. CA Cancer J Clin. 2021;71(1):7-33. Epub 2021/01/13. doi: 10.3322/caac.21654. PubMed PMID: 33433946.

187. Viale PH. The American Cancer Society's Facts & Figures: 2020 Edition. J Adv Pract Oncol. 2020;11(2):135-6. Epub 20200301. doi: 10.6004/jadpro.2020.11.2.1. PubMed PMID: 33532112; PubMed Central PMCID: PMC7848816.

188. Raychaudhuri R, Lin DW, Montgomery RB. Prostate Cancer: A Review. JAMA. 2025;333(16):1433-46. doi: 10.1001/jama.2025.0228. PubMed PMID: 40063046.

189. Chen CD, Welsbie DS, Tran C, Baek SH, Chen R, Vessella R, et al. Molecular determinants of resistance to antiandrogen therapy. Nat Med. 2004;10(1):33-9. doi: 10.1038/nm972.

190. Mohler JL, Gregory CW, Ford OH, 3rd, Kim D, Weaver CM, Petrusz P, et al. The androgen axis in recurrent prostate cancer. Clin Cancer Res. 2004;10(2):440-8. doi: 10.1158/1078-0432.ccr-1146-03. PubMed PMID: 14760063.

191. Castagnetta LA, Carruba G, Traina A, Granata OM, Markus M, Pavone-Macaluso M, et al. Expression of different 17beta-hydroxysteroid dehydrogenase types and their activities in human prostate cancer cells. Endocrinology. 1997;138(11):4876-82. doi: 10.1210/endo.138.11.5497. PubMed PMID: 9348218.

192. Schalken J, Fitzpatrick JM. Enzalutamide: targeting the androgen signalling pathway in metastatic castration-resistant prostate cancer. BJU Int. 2016;117(2):215-25. Epub 20150606. doi: 10.1111/bju.13123. PubMed PMID: 25818596; PubMed Central PMCID: PMC4744713.

193. Mostaghel EA, Montgomery B, Nelson PS. Castration-resistant prostate cancer: Targeting androgen metabolic pathways in recurrent disease. Urologic Oncology: Seminars and Original Investigations. 2009;27(3):251-7. doi: https://doi.org/10.1016/j.urolonc.2009.03.016.
194. Kirby M, Hirst C, Crawford ED. Characterising the castration-resistant prostate cancer population: a systematic review. Int J Clin Pract. 2011;65(11):1180-92. doi: 10.1111/j.1742-1241.2011.02799.x. PubMed PMID: 21995694.
195. Zhao SG, Lehrer J, Chang SL, Das R, Erho N, Liu Y, et al. The Immune Landscape of Prostate Cancer and Nomination of PD-L2 as a Potential Therapeutic Target. J Natl Cancer Inst. 2019;111(3):301-10. doi: 10.1093/jnci/djy141. PubMed PMID: 30321406.
196. Hirz T, Mei S, Sarkar H, Kfoury Y, Wu S, Verhoeven BM, et al. Dissecting the immune suppressive human prostate tumor microenvironment via integrated single-cell and spatial transcriptomic analyses. Nat Commun. 2023;14(1):663. Epub 20230207. doi: 10.1038/s41467-023-36325-2. PubMed PMID: 36750562; PubMed Central PMCID: PMC9905093.
197. Murray NP. Immunomodulation and Immunotherapy for Patients with Prostate Cancer: An Up-to-Date Review. Biomedicines. 2025;13(5). Epub 20250512. doi: 10.3390/biomedicines13051179. PubMed PMID: 40427006; PubMed Central PMCID: PMC12109314.
198. Koinis F, Xagara A, Chantzara E, Leontopoulou V, Aidarinis C, Kotsakis A. Myeloid-Derived Suppressor Cells in Prostate Cancer: Present Knowledge and Future Perspectives. Cells. 2021;11(1). Epub 20211222. doi: 10.3390/cells11010020. PubMed PMID: 35011582; PubMed Central PMCID: PMC8750906.
199. Lyu A, Fan Z, Clark M, Lea A, Luong D, Setayesh A, et al. Evolution of myeloid-mediated immunotherapy resistance in prostate cancer. Nature. 2025;637(8048):1207-17. Epub 20241204. doi: 10.1038/s41586-024-08290-3. PubMed PMID: 39633050; PubMed Central PMCID: PMC11779626.
200. Chesner LN, Polesso F, Graff JN, Hawley JE, Smith AK, Lundberg A, et al. Androgen Receptor Inhibition Increases MHC Class I Expression and Improves Immune Response in Prostate Cancer. Cancer Discov. 2025;15(3):481-94. doi: 10.1158/2159-8290.Cd-24-0559. PubMed PMID: 39652470; PubMed Central PMCID: PMC11873725.
201. Venturini NJ, Drake CG. Immunotherapy for Prostate Cancer. Cold Spring Harb Perspect Med. 2019;9(5). Epub 20190501. doi: 10.1101/cshperspect.a030627. PubMed PMID: 30201787; PubMed Central PMCID: PMC6496329.
202. Beer TM, Kwon ED, Drake CG, Fizazi K, Logothetis C, Gravis G, et al. Randomized, Double-Blind, Phase III Trial of Ipilimumab Versus Placebo in Asymptomatic or Minimally Symptomatic Patients With Metastatic Chemotherapy-Naive Castration-Resistant Prostate Cancer. J Clin Oncol. 2017;35(1):40-7. Epub 20161031. doi: 10.1200/jco.2016.69.1584. PubMed PMID: 28034081.
203. Kwon ED, Drake CG, Scher HI, Fizazi K, Bossi A, van den Eertwegh AJ, et al. Ipilimumab versus placebo after radiotherapy in patients with metastatic castration-resistant prostate cancer that had progressed after docetaxel chemotherapy (CA184-043): a multicentre, randomised, double-blind, phase 3 trial. Lancet Oncol. 2014;15(7):700-12. Epub 20140513. doi: 10.1016/s1470-2045(14)70189-5. PubMed PMID: 24831977; PubMed Central PMCID: PMC4418935.
204. Topalian SL, Hodi FS, Brahmer JR, Gettinger SN, Smith DC, McDermott DF, et al. Safety, activity, and immune correlates of anti-PD-1 antibody in cancer. N Engl J Med.

2012;366(26):2443-54. Epub 20120602. doi: 10.1056/NEJMoa1200690. PubMed PMID: 22658127; PubMed Central PMCID: PMC3544539.
205. Hansen AR, Massard C, Ott PA, Haas NB, Lopez JS, Ejadi S, et al. Pembrolizumab for advanced prostate adenocarcinoma: findings of the KEYNOTE-028 study. Ann Oncol. 2018;29(8):1807-13. doi: 10.1093/annonc/mdy232. PubMed PMID: 29992241.
206. Antonarakis ES, Piulats JM, Gross-Goupil M, Goh J, Ojamaa K, Hoimes CJ, et al. Pembrolizumab for Treatment-Refractory Metastatic Castration-Resistant Prostate Cancer: Multicohort, Open-Label Phase II KEYNOTE-199 Study. J Clin Oncol. 2020;38(5):395-405. Epub 20191127. doi: 10.1200/jco.19.01638. PubMed PMID: 31774688; PubMed Central PMCID: PMC7186583.
207. Wang I, Song L, Wang BY, Rezazadeh Kalebasty A, Uchio E, Zi X. Prostate cancer immunotherapy: a review of recent advancements with novel treatment methods and efficacy. Am J Clin Exp Urol. 2022;10(4):210-33. Epub 20220815. PubMed PMID: 36051616; PubMed Central PMCID: PMC9428569.
208. Small EJ, Schellhammer PF, Higano CS, Redfern CH, Nemunaitis JJ, Valone FH, et al. Placebo-controlled phase III trial of immunologic therapy with sipuleucel-T (APC8015) in patients with metastatic, asymptomatic hormone refractory prostate cancer. J Clin Oncol. 2006;24(19):3089-94. doi: 10.1200/jco.2005.04.5252. PubMed PMID: 16809734.
209. Kantoff PW, Higano CS, Shore ND, Berger ER, Small EJ, Penson DF, et al. Sipuleucel-T immunotherapy for castration-resistant prostate cancer. N Engl J Med. 2010;363(5):411-22. doi: 10.1056/NEJMoa1001294. PubMed PMID: 20818862.
210. Petrylak DP, Loriot Y, Shaffer DR, Braiteh F, Powderly J, Harshman LC, et al. Safety and Clinical Activity of Atezolizumab in Patients with Metastatic Castration-Resistant Prostate Cancer: A Phase I Study. Clin Cancer Res. 2021;27(12):3360-9. Epub 20210210. doi: 10.1158/1078-0432.Ccr-20-1981. PubMed PMID: 33568344.
211. Powles T, Yuen KC, Gillessen S, Kadel EE, 3rd, Rathkopf D, Matsubara N, et al. Atezolizumab with enzalutamide versus enzalutamide alone in metastatic castration-resistant prostate cancer: a randomized phase 3 trial. Nat Med. 2022;28(1):144-53. Epub 20220110. doi: 10.1038/s41591-021-01600-6. PubMed PMID: 35013615; PubMed Central PMCID: PMC9406237.
212. Fong L, Morris MJ, Sartor O, Higano CS, Pagliaro L, Alva A, et al. A Phase Ib Study of Atezolizumab with Radium-223 Dichloride in Men with Metastatic Castration-Resistant Prostate Cancer. Clin Cancer Res. 2021;27(17):4746-56. Epub 20210609. doi: 10.1158/1078-0432.Ccr-21-0063. PubMed PMID: 34108181; PubMed Central PMCID: PMC8974420.
213. Dorff T, Hirasawa Y, Acoba J, Pagano I, Tamura D, Pal S, et al. Phase Ib study of patients with metastatic castrate-resistant prostate cancer treated with different sequencing regimens of atezolizumab and sipuleucel-T. J Immunother Cancer. 2021;9(8). doi: 10.1136/jitc-2021-002931. PubMed PMID: 34376554; PubMed Central PMCID: PMC8356194.
214. Agarwal N, Azad A, Carles J, Chowdhury S, McGregor B, Merseburger AS, et al. A phase III, randomized, open-label study (CONTACT-02) of cabozantinib plus atezolizumab versus second novel hormone therapy in patients with metastatic castration-resistant prostate cancer. Future Oncol. 2022;18(10):1185-98. Epub 20220117. doi: 10.2217/fon-2021-1096. PubMed PMID: 35034502.
215. Kwan EM, Spain L, Anton A, Gan CL, Garrett L, Chang D, et al. Avelumab Combined with Stereotactic Ablative Body Radiotherapy in Metastatic Castration-resistant Prostate

Cancer: The Phase 2 ICE-PAC Clinical Trial. Eur Urol. 2022;81(3):253-62. Epub 20210904. doi: 10.1016/j.eururo.2021.08.011. PubMed PMID: 34493414.
216. Brown LC, Halabi S, Somarelli JA, Humeniuk M, Wu Y, Oyekunle T, et al. A phase 2 trial of avelumab in men with aggressive-variant or neuroendocrine prostate cancer. Prostate Cancer Prostatic Dis. 2022;25(4):762-9. Epub 20220315. doi: 10.1038/s41391-022-00524-7. PubMed PMID: 35292724; PubMed Central PMCID: PMC8923335.
217. Karzai F, VanderWeele D, Madan RA, Owens H, Cordes LM, Hankin A, et al. Activity of durvalumab plus olaparib in metastatic castration-resistant prostate cancer in men with and without DNA damage repair mutations. J Immunother Cancer. 2018;6(1):141. Epub 20181204. doi: 10.1186/s40425-018-0463-2. PubMed PMID: 30514390; PubMed Central PMCID: PMC6280368.
218. Castle JC, Uduman M, Pabla S, Stein RB, Buell JS. Mutation-Derived Neoantigens for Cancer Immunotherapy. Front Immunol. 2019;10:1856. Epub 20190807. doi: 10.3389/fimmu.2019.01856. PubMed PMID: 31440245; PubMed Central PMCID: PMC6693295.
219. Matsumoto T, Shiina H, Kawano H, Sato T, Kato S. Androgen receptor functions in male and female physiology. J Steroid Biochem Mol Biol. 2008;109(3-5):236-41. Epub 20080319. doi: 10.1016/j.jsbmb.2008.03.023. PubMed PMID: 18434134.
220. Jacobson DL, Gange SJ, Rose NR, Graham NM. Epidemiology and estimated population burden of selected autoimmune diseases in the United States. Clin Immunol Immunopathol. 1997;84(3):223-43. Epub 1997/09/01. doi: 10.1006/clin.1997.4412. PubMed PMID: 9281381.
221. Giefing-Kröll C, Berger P, Lepperdinger G, Grubeck-Loebenstein B. How sex and age affect immune responses, susceptibility to infections, and response to vaccination. Aging Cell. 2015;14(3):309-21. Epub 2015/02/28. doi: 10.1111/acel.12326. PubMed PMID: 25720438; PubMed Central PMCID: PMC4406660.
222. Cook MB, Dawsey SM, Freedman ND, Inskip PD, Wichner SM, Quraishi SM, et al. Sex disparities in cancer incidence by period and age. Cancer Epidemiol Biomarkers Prev. 2009;18(4):1174-82. Epub 2009/03/19. doi: 10.1158/1055-9965.Epi-08-1118. PubMed PMID: 19293308; PubMed Central PMCID: PMC2793271.
223. Kissick HT, Sanda MG, Dunn LK, Pellegrini KL, On ST, Noel JK, et al. Androgens alter T-cell immunity by inhibiting T-helper 1 differentiation. Proc Natl Acad Sci U S A. 2014;111(27):9887-92. Epub 2014/06/25. doi: 10.1073/pnas.1402468111. PubMed PMID: 24958858; PubMed Central PMCID: PMC4103356.
224. Ben-Batalla I, Vargas-Delgado ME, von Amsberg G, Janning M, Loges S. Influence of Androgens on Immunity to Self and Foreign: Effects on Immunity and Cancer. Front Immunol. 2020;11:1184. Epub 20200702. doi: 10.3389/fimmu.2020.01184. PubMed PMID: 32714315; PubMed Central PMCID: PMC7346249.
225. Trigunaite A, Dimo J, Jørgensen TN. Suppressive effects of androgens on the immune system. Cell Immunol. 2015;294(2):87-94. Epub 20150214. doi: 10.1016/j.cellimm.2015.02.004. PubMed PMID: 25708485.
226. Kwon H, Schafer JM, Song NJ, Kaneko S, Li A, Xiao T, et al. Androgen conspires with the CD8(+) T cell exhaustion program and contributes to sex bias in cancer. Sci Immunol. 2022;7(73):eabq2630. Epub 20220701. doi: 10.1126/sciimmunol.abq2630. PubMed PMID: 35420889; PubMed Central PMCID: PMC9374385.
227. Yang C, Jin J, Yang Y, Sun H, Wu L, Shen M, et al. Androgen receptor-mediated CD8(+) T cell stemness programs drive sex differences in antitumor immunity. Immunity.

2022;55(7):1268-83.e9. Epub 20220613. doi: 10.1016/j.immuni.2022.05.012. PubMed PMID: 35700739.
228. Sugimoto K, Maekawa Y, Kitamura A, Nishida J, Koyanagi A, Yagita H, et al. Notch2 signaling is required for potent antitumor immunity in vivo. J Immunol. 2010;184(9):4673-8. Epub 20100329. doi: 10.4049/jimmunol.0903661. PubMed PMID: 20351182.
229. De Gendt K, Swinnen JV, Saunders PT, Schoonjans L, Dewerchin M, Devos A, et al. A Sertoli cell-selective knockout of the androgen receptor causes spermatogenic arrest in meiosis. Proc Natl Acad Sci U S A. 2004;101(5):1327-32. Epub 2004/01/28. doi: 10.1073/pnas.0308114100. PubMed PMID: 14745012; PubMed Central PMCID: PMC337052.
230. Thompson LJ, Kolumam GA, Thomas S, Murali-Krishna K. Innate inflammatory signals induced by various pathogens differentially dictate the IFN-I dependence of CD8 T cells for clonal expansion and memory formation. J Immunol. 2006;177(3):1746-54. doi: 10.4049/jimmunol.177.3.1746. PubMed PMID: 16849484.
231. Martin MD, Badovinac VP. Defining Memory CD8 T Cell. Front Immunol. 2018;9:2692. Epub 20181120. doi: 10.3389/fimmu.2018.02692. PubMed PMID: 30515169; PubMed Central PMCID: PMC6255921.
232. Khanolkar A, Williams MA, Harty JT. Antigen experience shapes phenotype and function of memory Th1 cells. PLoS One. 2013;8(6):e65234. Epub 20130607. doi: 10.1371/journal.pone.0065234. PubMed PMID: 23762323; PubMed Central PMCID: PMC3676405.
233. Keppler SJ, Aichele P. Signal 3 requirement for memory CD8+ T-cell activation is determined by the infectious pathogen. Eur J Immunol. 2011;41(11):3176-86. Epub 20110926. doi: 10.1002/eji.201141537. PubMed PMID: 21830209.
234. Pace L. Temporal and Epigenetic Control of Plasticity and Fate Decision during CD8(+) T-Cell Memory Differentiation. Cold Spring Harb Perspect Biol. 2021;13(12). Epub 20211201. doi: 10.1101/cshperspect.a037754. PubMed PMID: 33972365; PubMed Central PMCID: PMC8635004.
235. Henning AN, Roychoudhuri R, Restifo NP. Epigenetic control of CD8(+) T cell differentiation. Nat Rev Immunol. 2018;18(5):340-56. Epub 20180130. doi: 10.1038/nri.2017.146. PubMed PMID: 29379213; PubMed Central PMCID: PMC6327307.
236. Penna C, Mercurio V, Tocchetti CG, Pagliaro P. Sex-related differences in COVID-19 lethality. Br J Pharmacol. 2020;177(19):4375-85. Epub 20200805. doi: 10.1111/bph.15207. PubMed PMID: 32698249; PubMed Central PMCID: PMC7405496.
237. Izumi K, Fang LY, Mizokami A, Namiki M, Li L, Lin WJ, et al. Targeting the androgen receptor with siRNA promotes prostate cancer metastasis through enhanced macrophage recruitment via CCL2/CCR2-induced STAT3 activation. EMBO Mol Med. 2013;5(9):1383-401. Epub 2013/08/29. doi: 10.1002/emmm.201202367. PubMed PMID: 23982944; PubMed Central PMCID: PMC3799493.
238. Mohammed H, Taylor C, Brown GD, Papachristou EK, Carroll JS, D'Santos CS. Rapid immunoprecipitation mass spectrometry of endogenous proteins (RIME) for analysis of chromatin complexes. Nat Protoc. 2016;11(2):316-26. Epub 20160121. doi: 10.1038/nprot.2016.020. PubMed PMID: 26797456.
239. Karantanos T, Corn PG, Thompson TC. Prostate cancer progression after androgen deprivation therapy: mechanisms of castrate resistance and novel therapeutic approaches. Oncogene. 2013;32(49):5501-11. Epub 20130610. doi: 10.1038/onc.2013.206. PubMed PMID: 23752182; PubMed Central PMCID: PMC3908870.

240. Han C, Deng Y, Xu W, Liu Z, Wang T, Wang S, et al. The Roles of Tumor-Associated Macrophages in Prostate Cancer. J Oncol. 2022;2022:8580043. Epub 20220907. doi: 10.1155/2022/8580043. PubMed PMID: 36117852; PubMed Central PMCID: PMC9473905.

241. Xu P, Yang JC, Chen B, Nip C, Van Dyke JE, Zhang X, et al. Androgen receptor blockade resistance with enzalutamide in prostate cancer results in immunosuppressive alterations in the tumor immune microenvironment. J Immunother Cancer. 2023;11(5). doi: 10.1136/jitc-2022-006581. PubMed PMID: 37147019; PubMed Central PMCID: PMC10163595.

242. Jiang Y, Li Y, Zhu B. T-cell exhaustion in the tumor microenvironment. Cell Death Dis. 2015;6(6):e1792. Epub 20150618. doi: 10.1038/cddis.2015.162. PubMed PMID: 26086965; PubMed Central PMCID: PMC4669840.

243. Roden AC, Moser MT, Tri SD, Mercader M, Kuntz SM, Dong H, et al. Augmentation of T cell levels and responses induced by androgen deprivation. J Immunol. 2004;173(10):6098-108. Epub 2004/11/06. doi: 10.4049/jimmunol.173.10.6098. PubMed PMID: 15528346.

244. Yuri P, Shigemura K, Kitagawa K, Hadibrata E, Risan M, Zulfiqqar A, et al. Increased tumor-associated macrophages in the prostate cancer microenvironment predicted patients' survival and responses to androgen deprivation therapies in Indonesian patients cohort. Prostate Int. 2020;8(2):62-9. Epub 20200210. doi: 10.1016/j.prnil.2019.12.001. PubMed PMID: 32647642; PubMed Central PMCID: PMC7335973.

245. Consiglio CR, Udartseva O, Ramsey KD, Bush C, Gollnick SO. Enzalutamide, an Androgen Receptor Antagonist, Enhances Myeloid Cell-Mediated Immune Suppression and Tumor Progression. Cancer Immunol Res. 2020;8(9):1215-27. Epub 2020/07/15. doi: 10.1158/2326-6066.Cir-19-0371. PubMed PMID: 32661092; PubMed Central PMCID: PMC7484281.

246. Mercader M, Sengupta S, Bodner BK, Manecke RG, Cosar EF, Moser MT, et al. Early effects of pharmacological androgen deprivation in human prostate cancer. BJU Int. 2007;99(1):60-7. doi: 10.1111/j.1464-410X.2007.06538.x. PubMed PMID: 17227493.

247. Montoro DT, Haber AL, Biton M, Vinarsky V, Lin B, Birket SE, et al. A revised airway epithelial hierarchy includes CFTR-expressing ionocytes. Nature. 2018;560(7718):319-24. Epub 20180801. doi: 10.1038/s41586-018-0393-7. PubMed PMID: 30069044; PubMed Central PMCID: PMC6295155.

248. Henry GH, Malewska A, Joseph DB, Malladi VS, Lee J, Torrealba J, et al. A Cellular Anatomy of the Normal Adult Human Prostate and Prostatic Urethra. Cell Rep. 2018;25(12):3530-42.e5. doi: 10.1016/j.celrep.2018.11.086. PubMed PMID: 30566875; PubMed Central PMCID: PMC6411034.

249. Korentzelos D, Wells A, Clark AM. Interferon-γ increases sensitivity to chemotherapy and provides immunotherapy targets in models of metastatic castration-resistant prostate cancer. Sci Rep. 2022;12(1):6657. Epub 20220422. doi: 10.1038/s41598-022-10724-9. PubMed PMID: 35459800; PubMed Central PMCID: PMC9033763.

250. Gillespie M, Jassal B, Stephan R, Milacic M, Rothfels K, Senff-Ribeiro A, et al. The reactome pathway knowledgebase 2022. Nucleic Acids Res. 2022;50(D1):D687-d92. doi: 10.1093/nar/gkab1028. PubMed PMID: 34788843; PubMed Central PMCID: PMC8689983.

251. Bander NH, Yao D, Liu H, Chen YT, Steiner M, Zuccaro W, et al. MHC class I and II expression in prostate carcinoma and modulation by interferon-alpha and -gamma. Prostate. 1997;33(4):233-9. doi: 10.1002/(sici)1097-0045(19971201)33:4<233::aid-pros2>3.0.co;2-i. PubMed PMID: 9397194.

252. He Y, Wang L, Wei T, Xiao YT, Sheng H, Su H, et al. FOXA1 overexpression suppresses interferon signaling and immune response in cancer. J Clin Invest. 2021;131(14). doi: 10.1172/jci147025. PubMed PMID: 34101624; PubMed Central PMCID: PMC8279591.
253. Lugano R, Ramachandran M, Dimberg A. Tumor angiogenesis: causes, consequences, challenges and opportunities. Cell Mol Life Sci. 2020;77(9):1745-70. Epub 20191106. doi: 10.1007/s00018-019-03351-7. PubMed PMID: 31690961; PubMed Central PMCID: PMC7190605.
254. van Moorselaar RJ, Voest EE. Angiogenesis in prostate cancer: its role in disease progression and possible therapeutic approaches. Mol Cell Endocrinol. 2002;197(1-2):239-50. doi: 10.1016/s0303-7207(02)00262-9. PubMed PMID: 12431818.
255. Sfanos KS, De Marzo AM. Prostate cancer and inflammation: the evidence. Histopathology. 2012;60(1):199-215. doi: 10.1111/j.1365-2559.2011.04033.x. PubMed PMID: 22212087; PubMed Central PMCID: PMC4029103.
256. Yang L, Lin PC. Mechanisms that drive inflammatory tumor microenvironment, tumor heterogeneity, and metastatic progression. Semin Cancer Biol. 2017;47:185-95. Epub 20170803. doi: 10.1016/j.semcancer.2017.08.001. PubMed PMID: 28782608; PubMed Central PMCID: PMC5698110.
257. Greten FR, Grivennikov SI. Inflammation and Cancer: Triggers, Mechanisms, and Consequences. Immunity. 2019;51(1):27-41. doi: 10.1016/j.immuni.2019.06.025. PubMed PMID: 31315034; PubMed Central PMCID: PMC6831096.
258. Zhang Y, Zheng D, Zhou T, Song H, Hulsurkar M, Su N, et al. Androgen deprivation promotes neuroendocrine differentiation and angiogenesis through CREB-EZH2-TSP1 pathway in prostate cancers. Nat Commun. 2018;9(1):4080. Epub 20181004. doi: 10.1038/s41467-018-06177-2. PubMed PMID: 30287808; PubMed Central PMCID: PMC6172226.
259. Melegh Z, Oltean S. Targeting Angiogenesis in Prostate Cancer. Int J Mol Sci. 2019;20(11). Epub 20190531. doi: 10.3390/ijms20112676. PubMed PMID: 31151317; PubMed Central PMCID: PMC6600172.
260. Sfanos KS, Yegnasubramanian S, Nelson WG, De Marzo AM. The inflammatory microenvironment and microbiome in prostate cancer development. Nat Rev Urol. 2018;15(1):11-24. Epub 20171031. doi: 10.1038/nrurol.2017.167. PubMed PMID: 29089606.
261. Deep G, Panigrahi GK. Hypoxia-Induced Signaling Promotes Prostate Cancer Progression: Exosomes Role as Messenger of Hypoxic Response in Tumor Microenvironment. Crit Rev Oncog. 2015;20(5-6):419-34. doi: 10.1615/CritRevOncog.v20.i5-6.130. PubMed PMID: 27279239; PubMed Central PMCID: PMC5308872.
262. Deonarine K, Panelli MC, Stashower ME, Jin P, Smith K, Slade HB, et al. Gene expression profiling of cutaneous wound healing. J Transl Med. 2007;5:11. Epub 20070221. doi: 10.1186/1479-5876-5-11. PubMed PMID: 17313672; PubMed Central PMCID: PMC1804259.
263. Jin S, Guerrero-Juarez CF, Zhang L, Chang I, Ramos R, Kuan CH, et al. Inference and analysis of cell-cell communication using CellChat. Nat Commun. 2021;12(1):1088. Epub 20210217. doi: 10.1038/s41467-021-21246-9. PubMed PMID: 33597522; PubMed Central PMCID: PMC7889871.
264. Bolitho C, Moscova M, Baxter RC, Marsh DJ. Amphiregulin increases migration and proliferation of epithelial ovarian cancer cells by inducing its own expression via PI3-kinase signaling. Mol Cell Endocrinol. 2021;533:111338. Epub 20210529. doi: 10.1016/j.mce.2021.111338. PubMed PMID: 34062166.

265. Wang S, Zhang Y, Wang Y, Ye P, Li J, Li H, et al. Amphiregulin Confers Regulatory T Cell Suppressive Function and Tumor Invasion via the EGFR/GSK-3β/Foxp3 Axis. J Biol Chem. 2016;291(40):21085-95. Epub 20160718. doi: 10.1074/jbc.M116.717892. PubMed PMID: 27432879; PubMed Central PMCID: PMC5076518.
266. Imada A, Shijubo N, Kojima H, Abe S. Mast cells correlate with angiogenesis and poor outcome in stage I lung adenocarcinoma. Eur Respir J. 2000;15(6):1087-93. doi: 10.1034/j.1399-3003.2000.01517.x. PubMed PMID: 10885428.
267. Wroblewski M, Bauer R, Cubas Córdova M, Udonta F, Ben-Batalla I, Legler K, et al. Mast cells decrease efficacy of anti-angiogenic therapy by secreting matrix-degrading granzyme B. Nat Commun. 2017;8(1):269. Epub 20170816. doi: 10.1038/s41467-017-00327-8. PubMed PMID: 28814715; PubMed Central PMCID: PMC5559596.
268. Shibuya M. Vascular Endothelial Growth Factor (VEGF) and Its Receptor (VEGFR) Signaling in Angiogenesis: A Crucial Target for Anti- and Pro-Angiogenic Therapies. Genes Cancer. 2011;2(12):1097-105. doi: 10.1177/1947601911423031. PubMed PMID: 22866201; PubMed Central PMCID: PMC3411125.
269. Zaiss DMW, Gause WC, Osborne LC, Artis D. Emerging functions of amphiregulin in orchestrating immunity, inflammation, and tissue repair. Immunity. 2015;42(2):216-26. doi: 10.1016/j.immuni.2015.01.020. PubMed PMID: 25692699; PubMed Central PMCID: PMC4792035.
270. Stuart T, Butler A, Hoffman P, Hafemeister C, Papalexi E, Mauck WM, 3rd, et al. Comprehensive Integration of Single-Cell Data. Cell. 2019;177(7):1888-902.e21. Epub 20190606. doi: 10.1016/j.cell.2019.05.031. PubMed PMID: 31178118; PubMed Central PMCID: PMC6687398.
271. Young MD, Behjati S. SoupX removes ambient RNA contamination from droplet-based single-cell RNA sequencing data. Gigascience. 2020;9(12). doi: 10.1093/gigascience/giaa151. PubMed PMID: 33367645; PubMed Central PMCID: PMC7763177.
272. McGinnis CS, Murrow LM, Gartner ZJ. DoubletFinder: Doublet Detection in Single-Cell RNA Sequencing Data Using Artificial Nearest Neighbors. Cell Syst. 2019;8(4):329-37.e4. Epub 20190403. doi: 10.1016/j.cels.2019.03.003. PubMed PMID: 30954475; PubMed Central PMCID: PMC6853612.
273. Korsunsky I, Millard N, Fan J, Slowikowski K, Zhang F, Wei K, et al. Fast, sensitive and accurate integration of single-cell data with Harmony. Nat Methods. 2019;16(12):1289-96. Epub 20191118. doi: 10.1038/s41592-019-0619-0. PubMed PMID: 31740819; PubMed Central PMCID: PMC6884693.
274. Song H, Weinstein HNW, Allegakoen P, Wadsworth MH, 2nd, Xie J, Yang H, et al. Single-cell analysis of human primary prostate cancer reveals the heterogeneity of tumor-associated epithelial cell states. Nat Commun. 2022;13(1):141. Epub 20220110. doi: 10.1038/s41467-021-27322-4. PubMed PMID: 35013146; PubMed Central PMCID: PMC8748675.
275. Mauvais-Jarvis F, Bairey Merz N, Barnes PJ, Brinton RD, Carrero JJ, DeMeo DL, et al. Sex and gender: modifiers of health, disease, and medicine. Lancet. 2020;396(10250):565-82. doi: 10.1016/s0140-6736(20)31561-0. PubMed PMID: 32828189; PubMed Central PMCID: PMC7440877.
276. Carrette F, Surh CD. IL-7 signaling and CD127 receptor regulation in the control of T cell homeostasis. Semin Immunol. 2012;24(3):209-17. Epub 20120501. doi: 10.1016/j.smim.2012.04.010. PubMed PMID: 22551764; PubMed Central PMCID: PMC3367861.

277. Proekt I, Miller CN, Lionakis MS, Anderson MS. Insights into immune tolerance from AIRE deficiency. Curr Opin Immunol. 2017;49:71-8. Epub 20171021. doi: 10.1016/j.coi.2017.10.003. PubMed PMID: 29065385; PubMed Central PMCID: PMC5705335.
278. Zhu ML, Bakhru P, Conley B, Nelson JS, Free M, Martin A, et al. Sex bias in CNS autoimmune disease mediated by androgen control of autoimmune regulator. Nat Commun. 2016;7:11350. Epub 20160413. doi: 10.1038/ncomms11350. PubMed PMID: 27072778; PubMed Central PMCID: PMC5512610.
279. Dragin N, Bismuth J, Cizeron-Clairac G, Biferi MG, Berthault C, Serraf A, et al. Estrogen-mediated downregulation of AIRE influences sexual dimorphism in autoimmune diseases. J Clin Invest. 2016;126(4):1525-37. Epub 20160321. doi: 10.1172/jci81894. PubMed PMID: 26999605; PubMed Central PMCID: PMC4811157.
280. Mariathasan S, Jones RG, Ohashi PS. Signals involved in thymocyte positive and negative selection. Semin Immunol. 1999;11(4):263-72. doi: 10.1006/smim.1999.0182. PubMed PMID: 10441212.
281. Huang Z, Chen B, Liu X, Li H, Xie L, Gao Y, et al. Effects of sex and aging on the immune cell landscape as assessed by single-cell transcriptomic analysis. Proc Natl Acad Sci U S A. 2021;118(33). doi: 10.1073/pnas.2023216118. PubMed PMID: 34385315; PubMed Central PMCID: PMC8379935.
282. Ribatti D, Crivellato E. Mast cells, angiogenesis, and tumour growth. Biochim Biophys Acta. 2012;1822(1):2-8. Epub 20101202. doi: 10.1016/j.bbadis.2010.11.010. PubMed PMID: 21130163.
283. Johansson A, Rudolfsson S, Hammarsten P, Halin S, Pietras K, Jones J, et al. Mast cells are novel independent prognostic markers in prostate cancer and represent a target for therapy. Am J Pathol. 2010;177(2):1031-41. Epub 20100708. doi: 10.2353/ajpath.2010.100070. PubMed PMID: 20616342; PubMed Central PMCID: PMC2913352.
284. Magnussen AL, Mills IG. Vascular normalisation as the stepping stone into tumour microenvironment transformation. Br J Cancer. 2021;125(3):324-36. Epub 20210407. doi: 10.1038/s41416-021-01330-z. PubMed PMID: 33828258; PubMed Central PMCID: PMC8329166.
285. Yates KB, Tonnerre P, Martin GE, Gerdemann U, Al Abosy R, Comstock DE, et al. Epigenetic scars of CD8(+) T cell exhaustion persist after cure of chronic infection in humans. Nat Immunol. 2021;22(8):1020-9. Epub 2021/07/28. doi: 10.1038/s41590-021-00979-1. PubMed PMID: 34312547; PubMed Central PMCID: PMC8600539.

Appendix I: Supplemental Figures

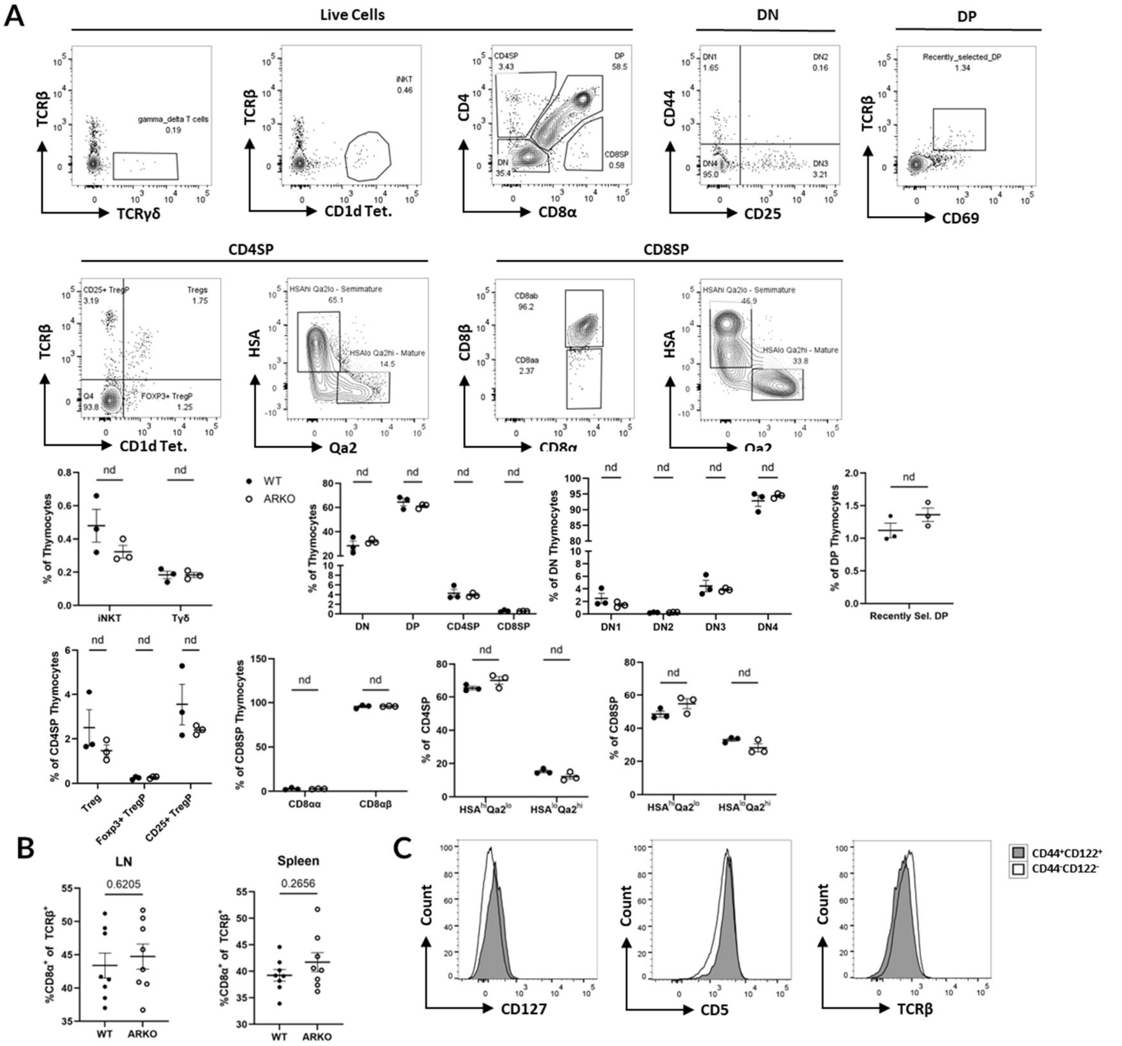

Supplemental Figure 1: ARKO mouse baseline phenotyping

(A) Example flow cytometry plots of thymocyte populations (top) and quantification of relative abundances of various thymocyte subsets (bottom). (B) Flow cytometric assessment of the frequency of CD8α+ T cells among TCRB+ cells in WT and ARKO male lymph nodes (LN) and spleens. (C) Comparison of naïve and virtual memory CD8 t cells from the same mouse, showing flow cytometric measurement of CD127, CD5, and TCRB expression.Mechanistically, in vitro models reveal AR cooperation with epigenetic modifying proteins, AR regulation of T cell epigenetic state, and repression of the expression of effector- and memory-associated genes.

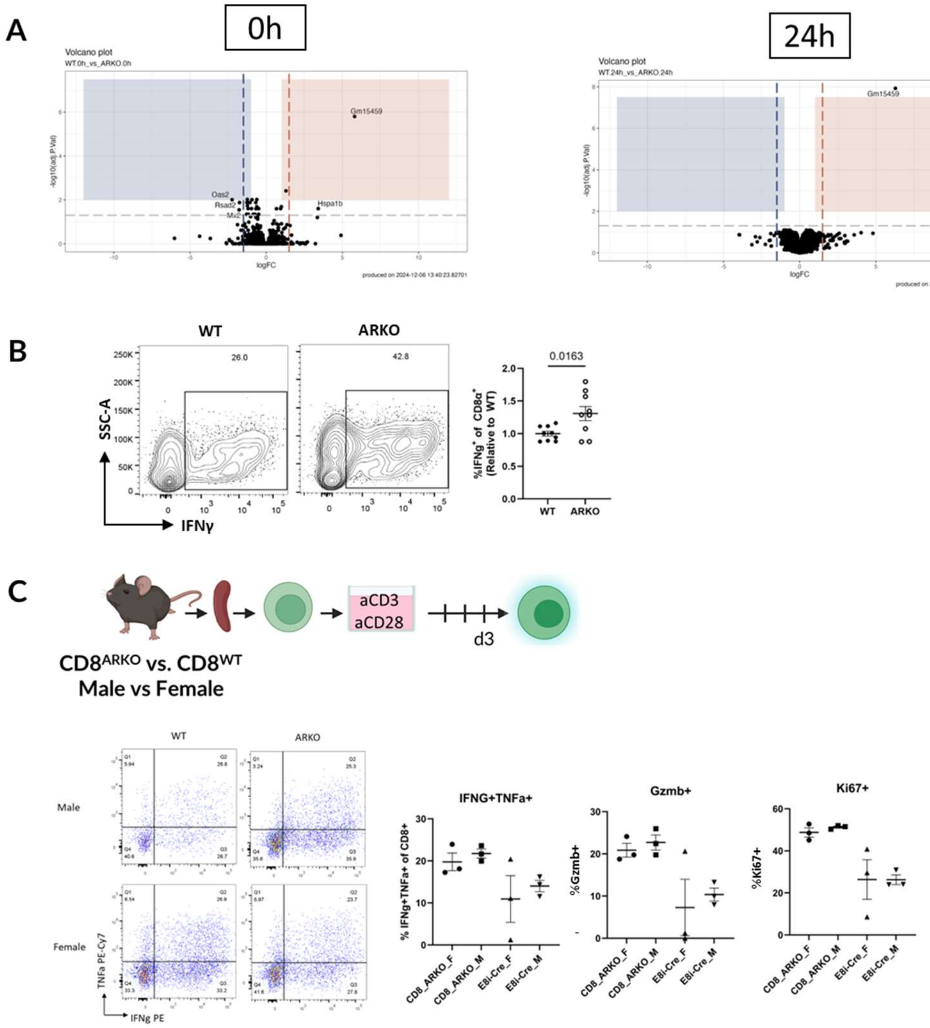

Supplemental Figure 2: Acute stimulation of WT versus ARKO CD8 T cells

(A) Volcano plots of DEGs between ARKO and WT mouse CD8 T cells 24 hours after in vitro stimulation with plate-bound anti-CD3 and anti-CD28. (B) Flow cytometric measurement of IFNγ and TNFα expression by male WT or ARKO CD8 T cells after three days in vitro with anti-CD3 and anti CD28 stimulation. Prior to permeabilization and staining, cells were re-stimulated with PMA/Ionomycin in the presence of brefeldin A for 4 hours. (C) Cells from male and female WT and ARKO mice were stimulated as described above and similarly assessed for cytokine and Ki67 expression on day 3 post-stimulation.

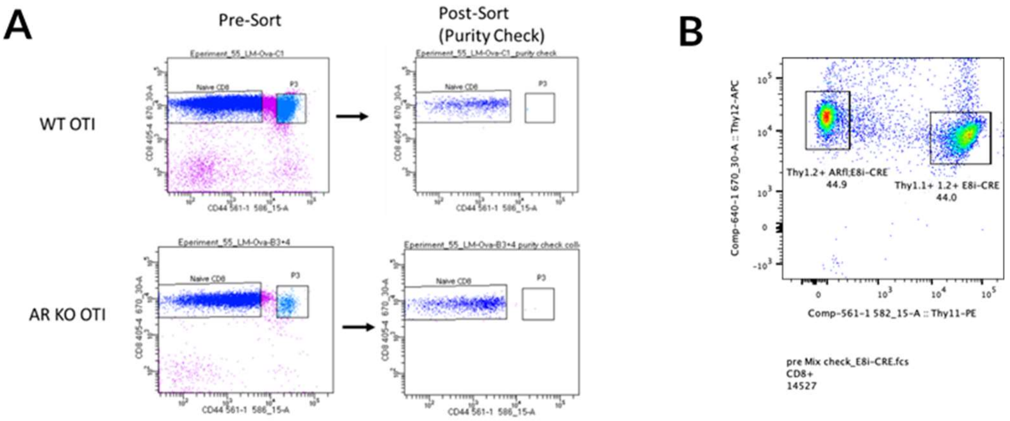

Supplemental Figure 3: FACS Sorting

(A) Flow cytometric purity test of sorted naïve OTI T cells used for adoptive transfers in figures 2 and 3. (B) Flow cytometric test of the mix ratio of WT and ARKO OTI cells mixed before adoptive transfer.

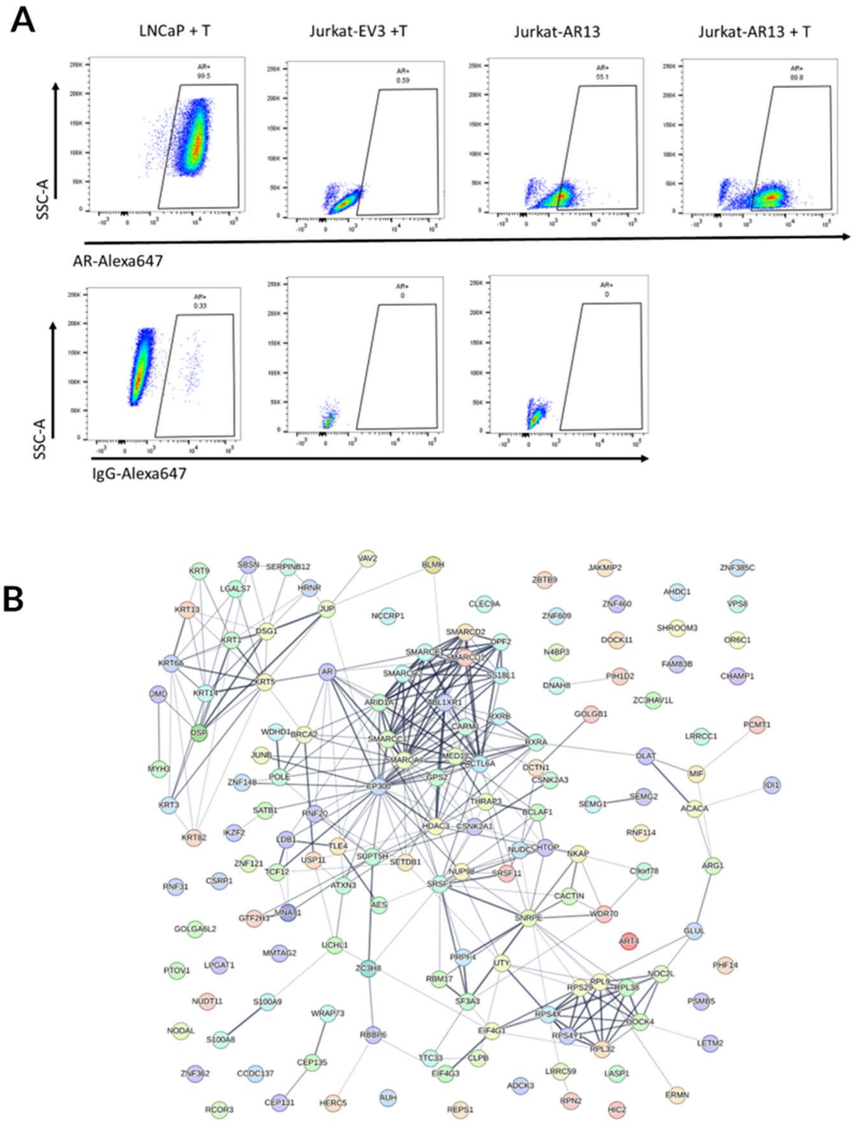

Supplemental Figure 4: Jurkat model validation and IP-MS

(A) Example flow cytometry staining for AR expression in LNCaP (human prostate cancer cells as positive control) and sub-clones of Jurkat-AR and Jurkat-EV cells. (B) StringDB network analysis of all proteins detected with net intensity >0 after pull-down with AR from two independent Jurkat-AR clones.

ARNSvEVNS

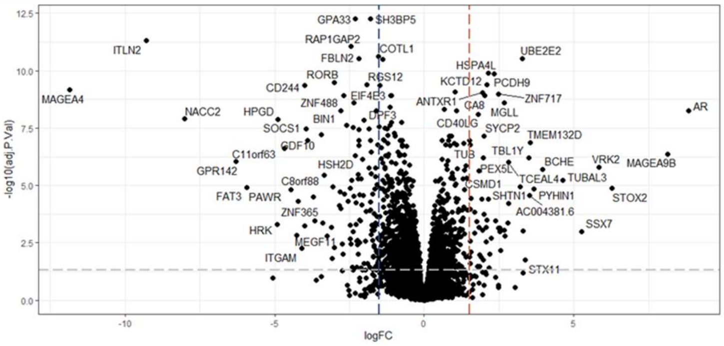

ARSvARNS

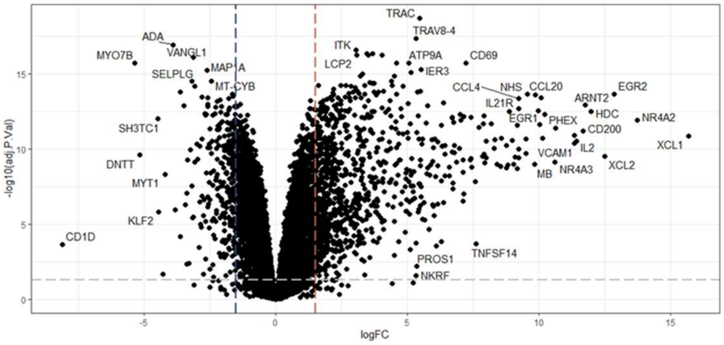

ARSvEVS

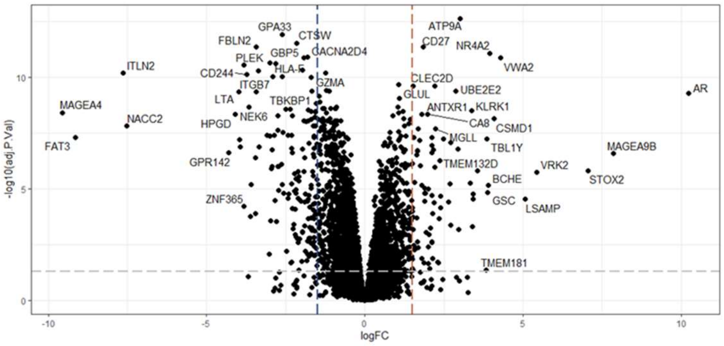

ARSRvARS

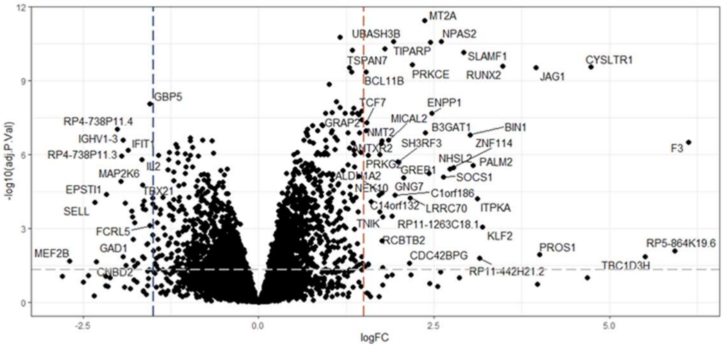

Supplemental Figure 5: Jurkat RNAseq DEG comparisons

Volcano plots of DEGs between paired conditions of Jurkat-AR and Jurkat-EV cells.

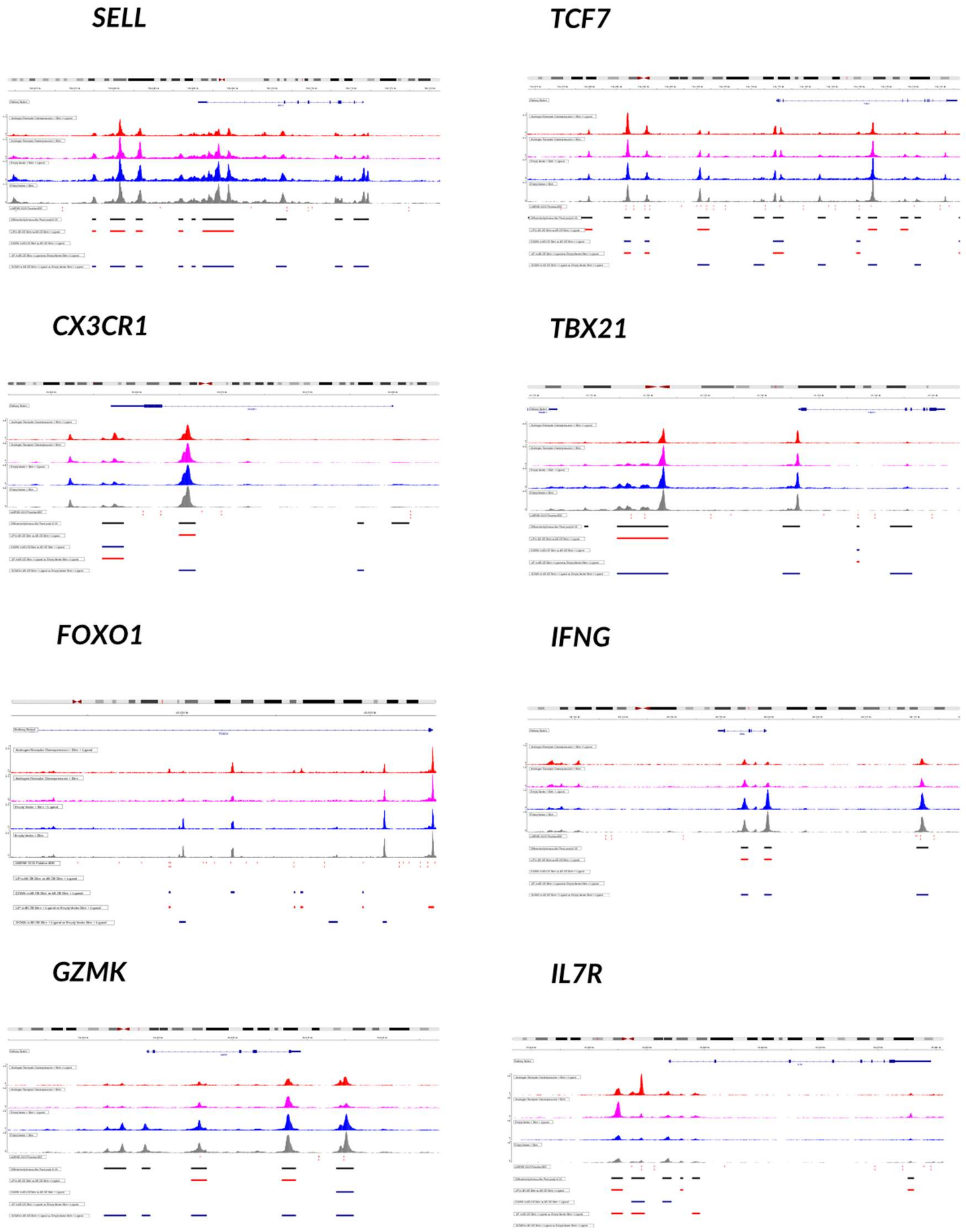

Supplemental Figure 6: Jurkat ATACseq selected gene tracks

Example genome tracks showing chromatin accessibility at regions of interest in the genome of Jurkat-AR and Jurkat-EV cells, including

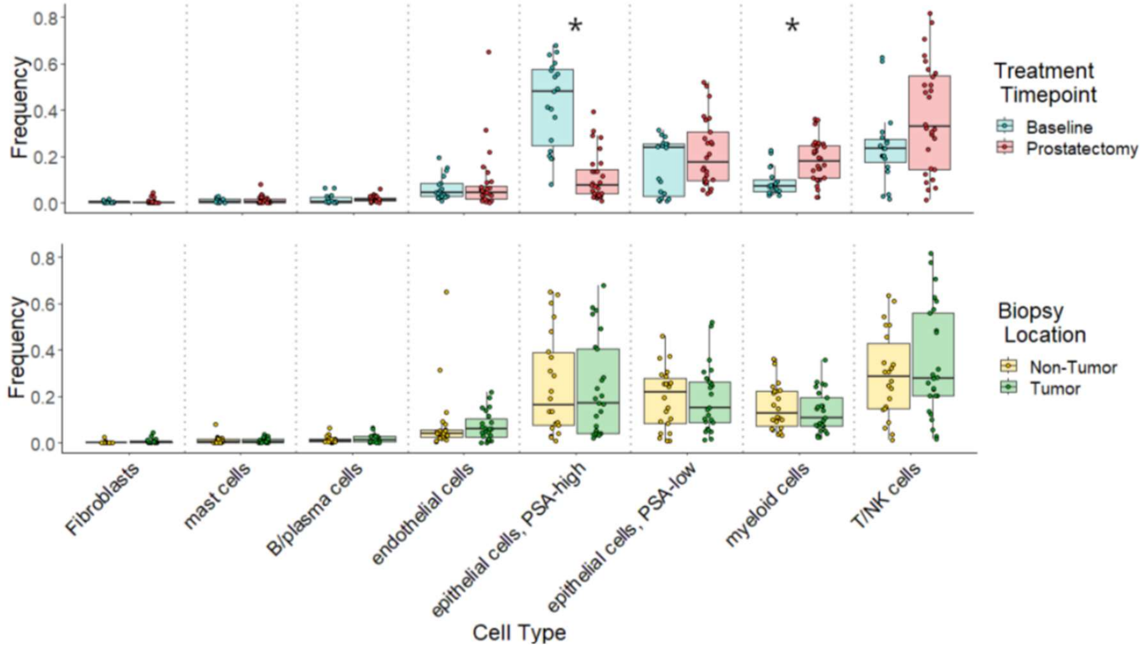

Supplemental Figure 7: Cell type proportions aggregated by tissue and time

Each of the 8 broadly identified cell types is represented by a set of boxes. Each sample is represented by a dot and aggregated by timepoint (top) or location (bottom). For time based aggregations samples aggregated at baseline are represented in blue and those aggregated at prostatectomy are represented in red. For location based comparison non-tumor and tumor aggregations are represented by yellow and green respectively. Asterisks (*) indicate significant difference (Wilcoxon rank-sum test, p

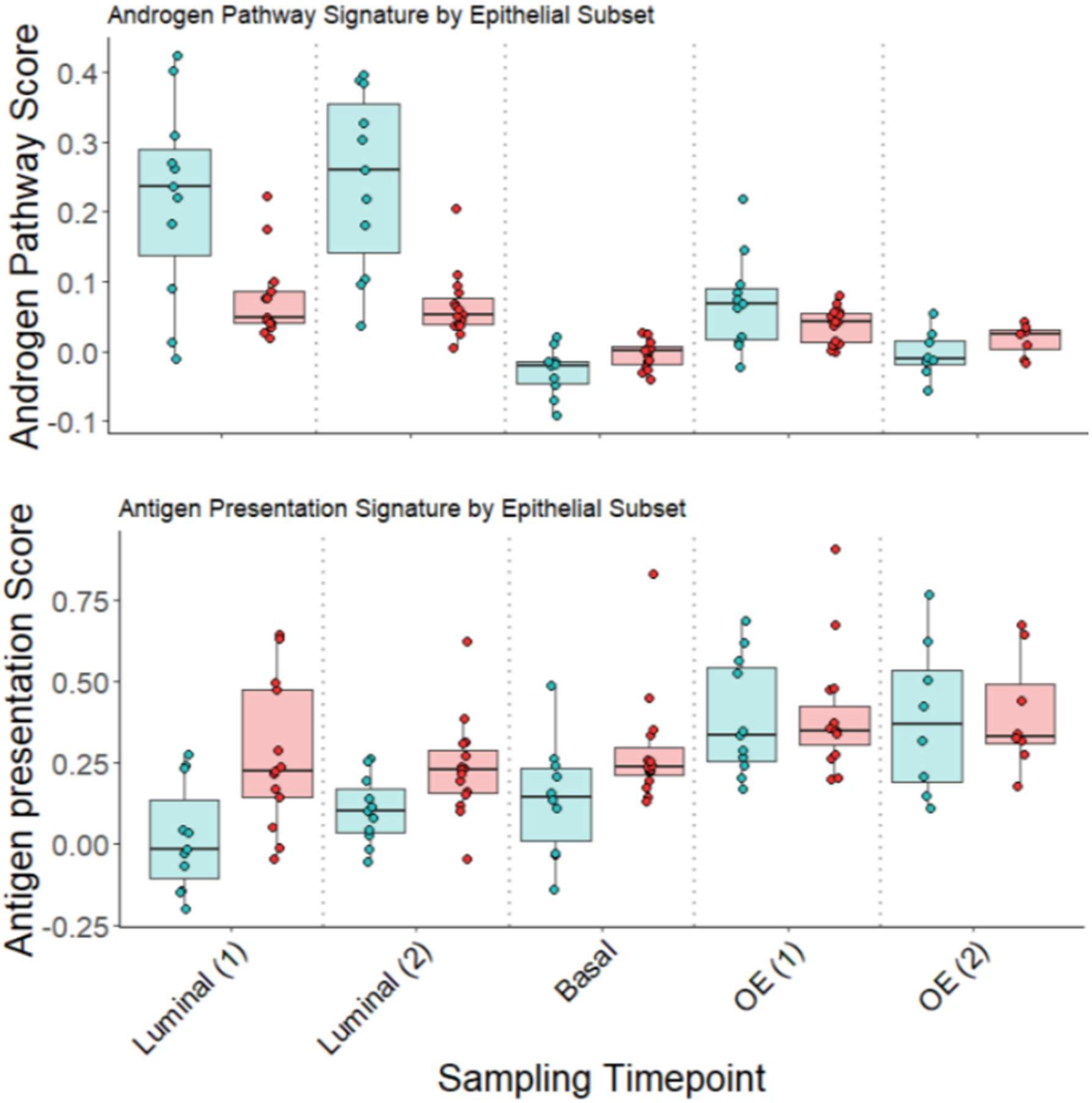

Supplemental Figure 8: Treatment based changes in androgen pathway and antigen presentation scores by epithelial sub group

Androgen pathway score (top) and antigen presentation score (bottom) are compared across baseline (blue) and prostatectomy (red) for each sub-population of epithelial cells.

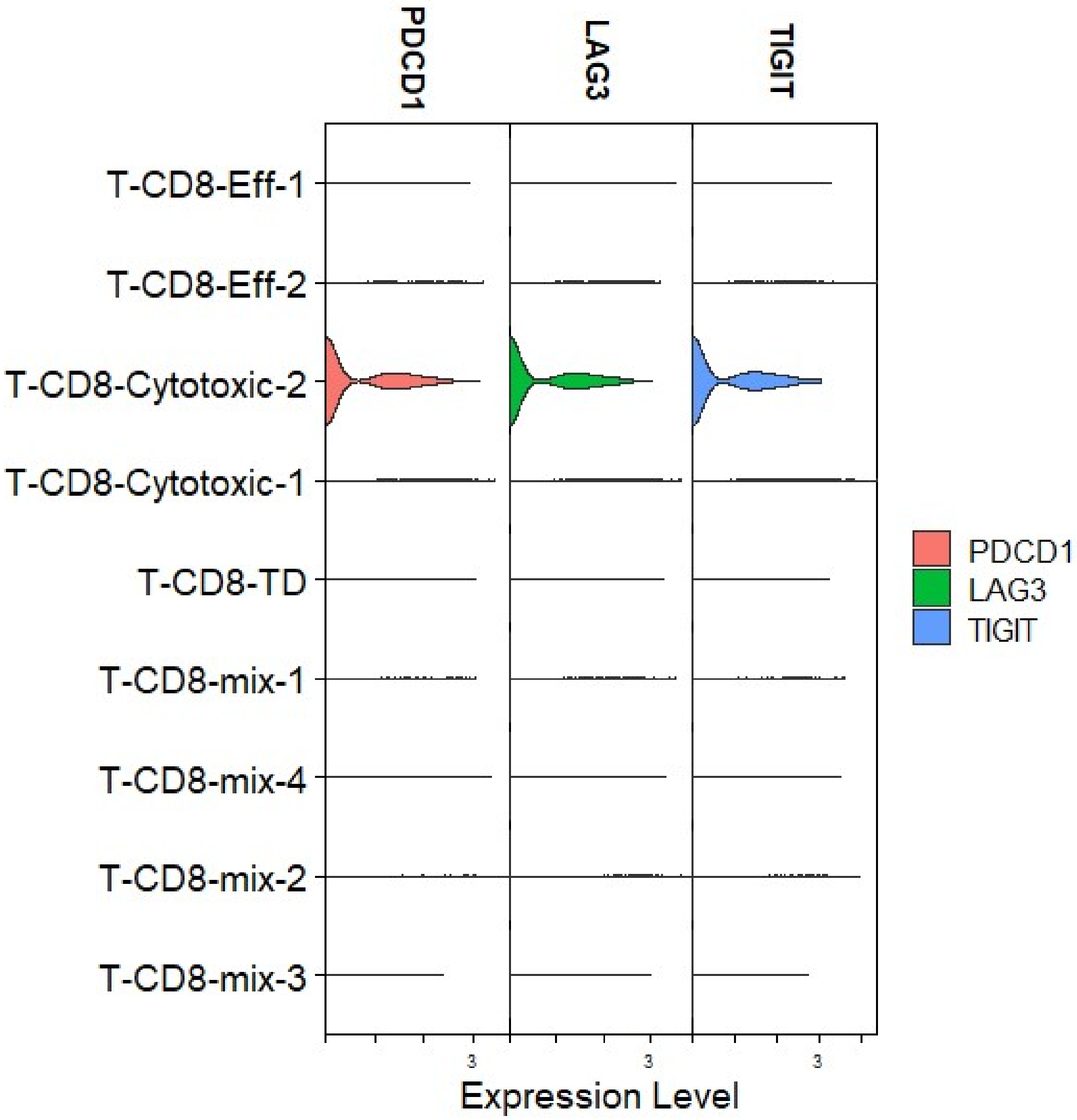

Supplemental Figure 9: CD8 T-cell expression of exhaustion markers

Y-axis shows each of the identified CD8 T-cell populations. X-axis represents normalized expression of each exhaustion-associated gene: PDCD1 (PD-1), LAG3, and TIGIT.

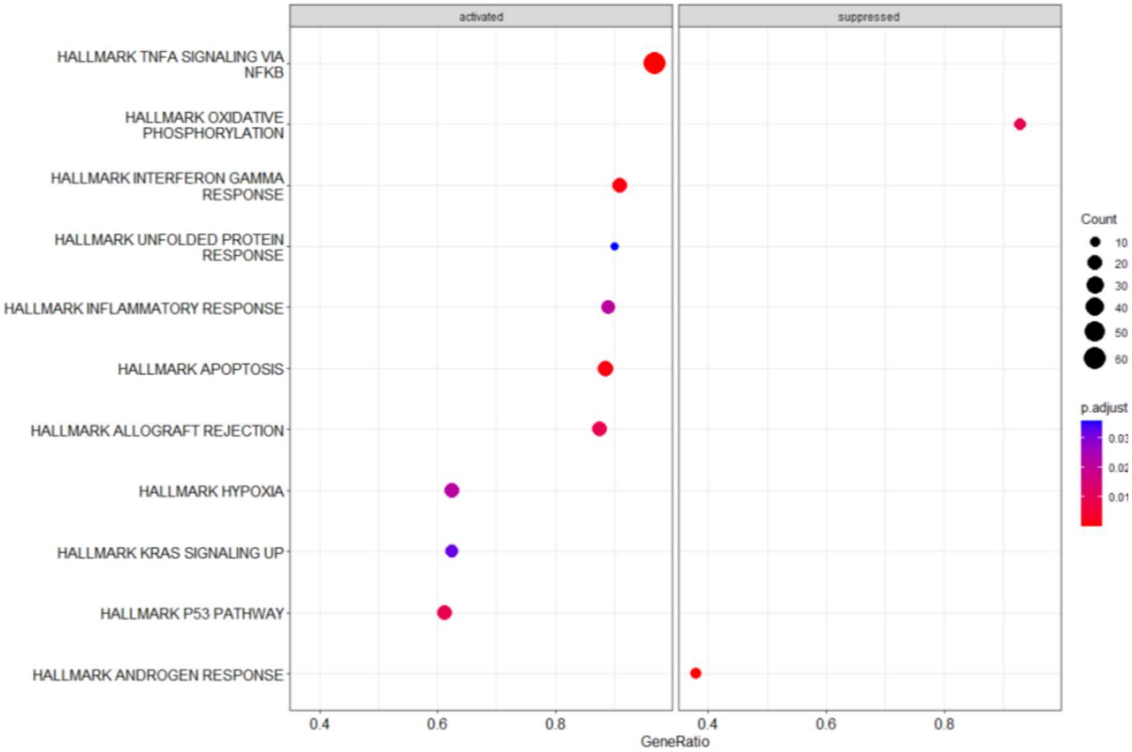

Supplemental Figure 10: Gene set enrichment analysis of hallmark pathways in pseudobulk tissue

Enrichment of hallmark pathways was assessed using differentially expressed genes identified through pseudobulk comparison of all cell types in aggregate between baseline and prostatectomy tissues.

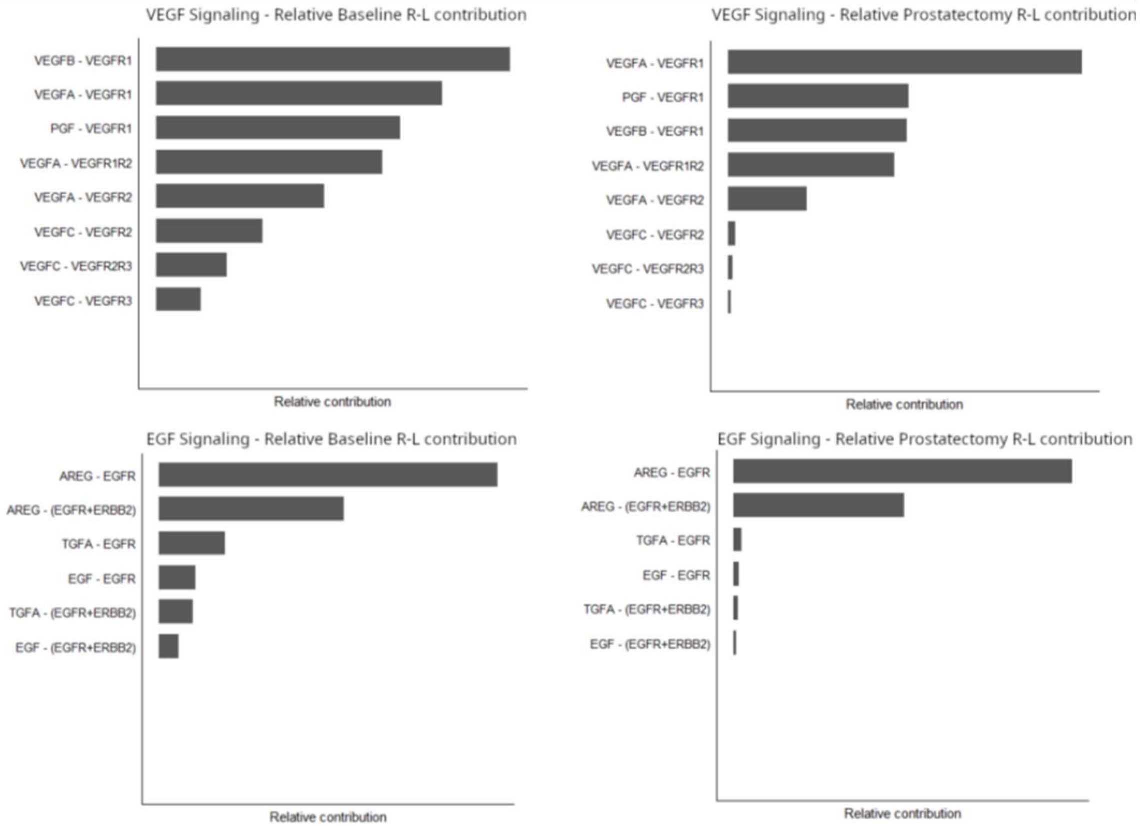

Supplemental Figure 11: Relative receptor-ligand contributions to pathway signaling

Receptor-ligand pairs (y-axes) active in VEGF signaling (top) and EGF signaling (bottom) are each represented by a bar. The relative size of bars within each plot represent the relative contribution of pairs within and not overall strength of receptor-ligand signaling. Left plots represent receptor-ligand pairs at baseline and right plots represent receptor-ligand pairs at prostatectomy.

Appendix II: Androgen receptor activity in T cells limits checkpoint blockade efficacy

I am a contributing author for the following manuscript that was published in *Nature* in 2022 and is being included here in an unedited form. My contributions to the manuscript include experimental design and analysis of mouse CD8 T cell *Ar* qPCR data and participating in the editing and peer review processes.

Androgen receptor activity in T cells limits checkpoint blockade efficacy

https://doi.org/10.1038/s41586-022-04522-6

Received: 12 August 2020

Accepted: 4 February 2022

Xiangnan Guan[1,2,10,12], Fanny Polesso[3,12], Chaojie Wang[3,11,12], Archana Sehrawat[3], Reed M. Hawkins[3], Susan E. Murray[2,4], George V. Thomas[5,6], Breanna Caruso[3], Reid F. Thompson[1,5,7,8], Mary A. Wood[8], Christina Hipfinger[3], Scott A. Hammond[9], Julie N. Graff[5,8], Zheng Xia[1,2,5,13] & Amy E. Moran[3,5,13] ✉

Immune checkpoint blockade has revolutionized the field of oncology, inducing durable anti-tumour immunity in solid tumours. In patients with advanced prostate cancer, immunotherapy treatments have largely failed[1–5]. Androgen deprivation therapy is classically administered in these patients to inhibit tumour cell growth, and we postulated that this therapy also affects tumour-associated T cells. Here we demonstrate that androgen receptor (AR) blockade sensitizes tumour-bearing hosts to effective checkpoint blockade by directly enhancing CD8 T cell function. Inhibition of AR activity in CD8 T cells prevented T cell exhaustion and improved responsiveness to PD-1 targeted therapy via increased IFNγ expression. AR bound directly to *Ifng* and eviction of AR with a small molecule significantly increased cytokine production in CD8 T cells. Together, our findings establish that T cell intrinsic AR activity represses IFNγ expression and represents a novel mechanism of immunotherapy resistance.

Sex-dependent differences in response to immunotherapy have been reported[6], and in metastatic castration-resistant prostate cancer (mCRPC), checkpoint blockade therapy has largely failed[1–5,7]. Despite evidence that androgens suppress T cell function and IFNγ production[8], it is unclear whether sex hormones can directly impact the effectiveness of T cell-targeted cancer immunotherapies. The mainstay of treatment for incurable prostate cancer is androgen deprivation therapy (ADT), which can be accomplished medically (GnRH agonists or antagonists) or surgically (bilateral orchiectomy), as well as by AR antagonists. Although therapy is intended to target tumour cells, T cells express sex hormone receptors including AR[9–11]. Since clinical response in cancer immunotherapy trials has been associated with a strong intratumour IFNγ signature before initiation of immunotherapy[12–14], we postulated that one mechanism of immunotherapy resistance could be through androgen-mediated repression of IFNγ. Notably, AR inhibition with PD-1 blockade (NCT02312557) (Extended Data Fig. 1a, b) resulted in a response rate of 18%, challenging the paradigm that immunotherapy would not work in patients with advanced prostate cancer[15,16]. This clinical response raised the possibility that AR inhibition had directly or indirectly enabled T cells to respond to PD-1 inhibition.

Immune landscape of mCRPC

We performed single-cell RNA sequencing (scRNA-seq) on cells isolated from eight individual metastatic tumour lesions from men with mCRPC who had biochemical or radiographic progression on enzalutamide prior to treatment with pembrolizumab. This included three responders and five non-responders, with response defined by a prostate-specific antigen (PSA) decline of > 25% upon immune checkpoint blockade (Extended Data Fig. 1b). Biopsies were obtained and tumour-infiltrating leukocytes (TILs) sorted (Extended Data Fig. 2a). We merged cells from all patients and clustered the data into tumour cell and major lymphoid and myeloid immune cell subsets (Fig. 1a, Extended Data Fig. 2b, c, Supplementary Table 1). Although responders and non-responders showed widespread heterogeneity (Extended Data Fig. 2c), there was no significant difference in CD4 T, CD8 T, natural killer (NK), B cell, or myeloid cell proportions or tumour mutational burden to explain the overall response to checkpoint therapy (Extended Data Figs. 1c, 2d). Consistent with other reports, all responders exhibited abundant CD8 T cells among total leukocytes[17,18] (Extended Data Fig. 2d). Two out of the five non-responders showed an abundance of CD8 T cells (Extended Data Fig. 2d), indicating that tumour-associated CD8 T cell abundance was insufficient to stratify responders from non-responders. We also noted the wide distribution of B cells and monocytes in non-responders compared to responders; an observation that is under further investigation.

Unsupervised clustering of all T and NK cells yielded three CD4 clusters, six CD8 clusters, and one NK cell cluster (Fig. 1b, c). Among the different subsets, responder lesions were enriched for CD8 T cells expressing genes associated with antigen encounter and dysfunction (C4 cluster, $P = 0.057$ two-tailed unpaired Student's t-test; Extended Data Fig. 2e) as noted by higher transcripts of *PDCD1*, *LAG3*, *HAVCR2*, *TIGIT* and *IFNG* (Fig. 1c, Extended Data Fig. 2f, Supplementary Table 2). Pathway analysis revealed enrichment of T cell receptor (TCR) signalling and PD-1 signalling in the C4 cluster (Extended Data Fig. 2g),

---

[1]Department of Biomedical Engineering, Oregon Health and Science University, Portland, OR, USA. [2]Molecular Microbiology and Immunology, Oregon Health and Science University, Portland, OR, USA. [3]Cell, Developmental and Cancer Biology, Oregon Health and Science University, Portland, OR, USA. [4]Department of Biology, University of Portland, Portland, OR, USA. [5]Knight Cancer Institute, Oregon Health and Science University, Portland, OR, USA. [6]Department of Pathology and Laboratory Medicine, Oregon Health and Science University, Portland, OR, USA. [7]Department of Radiation Medicine, Oregon Health and Science University, Portland, OR, USA. [8]VA Portland Health Care System, Portland, OR, USA. [9]Clinical IO Discovery, Oncology R&D, AstraZeneca, Gaithersburg, MD, USA. [10]Present address: Genentech, Inc., South San Francisco, CA, USA. [11]Present address: Bristol Myers Squibb, New Brunswick, NJ, USA. [12]These authors contributed equally: Xiangnan Guan, Fanny Polesso, Chaojie Wang. [13]These authors jointly supervised this work: Zheng Xia, Amy E. Moran. ✉e-mail: moranam@ohsu.edu

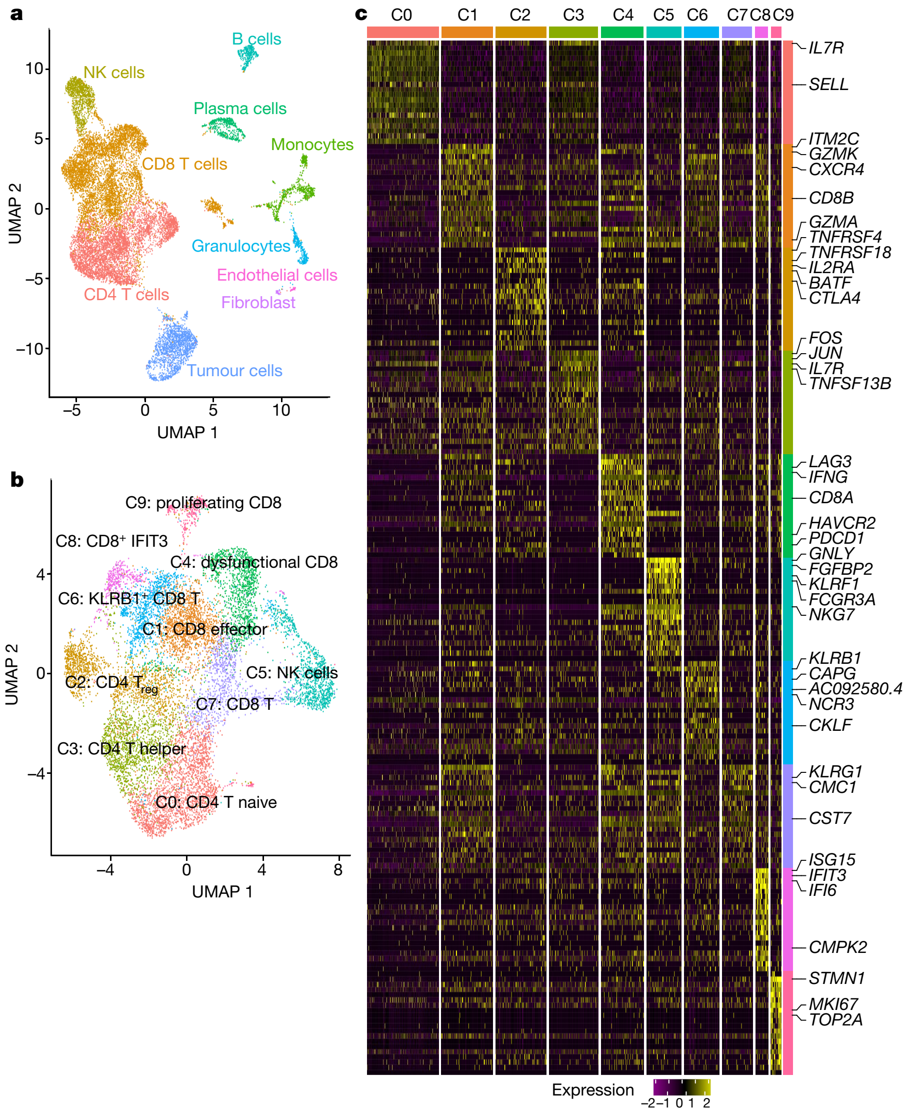

Fig. 1 | The immune landscape of tumours from patients with mCRPC prior to checkpoint therapy. a, Uniform manifold approximation and projection (UMAP) of all cells that passed quality control ($n = 16{,}044$ cells). Cells are coloured on the basis of cell type. **b**, UMAP of all T and NK cells collected in this study with cells coloured by cell type ($n = 12{,}073$ cells). **c**, Heat map showing scaled expression of the top 20 cell markers ranked by fold change in each cluster in **b**. Colours represent cell types as in **b**. A list of representative genes is shown on the right.

consistent with TCR signalling inducing transcripts shared by activated and exhausted CD8 T cells[19] (Extended Data Fig. 2h). Together, these data revealed multiple lymphocyte subsets in mCRPC lesions. To understand whether androgen signalling could limit immunotherapy efficacy, we focused our analysis on CD8 T cells because of their critical role in PD-1 targeted immunotherapy.

Unbiased CD8 T cell states

Given that two non-responder lesions were abundantly infiltrated with CD8 T cells, we considered whether a T cell intrinsic state correlated with response, as reported in non-prostate tumour studies[12–14]. Considering two therapeutic outcomes to PD-1 blockade, response or non-response, we performed unsupervised clustering of CD8 T cells from all eight patients to define two transcriptomic states (Fig. 2a). CD8 k1 cells (*k*-means cluster 1 CD8 T cells) had higher expression of inhibitory genes, and genes associated with cytotoxicity, and MHC II class, and CD8 k2 cells (*k*-means cluster 2 CD8 T cells) had increased expression of heat-shock genes (Fig. 2b, Supplementary Table 3). CD8 k2 cells also exhibited enhanced expression of *BTG1* and *BTG2* (Fig. 2b), which have been shown to be involved in the maintenance of T cell quiescence[20]. The unsupervised *k*-means clusters, CD8 k1 and CD8 k2, very closely overlapped with CD8 T cells from responders (CD8 R) and non-responders (CD8 NR) (Fig. 2c) in both cell-population and gene-expression profiles (Fig. 2b, d, Extended Data Fig. 3a, Supplementary Table 3). Furthermore, previously reported genes associated with a CD8 T cell state associated with response to PD-1 blockade (that is, *TOX*, *TCF7*, *FOXP1* and *BCL2*) were minimally expressed in CD8 k1 and CD8 R (Extended Data Fig. 3c, d). Although both CD8 T cell states existed in responders and non-responders, CD8 k1 cells were enriched in responder biopsies (Extended Data Fig. 3b). Importantly, similar to some non-responder lesions containing an abundance of CD8 T cells (Extended Data Fig. 2c, d), we also observed that some non-responder lesions contained CD8 k1 cells but failed to respond to PD-1 targeted therapy (Extended Data Fig. 3b). Notably, some non-responder lesions were enriched for monocytic cells (Extended Data Fig. 2c, d) compared with responders. CD4 T cells did not exhibit clear states that were associated with response (Extended Data Fig. 4a–c).

To define features associated with response in CD8 T cells, we computed differentially expressed genes between CD8 T cells from responders and

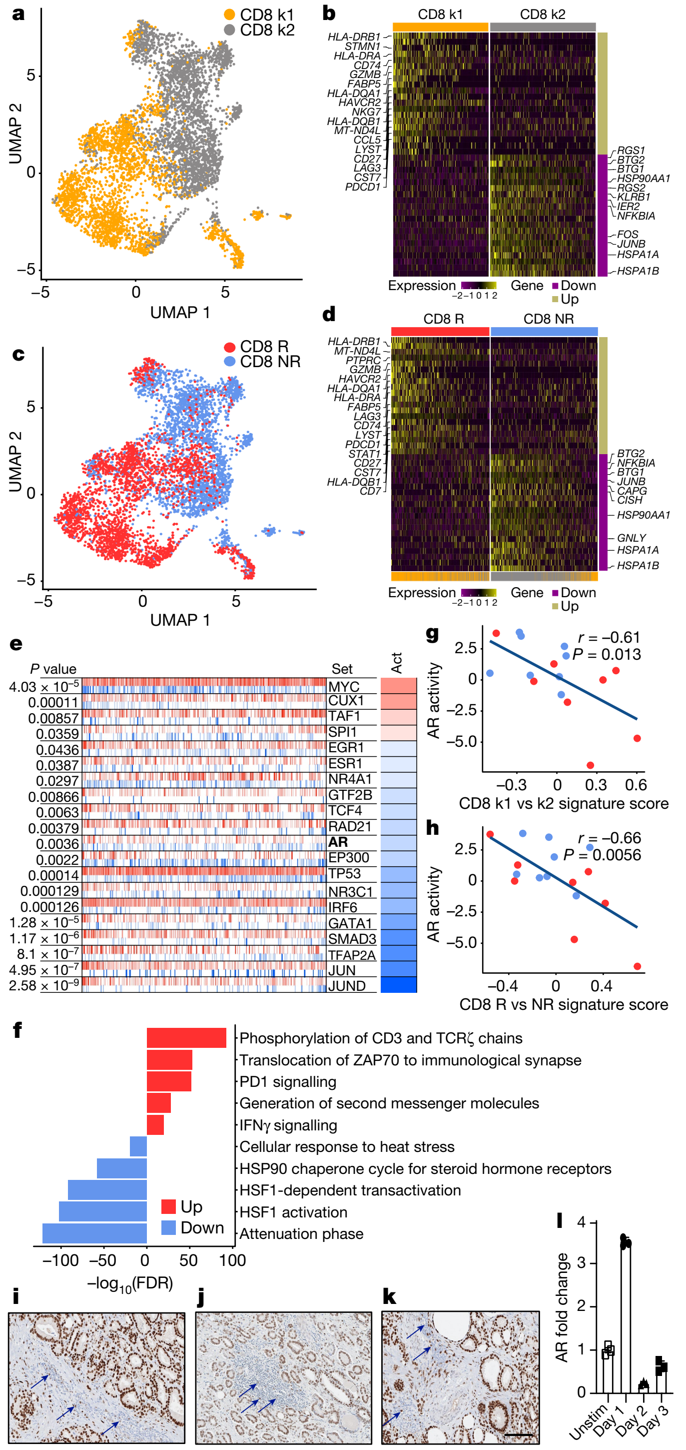

Fig. 2 | CD8 T cell signature associated with response implicates a functional role for AR. a, Unsupervised *k*-means clustering ($n = 5{,}664$ cells) of CD8 T cells. **b**, Scaled expression of top 20 differentially expressed genes ranked by fold change between CD8 k1 and CD8 k2 cells. **c**, UMAP plot showing CD8 T cells coloured by clinical response (CD8 R and CD8 NR) ($n = 5{,}664$ cells). **d**, Scaled expression of the top 20 differentially expressed genes ranked by fold change between CD8 R and CD8 NR T cells. **e**, Master regulator analysis to identify transcription factors whose activity is different between CD8 R and CD8 NR T cells. The top 20 transcription factors predicted to be most activated (red) or deactivated (blue) in CD8 R versus CD8 NR T cells. Tick marks depict targets of transcription factors that are positively (red) or negatively (blue) regulated. Act, inferred differential activity for each transcription factor. **f**, Pathway analysis of the top 10 molecular signatures distinguishing CD8 R versus CD8 NR T cells. **g**, **h**, Correlation between CD8 k1 versus CD8 k2 signature score (**g**) or CD8 R versus CD8 NR signature score (**h**) with AR activity in individual patients on our trial ($n = 16$ patients, from whom bulk RNA-seq but no single-cell RNA-seq data were available). Each dot represents data from 1 patient. Red, responder; blue, non-responder. Two-tailed Pearson correlation. **i**–**k**, Immunohistochemistry of AR in tumours from patients with treatment-naive prostate cancer, Gleason grades 4 + 3 (**i**), 3 + 3 (**j**) and 3 + 4 (**k**). Arrows indicate positive AR expression in immune cells. **l**, Kinetics of *AR* expression in purified human CD8 T cells after TCR stimulation. Individual data points represent technical replicates from one experiment. Data depict one representative experiment of two experiments; two donors of peripheral blood mononuclear cells (PBMC). Data are mean ± s.d. k1, *k*-means cluster 1; k2, *k*-means cluster 2.

non-responders (Fig. 2d, Supplementary Table 3) and performed master regulator (MR) analysis. This algorithm infers differentially activated transcription factors in a defined gene signature (that is, CD8 R versus CD8 NR) on the basis of the enrichment of each transcription factor's gene targets[21,22]. This analysis predicted the deactivation of multiple transcription factors, including AR, in responder CD8 T cells (Fig. 2e).

Next, we queried the biological processes enriched in CD8 T cells from responders versus non-responders. This analysis associated clinical PSA response with activation of pathways in CD8 T cells including TCR, PD-1 and IFNγ signalling (Fig. 2f). The increase in these pathways corresponded with the deactivation of the NR4A1 pathway (Fig. 2e), a transcription factor reported to limit the function of tumour-specific CD8 T cells and anti-PD-1 antibody targeted immunotherapy[23]. Resistance to PD-1 blockade was associated with an increase in the HSP90 steroid hormone receptor pathway (Fig. 2f), a chaperone protein that can facilitate AR function. Together, these data revealed distinct CD8 T cell states associated with response and resistance to PD-1 blockade and suggested that AR downregulation in CD8 T cells was correlated with improved function. To corroborate this hypothesis in an independent dataset, we derived a single-cell gene signature from differentially expressed genes between CD8 k1 and CD8 k2, or between CD8 R and CD8 NR and applied this to bulk RNA sequencing data from metastatic biopsies from patients. This approach revealed a negative correlation between single-cell signatures and AR signalling on the basis of either the CD8 k1 (Fig. 2g) or CD8 R cell states (Fig. 2h), which further suggested that favourable T cell signatures associated with low AR signalling, a state more likely to respond to PD-1 blockade.

Considering that our data suggested that AR signalling in CD8 T cells negatively correlated with cell function and response to immunotherapy, we evaluated whether there was evidence of lymphocytes expressing AR within biopsies from prostate cancer patients. In fact, in routine AR staining, we observed AR positive TILs in multiple patients including non-tumour tissue (Fig. 2i, j, k, Supplemental Fig. 1). Furthermore, *AR* mRNA was detectable in human CD8 T cells by quantitative PCR, and increased after TCR stimulation (Fig. 2l).

AR and PD-L1 blockade reduce tumours

Low AR activity in CD8 T cells appeared to contribute to effective PD-1/PD-L1 blockade in patients with prostate cancer. To determine whether AR perturbation with enzalutamide would enable effective PD-1 axis targeted therapy in mouse tumour models, we confirmed mouse CD8 T cells express *Ar* (Extended Data Fig. 5a), then implanted male mice subcutaneously with an ADT and anti-PD-1-resistant prostate tumour (*Pten*$^{-/-}$; *p53*$^{-/-}$; *Smad4*$^{-/-}$ PPSM)[24]. Following tumour initiation, mice either underwent surgical ADT or were left intact and were treated with enzalutamide and/or anti-PD-L1 antibodies (Fig. 3a). Although therapy with anti-PD-L1 antibody alone or ADT plus enzalutamide had a minimal effect on tumour growth, ADT plus enzalutamide with anti-PD-L1 antibodies led to significant tumour regression and

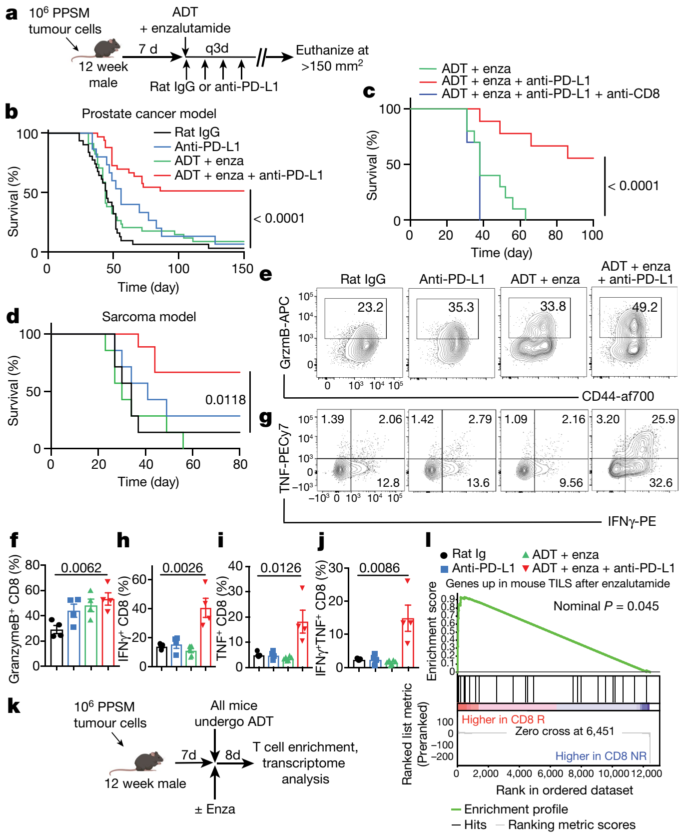

Fig. 3 | Dual inhibition of AR and PD-1/PD-L1 improves T cell function and overall survival in mouse tumour models. a, Experimental design for mouse tumour model (created with BioRender.com). q3d, dose given every three days. **b**, Survival curves of PPSM tumour-bearing mice treated as indicated. Data combined from 4 independent experiments, 8 to 10 mice per group per experiment. Enza, enzalutamide. **c**, Survival curves of PPSM tumour-bearing mice treated with combination therapy and anti-CD8 depleting antibody (10 mice per group). Data depict one representative experiment of two experiments. **d**, Survival curves of MCA-205 tumour-bearing mice treated as in **a**. Data depict one representative experiment of two experiments, 8 mice per group. **e**–**j**, PPSM tumour-bearing mice were treated as in **a** and tumours were collected the day after the third anti-PD-L1 antibody treatment. **e**, CD44 and granzyme B expression in CD8 TILs. **f**, Percentage of granzyme B^+ CD8 T cells. **g**, IFNγ and TNF expression in CD8 TILs. **h**–**j**, Percentage of $IFN\gamma^+$ (**h**), TNF^+ (**i**) and $IFN\gamma^+TNF^+$ (**j**) CD8 TILs. Data representative of three independent experiments; three mice per group. **k**, Experimental design (created with Biorender.com). **l**, GSEA illustrating the association of AR-inhibited genes in mouse TILs with CD8 R single-cell signature (nominal $P = 0.045$, nonparametric permutation test). Data are mean ± s.e.m.; log-rank (Mantel–Cox) test was used for **b**–**d**. Two-tailed unpaired Student *t*-test was used for **f** and **h**–**j**.

increased overall survival (Fig. 3b, Extended Data Fig. 5b, c). Similar synergy was observed in orthotopic PPSM tumours (Extended Data Fig. 5d). Anti-PD-L1 antibodies plus enzalutamide without ADT was not as effective as anti-PD-L1 antibodies plus enzalutamide with ADT (Extended Data Fig. 5e, f), suggesting that the functional perturbation of AR with enzalutamide together with reduced testosterone was critical for optimal effect. Of note, ADT alone had no effect on tumour growth (Extended Data Fig. 5g). Given the crucial importance of CD8 T cells in effective PD-1-targeted immunotherapy[17], we depleted CD8 T cells from tumour-bearing mice and observed a loss of tumour control with combination therapy (Fig. 3c, Extended Data Fig. 5h). Last, male mice implanted with *Ar*-negative sarcoma tumours were treated with single or combination therapy. We observed that ADT plus enzalutamide also sensitized these mice to anti-PD-L1 antibody therapy (Fig. 3d), suggesting a direct effect of ADT and enzalutamide on immune cells in the tumour.

AR inhibition improves T cell function

The total number of CD8 TILs was unchanged with monotherapy, but increased significantly with ADT plus enzalutamide plus anti-PD-L1 antibody treatment (Extended Data Fig. 6a), possibly reflecting an increase in proliferation of these cells (Extended Data Fig. 6b). The major difference between groups was the ability of CD8 TILs to produce effector cytokines. Production of granzyme B, IFNγ and TNF was significantly increased in T cells from mice treated with ADT plus enzalutamide plus anti-PD-L1 antibody (Fig. 3e–j). Critically, ADT plus enzalutamide or anti-PD-L1 antibody alone was insufficient to improve the polyfunctionality of tumour-associated CD8 T cells (Fig. 3e–j), suggesting that reduced AR signalling could establish a CD8 T cell state permissive to T cell re-invigoration through PD-1/PD-L1 blockade. Consistent with this idea, ADT plus enzalutamide slightly decreased the overall protein expression of PD-1 and CD44 (Extended Data Fig. 6c, d). Similar increases in cytokine production were observed in orthotopic PPSM tumours (Extended Data Fig. 6e–g) or via ADT with the GnRH antagonist degarelix instead of orchiectomy (Extended Data Fig. 6h–l). Notably, mice treated with enzalutamide plus anti-PD-L1 antibody in the absence of ADT showed a partial increase in T cell effector function (Extended Data Fig. 6m–o). Finally, we used a model of T cell adoptive therapy in male and female tumour-bearing mice. All male mice underwent ADT (degarelix) and were subsequently treated or not treated with enzalutamide (Extended Data Fig. 7a). In this model, enzalutamide treatment increased IFNγ production of tumour-antigen specific CD8 T cells in both male and female mice (Extended Data Fig. 7b, c).

To further investigate whether AR inhibition with enzalutamide plus ADT enhanced T cell function, we transcriptionally profiled T cells isolated from the tumour of orchiectomized mice implanted with PPSM tumours and treated with or without enzalutamide[24] (Fig. 3k). Using the genes upregulated in T cells after enzalutamide treatment (Supplementary Table 4), we performed gene set enrichment analysis (GSEA) with the ranked gene list derived from CD8 R versus CD8 NR (Fig. 2d). These results showed that AR-inhibited genes in mouse TILs were significantly enriched in T cells from CD8 R patients (Fig. 3l).

T cell intrinsic AR represses IFNγ

Effector memory CD8 T cells harbour open chromatin regions (OCRs) associated with *Ifng* and *Gzmb*[25–27], which enable rapid production of IFNγ and granzyme B upon TCR ligation. We hypothesized that AR interacted with the *Ifng* and *Gzmb* genes in OCRs associated with functional state. To test this hypothesis, we screened OCRs in *Ifng* and *Gzmb* genes at either the CD8 effector or memory cell state[28] for canonical androgen response elements (AREs) using the JASPAR database of transcription factor binding profiles[29]. We identified robust AREs in OCRs associated with *Ifng* (Extended Data Fig. 8a) in effector memory CD8 T cells (Supplementary Table 5) and in OCRs associated with *Gzmb* (Extended Data Fig. 8a).

To assess whether AR could be regulating CD8 T cell function through binding to the OCRs (Supplementary Table 5), we performed chromatin immunoprecipitation with quantitative PCR (ChIP–qPCR) of AR from activated T cells. AR bound *Ifng* and *Gzmb* OCRs (Fig. 4a), which was reduced by enzalutamide treatment (Fig. 4b). Together, this suggests that AR can directly bind and regulate the expression of *Ifng*, and that enzalutamide perturbs this by dislodging AR from the chromatin. To further investigate this observation, we deleted *Ar* from primary CD8 T cells[30] and stimulated them for 3 days in vitro (Extended Data Fig. 8b–d) before performing RNA sequencing. We performed GSEA analysis on the ranked gene list generated by comparing *Ar*-deficient and -sufficient effector CD8 T cells and revealed significant enrichment of the hallmark IFNγ response in *Ar*-knockout CD8 T cells compared with wild-type controls (Fig. 4c). Moreover, the CD8 R signature was significantly enriched in *Ar*-knockout CD8 T cells (Fig. 4d).

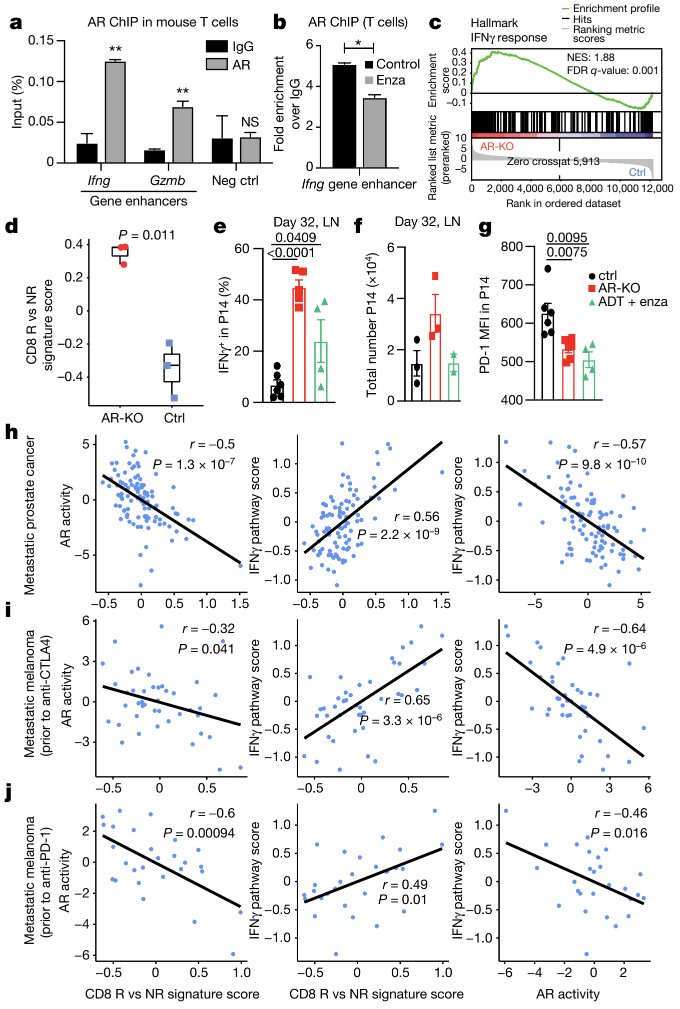

Fig. 4 | Suppressing AR function in T cells promotes *IFNG* activity. a, **b**, AR ChIP–qPCR data shows specific binding of AR to the predicted AREs of *Ifng* and *Gzmb* genes in activated mouse T cells (**a**) and the effect of enzalutamide on AR binding to these AREs (**b**). Data are representative of $n = 3$ independent experiments; unpaired Student *t*-test. **c**, GSEA illustrating the significant enrichment of IFNγ response in mouse *Ar*-knockout (AR-KO) versus control CD8 T cells ($n = 3$ biological replicates). NES, normalized enrichment score. **d**, Enrichment of the human CD8 R versus NR signature in mouse *Ar*-knockout versus control CD8 T cells. Two-tailed unpaired Student's *t*-test. In box plots: centre line, median; box, interquartile range (IQR; the range between the 25th and 75th percentile); whiskers, 1.58 × IQR. **e**–**g**, Wild-type or *Ar*-KO P14 T cells were transferred into congenic recipients; recipients were infected with LCMV clone 13, and transferred T cells in the draining lymph nodes were assessed 32 days later for IFNγ$^+$ (**e**), total number (**f**) and PD-1 mean fluorescence intensity (MFI) (**g**). **h**–**j**, Correlation between CD8 R versus NR signature score and AR activity (left) or IFNγ pathway activity (middle) and between AR activity and IFNγ pathway activity (right) in a larger mCRPC patient cohort (**h**; $n = 99$ patients) and two metastatic melanoma cohorts (**i**; $n = 42$ patients and **j**; $n = 27$ patients). Two-tailed Pearson correlation. LN, lymph node. Error bars represent s.e.m.; two-tailed unpaired Student *t*-test used in **e**–**g**.

On the basis of these observations, we hypothesized that loss of AR may protect chronically stimulated CD8 T cells from losing their capacity to make IFNγ[31]. To test this, we used a model of T cell exhaustion, the lymphocytic choriomeningitis virus 13 (LCMV Cl13) model[32] (Extended Data Fig. 8e). The expression of *Ar* remained low in *Ar*-knockout CD8 T cells at day 7 after infection (Extended Data Fig. 8f). Notably, *Ar*-deficient CD8 T cells from P14 transgenic mice (hereafter, P14 T cells) were functionally equivalent at day 7 after infection (Extended Data Fig. 8g), but unlike control transgenic P14 T cells, they retained the capacity to produce IFNγ upon peptide stimulation more than 30 days after infection (Fig. 4e). Likewise, treatment of infected mice with ADT plus enzalutamide 2 weeks before collection partially restored IFNγ production in P14 T cells (Fig. 4e). Notably, there were more antigen-specific CD8 T cells (Fig. 4f) and PD-1 expression levels were lower when *Ar* was deleted (Fig. 4g).

Last, we evaluated whether the single-cell signature derived from features in CD8 R could delineate patients with mCRPC into AR^{low}IFNγ^{hi} and AR^{hi}IFNγ^{low}, which could be used as a biomarker to identify individuals who might benefit from PD-1 blockade. Indeed, we observed that our CD8 R signature negatively correlated with AR activity (Fig. 4h) and positively correlated with IFNγ pathway activity in a larger cohort of patients with mCRPC[33]. Moreover, we postulated that this relationship between our CD8 R signature, IFNγ pathway activity and AR activity could be extended beyond prostate cancer, similar to the therapeutic synergy demonstrated in mouse models of sarcoma and adoptive T cell therapy (Fig. 3d, Extended Data Fig. 7). In two independent melanoma datasets from patients prior to treatment with anti-CTLA4 therapy[34] (Fig. 4i) or anti-PD-1 therapy[35] (Fig. 4j), we observed similar negative correlations between AR activity and CD8 R signature and IFNγ pathway activity. Together, our findings establish that T cell intrinsic AR activity is a mechanism of IFNγ suppression and immunotherapy resistance, limiting checkpoint blockade efficacy. We propose that in advanced prostate and immunotherapy-resistant cancer patients, intratumour androgens may represent a mechanism of resistance to therapy. Moreover, CD8 T cell intrinsic AR activity may serve as a useful biomarker for identifying patients who could achieve clinical benefit with PD-1/PD-L1 inhibitors.

Discussion

Androgens are described as suppressors of inflammation and immune function[8,36–38], potentially contributing to a male bias in the incidence of cancers of nonreproductive organs[39–44]. Despite low levels of testosterone in the serum of patients with prostate cancer undergoing ADT, the metastatic tumour microenvironment remains enriched with sex hormones[45]—the source of which is under investigation[46]. Resistance to immunotherapy is a clinical challenge in patients with advanced prostate cancer, and common mechanisms of resistance to therapy do not explain the lack of durable anti-tumour T cell responses in this disease. Notably, a strong indicator of response to immunotherapy is *IFNG* expression within the tumour[12–14] and androgens can suppress *IFNG*[8]. In this study, we leveraged a clinical trial that combined androgen-axis inhibition with checkpoint blockade to identify a novel mechanism of immunotherapy resistance. We note that our observations are restricted to a population of men with European ancestry and may not capture the variability in AR transcriptional activity reported among different ethnic groups[47,48]. Notably, in a single study of men of African descent, prostate tumour transcriptional analysis showed enrichment for genes associated with inflammation, including the IFNγ pathway[49]. In addition, sipuleucel-T therapy has higher activity in African Americans than in non-Hispanic white people[50]. This underscores the need to better understand how racial ancestry infuences hormone receptor biology and cancer immunotherapy outcomes. In addition, our findings provide a mechanistic understanding of how ADT might modify the T cell repertoire in patients with mCRPC[51,52]. Finally, our data reveal a T cell intrinsic role for AR regulation of IFNγ activity that limits anti-tumour immunity and T cell re-invigoration. The direct binding of AR to critical inflammatory gene enhancer regions provides insight into a mechanism of sexual dimorphism of immunity.

Online content

Any methods, additional references, Nature Research reporting summaries, source data, extended data, supplementary information, acknowledgements, peer review information; details of author contributions and competing interests; and statements of data and code availability are available at https://doi.org/10.1038/s41586-022-04522-6.

1. Beer, T. M. et al. Randomized, double-blind, phase III trial of ipilimumab versus placebo in asymptomatic or minimally symptomatic patients with metastatic chemotherapy-naive castration-resistant prostate cancer. *J. Clin. Oncol.* **35**, 40–47 (2017).
2. Kwon, E. D. et al. Ipilimumab versus placebo after radiotherapy in patients with metastatic castration-resistant prostate cancer that had progressed after docetaxel chemotherapy (CA184-043): a multicentre, randomised, double-blind, phase 3 trial. *Lancet Oncol.* **15**, 700–712 (2014).
3. Fong, P. C. et al. Pembrolizumab plus enzalutamide in abiraterone-pretreated patients with metastatic castrate resistant prostate cancer: cohort C of the phase 1b/2 KEYNOTE-365 study. *J. Clin. Oncol.* **37**, suppl:abstr 5010 (2019)
4. Sharma, P. et al. Nivolumab plus ipilimumab for metastatic castration-resistant prostate cancer: preliminary analysis of patients in the CheckMate 650 trial. *Cancer Cell.* **38**, 489–499 (2020).
5. Antonarakis, E. S. et al. Pembrolizumab for treatment-refractory metastatic castration-resistant prostate cancer: multicohort, open-label phase II KEYNOTE-199 study. *J. Clin. Oncol.* **38**, 395–405 (2020).
6. Conforti, F. et al. Cancer immunotherapy efficacy and patients' sex: a systematic review and meta-analysis. *Lancet Oncol.* **19**, 737–746 (2018).
7. Small, E. J. et al. A pilot trial of CTLA-4 blockade with human anti-CTLA-4 in patients with hormone-refractory prostate cancer. *Clin. Cancer Res.* **13**, 1810–1815 (2007).
8. Kissick, H. T. et al. Androgens alter T-cell immunity by inhibiting T-helper 1 differentiation. *Proc. Natl Acad. Sci. USA* **111**, 9887–9892 (2014).
9. Benten, W. P. et al. Functional testosterone receptors in plasma membranes of T cells. *FASEB J.* **13**, 123–133 (1999).
10. Liva, S. M. & Voskuhl, R. R. Testosterone acts directly on CD4$^+$ T lymphocytes to increase IL-10 production. *J. Immunol.* **167**, 2060–2067 (2001).
11. Walecki, M. et al. Androgen receptor modulates *Foxp3* expression in CD4$^+$CD25$^+$Foxp3$^+$ regulatory T-cells. *Mol. Biol. Cell* **26**, 2845–2857 (2015).
12. Ayers, M. et al. IFN-gamma-related mRNA profile predicts clinical response to PD-1 blockade. *J. Clin. Invest.* **127**, 2930–2940 (2017).
13. Prat, A. et al. Immune-related gene expression profiling after PD-1 blockade in non-small cell lung carcinoma, head and neck squamous cell carcinoma, and melanoma. *Cancer Res.* **77**, 3540–3550 (2017).
14. Riaz, N. et al. Tumor and microenvironment evolution during immunotherapy with nivolumab. *Cell* **171**, 934–949.e916 (2017).
15. Graff, J. N. et al. Early evidence of anti-PD-1 activity in enzalutamide-resistant prostate cancer. *Oncotarget* **7**, 52810–52817 (2016).
16. Graff, J. N. et al. A phase II single-arm study of pembrolizumab with enzalutamide in men with metastatic castration-resistant prostate cancer progressing on enzalutamide alone. *J. Immunother. Cancer.* **8**, e000642 (2020).
17. Tumeh, P. C. et al. PD-1 blockade induces responses by inhibiting adaptive immune resistance. *Nature* **515**, 568–571 (2014).
18. Chen, P. L. et al. Analysis of immune signatures in longitudinal tumor samples yields insight into biomarkers of response and mechanisms of resistance to immune checkpoint blockade. *Cancer Discov.* **6**, 827–837 (2016).
19. Wherry, E. J. et al. Molecular signature of CD8$^+$ T cell exhaustion during chronic viral infection. *Immunity* **27**, 670–684 (2007).
20. Hwang, S. S. et al. mRNA destabilization by BTG1 and BTG2 maintains T cell quiescence. *Science* **367**, 1255–1260 (2020).
21. Lefebvre, C. et al. A human B-cell interactome identifies MYB and FOXM1 as master regulators of proliferation in germinal centers. *Mol. Syst. Biol.* **6**, 377 (2010).
22. Alvarez, M. J. et al. Functional characterization of somatic mutations in cancer using network-based inference of protein activity. *Nat. Genet.* **48**, 838–847 (2016).
23. Chen, J. et al. NR4A transcription factors limit CAR T cell function in solid tumours. *Nature* **567**, 530–534 (2019).
24. Lu, X. et al. Effective combinatorial immunotherapy for castration-resistant prostate cancer. *Nature* **543**, 728–732 (2017).
25. Northrop, J. K., Thomas, R. M., Wells, A. D. & Shen, H. Epigenetic remodeling of the IL-2 and IFN-γ loci in memory CD8 T cells is influenced by CD4 T cells. *J. Immunol.* **177**, 1062–1069 (2006).
26. Zediak, V. P., Johnnidis, J. B., Wherry, E. J. & Berger, S. L. Cutting edge: persistently open chromatin at effector gene loci in resting memory CD8$^+$ T cells independent of transcriptional status. *J. Immunol.* **186**, 2705–2709 (2011).
27. Kersh, E. N. et al. Rapid demethylation of the IFN-γ gene occurs in memory but not naive CD8 T cells. *J. Immunol.* **176**, 4083–4093 (2006).
28. Pauken, K. E. et al. Epigenetic stability of exhausted T cells limits durability of reinvigoration by PD-1 blockade. *Science* **354**, 1160–1165 (2016).
29. Fornes, O. et al. JASPAR 2020: update of the open-access database of transcription factor binding profiles. *Nucleic Acids Res.* **48**, D87–D92 (2020).
30. Nussing, S. et al. Efficient CRISPR/Cas9 gene editing in uncultured naive mouse T cells for in vivo studies. *J. Immunol.* **204**, 2308–2315 (2020).
31. Wherry, E. J., Blattman, J. N., Murali-Krishna, K., van der Most, R. & Ahmed, R. Viral persistence alters CD8 T-cell immunodominance and tissue distribution and results in distinct stages of functional impairment. *J. Virol.* **77**, 4911–4927 (2003).
32. Ahmed, R., Salmi, A., Butler, L. D., Chiller, J. M. & Oldstone, M. B. Selection of genetic variants of lymphocytic choriomeningitis virus in spleens of persistently infected mice. Role in suppression of cytotoxic T lymphocyte response and viral persistence. *J. Exp. Med.* **160**, 521–540 (1984).
33. Quigley, D. A. et al. Genomic hallmarks and structural variation in metastatic prostate cancer. *Cell* **174**, 758–769.e759 (2018).
34. Van Allen, E. M. et al. Genomic correlates of response to CTLA-4 blockade in metastatic melanoma. *Science* **350**, 207–211 (2015).
35. Hugo, W. et al. Genomic and transcriptomic features of response to anti-PD-1 therapy in metastatic melanoma. *Cell* **168**, 542 (2016).
36. Bebo, B. F., Schuster, J. C., Vandenbark, A. A. & Offner, H. Androgens alter the cytokine profile and reduce encephalitogenicity of myelin-reactive T cells. *J. Immunol.* **162**, 35–40 (1999).
37. Gubbels Bupp, M. R., Potluri, T., Fink, A. L. & Klein, S. L. The confluence of sex hormones and aging on immunity. *Front. Immunol.* **9**, 1269 (2018).
38. Lin, A. A., Wojciechowski, S. E. & Hildeman, D. A. Androgens suppress antigen-specific T cell responses and IFN-γ production during intracranial LCMV infection. *J. Neuroimmunol.* **226**, 8–19 (2010).
39. Ashley, D. J. The two "hit" and multiple "hit" theories of carcinogenesis. *Br. J. Cancer* **23**, 313–328 (1969).
40. Cartwright, R. A., Gurney, K. A. & Moorman, A. V. Sex ratios and the risks of haematological malignancies. *Br. J. Haematol.* **118**, 1071–1077 (2002).
41. Fish, E. N. The X-files in immunity: sex-based differences predispose immune responses. *Nat. Rev. Immunol.* **8**, 737–744 (2008).
42. Cook, M. B., Chow, W. H. & Devesa, S. S. Oesophageal cancer incidence in the United States by race, sex, and histologic type, 1977–2005. *Br. J. Cancer* **101**, 855–859 (2009).
43. Edgren, G., Liang, L., Adami, H. O. & Chang, E. T. Enigmatic sex disparities in cancer incidence. *Eur. J. Epidemiol.* **27**, 187–196 (2012).
44. Klein, S. L. & Flanagan, K. L. Sex differences in immune responses. *Nat. Rev. Immunol.* **16**, 626–638 (2016).
45. Montgomery, R. B. et al. Maintenance of intratumoral androgens in metastatic prostate cancer: a mechanism for castration-resistant tumor growth. *Cancer Res.* **68**, 4447–4454 (2008).
46. Pernigoni, N. et al. Commensal bacteria promote endocrine resistance in prostate cancer through androgen biosynthesis. *Science* **374**, 216–224 (2021).
47. Edwards, A., Hammond, H. A., Jin, L., Caskey, C. T. & Chakraborty, R. Genetic variation at five trimeric and tetrameric tandem repeat loci in four human population groups. *Genomics* **12**, 241–253 (1992).
48. Kazemi-Esfarjani, P., Trifiro, M. A. & Pinsky, L. Evidence for a repressive function of the long polyglutamine tract in the human androgen receptor: possible pathogenetic relevance for the $(CAG)_n$-expanded neuronopathies. *Hum. Mol. Genet.* **4**, 523–527 (1995).
49. Rayford, W. et al. Comparative analysis of 1152 African-American and European-American men with prostate cancer identifies distinct genomic and immunological differences. *Commun. Biol.* **4**, 670 (2021).
50. Higano, C. S. et al. Real-world outcomes of sipuleucel-T treatment in PROCEED, a prospective registry of men with metastatic castration-resistant prostate. cancer. *Cancer* **125**, 4172–4180 (2019).
51. He, M. X. et al. Transcriptional mediators of treatment resistance in lethal prostate cancer. *Nat. Med.* **27**, 426–433 (2021).
52. Bishop, J. L. et al. PD-L1 is highly expressed in Enzalutamide resistant prostate cancer. *Oncotarget* **6**, 234–242 (2015).

Methods

Patient samples

Patients with mCRPC enrolled in clinical trial NCT02312557[15,16] underwent biopsy of a metastatic lesion at Oregon Health and Science University (Portland, OR). All patients had progressive disease on enzalutamide. Response to immune checkpoint inhibitor was defined by sustained reduction in PSA from baseline throughout treatment with PD-1 blockade of > 25%. All human investigations were carried out after approval by a local Human Investigations Committee and in accord with an assurance filed with and approved by the Department of Health and Human Services. Data has been anonymized to protect the privacy of the participants. Investigators obtained informed consent from each participant. For single-cell RNA-seq analysis, fresh needle biopsies prior to pembrolizumab infusion were collected from patients enrolled between September 2017 and January 2019 (n = 8 patients) which included three responders and five non-responders. Bulk RNA-seq libraries were made from flash frozen biopsies. Prostate, colon and tonsil tissue sections were obtained through the Knight Biolibrary in compliance with all applicable institutional policies, including Hospital and Clinics and Institutional Review Board (IRB) policies, and with state (Oregon Genetic Privacy Law) and federal (Common Rule and HIPAA Privacy and Security) regulations. AR protein expression was analysed using immunohistochemical analysis (AR (C6F11) XP Rabbit monoclonal antibody), on formalin-fixed, paraffin embedded tissue, using a biotin-free protocol[53] (Ventana Ultraview). Images were scanned on a Leica Aperio AT2 digital slide imager.

Dissociation of human samples

Fresh isolated tumour samples were collected immediately upon biopsy and processed the same day. Tissue was first minced into small pieces using a scalpel and transferred to a 15 ml tube followed by digestion at room temperature in a shaker at 180 rpm for 30 min in 1 mg ml^{-1} collagenase type IV (Worthington Biochemicals), 100 µg ml^{-1} hyaluronidase (Sigma-Aldrich) and 20 mg ml^{-1} DNase (Roche) in PBS. Cells were then further disrupted with a 1 cm^3 syringe plunger through a 70-µm nylon cell strainer (BD Biosciences) and filtered to obtain a single-cell suspension. Dissociated cells were stained with PE anti-human CD45 (Invitrogen, Clone HI30) for 30 min at 4 °C and subsequently washed three times with PBS + 1% FBS, resuspended, and counted for yield and viability by trypan blue.

Immune cell enrichment for single-cell RNA-seq

To enrich for leukocytes, FACS-sorting of live (Fixable viability dye eF780 negative), CD45 positive cells was performed on a BD Bioscience InFlux cell sorter. Fluidic pressure was minimized at less than 7 PSI and cells were sorted using a large flow nozzle. Sorted cells were collected into cold PBS + 1% FBS. This strategy was used for 7 of 8 samples. One sample used a PE anti-human CD45 magnetic enrichment and release strategy (Stemcell Technologies).

RNA-seq 10X Genomics library preparation and sequencing

The enriched immune cells are immediately proceeded for single-cell RNA-seq library preparation. Single-cell capturing and cDNA library generation were performed using the 10X genomics Chromium single-cell 3′ library construction kit v2 (catalogue (cat.) no. 120267) according to the manufacture's instructions. Libraries were pooled prior to sequencing based on estimated number of cells in each library as determined by flow cytometry cell counts. Sequencing was performed following 10x Genomics instructions using NextSeq (Illumina) at the Massively Parallel Sequencing Shared Resource (MPSSR) at OHSU.

RNA and DNA isolation from fresh frozen OCT samples and sequencing

OCT samples were first cut with cryostat to remove excessive OCT as much as possible. The remaining tissue block was cut at 50 µm per section and immediately transfer to RiboZol (VWR, cat. no. N580). The tissues were incubated in RiboZol at room temperature with shaking every 3 min until the tissues were completely homogenized. The homogenate was centrifuged at 4 °C for 10 min at 12,000g and the supernatant was transferred to a new tube and proceeded with RNA isolation following the manufacturer's instructions. DNA was isolated from the lower two layers after removal of the supernatant following the manufacturer's instructions. RNA-seq library preparation and sequencing were performed by the MPSSR at OHSU. Whole-exome sequencing (WES) was performed by Novogene at a depth of 100×.

Mice, tumour models and antibodies

C57BL/6 (stock no. 000664), RIP-mOVA (stock no. 005431), OTI (stock no. 003831), C57Bl/6;CD90.1 (also known as Thy1.1) congenic mice (stock no. #000406) were purchased from the Jackson Laboratory. P14;Thy1.1 transgenic mice were obtained from the laboratory of S. Kaech. All mice were maintained under specific pathogen-free conditions in the Oregon Health and Science University (Portland, OR) animal facility. Mouse sample size estimates were determined using power analysis (power = 80% (tumour survival) or 90% (phenotyping) and a = 0.05) based on the mean and s.d. from our previous studies. Survival experiments used at least seven mice per group and phenotyping and functional studies at least three mice per group. Mice were randomly assigned to a treatment group based on the initial tumour size to create tumour-size balanced cohorts to eliminate tumour-size differences at the beginning of the experiments. Investigators were blinded to treatment groups during experiments and survival monitoring. Sexually mature 12-week-old males were used for the mouse *Pten*$^{-/-}$; *p53*$^{-/-}$; *Smad4*$^{-/-}$ (PPSM) castration-resistant prostate tumour model and 3′-methylcholanthrene (MCA) 205 sarcoma tumour model studies. PPSM (a gift from R. DePinho), MCA-205 cells (a gift from S. Shu) and MCA-205-OVA (a gift from M. Gough) were propagated in vitro using complete media, RPMI 1640 (Lonza) containing 0.292 ng ml^{-1} glutamine, 100 U ml^{-1} streptomycin/penicillin, 0.1 mM non-essential amino acids, 1 mM sodium pyruvate, and 10mM HEPES (Sigma-Aldrich) as previously described[54–56]. Cell lines were authenticated by genome and/or targeted sequencing and tested and confirmed to be mycoplasma and endotoxin-free using the MycoAlert Detection kit (Lonza). All culture media reagents were purchased from Hyclone Laboratories unless noted otherwise. Control rat IgG (mIgG1) and anti-PD-L1 (mIgG1, clone 80) antibodies were obtained from MedImmune (Astra Zeneca)[57]. Anti-PD-L1 antibodies were used in lieu of PD-1 blocking antibodies as previously described[58]. Mice were randomly assigned to treatment cohorts, and tumours were about 25 to 50 mm^2 (by two-dimension caliper measurement) at the start of treatment. Any mouse with a tumour larger than 150 mm^2 was euthanized per our guidelines from the Institutional Animal Care and Use Committee. No outliers were excluded from the data presented. All animal experiments were approved by the Institutional Animal Care and Use Committee of OHSU.

Tumour challenge, treatments and orchiectomy surgeries

One million PPSM or 0.5×10^6 MCA-205 tumour cells were injected on the hind flank of 12-week old C57BL/6 male mice (8 mice per group for survival experiments or 3 per group for phenotyping experiments). On day 7 (survival) or day 14 (phenotyping) post tumour inoculation, the tumour-bearing mice were left intact, orchiectomized as previously described[59], or treated with 0.5 µg of degarelix by subcutaneous injection once every 14 days. On the same day, mice were started on enzalutamide diet (50 mg kg^{-1} in Purina chow 5053, Research Diet, 0.25 mg per mouse per day) or control diet, and treated with 4 doses of 200 µg rat IgG or anti-PD-L1 antibodies 3 days apart (see Fig. 3d). For CD8 depletion studies, 200 µg anti-CD8α (Clone 53-6.7, BioXcell) was given on days 7 and 11. All antibody injections were given intraperitoneally. For orthotopic tumour implantation in the prostate, 10^6 PPSM cells were injected as previously described[60] and orchiectomy was performed during the same surgery. For tumour antigen specific experiments, 0.5×10^6 MCA-205-OVA tumour cells were injected on both flanks of RIP-mOVA mice (4 to 5 mice per group). All males were treated with 0.5 µg of degarelix by subcutaneous injection at time of tumour injection. Seven days later, 1×10^5 OTI;Thy1.1 CD8 T cells isolated from splenocytes of OTI;Thy1.1 mice were adoptively transferred by intravenous injection into the tumour-bearing mice, and mice started on enzalutamide or control diet.

Lymphocyte isolation

Lymph node (inguinal) and spleens were processed to obtain single-cell suspensions using frosted ends of microscope slides. Spleens were incubated with ammonium chloride potassium lysing buffer (Lonza) for 3 min at room temperature to lyse red blood cells. Cells were rinsed with PBS containing 1% FBS and 4 mM EDT. Tumours were collected the day after the third treatment with anti-PD-L1 antibodies, or 12 days post adoptive transfer of OTI T cells into MCA-OVA tumour-bearing mice. TILs were isolated by dissection of tumour tissue into small fragments in a 50-cm^3 conical tube followed by digestion at room temperature in a bacterial shaker at 180 rpm for 30 min in 1 mg ml^{-1} collagenase type IV (Worthington Biochemicals) and 20 mg ml^{-1} DNAse (Roche) in PBS. Cells were then further disrupted with a 1-cm^3 syringe plunger through a 70-µm nylon cell strainer (BD Biosciences) and filtered to obtain a single-cell suspension.

Flow cytometry

Cells were incubated for 20 min on ice with e506 fixable viability dye and the following antibodies: TCRβ (H57-597), CD4 (RM4-5), CD8 (53-6.7), CD44 (IM7), PD-1 (J43) and Thy1.1 (HIS51). Intracellular proteins Ki67 (SolA15), IFNγ (XMG1.2), TNF (MP6-CT22), Nur77 (12.14) and granzyme B (NGZB) were detected using the Fixation/Permeabilization Solution kit from BD Biosciences. All antibodies and viability dyes were purchased from eBioscience, Biolegend, or BD Biosciences[61]. Data were collected with a Fortessa flow cytometer (BD Biosciences) and analyzed using FlowJo software (Tree Star). Unless noted otherwise in the figure legend, cells were gated through live/TCRβ$^+$/CD8$^+$ gates for analysis.

In vitro activation and intracellular cytokine staining

Bulk TILs, splenocytes and/or blood were plated in 96-well plates and stimulated for 4–5 h with PMA (80 nmol) and ionomycin (1.3 µmol), SIINFEKL peptide (1 nM, GenScript) or gp33 peptide (10 nM, GenScript) in presence of brefeldin A (BFA). Cells were then stained for surface markers, fixed and permeabilized, and stained for intracellular cytokines.

NanoString sample preparation and processing

PPSM tumour-bearing mice were treated with one dose of degarelix and started on enzalutamide or control diet on day 7 post tumour inoculation. One week later, tumours were collected and processed to single-cell suspension. For tumour samples, EpCam positive tumour cells were removed using PE positive selection kit (EasySep, STEMCELL) after staining the samples with EpCam-PE antibody. Enriched tumour infiltrated T cells were used to isolate RNA using RNeasy Kit (Qiagen). 50 ng RNA from each sample was used to measure RNA expression of genes in the nCounter mouse immunology panel using nCounter SPRINT profiler.

Chromatin immunoprecipitation

Male splenic T cells were isolated using magnetic separation (Mouse total T cell EasySep, STEMCELL) and plated in a dish coated with 5 µg ml^{-1} anti-CD3 (145-2C11) and 1.5 µg ml^{-1} anti-CD28 (37.51) antibodies (ebioscience) to activate T cells, and treated with DMSO or 2.5 µM enzalutamide. After 72 h, the cells were collected, and AR ChIP was performed using the iDeal ChIP kit for transcription factor from Diagenode. In brief, cells were cross-linked using 1% formaldehyde, followed by chromatin isolation. The isolated chromatin was then sheared to obtain a size of 300 to 700 base pairs using Diagenode Bioruptor Pico sonicator. For immunoprecipitation, 250 µl of the sheared chromatin solution was incubated with 5 µg of anti-AR antibody (Sigma-Aldrich 17-10489) or control normal rabbit IgG antibody (Sigma-Aldrich 12-370) bound to protein A/G coated magnetic beads overnight at 4 °C with rotation. The immunoprecipitated protein-DNA complex was washed rigorously, followed by reverse-crosslinking and DNA elution. 2.5 µl of sheared chromatin (1% of input) from control as well as enzalutamide treated samples were processed separately for preparing input sample DNA. The chromatin regions were measured by qPCR in the eluted DNA samples. The primers to amplify OCRs in *Ifng* (forward: GGTGTTGCAAAG ACCTAG, reverse: GCAGTCCTTTTAATTACCCTG) gene were used in qPCR. qPCR signals from each treatment group were normalized to the signal from the corresponding 1% input sample. The relative abundance of the chromatin regions bound to AR was calculated by normalizing to IgG control.

CRISPR–Cas9 *Ar* gene deletion in naive CD8 T cells

Naive WT or P14 CD8 T cells were purified from spleens using magnetic separation (Mouse CD8 T cell EasySep, STEMCELL). *Ar* was then deleted in purified naive CD8 T cells according to the detailed protocol[30]. sgRNA targeting the mouse *Ar* gene (sgRNA 1: AATACTG AATGACCGCCATC; sgRNA 2: AGGCTTCCGCAACTTGCATG; sgRNA 3: ATTGCCCATCTTGTCGTCTC; sgRNA 4: GGGTGGAAAGTAATAGTCGA) and the mouse genome nontargeting Control sgRNA (5′-GCACUA CCAGAGCUAACUCA-3′) were obtained from Synthego. Cas9 recombinant protein was obtained from IDT. Following electroporation of the Cas9–sgRNA complex into wild-type or P14 purified naive CD8 T cells, cells were either put in culture for 3 days in plates coated with 5 µg ml^{-1} of anti-CD3 and anti-CD28 antibodies, or adoptively transferred in recipient mice.

LCMV Clone 13 experiment

Immediately after Cas9 and mouse *Ar* or NT (non-targeting) sgRNAs were electroporated in naive purified splenic male P14;Thy1.1 CD8 T cells, 1×10^4 *Ar*-knockout, NT P14 or wild-type CD8 T cells were adoptively transferred into wild-type recipient male mice by intravenous injection. At the same time, 2×10^6 PFU of LCMV clone 13 was injected intravenously At day 7 post adoptive transfer and LCMV inoculation, mice were bled, red blood cells lysed with ACK buffer, and cells were stimulated for 6 h with 10 µM gp33 peptide in the presence of brefeldin a, and analysed by flow cytometry. One mouse per group was euthanized, adoptively transferred P14;Thy1.1 were sorted from the spleen based on Thy1.1 expression, RNA was extracted and AR levels assessed by qPCR. At day 18, mice adoptively transferred with wild-type CD8 T cells were treated with 0.5 µg degarelix by subcutaneous injection and put on enzalutamide diet for the rest of the experiment. On day 32, spleens and lymph nodes were collected, stimulated with 10 µM gp33 peptide, and analysed by flow cytometry.

Healthy human donor PBMCs and human *AR* RT–qPCR

Donor deidentified PBMC were from CMV, HIV and HBV seronegative male donors. PBMCs were thawed, and untouched total T cells or CD8 T cells were purified via magnetic separation (human T cell or human CD8$^+$ T cell, EasySep, STEMCELL). T cells were stimulated for 0–3 days with plate bound anti-CD3 (OKT3, 4 µg ml^{-1}) and anti-CD28[62] (CD28.2, 2 µg ml^{-1}). Total RNA from unstimulated and TCR stimulated T cells was extracted (RNeasy, Qiagen) and subjected to one-step quantitative PCR with reverse transcription (RT–qPCR) for *AR* and *SDHA* (GoTaq 1-step RT–qPCR) amplified in a QuantStudio 3 thermocycler (Applied Biosystems). *AR* for each sample was internally normalized to *SDHA*, and data are reported as fold change versus *AR* expressed in unstimulated T cells.

Human quantitative PCR (qPCR) primer sequences: human *AR* (forward: 5′-CAGCAGAAATGATTGCACTATTGA-3′; reverse: 5′-AGAG

TCATCCCTGCTTCATAAC-3′); human *SDHA* (forward: 5′-CAGCACAGGGAGGAATCAAT-3′; reverse: 5′-GTGTCGTAGAAATGCCACCT-3′).

Mouse *Ar* RT–qPCR

P14 T cells were sorted 7 days after adoptive transfer. Total RNA from unstimulated, TCR stimulated T cells, sorted P14, PPSM, or mouse pancreatic tumour cell line 688m[63] was extracted (RNeasy, Qiagen) and subjected to one-step RT-qPCR for *Ar* and *Gapdh* (GoTaq 1-step RT–qPCR) amplified in a QuantStudio 3 thermocycler (Applied Biosystems). Mouse qPCR primer sequences: mouse *Ar* (forward: 5′-GGAGAACTACTCCGGACCTTAT-3′; reverse: 5′-GGGTGGAAAGTAATAGTCGATGG-3′), mouse *Gapdh* (forward: 5′-CTGGCCAAGGTCATCCAT-3′; reverse: 5′-TTCTGGGTGGCAGTGATG-3′).

Quantification and statistical analysis

Preprocessing of single-cell RNA-seq data. FASTQ files were mapped to human genome (hg19) and unique molecular identifier (UMI) counts quantified per gene per cell to generate a gene-barcode matrix using Cell Ranger software pipeline (version 2.1.1). To account for different sequencing depth of multiple libraries, reads of all samples were aggregated and libraries were normalized to the same sequencing depth using the ‘cellranger aggr’ function with normalize = mapped. The preprocessed matrix of gene counts versus cells contained 16,335 cells at an average sequencing depth of 7,655 reads per cell.

Unsupervised clustering of all cells. The preprocessed matrix generated by the cellranger pipeline was imported into the Seurat (version 3.0.0) R (version 3.5.1) package[64]. As a quality control step, we first filtered out cells with fewer than 100 genes and genes expressed in less than 0.1% of cells using zero as a cut-off for UMI counts. We further removed cells based on mitochondrial gene content, UMI counts, and gene counts (mitochondrial % counts ≥10%, UMI counts > 9,000, gene counts > 2,500). The filtered gene-expression matrix (14,609 genes and 16,044 cells) was normalized using the NormalizeData function with the LogNormalize normalization method and scale.factor equal to 10,000. Prior to dimension reduction and clustering analysis, we scaled the data and regressed out the effects of variation of UMI counts and percent mitochondrial contents. Furthermore, we focused on genes that exhibited high cell-to-cell variation and identified 1,608 genes using the FindVariableFeatures function in the Seurat package with mean.var.plot method (mean cut-off between 0.0125 and 8, and dispersion over 0.5). Principal components analysis was performed on the scaled data cut to variable genes and the first 20 principal components were selected for downstream analysis, based on the elbow point on the plot of standard deviations of principal components. Cells were embedded in a shared nearest neighbour (SNN) graph constructed on the selected principal components and partitioned into clusters using the FindClusters function with the resolution parameter set to 0.6 and the other parameters left as default. To visualize cells in two dimensions, UMAP was generated using the RunUMAP function with the same principal components used in clustering analysis. Throughout the analysis, we confirmed the absence of batch effects introduced by samples or other technical factors, and thus did not perform batch effect removal in our data.

This analysis yielded 17 clusters (data not shown). Cell types were identified based on the enrichment of a set of canonical markers for each cluster. We annotated a total of nine T cells clusters, one NK cell cluster, two myeloid cell clusters, one B cell cluster, one plasma cell cluster, one tumour cells cluster, one fibroblast cells cluster, and one endothelial cell cluster. At the all-cells clustering stage, we did not intend to identify distinct cell types in detail and therefore merged clusters into tumour cells and major lymphoid and myeloid immune cell subsets. The fraction of cells in each sample assigned to a given cluster *c* was computed, and we used Student’s *t*-test to determine if there was a significant difference between responders and non-responders samples for cluster *c*. Percentage was calculated out of all leucocytes.

Unsupervised clustering of T and NK cells. To reveal different cell types in T and NK cells, we extracted all cells classified as T and NK cells in our all-cells clustering analysis. The expression matrix of these cells was extracted from the preprocessed matrix (cellranger output), and analysed through Seurat following the exact steps described above. This analysis used 1,496 variable genes, top 14 principal components, and a resolution of 0.5 in FindClusters. The fraction of cells in each sample assigned to a given cluster *c* was computed, and we used Student’s *t*-test to determine whether there was a significant difference between responders and non-responders samples for cluster *c*.

Unsupervised clustering of CD8 and CD4 T cells. To identify CD8 T cells states associated with response or resistance, we extracted all single cells classified as CD8 T cells in our T and NK cells clustering analysis, subset the expression matrix from the preprocessed matrix (cellranger output), and processed these cells using Seurat following the exact steps described above. Principal components analysis was performed on the scaled data cut to 1,728 variable genes and the top 14 principal components were used to generate UMAP for cell visualization. *k*-means clustering was performed on the top 50 principal components and CD8 T cells were classified into two clusters. A similar clustering analysis was performed on CD4 T cells, which used 2,042 variable genes.

Differential gene-expression analysis and marker gene identification. For all single-cell differential gene-expression tests, we used Wilcoxon rank-sum test implemented in Seurat. The differentially expressed genes for each cluster compared with all other cells were identified using the FindAllMarkers function. Differential gene-expression testing was also performed using the FindMarkers function between responder cells (CD8 R) and non-responder cells (CD8 NR), and between CD8 k1 cells and CD8 k2 cells. To identify top differentially expressed genes, we required an expression difference of at least 1.25 times fold change (FC) (average logFC ≥ log(1.25)) and an adjusted *P* value (p_val_adj) of ≤0.05 with gene expression detected in at least 10% of cells in either one of the two comparison groups. The top 20 highly and differentially expressed genes, as ranked by the average fold change, were selected and scaled expression data of these genes was visualized in heatmaps.

Pathway enrichment analysis of single cells. To compute the gene-expression signature which required fold change and *P* value, we used the output of the Seurat FindMarkers or FindAllMarkers function with the following parameters: logfc.threshold = log(1), min.pct = 0.001, and others set to default. This allowed us to interrogate the fold change and *P* value for all genes that were expressed in at least 0.1% of cells in either comparison group. The gene-expression signature was calculated using the following formula: average logFC × $\log_{10}(1/(P+10^{-300}))$, where average logFC and *P* were the outputs from Seurat. The gene-expression signature of each comparison was imported into Camera to identify enriched pathways[65] and we used C2 canonical pathway reactome from the MSigDB database (version 7.0).

Master regulator analysis of single cells. Transcription factor activity was inferred using the master regulator (MR) inference algorithm (MARINa)[21] compiled in the viper R package[22]. Gene-expression signature and a regulatory network (regulome) are the two sources of data required as input for viper analysis. Gene-expression signature was computed as described above. The transcription factor regulome used in this study was curated from several databases as previously described[66].

NanoString nCounter data analysis. NanoString nCounter data were normalized and gene-expression fold change calculated using nSolver software from NanoString (version 4.0). A gene was nominated as differentially expressed when the fold change between a comparison group was greater than 1.2 and the gene raw count was above the background threshold for all samples. To determine whether genes upregulated in TIL-enza versus control were enriched in CD8 R single cells, GSEA Preranked tool was used to perform GSEA[67] (version 4.0.3), with the ranked gene list computed as described above and a permutation number of 3,000.

Whole transcriptome analysis of bulk tumour samples. FastQC v0.11.8 software (http://www.bioinformatics.bbsrc.ac.uk/projects/fastqc/) was used to determine the quality of raw fastq files. Sequencing reads were aligned to hg19 human reference genome and per-gene counts and TPM (transcripts per kilobase million) quantified by RSEM[68] (1.3.1) based on the gene annotation gencode.v19.annotation.gtf. The regulon activity of AR for each bulk sample was inferred using single-sample VIPER analysis with TPM gene expression as input[22]. The CD8 R versus NR score of each bulk sample was calculated using the *z*-score method. In brief, gene-expression values ($\log_2(\text{TPM} + 1)$) of each sample were converted to *z*-scores by: $z = (x - \mu)/\sigma$, where μ is the average $\log_2(\text{TPM} + 1)$ across all samples of a gene and σ is the s.d. of $\log_2(\text{TPM} + 1)$ across all samples of a gene. The CD8 R versus NR score of each sample was the difference between average *z*-score of all up-regulated genes in CD8 R versus NR and average *z*-score of all down-regulated genes in CD8.R versus NR. The CD8 k1 versus k2 score was calculated in the same way.

Whole transcriptome analysis of mouse CD8 T cell *Ar*-knockout and control samples. Sequencing FASTQ files were aligned to the mouse reference genome (GRCh38.p6) using RSEM (1.3.1)[68]. The RSEM output of the number of reads per gene was used to quantify the expression level of each gene for downstream analysis. The Broad Institute GSEA software (GSEA, version 4.0.3)[67] was used to determine the enrichment of the interferon gamma response pathway from the MSigDB hallmarks gene sets (version 7.0). The CD8 R versus NR score of each sample was calculated using the *z*-score method as described above.

Tumour mutational burden. WES reads were aligned against the GrCH37d5 genome using the Sanger cgpmap workflow (https://github.com/cancerit/dockstore-cgpmap) with realignment around indels and base recalibration performed using the Open Genomics GATK cocleaning workflow (https://github.com/OpenGenomics/gatk-cocleaning-tool). Somatic variants were called using a collection of callers via the mc3 workflow[69] (https://github.com/opengenomics/mc3), retaining all variants produced by Pindel and all variants reported by two or more tools that were not overlapped by a Pindel variant. The Mbp of genome covered by WES was determined using bedtools genomecov (V.2.26.0), where any base pair covered by at least six aligned reads was considered covered. Coverage-adjusted tumour mutational burden was calculated on a per-sample basis by dividing the total number of somatic variants detected by the Mbp of genome covered.

Analysis of public prostate and melanoma datasets. The West Coast Dream Team (WCDT) human mCRPC mRNA data[33] ($n = 99$ individuals) was obtained from http://davidquigley.com/prostate.html. The Hugo cohort[35] ($n = 27$ tumours) was downloaded from GSE78220 and the Van Allen cohort[34] ($n = 42$ tumours) was downloaded from the database of Genotypes and Phenotypes (dbGAP) under the accession number phs000452.v2.p1.The gene expressions were quantified by the transcripts per kilobase million (TPM). The regulon activity of AR in each sample was calculated using VIPER as described above. The IFNG pathway gene set was downloaded from the MSigDB database (version 7.0). Single-sample IFNG activity was calculated using *z*-score as described above. The CD8 R versus NR score of each bulk sample was calculated using *z*-score method as described above.

Mouse data statistical analysis. Statistical analysis was performed using two-tailed unpaired Student's *t*-test (for comparison between two groups), one-way ANOVA for multiple comparisons or log-rank (Mantel-Cox) test for survival curves using GraphPad Prism 6 (GraphPad Software). Error bars represent s.e.m. unless noted otherwise in the figure legend. Statistical tests and *P* values are specified for each panel in the respective figure legends, and *P* values < 0.05 were considered significant. Biological replicates (individual mice) for each experiment are indicated in the figure legends.

Reporting summary

Further information on research design is available in the Nature Research Reporting Summary linked to this paper.

Data availability

The sequence data generated in this study will be deposited in the Gene Expression Omnibus (GEO). Additional datasets generated during the current study for Clinical Trial NCT02312557 are available from the corresponding author on reasonable request. Source data are provided with this paper.

Code availability

The code for reproducibility of data is publicly available or will be available upon request.

53. Aggarwal, R. et al. Clinical and genomic characterization of treatment-emergent small-cell neuroendocrine prostate cancer: a multi-institutional prospective study. *J. Clin. Oncol.* **36**, 2492–2503 (2018).
54. Moran, A. E., Polesso, F. & Weinberg, A. D. Immunotherapy expands and maintains the function of high-affinity tumor-infiltrating CD8 T cells in situ. *J. Immunol.* **197**, 2509–2521 (2016).
55. Polesso, F., Sarker, M., Weinberg, A. D., Murray, S. E. & Moran, A. E. OX40 agonist tumor immunotherapy does not impact regulatory T cell suppressive function. *J. Immunol.* **203**, 2011–2019 (2019).
56. Polesso, F., Weinberg, A. D. & Moran, A. E. Late-stage tumor regression after PD-L1 blockade plus a concurrent OX40 agonist. *Cancer Immunol. Res.* **7**, 269–281 (2019).
57. Schofield, D. J. et al. Activity of murine surrogate antibodies for durvalumab and tremelimumab lacking effector function and the ability to deplete regulatory T cells in mouse models of cancer. *mAbs* **13**, 1857100 (2021).
58. Polesso, F. et al. PD-1-specific "blocking" antibodies that deplete PD-1$^+$ T cells present an inconvenient variable in preclinical immunotherapy experiments. *Eur. J. Immunol.* **51**, 1473–1481 (2021).
59. Valkenburg, K. C., Amend, S. R. & Pienta, K. J. Murine prostate micro-dissection and surgical castration. *J. Vis. Exp.* https://doi.org/10.3791/53984 (2016).
60. Pavese, J., Ogden, I. M. & Bergan, R. C. An orthotopic murine model of human prostate cancer metastasis. *J. Vis. Exp.* https://doi.org/10.3791/50873 (2013).
61. Moran, A. E. et al. T cell receptor signal strength in T_{reg} and iNKT cell development demonstrated by a novel fluorescent reporter mouse. *J. Exp. Med.* **208**, 1279–1289 (2011).
62. Murray, S. E. et al. Fibroblast-adapted human CMV vaccines elicit predominantly conventional CD8 T cell responses in humans. *J. Exp. Med.* **214**, 1889–1899 (2017).
63. Gruner, B. M. et al. An in vivo multiplexed small-molecule screening platform. *Nat. Methods* **13**, 883–889 (2016).
64. Satija, R., Farrell, J. A., Gennert, D., Schier, A. F. & Regev, A. Spatial reconstruction of single-cell gene expression data. *Nat. Biotechnol.* **33**, 495–502 (2015).
65. Wu, D. & Smyth, G. K. Camera: a competitive gene set test accounting for inter-gene correlation. *Nucleic Acids Res.* **40**, e133 (2012).
66. Robertson, A. G. et al. Integrative analysis identifies four molecular and clinical subsets in uveal melanoma. *Cancer Cell* **32**, 204–220.e215 (2017).
67. Subramanian, A. et al. Gene set enrichment analysis: a knowledge-based approach for interpreting genome-wide expression profiles. *Proc. Natl Acad. Sci. USA* **102**, 15545–15550 (2005).
68. Li, B. & Dewey, C. N. RSEM: accurate transcript quantification from RNA-seq data with or without a reference genome. *BMC Bioinf.* **12**, 323 (2011).
69. Ellrott, K. et al. Scalable open science approach for mutation calling of tumor exomes using multiple genomic pipelines. *Cell Syst.* **6**, 271–281.e277 (2018).

Acknowledgements We thank A. Adey and R. Searle for sharing expertise as we developed protocols for single-cell RNA-seq. We are grateful to the OHSU Department of Comparative Medicine for outstanding animal husbandry, the Massively Parallel Sequencing Shared Resource (MPSSR) for their support, and the Knight Cancer Institute Prostate Programs outstanding clinical research team. This work is funded in part by the Collins Medical Trust, OHSU Foundation, Prostate Cancer Foundation, Pacific Northwest Prostate Cancer SPORE NCI 5P50CA097186, NIH 1R37 CA263592-01 (to A.E.M.), M.J. Murdock Charitable Trust NS-201812034 (to S.E.M.), and a sponsored research agreement with MedImmune (to A.E.M.). This work is also supported by Medical Research Foundation at Oregon, NIH 5K01LM012877 and NIH 1R21HL145426 (to Z.X.). The resources of the Exacloud high performance computing environment developed jointly by OHSU and Intel and the technical support of the OHSU Advanced Computing Center are gratefully acknowledged. BioRender.com software was used for the creation of some figures.

Author contributions A.E.M. conceived the study, designed and performed experiments, interpreted data and wrote the manuscript. Z.X., X.G., and C.W. designed, performed and interpreted computational analysis. X.G., F.P. and A.E.M. wrote the manuscript. F.P. and C.H. designed, performed and interpreted mouse experiments. C.W. prepared samples for sequencing. A.S. performed ChIP experiments. S.A.H. interpreted data and contributed to manuscript writing. J.N.G. conducted the clinical trial. R.F.T. and M.A.W. performed WES analysis, variant calling and tumour mutational analysis. R.M.H., S.E.M. and B.C. performed experiments for resubmission, interpretated data and contributed to writing and/or editing the manuscript. G.V.T. reviewed pathology.

Competing interests R.F.T. and J.N.G. are employees of the US Government. The contents do not represent the views of the US Department of Veterans Affairs or the United States Government. S.A.H. is an employee of AstraZeneca. A.E.M. received research funding from AstraZeneca.

Additional information

Supplementary information The online version contains supplementary material available at https://doi.org/10.1038/s41586-022-04522-6.

Correspondence and requests for materials should be addressed to Amy E. Moran.

Peer review information *Nature* thanks Gerhardt Attard, Joushua Rubin and the other, anonymous, reviewers for their contribution to the peer review of this work. Peer review reports are available.

Reprints and permissions information is available at http://www.nature.com/reprints.

a

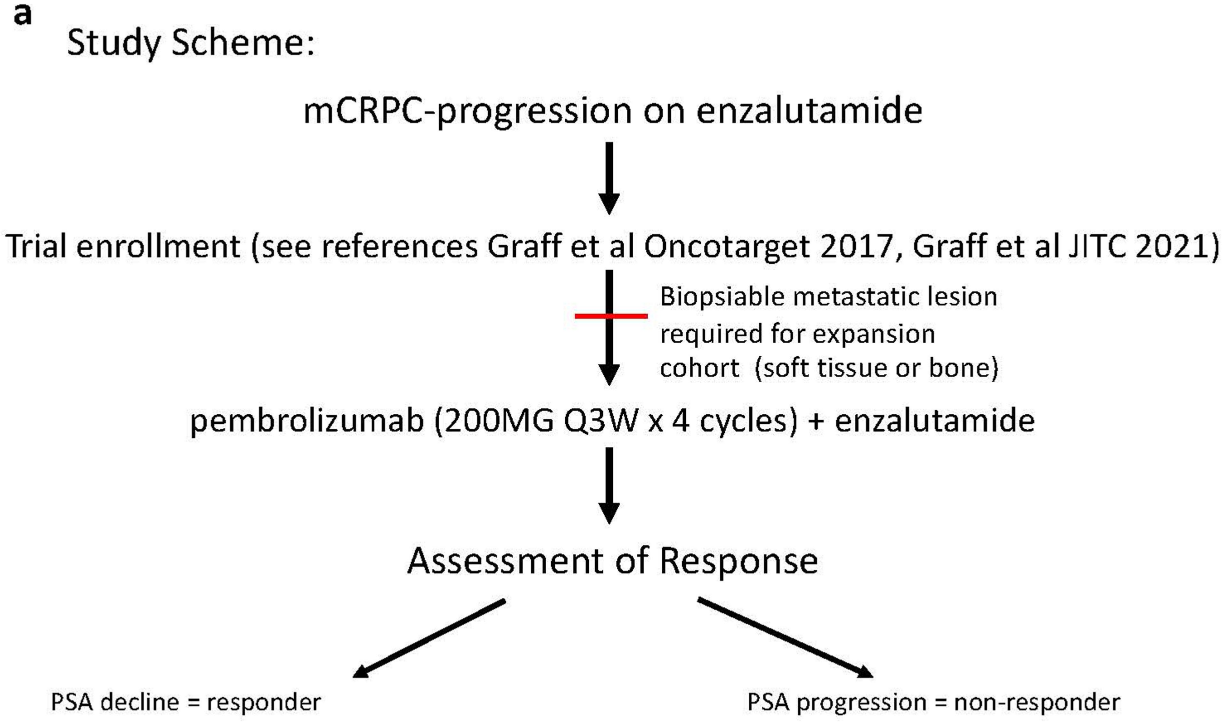

b

StudyID	Outcome	Biopsy Site	PSA change	Somatic_variant_count	Coverage_adj_mtl_burden
NR1	Non-responder	Bone	73.7%	362	2.205800263
NR2	Non-responder	Bone	9.39%	296	1.501075977
NR3	Non-responder	LN	159.46%	342	2.321639108
NR4	Non-responder	LN	304.32%	195	1.190478683
NR5	Non-responder	Bone	140.15%	1023	6.41025388
R1	Responder	Liver	-99.93%	759	5.049823125
R2	Responder	LN	-98.57%	362	2.780904845
R3	Responder	LN	-27.53%	640	4.369154208

c

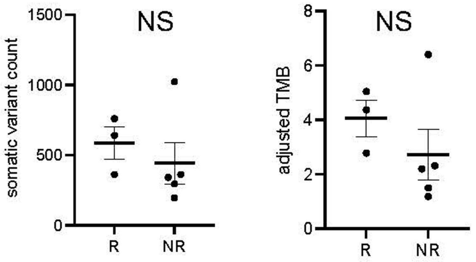

Extended Data Fig. 1 | Clinical trial scheme of patients enrolled and details on biopsy location and genomics. a. Clinical trial study scheme. **b**. Per-patient tumor mutations are shown in a table with each row representing an individual participant on study, and each column representing the unique participant identifier (StudyID), the participant's response to study treatment (Outcome), the site of biopsied tissue specimen analyzed (Biopsy Site), the relative (%) change in PSA with treatment (PSA change), the number of somatic variants detected in that tumor specimen (Somatic_variant_count), and the coverage-adjusted tumor mutational burden defined as the Somatic_variant_count / #Mbp genome covered by ≥ 6 reads (Coverage_adj_mtl_burden). **c**. Comparison of the somatic variant counts (left) or coverage-adjusted tumor mutational burdens (right) for study responders (R, n = 3 patients) versus non-responders (NR, n = 5 patients); NS represents no significant difference detected by two-tailed Student's *t*-test; mean values are depicted as bold horizontal lines. Error bars represent S.E.M.

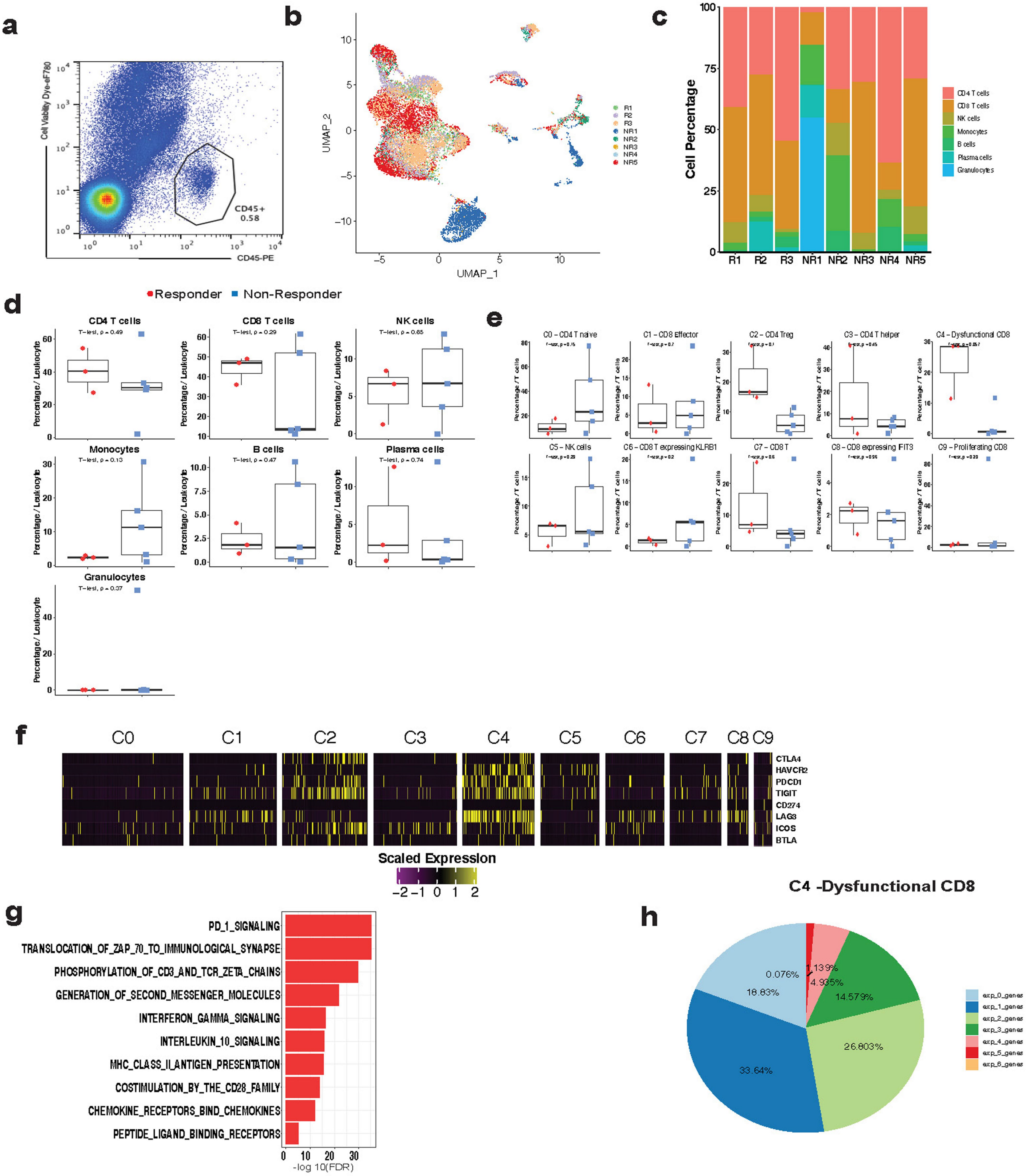

Extended Data Fig. 2 | CD8 T cell subset associated with response to checkpoint therapy in mCRPC patients. a, Representative flow cytogram for sorting tumor-associated leukocytes prior to scRNAseq. **b**, UMAP of all single cells (n = 16,044 cells) in this study colored by patient. **c**, Stack bar graph showing the % of cells per sample for immune cell clusters across each patient biopsy. **d, e**, Box plots comparing the % of cells per sample for immune cell clusters between responders (n = 3 patients) and non-responders (n = 5 patients). Percentage was calculated out of all immune cells (**d**) or all T/NK cells (**e**). Two-tailed unpaired Student's *t*-test. Box center line, median; box, the interquartile range (IQR, the range between the 25th and 75th percentile); whiskers, 1.58 times IQR. **f**, Heatmap showing the expression of *CTLA4*, *HAVCR2*, *PDCD1*, *TIGIT*, *CD274*, *LAG3*, *ICOS*, *BTLA* in various T cell clusters. **g**, Pathways enriched in dysfunctional CD8 T cells (C4 cluster). **h**, Percentage of cells co-expressing a combination of *PDCD1*, *LAG3*, *HAVCR2*, *CTLA4*, *TNFRSF4*, and *TIGIT* in dysfunctional CD8 T cells (C4 cluster).

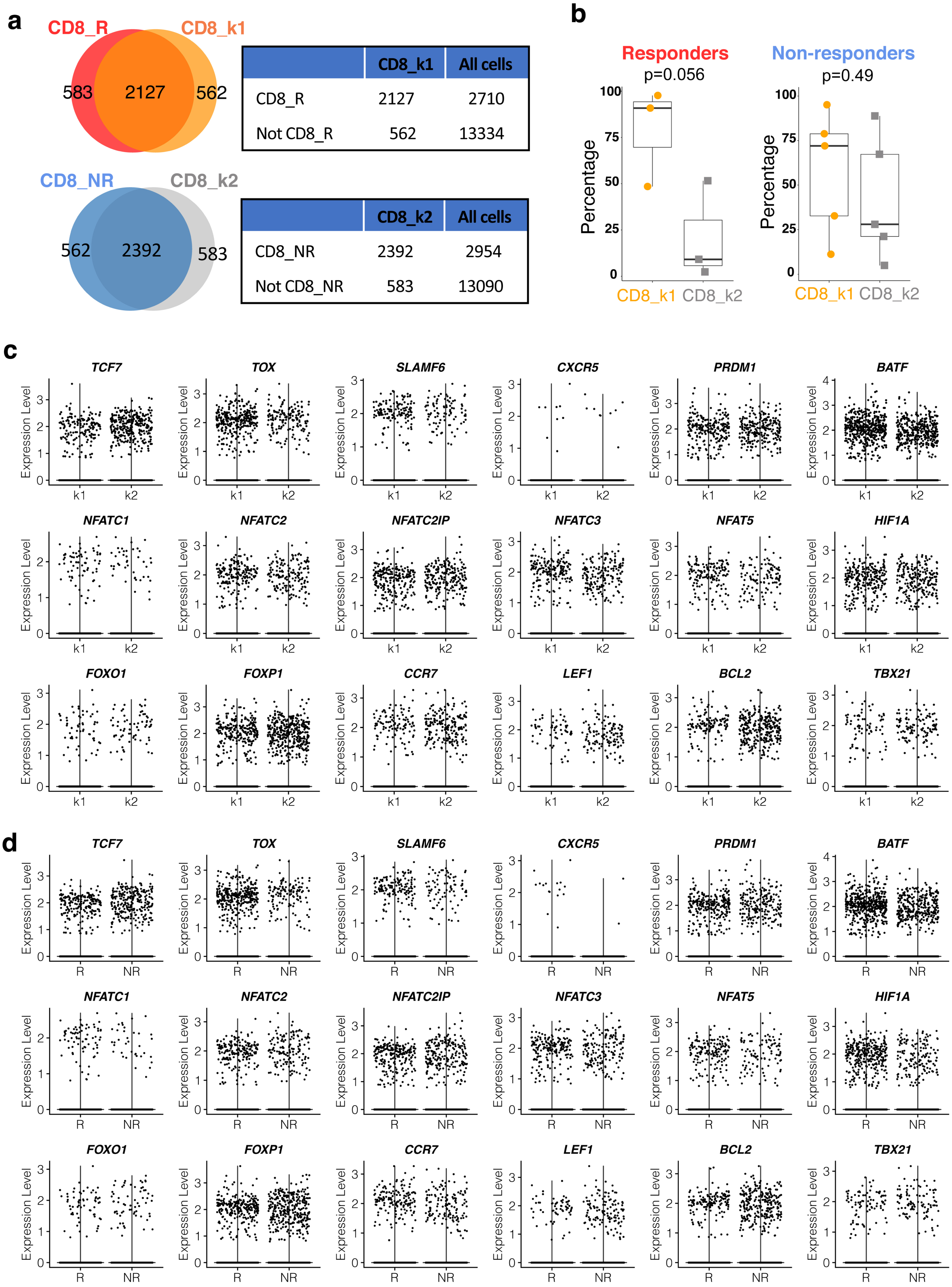

	CD8_k1	All cells
CD8_R	2127	2710
Not CD8_R	562	13334

	CD8_k2	All cells
CD8_NR	2392	2954
Not CD8_NR	583	13090

Extended Data Fig. 3 | Expression of various genes associated with CD8 T cytotoxicity and exhaustion. a, Venn diagram and contingency table showing the significant overlap between CD8_R and CD8_k1 (Top, $P < 0.0001$) and between CD8_NR and CD8_k2 (Bottom, $P < 0.0001$). All cells: all the single cells that passed quality control in this study, as shown in Fig. 1a. Two-tailed Fisher's exact test. **b**, Percentage of CD8_k1 or CD8_k2 clusters per sample in responders ($n = 3$ patients) and non-responders ($n = 5$ patients). Two-tailed unpaired Student's *t*-test. Box center line, median; box, the interquartile range (IQR, the range between the 25th and 75th percentile); whiskers, 1.58 times IQR. **c, d**, Violin plot comparing the gene expression in CD8_k1 and CD8_k2 (**c**), and CD8_R and CD8_NR (**d**). R, responder; NR, non-responder.

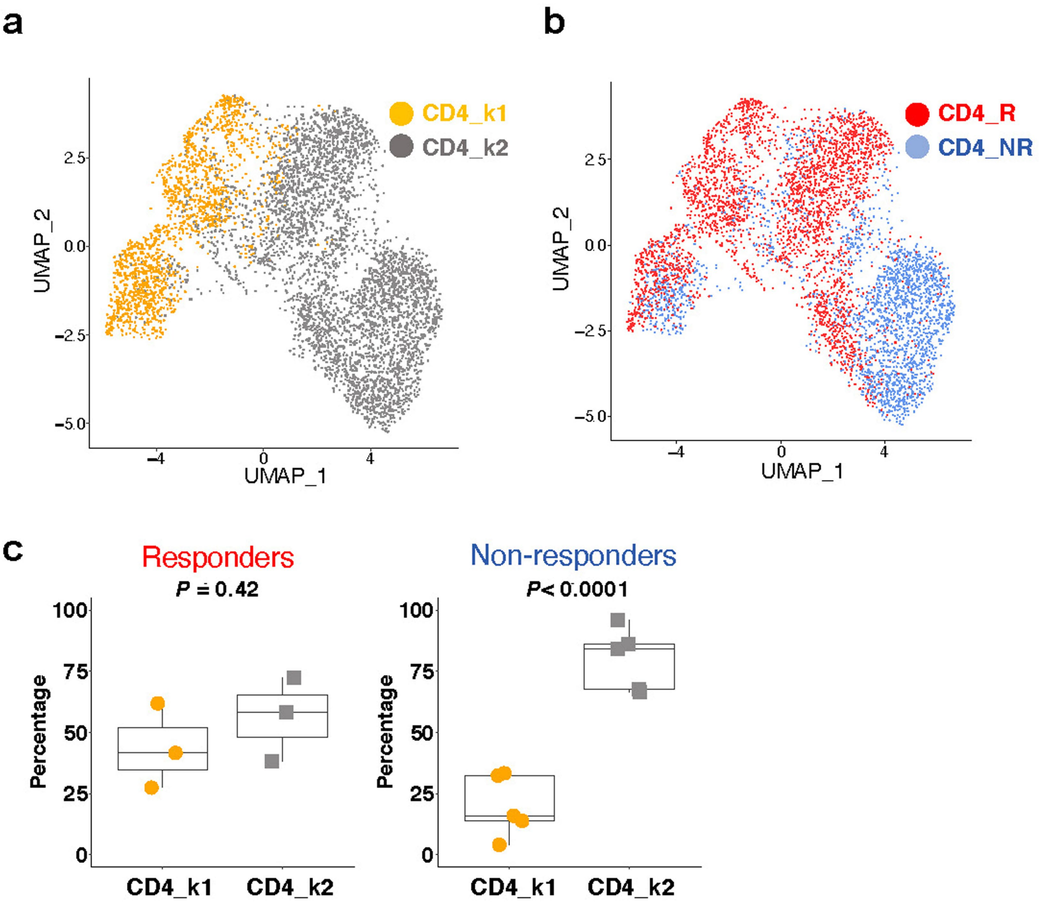

Extended Data Fig. 4 | CD4_k1 is not associated with response. a, UMAP plot showing the two distinct CD4 T cells states identified using *k*-means clustering (n = 5,322 cells). **b**, UMAP plot showing CD4 T cells colored by response and non-response patient groups (n = 5,322 cells). **c**, Percentage of CD4_k1 or CD4_k2 clusters per sample in responders (n = 3 patients) and non-responders (n = 5 patients). Two-tailed unpaired Student's *t*-test. Box center line, median; box, the interquartile range (IQR, the range between the 25th and 75th percentile); whiskers, 1.58 times IQR. R, responder; NR, non-responder.

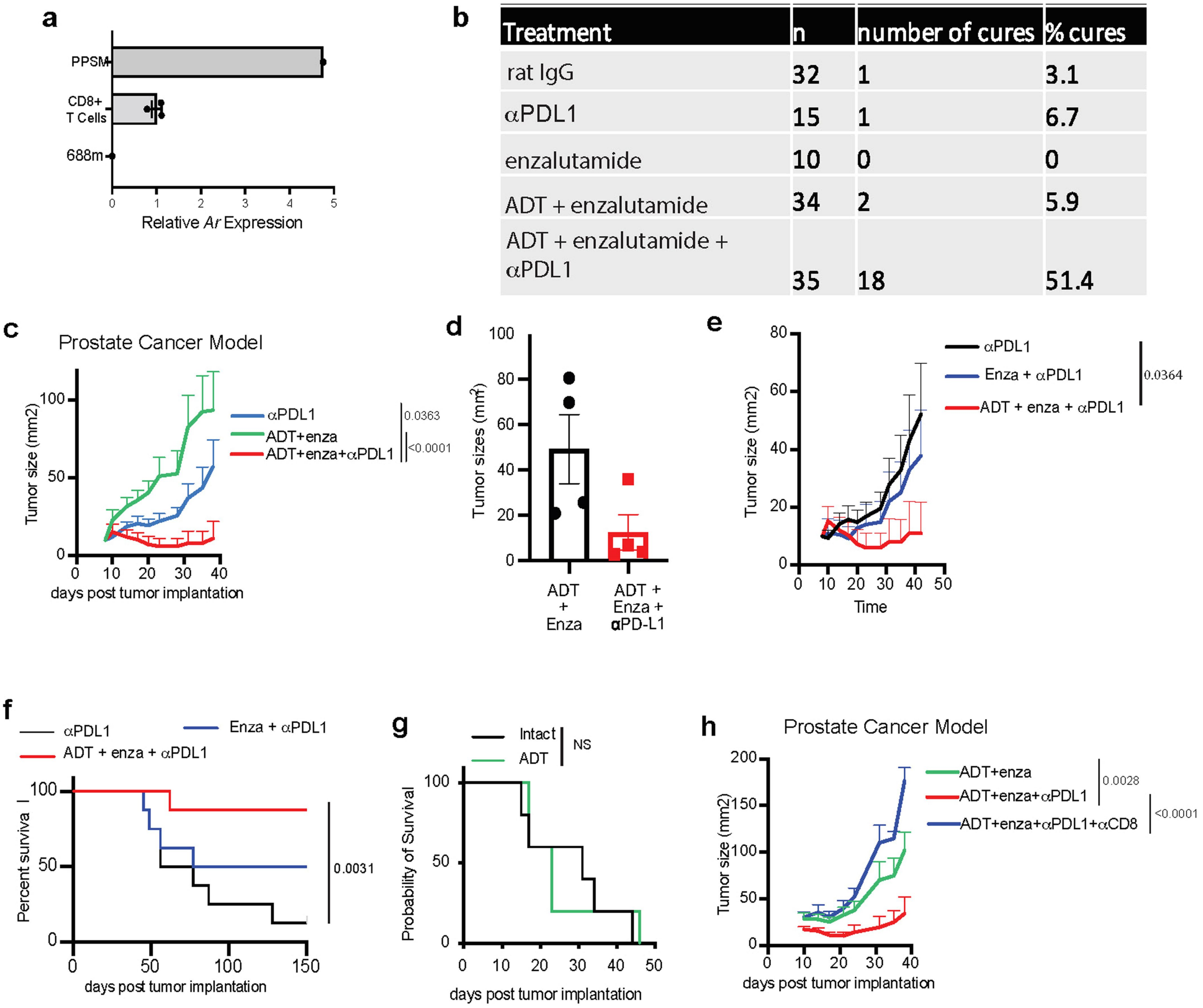

Treatment	n	number of cures	% cures
rat IgG	32	1	3.1
αPDL1	15	1	6.7
enzalutamide	10	0	0
ADT + enzalutamide	34	2	5.9
ADT + enzalutamide + αPDL1	35	18	51.4

Extended Data Fig. 5 | Survival data following orthotopic PPSM implantation and enzalutamide + anti-PD-L1 treatment. a, *Ar* expression by qPCR in mouse CD8 T cells, as compared with PPSM and 688m AR positive and negative control cell lines, respectively. Data combined from 3 independent experiments. **b**, Summary table of the experiments described in Fig. 3a. **c**, Average tumor growth of PPSM tumor bearing animals treated with different treatment combination as described in Fig. 3a. Data combined from 4 independent experiments, 8 to 10 animals per group. **d**, 12–14 wk old male mice were orchiectomized and PPSM tumor cells were injected orthotopically in the anterior lobe of the prostate. One week later, animals were treated with enzalutamide or enzalutamide + anti-PD-L1 (5 animals per group). 4 weeks post tumor inoculation, tumors were collected and measured. **e**–**f**, PPSM tumor bearing animals were treated along the same timeline as Fig. 3a but in the absence of ADT. Average tumor growth (**e**) and survival curves (**f**) of tumor bearing animals treated with combination therapy in the presence or absence of ADT (data depict one representative experiment of two experiments, 8 animals per group). **g**, Survival curves of PPSM tumor bearing animals orchiectomized or not at day 7 (5 animals per group). **h**, Average tumor growth of PPSM tumor bearing animals treated with combination therapy and α-CD8 depleting antibody (data depict one representative experiment of two experiments, 10 animals per group). Error bars represent S.E.M. Two-way ANOVA was used for **c**, **e** and **h**, and log-rank (Mantel-Cox) was used for **f** and **g**.

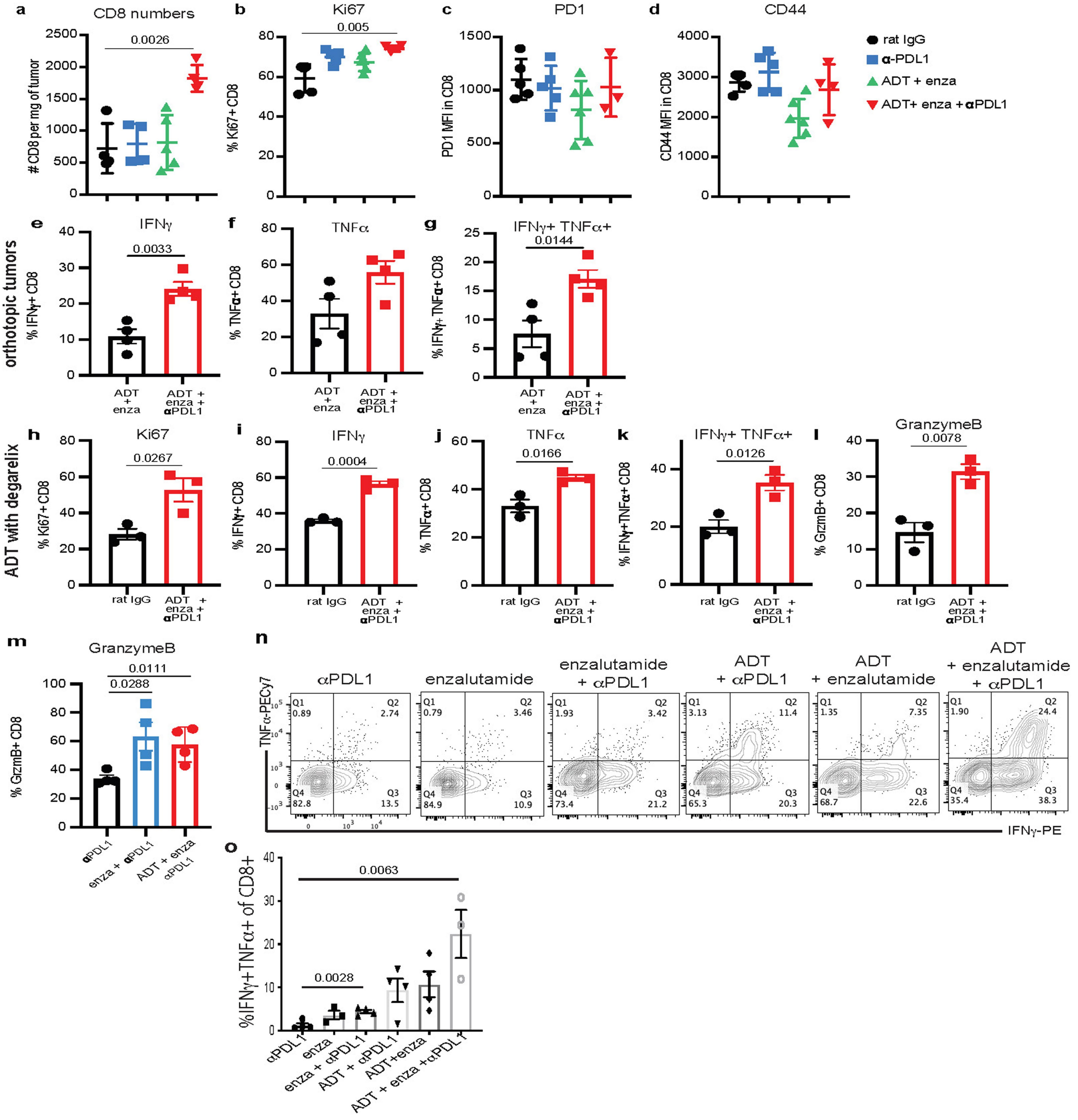

Extended Data Fig. 6 | Phenotyping data of tumor infiltrating CD8 T cells from orthotopic PPSM tumors, degarelix treated, and enzalutamide + anti-PD-L1 treated. a–d, PPSM tumor bearing animals were treated as in Fig 3a. CD8 T cell number (**a**), Ki67 expression (**b**), PD-1 MFI (**c**) and CD44 MFI (**d**) in CD8 T cells in the tumor the day after the 3rd treatment with α-PD-L1. Data representative of 3 independent experiments with 3 animals per group. **e–g**, PPSM tumor cells were surgically injected orthotopically in the prostate, and orchiectomy was performed. One week later, animals were treated with enzalutamide only or enzalutamide + α-PD-L1 (5 animals per group). 4 weeks post tumor inoculation, tumors were harvested and processed for flow cytometry. Graphs show percent IFNγ+ (**e**), TNFα+ (**f**) and IFNγ+TNFα+ double producing (**g**) CD8 T cells in the tumor (n = 5 animals). **h–l**, PPSM tumor bearing animals underwent ADT (degarelix, 1 dose, d14 post tumor inoculation), enzalutamide (started at d14) and α-PD-L1 (3 doses, d14, 17, 20). Tumors were harvested on day 21 and processed for flow cytometry. Graphs show percent Ki67+ (**h**), IFNγ+ (**i**), TNFα+ (**j**), IFNγ+TNFα+ (**k**) and granzyme B+ (**l**) CD8 T cells in the tumor. Data representative of 2 independent experiments with 3 animals per group. **m–o**, PPSM tumor bearing animals were treated with the same timeline as in Fig. 3a, but with enzalutamide + α-PD-L1 or ADT + α-PD-L1. Tumors were harvested the day after the 3rd dose of α-PD-L1 and processed for flow cytometry. **m**, Percent granzyme B+ CD8 T cells in the tumor. **n**, Representative flow cytogram showing IFNγ and TNFα expression in CD8 T cells in the tumor, and **o**, Summarized percent IFNγ+TNFα+ CD8 T cells in the tumor. Data representative of 2 independent experiments with 3 animals per group. Error bars represent S.E.M. Two-tailed unpaired Student *t*-test.

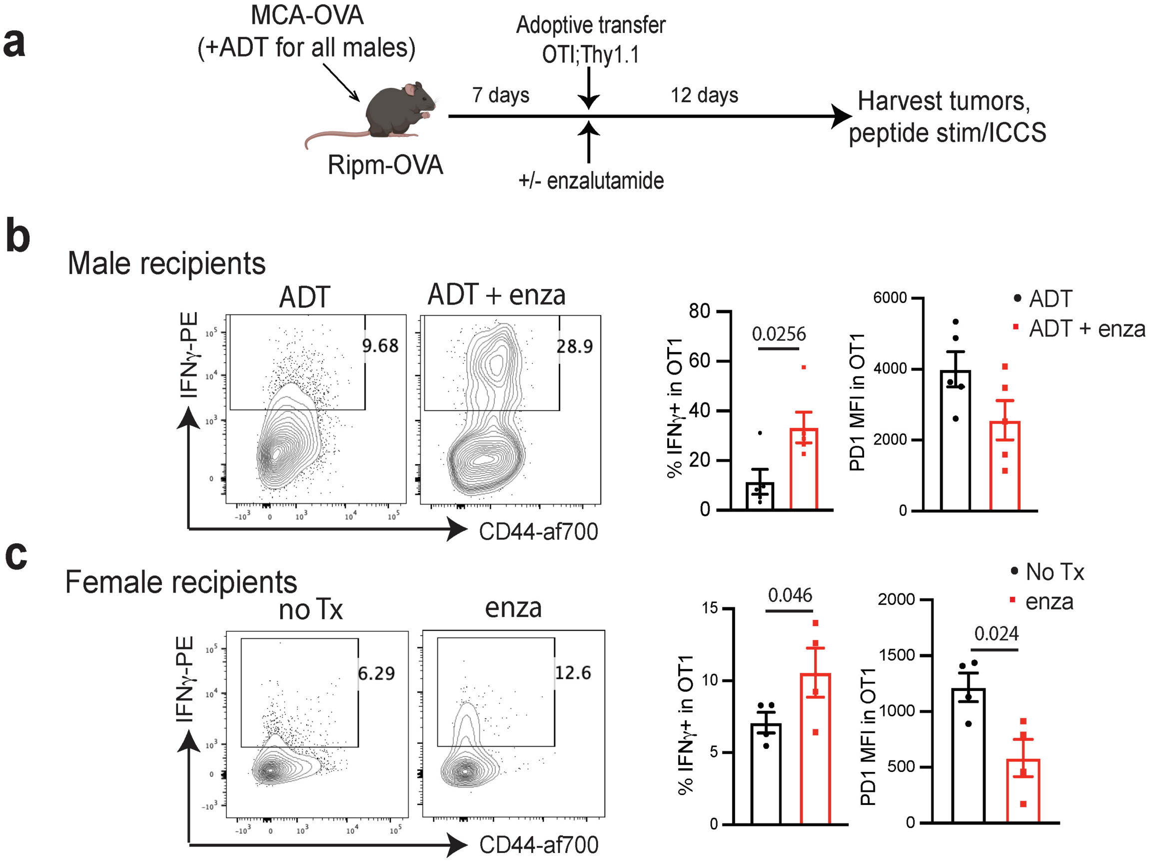

Extended Data Fig. 7 | Enzalutamide treatment leads to increased cytokine production in tumour specific T cells. a, Experimental design. Male or female Ripm-OVA animals were implanted with MCA-OVA tumours. Male animals were treated with ADT (degarelix) at time of tumour inoculation. At d7 animals were adoptively transferred with OT1;Thy1.1 CD8 T cells, and half of the animals were started on enzalutamide treatment (5 animals per group). 12 days post adoptive transfer, tumors were harvested, and TILs were stimulated with SIINFEKL peptide followed by ICCS. **b, c**, Representative flow cytograms showing CD44 and IFNγ expression in OTI T cells in the tumor, and summarized % IFNγ+ and PD-1 MFI in OTI in the tumor in males **(b)** and females **(c)**. Data representative of 2 independent experiments with 5 animals per group ICCS; intra-cellular cytokine staining. Error bars represent S.E.M. Two-tailed unpaired Student *t*-test.

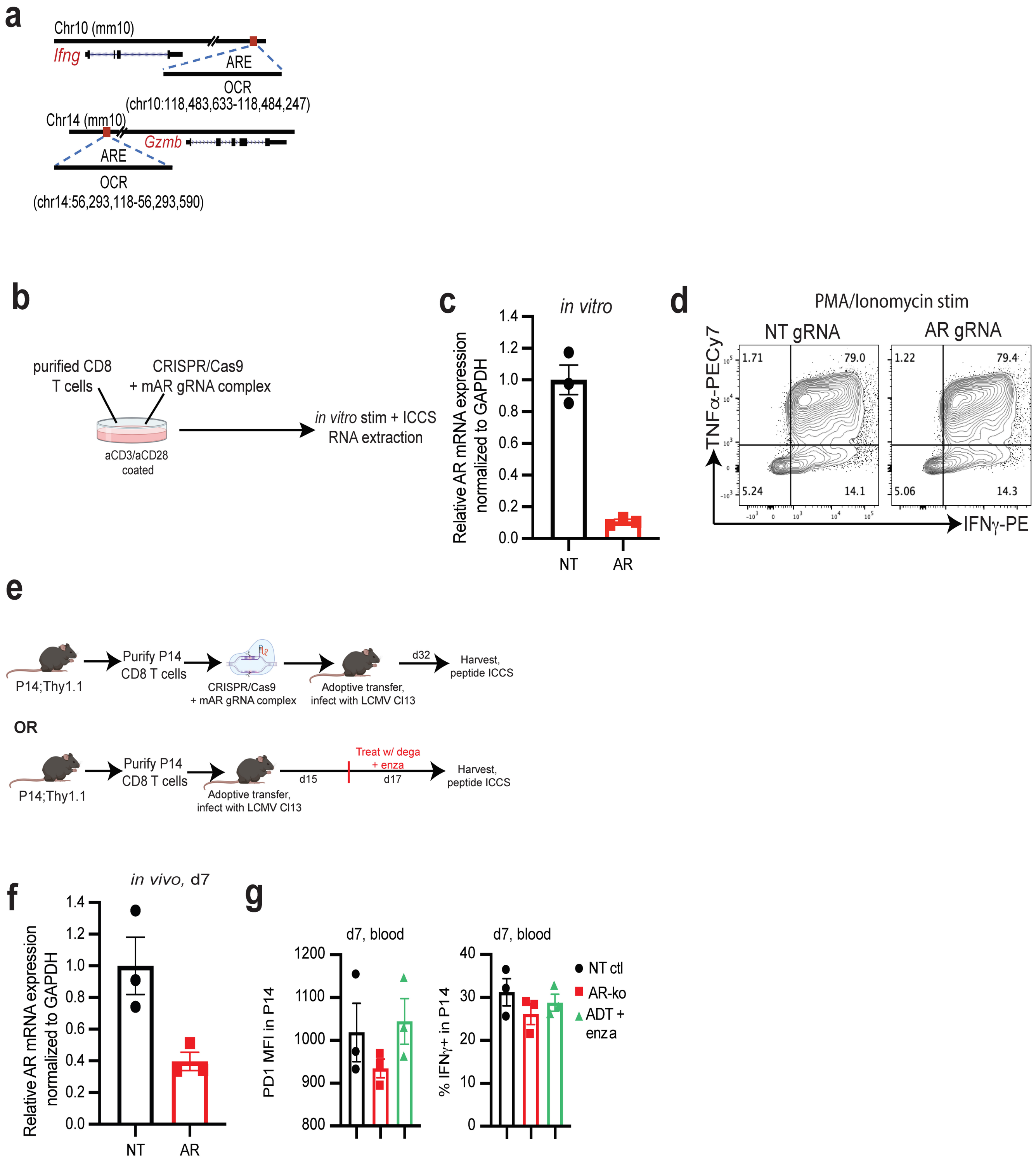

Extended Data Fig. 8 | T cell deletion of *Ar*. **a**, Open chromatin regions (OCRs) containing predicted androgen receptor elements (AREs) in *Ifng* and *Gzmb* loci. **b**, Experimental design of the generation of *Ar*-KO CD8 T cells *in vitro* using CRISPR/Cas9. Purified CD8 T cells were electroporated with Cas9/gRNA complex (NT or AR gRNA), and put in culture *in vitro* for 3 days in plates coated with α-CD3 and α-CD28. 3 days later, stimulated cells were harvested, and RNA was extracted or cells were restimulated *in vitro* for 5 h with PMA/Ionomycin, followed by ICCS (made with www.BioRender.com). **c**, *Ar* mRNA levels by qPCR in CD8 T cells electroporated with non-targeting (NT) or *Ar* gRNA/Cas9 after 3 days of *in vitro* stimulation. Data representative of 4 independent experiments with 3 replicate wells. **d**, Representative flow cytograms of IFNγ and TNFα expression after restimulation with PMA/Ionomycin. **e**, Schematic of LCMV experiment (made with www.BioRender.com), 3 animals per group. **f**, *Ar* mRNA levels in purified P14 at day 7 post adoptive transfer (from experiment described in Fig. 4e–g). Data representative of 2 independent experiments with 3 replicate wells. **g**, PD1 MFI and percent IFNγ+ in P14 in the blood at day 7 post adoptive transfer. Error bars represent S.D. for c and f, and S.E.M for g.

Appendix III: Androgen receptor inhibition increases MHC class I expression and improves immune response in prostate cancer

I am a contributing author for the following manuscript that was published in *Cancer Discovery* in 2025 and is being included here in an unedited form. I contributed data from the neoadjuvant trial described in **Chapter** 3 for response to reviewers during the peer review process.

Androgen Receptor Inhibition Increases MHC Class I Expression and Improves Immune Response in Prostate Cancer

Lisa N. Chesner[1,2], Fanny Polesso[3], Julie N. Graff[4,5], Jessica E. Hawley[6,7], Alexis K. Smith[1,2], Arian Lundberg[1,2,18], Rajdeep Das[1,2], Tanushree Shenoy[1,8], Martin Sjöström[1,2], Faming Zhao[9], Ya-Mei Hu[9], Simon Linder[10], William S. Chen[1,2], Reed M. Hawkins[3], Raunak Shrestha[1,2], Xiaolin Zhu[1,8], Adam Foye[1,8], Haolong Li[1,2], Lisa M. Kim[1,2], Megha Bhalla[1,2], Thomas O'loughlin[1,11], Duygu Kuzuoglu-Ozturk[1,11], Junjie T. Hua[1,2], Michelle L. Badura[1,2], Scott Wilkinson[12], Shana Y. Trostel[12], Andries M. Bergman[10], Davide Ruggero[1,11,13], Charles G. Drake[14,15], Adam G. Sowalsky[12], Lawrence Fong[1,6,7,8], Matthew R. Cooperberg[1,11,16], Wilbert Zwart[10], Xiangnan Guan[9], Alan Ashworth[1,8], Zheng Xia[4,9,17], David A. Quigley[1,11,16], Luke A. Gilbert[1,11], Felix Y. Feng[1,2,8,11], and Amy E. Moran[3,4]

ABSTRACT Tumors escape immune detection and elimination through a variety of mechanisms. Here, we used prostate cancer as a model to examine how androgen-dependent tumors undergo immune evasion through downregulation of the major histocompatibility complex class I (MHCI). We report that response to immunotherapy in late-stage prostate cancer is associated with elevated MHC expression. To uncover the mechanism, we performed a genome-wide CRISPR interference (CRISPRi) screen and identified androgen receptor (*AR*) as a repressor of the MHCI pathway. Syngeneic mouse models of aggressive prostate cancer deficient in *Ar* also demonstrated increased tumor immunogenicity and promoted T cell–mediated tumor control. Notably, the increase in MHCI expression upon AR blockade is transient and correlates with resistance to AR inhibition. Mechanistic studies identified androgen response elements upstream of MHCI transcription start sites which increased MHCI expression when deleted. Together, this body of work highlights another mechanism by which hormones can promote immune escape.

SIGNIFICANCE: Immunotherapy options for immune cold tumors, like prostate cancer, are limited. We show that AR downregulates MHCI expression/antigen presentation and that AR inhibition improves T-cell responses and tumor control. This suggests that treatments combining AR inhibitors and checkpoint blockade may improve tumor immune surveillance and antitumor immunity in patients.

---

[1]Helen Diller Family Comprehensive Cancer Center, University of California, San Francisco, San Francisco, California. [2]Department of Radiation Oncology, University of California, San Francisco, San Francisco, California. [3]Department of Cell, Developmental and Cancer Biology, Oregon Health and Science University, Portland, Oregon. [4]Knight Cancer Institute, Oregon Health and Science University, Portland, Oregon. [5]VA Portland Health Care System, Portland, Oregon. [6]Department of Medicine, University of Washington, Seattle, Washington. [7]Clinical Research Division, Fred Hutch Cancer Center, Seattle, Washington. [8]Divsion of Hematology and Oncology, Department of Medicine, University of California, San Francisco, San Francisco, California. [9]Department of Biomedical Engineering, Oregon Health & Science University, Portland, Oregon. [10]Division of Oncogenomics, Oncode Institute, The Netherlands Cancer Institute, Amsterdam, the Netherlands. [11]Department of Urology, University of California San Francisco, San Francisco, California. [12]Genitourinary Malignancies Branch, National Cancer Institute, Bethesda, Maryland. [13]Department of Cellular and Molecular Pharmacology, University of California, San Francisco, San Francisco, California. [14]Department of Medicine, Herbert Irving Comprehensive Cancer Center, Columbia University, New York, New York. [15]Department of Urology, Herbert Irving Comprehensive Cancer Center, Columbia University, New York, New York. [16]Department of Epidemiology and Biostatistics, University of California, San Francisco, San Francisco, California. [17]Center for Biomedical Data Science, Oregon Health & Science University, Portland, Oregon. [18]Department of Protein Science, SciLifeLab, KTH Royal Institute of Technology, Stockholm, Sweden.

F.Y. Feng and A.E. Moran contributed equally to this article.

Current address for R. Das, University Hospitals Cleveland Medical Center and Case Western Reserve University School of Medicine, Cleveland, Ohio; and current address for C.G. Drake, Janssen R&D, Spring House, Pennsylvania.

Corresponding Authors: Amy E. Moran, Department of Cell, Developmental and Cancer Biology, Oregon Health and Science University, Knight Cancer Research Building, Room 3006, 2720 S Moody Avenue, Portland, OR 97201. E-mail: moranam@ohsu.edu; and Felix Y. Feng, Department of Radiation Oncology, University of California, San Francisco, Box 3110, Room 450, 1450 3rd Street, San Francisco, CA 94158. E-mail: Felix.Feng@ucsf.edu

Cancer Discov 2025;15:481–94

doi: 10.1158/2159-8290.CD-24-0559

INTRODUCTION

A fundamental component of antitumor immunity is the expression of the major histocompatibility complex class I (MHCI) on tumor cells. In the past decade, mechanisms of immune escape via loss of MHCI have been described (1–6). Furthermore, resistance to immune checkpoint blockade (ICB) is associated with loss of MHCI (5). Given this, efforts have been invested toward understanding the mechanisms of immunotherapy resistance. Some seem to be shared between tumor types (i.e., PD-1+ lymphocytes) and others unique to the tissue of origin (6–8). It is plausible that just as viruses utilize distinct immune evasion tactics based on tissue tropism, cancer cells might have mechanisms of immune evasion that reflect unique attributes of their tissue microenvironment and/or oncogene addiction. In this regard, prostate cancer represents an appropriate disease for investigating the crosstalk between androgens and tumor immune evasion.

Prostate cancer, as compared with lung cancer, has a low response rate to ICB and markedly lower MHCI expression (Fig. 1A; refs. 1, 9, 10). The molecular mechanisms that control MHCI expression in prostate cancer remain unknown despite evidence that androgen deprivation therapy (ADT) is initially immunogenic, recruiting leukocytes into the tissue (11, 12). In a clinical trial designed to investigate the early effects of ADT on the prostate tumor landscape, there was an initial infiltration of mononuclear cells that corresponded to increased cell death (13). By week 4 after ADT initiation, tumor cell death plateaued, as did the infiltration of mononuclear cells. Despite evidence of ADT-induced immunogenicity, prostate cancer immunotherapy trials are repeatedly negative. Therefore, there is a critical need to understand the mechanisms of immunotherapy resistance in this disease.

In this study, we employed a genome-wide CRISPR interference (CRISPRi) flow cytometry-based screen to identify the regulators of MHCI in prostate cancer cells. Significant hits involved in androgen receptor (*AR*) signaling were validated as suppressors of MHCI using *in vitro* and *in vivo* models as well as observed in four phase II clinical trials. Interestingly, the top regulators of MHCI in prostate cancer were distinct from those recently identified in a similar immune evasion CRISPR screen in AML (2) or reported in melanoma (4–6). Thus, these screens undoubtedly help identify disease-specific regulators of immune evasion to inform tumor-specific combination therapies and improve ICB efficacy in MHC-low tumors, such as prostate cancer.

RESULTS

AR Represses MHCI in Prostate Cancer

We previously reported that one mechanism of ICB resistance in advanced prostate cancer is through AR suppression of CD8 T-cell function (14). Using the same dataset, we observed an increased MHCI expression in ICB responders (Fig. 1B). To explore MHCI regulation in prostate cancer, we conducted a genome-wide CRISPRi screen using a metastatic castration-resistant prostate cancer (mCRPC) line, C42B, stably expressing a non-catalytic Cas9 (dCas9-KRAB fusion protein). Cells were infected (15), selected, and sorted based on highest and lowest (25%–30%) MHCI expression (Fig. 1C). Gene hits were ranked by phenotype score (Fig. 1D; Supplementary Table S1). As expected, gene hits in the MHCI processing pathway (*B2M*, *TAP1*, *HLA-A*, *TAPBP*, *TAP2*, and *IRF2*) decreased MHCI expression upon knockdown. Interestingly, suppression of *AR* increased MHCI expression. AR coregulators (16, 17), *GRHL2* and *FOXA1*, were also shown to significantly increase MHCI expression upon knockdown. We validated these findings by knocking down *AR*, *GRHL2*, *FOXA1*, and *B2M* using individual sgRNAs and compared MHCI expression to control (*GAL4*) in C42B and LNCaP cells (Fig. 1E; Supplementary S1A and S1B). These results revealed increased MHCI expression upon knockdown of *AR* and AR signaling genes. Further, knocking down AR genes improved MHCI upregulation in response to interferon gamma (IFNγ) treatment (Supplementary Fig. S1C and S1D). Overexpressed *AR* in the AR-null PC3 prostate cancer cell line demonstrated decreased MHCI processing and presentation genes and expression in *AR*-positive PC3 cells compared with *AR*-null cells (Fig. 1F–H).

Pharmacologic Inhibition of AR Modulates MHCI

sgRNA gene targeting has variable knockdown efficiency (Supplementary Fig. S1E and S1F); thus, we treated C42B cells with various AR inhibitors and observed increasing MHCI over time (Fig. 2A). Expression of MHCI-associated genes/protein could be repressed by the exogenous AR ligand R1881 (Fig. 2B; Supplementary Fig. S2A and S2B). Additional prostate cancer models with various *AR* expression levels (C42B, LNCaP, VCaP, PC3) were treated with enzalutamide (Fig. 2C–F), the AR degrader (ARD; Supplementary Fig. S2C–S2F; refs. 18, 19), or CSS (Supplementary Fig. S2G–S2J) and also demonstrated increased expression of MHCI and antigen presentation genes. Given AR inhibition is reported to induce type I interferons (20, 21), we evaluated interferon response genes following enzalutamide treatment and observed an increase in a few genes (Supplementary Fig. S2K).

Notably, we observed a rapid drop of MHCI within a week after removing AR inhibition, which returned to baseline by 2 weeks (Fig. 2G), suggesting active AR inhibition is required to maintain MHCI. To determine the stability of elevated MHCI with AR inhibition, C42B cells were treated with enzalutamide and MHCI expression measured over 3 months revealing two phases of sensitivity to androgen blockade and MHCI expression. In the first 30 days, MHCI expression was significantly increased, corresponding with growth arrest (Fig. 2H), followed by loss of expression and tumor cell growth. Curious if this was associated with AR reactivation, we evaluated the mRNA expression via RNA sequencing (RNA-seq) at 28, 49, and 91 days posttreatment (Fig. 2I; Supplementary Tables S2A–S2C). Interestingly, loss of MHCI is proceeded by an increase in *NR3C1*, the glucocorticoid receptor (Fig. 2J).

AR Transcriptionally Represses MHCI Gene Expression

To determine if AR regulated MHCI through binding to androgen response elements (ARE), we identified AREs within 10 kb of MHCI transcriptional start sites (TSS) and designed sgRNAs to target these sites using Cas9 nuclease (Supplementary Table S3). We conducted a lentiviral pooled CRISPR

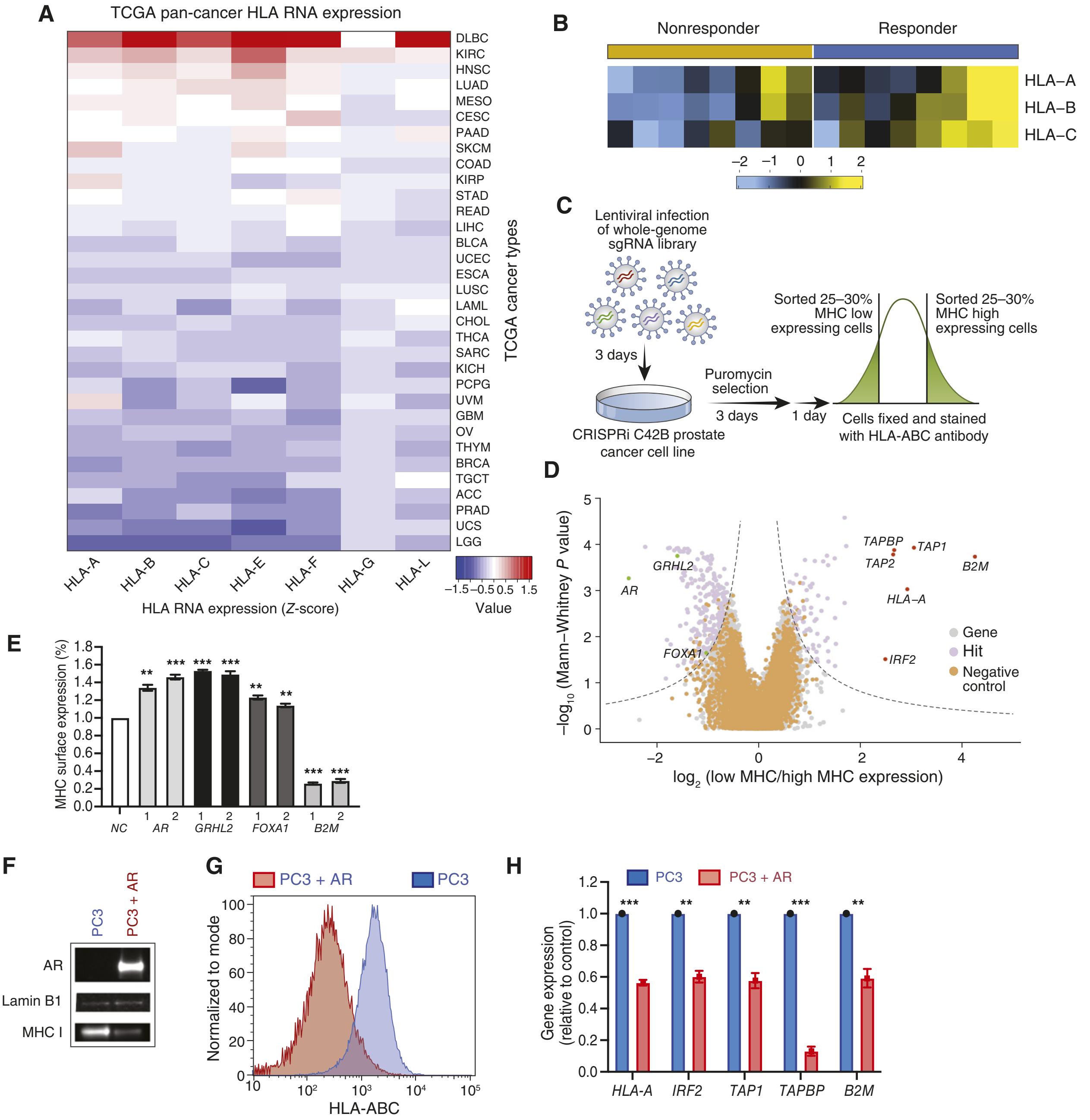

Figure 1. *AR* represses MHCI in prostate cancer. **A,** Heatmap of median RNA expression of HLA genes in the TCGA Pan Cancer cohort. **B,** Heatmap of scaled RNA expression of MHC genes in nonresponders and responders to pembrolizumab treatment of patients with mCRPC. **C,** Schematic of a genome-wide CRISPRi screen based on surface expression of MHCI in C42B-dCas9 prostate cancer cells. **D,** Volcano plot showing Mann–Whitney statistical significance and average phenotype score of gene hits (purple) and negative controls (orange). **E,** MHCI expression of C42B-dCas9 cells infected with sgRNAs targeting *GAL4* (control), *AR*, *GRHL2*, *FOXA1*, or *B2M* ($n = 3$ as biological replicates; mean ± SEM). **F–H,** MHCI expression assessed using Western blot (**F**), flow cytometry (**G**), or qRT-PCR (**H**) of *AR*-null or *AR*-positive PC3 cells. ** p<0.01, *** p<0.001.

screen targeting 41 AREs, as well as *AR*, *GRHL2*, and *FOXA1* (positive controls) and *B2M*, *HLA-A*, and *TAP* genes (negative controls; Fig. 2K). The screen confirmed that *AR*, *FOXA1*, and *GRHL2* inhibition increased MHCI expression and knockout of *B2M*, *TAP*, and *HLA-A* decreased MHCI expression (Fig. 2L). ARE motifs in *NLRC5*, *CANX*, *TAP2*, *TAP1*, and *IRF2* were individually targeted using sgRNAs, single-cell cloned, and confirmed on-target cutting efficiency. ARE-deleted clones showed increased MHCI expression by flow cytometry (Fig. 2M) and qRT-PCR (Fig. 2N). We also utilized publicly available ChIP-seq data (22) to query AREs targeted in our CRISPR screen and found decreased *AR* binding (Fig. 2O; Supplementary Fig. S3A and S3B) and increased H3K27ac (Supplementary Fig. S3C and S3D) after enzalutamide treatment.

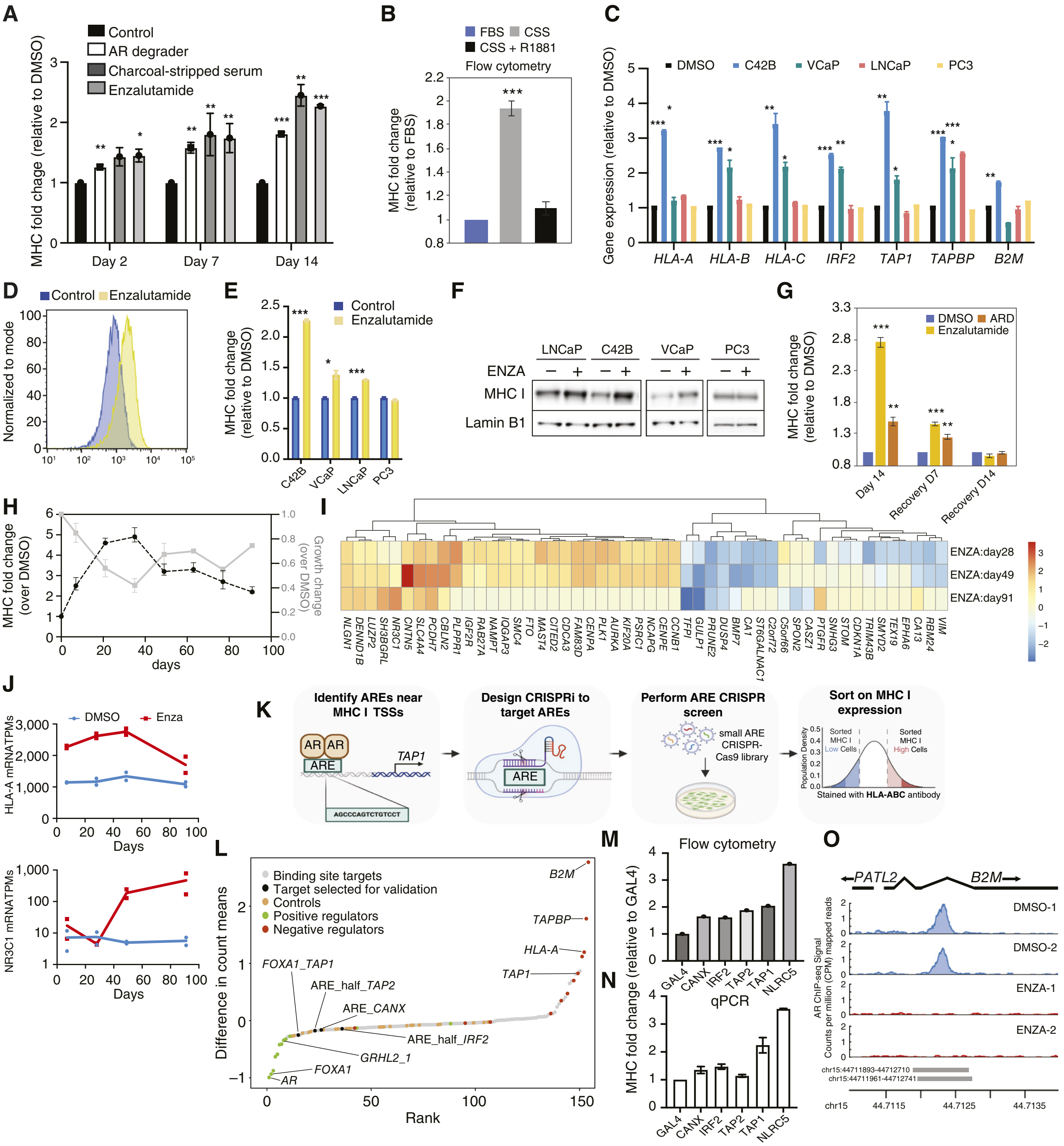

Figure 2. *AR* transcriptionally represses MHCI expression. **A,** MHCI expression of C42B cells treated with ARD-61, CSS, or enzalutamide for 2, 7, or 14 days (*n* = 3 as biological replicates; mean ± SEM). **B,** MHCI expression of C42B cells treated with CSS for 14 days with or without R1881 (*n* = 3 as biological replicates; mean ± SEM). **C–F,** C42B, VCaP, LNCaP, and PC3 cells treated with enzalutamide for 14 days. **C,** Gene expression of MHCI processing genes (*n* = 3 as biological replicates; mean ± SEM), (**D**) C42B cells stained with an HLA-ABC antibody, (**E**) MFI of cells stained with an HLA-ABC antibody (*n* = 3 as biological replicates; mean ± SEM), and (**F**) MHCI protein levels. **G,** MHCI expression of C42B cells treated with either ARD-61 or enzalutamide for 14 days after which the drug was removed and MHC expression assessed 7 or 14 days later (*n* = 3 as biological replicates; mean ± SEM). **H,** C42B cells treated with DMSO or enzalutamide for 91 days. Black: MFI fold change after staining with an HLA-ABC antibody. Gray: Change in growth compared with DMSO-treated cells (*n* = 3 as biological replicates; mean ± SEM). **I,** Heatmap of effect size on mRNA expression after enzalutamide treatment in C42B cells for the top 50 most significant genes evaluated for treatment × time interaction. **J,** mRNA of *HLA-A* and *NR3C1* (in length-scaled TPM) over time. **K,** Schematic of a CRISPR screen targeting AREs near MHCI TSSs (Created in BioRender. Chesner, L. (2024) BioRender.com/r09b289). **L,** Differences in means of gene hits ranked from a CRISPR screen targeting AR and FOXA1 binding sites near MHCI genes. **M,** MHCI expression of C42B ARE-deficient clones near *CANX*, *IRF2*, *TAP2*, *TAP1*, or *NLRC5*. **N,** Gene expression of *CANX*, *IRF2*, *TAP2*, *TAP1*, or *NLRC5* in ARE-deficient clones compared with *GAL4*. **O,** AR ChIP-seq peak signal around an ARE near the *B2M* promoter (*P* value = 0.001) after DMSO (blue) or enzalutamide treatment (red). Horizontal bars at the bottom indicate ARE. * p<0.05, ** p<0.01, *** p<0.001.

Finally, we treated two control (GAL4) or ARE-deleted (CANX) clones with enzalutamide and assessed MHCI expression after 7 days (Supplementary Fig. S3E–S3G). These experiments showed a larger increase in MHCI expression in the control than in the ARE-deleted clones (Supplementary Fig. S3H), suggesting that the deletion of AREs prevents the transcriptional repression of MHCI genes.

AR Inhibition Increases T-cell Cytotoxicity

To see if increasing MHCI expression by AR inhibition could improve antitumor T-cell responses, we transfected human CD8 T cells with an *HLA-A2*-restricted TCR specific for the cancer testis antigen *NY-ESO1* (Supplementary Fig. S4A). *HLA-A2*-restricted *NY-ESO1*-expressing C42B cells (Fig. 3A) were treated with AR inhibitors, washed, replated, and cocultured with *NY-ESO1*-reactive CD8 T cells. These experiments showed increased T-cell cytotoxicity and a reduction in tumors pretreated with an AR inhibitor compared with control (Fig. 3B and C; Supplementary Fig. S4B–S4E), an observation that was dependent upon MHCI expression on the tumor cells (Fig. 3D; Supplementary Fig. S4D). C42B cells that did not express *NY-ESO1* and cocultured with T cells were not killed when treated with AR inhibitors (Supplementary Fig. S4F), demonstrating that AR inhibition enhances T-cell recognition of target cells in an MHCI-dependent manner.

Tumor Cell-Intrinsic AR Knockdown Increases CD8 T cell–Mediated Antitumor Immunity

To explore our observation *in vivo*, the TrampC1 tumor model, which has a known MHCI-restricted tumor antigen, stimulator of prostatic adenocarcinoma (*Spas-1*; ref. 23), and low expression of MHCI, and the PPSM (*Pten*−/−; *p53*−/−; *Smad4*−/−) model, which is androgen insensitive, were employed (24). We knocked down *Ar* (*Ar*-KD; Supplementary Fig. S5A and S5B), generated single-cell clones, and observed comparable growth *in vitro* to wild-type (WT) cells (Supplementary Fig. S5C and S5D). Loss of *Ar* in TrampC1 cells increased MHCI expression (Fig. 3E) and sensitivity to IFNγ-induced MHCI expression (Fig. 3F). *In vivo* (Fig. 3G), TrampC1 *Ar*-KD tumors were significantly smaller (Fig. 3H), and the number of tumor-infiltrating CD8 T cells was significantly greater in *Ar*-KD tumors (Fig. 3I). Using the *Nur77*GFP mouse in which GFP is upregulated by TCR engagement (25) and can be used as a tool to identify tumor-reactive T cells that recently received strong TCR signals (26), we observed significantly increased *Nur77*GFP^{hi} CD8 T cells in *Ar*-KD tumors (Fig. 3J). Furthermore, we recovered more *Spas1* tetramer-positive CD8 T cells in *Ar*-KD tumors (Fig. 3K and L; Supplementary Fig. S5E) and upon stimulation observed a significant increase in the total number of IFNγ-producing CD8 T cells in *Ar*-KD tumors compared with WT (Fig. 3M and N). Finally, we explored the requirement for T cell–mediated tumor control in our models. In the absence of lymphocytes (*Rag*-KO), we observed no difference in tumor growth in *Ar*-KD versus WT (Fig. 3O and P) and extended these observations into the PPSM model (Supplementary Fig. S5F–S5H). Overall, our data suggest that loss of tumor-intrinsic *Ar* expression increases MHCI expression and the frequency and function of tumor-specific CD8 T cells, enhancing tumor control.

MHCI Expression Increases following *AR* Inhibition in Patients with Prostate Cancer

Last, we explored evidence for androgen axis-targeted therapies modulating MHCI in patients. We analyzed RNA expression data from a phase 2 clinical trial that studied the effects of enzalutamide in early prostate cancer (NCT03297385; ref. 27). Paired biopsies from treatment-naïve patients and 3 months after neoadjuvant enzalutamide treatment without ADT showed significantly increased transcription of *HLA-A* and *B2M* and MHC-regulating genes *IRF1* and *IRF2* posttreatment (Fig. 4A) and an enrichment of interferon activity (Supplementary Fig. S6A). These data were consistent with data from a second cohort of patients (NCT02430480) treated for 6 months with neoadjuvant ADT plus enzalutamide (Fig. 4B; Supplementary Fig. S6B; ref. 28). Pathway analysis of these paired biopsies also revealed an increase in antigen presentation (Supplementary Tables S4 and S5). To determine if this correlation was observed in lethal, metastatic castration-resistant disease, we generated an MHCI signature (see “Methods”), applied it to a hormone-refractory metastatic prostate cancer biopsy dataset (29), and observed a significant negative correlation between MHCI activity and *AR* activity (Fig. 4C).

To determine if there was clinical significance to our observations in the context of immunotherapy, we leveraged a single-cell dataset in metastatic hormone-sensitive prostate cancer (mHSPC; ref. 30). Two groups of patients permitted analysis of tumor cell-intrinsic changes in MHCI with ADT (on ADT) versus ADT with anti-PD1 (on combination). Cells from all patients were combined and clustered into hematopoietic and non-hematopoietic cells (Fig. 4D; Supplementary Fig. S6C). There was a distinct luminal epithelia cell cluster (EPCAM+AR+TMPRSS2+, Supplementary Fig. S6C), which we evaluated for pretreatment *AR* and MHCI gene expression. Pretreatment lesions had low MHCI processing and presentation gene expression and high *AR* and *AR* target genes (Fig. 4E). Using the Virtual Inference of Protein-activity by Enriched Regulon analysis (VIPER) to infer protein activity (31), we observe decreased *AR* activity and a corresponding increase in MHCI activity with treatment (Supplementary Fig. S6D and S6E). Isolating only epithelial cells, we observed a clear conserved reduction of *AR* activity in paired individual biopsies in both treatment groups with a strong increase in MHCI with ADT that was further increased with ADT+anti-PD1 (Fig. 4F and G). The increased MHCI with anti-PD1 treatment likely reflects an increase in T-cell-derived IFNγ activity (14) that was not observed with ADT alone but was significantly increased with ADT+anti-PD1 (Supplementary Fig. S6F and S6G).

DISCUSSION

Immunotherapy has become a mainstay of the oncology landscape for many solid tumors. In prostate cancer, the low response rate to immunotherapy has been seen as a failure of the treatment to restore T-cell function. However, an alternative hypothesis is plausible; failure of immunotherapy responses in patients with prostate cancer reflects our

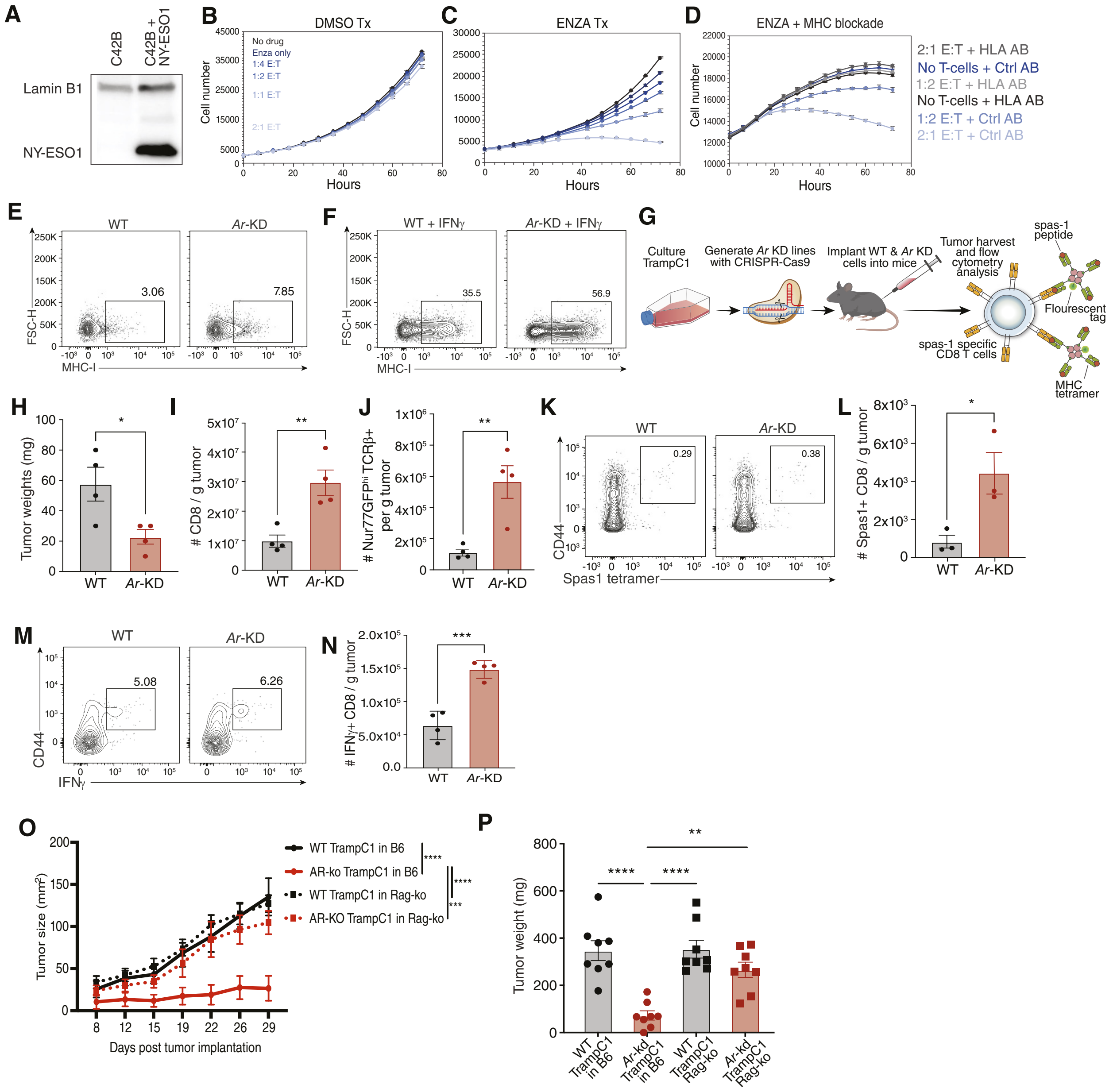

Figure 3. *AR* inhibition increases T-cell cytotoxicity *in vitro* and *in vivo*. **A,** Expression of *NY-ESO1* in C42B cells. **B** and **C,** *NY-ESO1*-expressing C42B cells treated with either DMSO (**C**) or enzalutamide (**D**) for 14 days and then cocultured with CD8 T cells transduced with a *NY-ESO1* TCR for 3 days. **D,** *NY-ESO1*-expressing C42B cells treated with enzalutamide for 14 days and then cocultured with CD8 T cells transduced with a *NY-ESO1* TCR for 3 days in the presence of an HLA-blocking antibody or control antibody. **E** and **F,** MHCI expression of WT or *Ar*-KD TrampC1 cells without (**E**) or with (**F**) rIFNγ treatment. **G,** Schematic of *in vivo* TrampC1 tumor experiment. **H,** Tumor weights at time of harvest (day 12 posttumor implantation). **I,** Number of CD8 T cells in WT or *Ar*-KD TrampC1 tumors. **J,** Number of *Nur77*-GFP+ T cells in WT or *Ar*-KD TrampC1 tumors. **K,** Representative cytograms showing CD44 and *Spas1* tetramer staining in the tumor. Gated on live, TCRβ+, CD8+. **L,** Number of *Spas1* tetramer + CD8 T cells in the tumor. **M,** Representative cytograms showing CD44 and IFNγ expression in CD8 T cells in the tumor. Gated on live, TCRβ+, CD8+. **N,** Number of IFNγ-expressing CD8 T cells in the tumor. **O,** Growth curves of WT and *Ar*-KD TrampC1 tumors in WT and *Rag*-KO animals. **P,** Tumor weights on day 29. Data representative of two to four independent experiments, with three to four animals per group for **D–J** and eight animals per group for **K** and **L**. For **D–F**, **H**, and **J**, unpaired two-tailed Student *t* test. For **K** and **L**, Two-way ANOVA, *, $P < 0.05$; **, $P < 0.01$; ***, $P < 0.001$; ****, $P < 0.0001$.

limited understanding of what regulates immunity in this tissue microenvironment. In this regard, we set out to identify regulators of MHCI in prostate cancer with the goal of understanding the mechanisms of response and resistance in this disease. Importantly, our investigation herein compliments a previous report that *AR* inhibition leads to aberrant endogenous retrovirus regulation, thereby inducing type I interferons and MHCI (21), a mechanism that is likely synergistic with the work presented here.

The interaction between hormones and immune responses is extremely complex with cell-intrinsic and cell-extrinsic mechanisms at play. There is growing evidence that the sexual

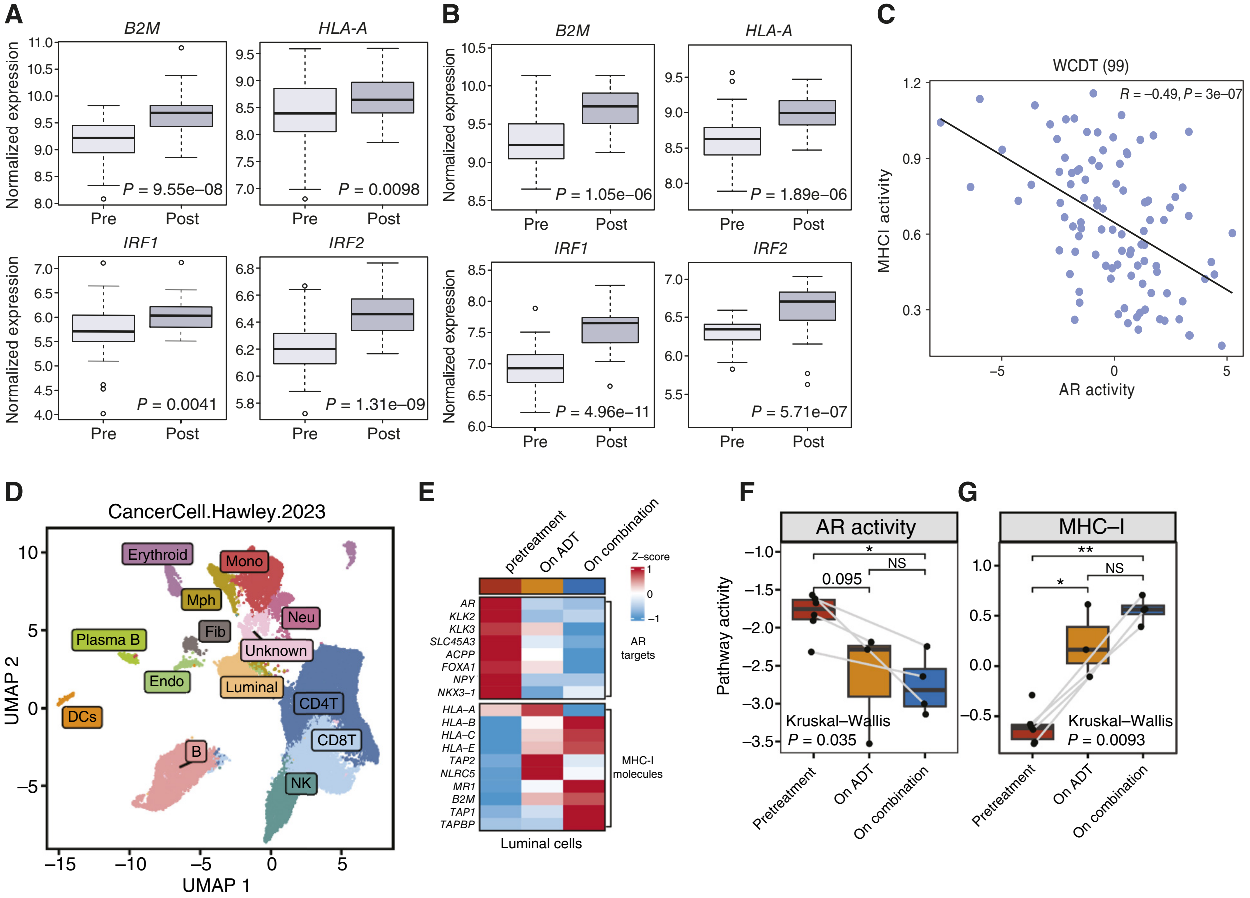

Figure 4. MHCI expression increases following AR inhibition in patients with prostate cancer. **A,** Bulk RNA expression of MHCI-related genes from primary prostate cancer tissues before and after 3 months of neoadjuvant enzalutamide treatment without ADT. **B,** Bulk RNA expression of MHCI-related genes from paired prostate tissues pre- and posttreatment with 6 months neoadjuvant ADT plus enzalutamide. **C,** Scatterplot showing the correlation between AR activity and MHCI activity in WCDT cohort ($n = 99$). Statistical significance was evaluated using two-tailed Pearson's correlation test. **D,** UMAP showing the distribution of 14 major cell types from human PCa scRNA-seq dataset (30). DCs, dendritic cells; Endo, endothelial cells; Fib, fibroblasts; Mono, monocytes; Mph, macrophages; Neu, neutrophils. +ADT = 4 weeks after ADT, +ADT + anti-PD1 = 10 weeks after ADT+anti-PD1 and/or upon recurrence. **E,** Heatmap illustrating expression (*Z*-score normalization) of genes associated with indicated pathways within luminal cells among different treatment groups. On combination, ADT+anti-PD1 treatment group. **F** and **G,** Box plots showing the activity of *AR* (**F**) or MHCI (**G**) pathways within luminal cells among treatment groups from the PCa scRNA-seq dataset. Each dot represents an individual sample of PCa. Paired patient analysis (indicated by gray line); NS, not significant ($P \geq 0.05$); *, $P < 0.05$; **, $P < 0.01$.

dimorphism observed in inflammatory diseases, such as cancer, is in part mediated by androgen signaling (32–36). In a recent study of individuals receiving gender-affirming hormone therapy, testosterone treatment repressed antigen presentation pathways in circulating monocytes (37). In another study, 17 different mouse tissues were profiled to reveal sex differences mediated by androgens, and of the top 10 genes differentially expressed in male and female mice, 9 were MHCI genes (38). Together, these recent bodies of work highlight the immunomodulatory nature of androgens but come up short in providing a mechanism. Herein, we provide a mechanistic link via *AR* which directly represses MHCI expression (Supplementary Fig. S7). Interestingly, in a phase I clinical trial in men with nivolumab-refractory melanoma, patients were treated for 28 days with an *AR* axis inhibitor in an effort to make them sensitive to immunotherapy. A RECIST of 42.8% was reported in this small study (39), suggesting the potential clinical application of androgen axis inhibition in improving immunotherapy responses in other tumors that have hijacked androgen signaling to evade immunity.

Our investigation of AR regulation of MHCI expression also revealed a temporal period in which androgen axis blockade was immunostimulatory. Over 91 days, early androgen axis inhibition was immunomodulatory and corresponded with tumor cell growth arrest. As the tumor cells transitioned from a period of arrest to growth, MHCI expression also decayed. Notably, under chronic AR inhibition, tumor cells increased *GR* expression prior to loss of MHCI, suggesting a possible transition of AR- to GR-mediated repression of MHCI (40). GR-conferred repression of MHCI upon chronic *AR* inhibition is perhaps not surprising as this has been reported for tumor cell survival in other prostate cancer models (41). Unique to our discovery is the idea that perhaps GR promotes immune evasion in addition to cell survival.

Finally, our observation of a potential AR-to-GR switch is interesting considering the design of immunotherapy clinical trials in prostate cancer and standard of care treatment for this patient population. The KEYNOTE 991 trial (35) was the largest clinical study to date that tested the hypothesis that early combination of androgen axis inhibition with immunotherapy in patients with mHSPC would be effective. Unfortunately, the trial was ended due to a lack of signal in combination therapy over the control arm. The trial was designed to enroll patients with no prior history of androgen axis blockade; however, patients were allowed to be treated for up to 3 months with ADT prior to starting immunotherapy. Given the work of others, as well as data presented herein, androgen axis blockade might be initially immunogenic but then lost due to the activation of other nuclear receptors that repress MHCI. Future immunotherapy clinical trials should be designed to harness the window of ADT-induced immunogenicity and/or the development of biomarkers to identify patients for which androgen axis blockade remains immunogenic.

METHODS

Cell Lines and Reagents

Most cell lines were originally purchased from the ATCC and cultured following standard ATCC protocols. C42B-dCas9 and LNCaP-dCas9 cell lines [generated by Das and colleagues (RRID: CVCL_0395; ref. 42)] and TrampC1 cells were cultured in RPMI 1640 medium (Gibco) with 10% (Gibco) and 5% penicillin/streptomycin (Invitrogen). VCaP (RRID:CVCL_2235), PC3 (RRID:CVCL_0035), and HEK293T cells (RRID:CVCL_0063) were cultured in DMEM (Gibco) with 10% FBS and 5% penicillin/streptomycin. For *AR*-positive PC3 cells, a lentiviral vector was designed to express *AR*-ORF and mCherry selection marker in PC3 cells. HEK293T cells were transfected with *AR*/mCherry-expressing lentiviral plasmid together with a second-generation psPAX2 (RRID:Addgene_12260) packaging vector and pMD2.G (RRID:Addgene_12259) envelope-expressing plasmid. The virus was harvested 24 and 48 hours post-transfection and precipitated using Lenti-X concentrator (Takara). PC3 cells were transduced with virus in the presence of polybrene (4 μg/mL) for 24 hours, and mCherry-positive cells were sorted using Aria (BD). All cells were grown in a 5% CO_2 humidified incubator at 37°C. Cell line STR authentications were done at the UC Berkeley DNA Sequencing Facility. Mouse *Pten*$^{-/-}$; *p53*$^{-/-}$; *Smad4*$^{-/-}$ (PPSM) castration-resistant prostate tumor model was a gift from R. DePinho. TrampC1 cells were purchased from ATCC (RRID:CVCL_3614). Cell lines were STR authenticated prior to use, tested for mycoplasma monthly, and used under passage 50. Enzalutamide was purchased from Selleckchem, and the AR PROTAC degrader ARD-61 was a gift from Dr. Shaomeng Wang's lab at the University of Michigan (18).

CRISPRi Flow Cytometry Screen

The genome-wide CRISPRi flow cytometry screen was performed using the Weissman lab protocol (weissmanlab.ucsf.edu) with some modifications (43). In brief, C42B-dCas9 cells were generated by infecting C42B cells with a lentivirus containing dCas9-KRAB (KRAB domain, Krüppel-associated box), a repressive chromatin-modifying complex to induce transcriptional silencing. dCas9 (from *Streptococcus pyogenes*) was fused to two copies of a nuclear localization signal, HA tag, and blue fluorescent protein (44). Approximately 132 million C42B-dCas9 cells were then infected in duplicate with a lentivirus containing the CRISPRi-V2 library (RRID:Addgene_1000000093), a kind gift from Dr. Luke Gilbert's lab at UCSF, at an MOI of 0.3 and 8 μg/mL polybrene (TR-1003-G). After 3 days, cells were put into media containing 8 μg/mL puromycin (A11138-03). After another 3 days, cells were placed into drug-free media and allowed to recover for 24 hours. Cells were then harvested and fixed in 4% PFA (5 million cells per 1 mL of PFA solution) at room temperature for 20 minutes, washed with cold 1× PBS, and incubated with human Fc Block (564220) in FACS buffer for 10 minutes at room temperature. An anti-human HLA-ABC antibody was then added (Thermo Fisher Scientific, Cat# 17-9983-42, RRID:AB_10733389) and incubated on ice for 20 minutes in the dark. Finally, cells were washed and resuspended in cold FACS buffer and sorted on a BD FACSAria Fusion cell sorter to collect the 25% to 30% highest and lowest HLA-ABC-expressing cells. This protocol was also followed for the ARE sub-library CRISPR screen in C42B cells, using virus generated as described below. DNA was extracted using the Zymo Quick-DNA FFPE Kit (56404) and amplified for 26 cycles using NEBNext Ultra II Q5 Master Mix (M0544S) and primers containing TruSeq indexes for NGS analysis. Libraries were gel purified and extracted using the Zymoclean Gel DNA Recovery Kit (11-301C) and assessed on a high-sensitivity DNA bioanalyzer kit (5067-4626). Sample libraries were run on a HiSeq 4000 and analyzed using standard protocols (ScreenProcessing) as previously described (43).

Lentivirus Generation and Infection

To validate gene hits from the CRISPRi flow cytometry screen, sgRNA sequences (Supplementary Table S6) were cloned into the pLG20 pU6-sgRNA Ef1 alpha Puro-T2A GFP vector (RRID:Addgene_111596) and lentivirus generated as previously described (42). Cells were plated in a six-well dish at 150,000 cells/well in 2 mL of media and infected with virus the next day with 10 μg/mL polybrene (TR-1003-G). Cells were harvested after 72 hours and analyzed as described above. Gene knockdown was measured by extracting RNA using the Zymo Quick-RNA MiniPrep Kit (R1054), performing cDNA synthesis using SuperScript III First Strand Synthesis Kit (18080051), and conducting qRT-PCR using Fast SYBR Green Master Mix (4385612) all according to the manufacturer's protocols.

Drug Treatments and Antibodies

C42B, LNCaP, VCaP, and PC3 cells were treated in their respective media with either DMSO, 10 μmol/L enzalutamide, or 100 nmol/L ARD for 14 days and refreshed every 5 days at minimum. Cells treated with CSS (Gibco) were maintained in phenol red-free media and refreshed every 7 days at minimum. Cells treated with the synthetic androgen R1881 (10 nmol/L) were refreshed every 3 days. Following 14 days of treatment, cells were harvested for flow cytometry and qRT-PCR (Supplementary Table S7), as described above, or Western blot analysis using anti-*AR* (D6F11), anti-MHCI (OriGene, Cat# AM33035PU-N, RRID:AB_3662758), or anti-Lamin B1 (Cell Signaling Technology, Cat# 15068, RRID:AB_2798695) antibodies. Gene expression of MHCI processing genes (normalized to *GAPDH*) was measured by qRT-PCR and compared with control. Drug-treated cells were stained with a fluorescent HLA-ABC antibody (17-9983-42) and analyzed using flow cytometry. Median fluorescence intensity (MFI) of cells stained with a fluorescent HLA-ABC antibody was measured by flow cytometry and compared with control to determine MHC fold change. MHCI expression of cells infected with sgRNAs targeting *GAL4* (nontargeting control), *AR*, *GRHL2*, *FOXA1*, or *B2M* was measured by flow cytometry and compared with *GAL4* to determine MHC fold change.

RNA Expression Analysis of Neoadjuvant Enzalutamide Patient Samples

Bulk RNA expression analysis of MHCI-related genes was performed on primary prostate cancer tissues before and after neoadjuvant enzalutamide treatment without ADT from the phase 2, prospective, single-arm DARANA study (ClinicalTrials.gov #NCT03297385) at the

Netherlands Cancer Institute Antoni van Leeuwenhoek Hospital. RNA-seq was performed as previously described (27). In brief, RNA from FFPE material was isolated from 2 to 10 sections of 10 μm using the AllPrep DNA/RNA FFPE Kit (Qiagen). cDNA was synthesized from 250 ng of RNA using SuperScript III Reverse Transcriptase (Invitrogen) with random hexamer primers. For RNA-seq, strand-specific libraries were generated with the TruSeq RNA Exome Kit (Illumina) and sequenced on a HiSeq 2500 (65-bp reads, single end). Sequencing data were aligned to hg38 using Hisat2 (RRID:SCR_015530; ref. 45), and the number of reads per gene was measured with HTSeq count (RRID:SCR_005514; ref. 46). For analyses, gene counts were normalized using DESeq2 (RRID:SCR_015687; ref. 47) and subsequently log transformed. Significance of expression level differences between pre- and posttreatment samples was determined using a Mann–Whitney U test. RNA-seq data from paired pre- and posttreatment prostate tumors from patients enrolled in a phase 2 clinical trial of 6 months of neoadjuvant ADT plus enzalutamide (ClinicalTrials.gov #NCT02430480) at the National Cancer Institute were downloaded from GEO (Study Accession: GSE183100; refs. 28, 48). Responding tumors with residual disease volumes less than 0.001 cm^3 were omitted from analysis ($n = 5$).

RNA-seq Analysis

RNA extraction was performed using the Zymo Quick-RNA MiniPrep Kit (R1054) and sent to the QB3 Genomics Sequencing Facility at UC Berkeley for library preparation and sequencing (RRID:SCR_022170). RNA-seq data were generated in FASTQ format. We quantified the gene-level expression using *kallisto* (49) and then used the abundance calls for downstream analysis. *DESeq2* (50) was used for differential gene expression analysis, including evaluating the effect size and statistical significance. Length-scaled transcripts per million (TPM) generated by *tximport* (51) were used for plotting gene expression values. For treatment × time interaction analysis, *P* values were evaluated using the likelihood ratio test implemented in DESeq2 to compare the full model [treatment (ENZA vs. DMSO), time (day 7, day 28, day 49, and day 91), and treatment × time interaction] with the reduced model (treatment and time without the interaction term). All statistical analyses were performed using R 4.2.0, and plots were generated using *ggplot2* (RRID:SCR_014601; https://cran.r-project.org/web/packages/ggplot2/citation.html).

ChIP-seq Analysis

ChIP-seq data for *AR* and H3K27ac were obtained from Hwang and colleagues (22). Briefly, Raw ChIP-seq data were downloaded from SRA (SRP222785). Reads with base quality scores more than 30 across all bases were aligned using bwa-mem v0.7.17 (RRID:SCR_022192; ref. 52) to build hg38. The aligned reads were deduplicated, and peaks were called using MACS2 v.2.2.5 (53) with a FDR threshold of 0.01. Peaks in ENCODE (RRID:SCR_015482) hg38 blacklist (ENCSR636HFF) were excluded, and only peaks that were enriched at least 10-fold more than background were kept for further analysis. The hg38 reference genome was segmented into 200-bp windows. The number of sequencing reads aligning to each window was determined and adjusted relative to the total number of mapped reads in the sample, yielding counts per million (CPM) values. Nonoverlapping unique ChIP-seq narrow peak regions were obtained from the samples analyzed, and CPM values for the 200-bp bins overlapping the ChIP-seq peaks were obtained. Further, the differential ChIP-seq analysis on the CPM values was performed using the Student *t* test.

ARE Identification, Sub-library Generation, and Screen Analysis

Genomic DNA was extracted from C42B cell lines using the ENZA tissue DNA kit (D3396-02), sheered using Covaris ME220 Focused Ultrasonicator (RRID:SCR_019818), and cleaned up using the MinElute Reaction Cleanup Kit (28204). Sample quality was assessed using a high-sensitivity DNA bioanalyzer kit (5067-4626) and sequenced on a NovaSeq S4 PE150 to reach 50× coverage per samples. Whole-genome sequence data were aligned to GRCh38 using the Burrows–Wheeler Aligner version 0.7.17 (52). The consensus sequence FASTA files were generated using bcftools algorithm version 1.9-213 (54). A list of AREs, including full, half-site, and lenient motifs (55), were downloaded as position site-specific matrix models from JASPAR database (RRID:SCR_003030; ref. 56). The Find Individual Motif Occurrences (FIMO) version 5.1 was employed to identify potential AREs upstream of MHC that may exist within FASTA files derived from the cell lines or using the Cistrome database (http://cistrome.org; ref. 57). Hits passing the FDR *q* value ≤ 0.05 were considered significant and prioritized by the highest FIMO occurrence score.

The Broad Institute sgRNA designer CRISPick was used to generate sgRNA sequences based on the location of the cut site (within the ARE sequence or a maximum of 3 bp outside), on-target cutting efficiency >0.2, and minimal off-target binding. In addition to ARE-targeting guides, 10% of the sub-library contained control guides targeting nonessential genes, positive control genes (*AR*, *GRHL2*, and *FOXA1*), negative control genes (*B2M*, *TAP1*, and *HLA-A*), and nontargeting guides. A 1-pmol guide pool was ordered from IDT with the addition of forward/reverse primer adapter sequences and a BSMBI cut site flanking the guide sequences. Cloning was performed using the Weissman lab protocol for cloning of pooled sgRNAs into lentiviral vectors with some modifications. In brief, libraries were amplified using HF Phusion enzymes (F-530S), purified using the MinElute Kit (28204), and cloned into the Lenti-CRISPR-V2 plasmid (Addgene, #52961). Ligation products were transformed with Stellar chemically competent cells (636736) and purified using Qiagen Maxi Prep Kit (12263). Guide distribution was validated by PCR using the Broad Institute's protocol for PCR of sgRNAs for Illumina sequencing using Ex Taq DNA Polymerase (RR001) and purified using SPRI select reagent (B23317) according to the Weissman lab protocol for Illumina Sequencing Sample Prep. Sample quality was assessed using a high-sensitivity DNA bioanalyzer kit (5067-4626) and sequenced on the MiSeq V3 150SR (RRID:SCR_016379) at the California Institute for Quantitative Biosciences at UC Berkeley. In evaluating element distribution, we took into account the 90% confidence interval of element abundance (i.e., the ratio between read counts of the 95th percentile most expressed element and that of the 5th percentile element). A 90% confidence interval less than 10 suggests a reasonably tight distribution with few missing elements.

Lentivirus was generated, and a FACS-based screen was performed as described above. In brief, C42B-dCas9 cells were infected with lentivirus containing an ARE-targeted sub-library at a 30% MOI for 3 days, selected with puromycin for 3 days, and allowed to recover for 24 hours. Cells were then fixed, stained with a HLA-ABC antibody, and sorted for 25% to 30% high and low MHC expression. DNA was extracted using the Zymo Quick-DNA FFPE Kit (56404) and amplified for 26 cycles using NEBNext Ultra II Q5 Master Mix (M0544S) and primers containing TruSeq indexes for NGS analysis. Libraries were purified using SPRI select reagent (B23317) according to the Weissman lab protocol for Illumina Sequencing Sample Prep. Sample quality was assessed using a high-sensitivity DNA bioanalyzer kit (5067-4626) and sequenced on a HiSeq 4000, SE50, at the UCSF Core Facility. Counts per target guide were calculated using MAGeCK (50) and normalized per sample by dividing by the total number of counts and multiplying with 1,000. Normalized counts were transformed by $\log_2$(normalized counts + 1). Differences between high and low MHCI groups were calculated at day 0 using the average of log-transformed counts across replicates. A *t* test was used to test for statistical significance per guide.

T-cell Isolation and Coculture

PBMCs were ordered from STEMCELL Technologies and T cells isolated using EasySep Human T Cell Isolation Kit (17951) according to the manufacture's protocol. Cells were resuspended in complete X VIVO media with 5% FBS, 10 mmol/L N-acetyl cysteine, 55 μmol/L ß-mercaptoethanol, and 50 IU/mL IL2. T cells were activated using Dynabeads Human T-Activator CD3/CD28 for T-Cell Expansion and Activation (11132D) and infected with lentivirus containing the *NY-ESO1* expression construct (Genecopoeia EX-Q0397-LV205) and 8 μg/mL polybrene 24 hours after activation. *NY-ESO1* expression was validated by flow cytometry 6 days postinfection. T cells were thawed the day prior to coculture in ATCC-modified RPMI media +10% FBS +5% penicillin/streptomycin + 1/10,000 IL2 + 5% human serum (H4522).

NY-ESO1 was expressed in C42B cells by infecting with lentivirus containing the *NY-ESO1* expression construct (Genecopoeia EX-Q0397-LV205) and 8 μg/mL polybrene and sorted twice for GFP expression. *NY-ESO1* expression was confirmed via Western blot (D1Q2U). For use in Incucyte experiments, C42B-NY-ESO1-expressing cells were infected with Nuclight Lentivirus Reagent (NLR; 4627) and sorted for RFP expression. For coculture experiments, C42B-NY-ESO1-NLR cells were treated with either DMSO, 10 μmol/L enzalutamide, 100 nmol/L ARD, or CSS for 14 days; drug treatment was refreshed at minimum every 5 days. Tumor cells were then harvested, washed, and replated in triplicate in a 96-well plate at either 2,500 or 10,000 cells per well, and T cells were added the following day. Cells were imaged and counted every 6 hours for 3 days using an Incucyte. For the indicated experiments, 5,000 U/mL of interferon gamma (I17001) was added 2 days prior to plating for coculture experiments and mouse anti-human HLA-ABC (311402) or IgG2a isotype control (400202) was added 2 hours prior to adding T cells.

Ar Knockdown TrampC1/PPSM Cells, Ar qPCR, and In Vitro Cell Growth Assessment

AR was deleted in TrampC1 or PPSM cells according to the protocol (58). sgRNA targeting the murine *Ar* gene (sgRNA 1: AATACTGAA TGACCGCCATC and sgRNA 4: GGGTGGAAAGTAATAGTCGA) and the mouse genome nontargeting *Ctrl* sgRNA (5′-GCACUACC AGAGCUAACUCA-3′) were obtained from Synthego. Cas9 recombinant protein was obtained from IDT. Following electroporation of the Cas9/sgRNA complex into 2 × 10^6 TrampC1 tumor cells, cells were plated in complete media and allowed to grow for 3 days. Cells were then subcloned, and 10 clones were analyzed for *Ar* expression by qPCR. Total RNA was extracted (RNeasy, Qiagen) and subjected to one-step RT-qPCR for *Ar* and *Sdha* (GoTaq one-step RT-qPCR) amplified in a QuantStudio 3 thermocycler (Applied Biosystems). Mouse qPCR primer sequences were as follows: mouse *Ar* (forward: 5′GGAGAACTACTCCGGACCTTAT3′; reverse: 5′GGGTGGAAAGT AATAGTCGATGG3′) and mouse *Sdha* (forward: 5′GAGATACGC ACCTGTTGCCAAG3′; reverse: 5′GGTAGACGTGATCTTTCTCA GGG3′). One clone with the lowest *Ar* mRNA expression was selected for further studies, referred to as TrampC1 *Ar*-KD. *In vitro* growth potential of TrampC1 *Ar*-KD cells was assessed by platting 5,000 cells in a 96-well plate, and confluency was measured using an Incucyte, with measurements every 2 hours for 30 hours.

MHCI Expression in TrampC1 and PPSM Cells by Flow Cytometry

To measure MHCI expression, 1 × 10^5 TrampC1 WT and TrampC1 *Ar*-KD or PPSM WT and PPSM *Ar*-KDc7 cells were plated in a six-well plate. Approximately 10 ng/mL of rIFNγ (BioLegend) was added. After 24 hours, cells were harvested and incubated on ice for 20 minutes with e506 fixable viability dye (eBioscience) and H-2Kb antibody (AF6-88.5, BioLegend, RRID:AB_2721683). Data were collected with a Fortessa Flow Cytometer (BD Biosciences) and analyzed using FlowJo software (Tree Star; RRID:SCR_008520).

In Vivo Mouse Studies

C57BL/6 (RRID:IMSR_JAX:000664), *Nur77*-GFP (RRID:IMSR_JAX:016617), and *Rag2*-KO (RRID:IMSR_JAX:008449) were purchased from the Jackson Laboratory. All animals were maintained under specific pathogen-free conditions in the Oregon Health & Science University animal facility. Eight-week-old males were used in all the experiments described. All cell lines were tested and confirmed to be *Mycoplasma*- and endotoxin-free using the MycoAlert Detection Kit (Lonza) and the Endosafe-PTS system (Charles River Laboratories). All animal experiments were approved by the Institutional Animal Care and Use Committee of OHSU. Animals were implanted with 1 × 10^6 TrampC1 WT, TrampC1 *Ar*-KDc6, PPSM WT, or PPSM *Ar*-KDc7 tumor cells passaged no more than three times after thawing on both hind flanks. Tumors were harvested and weighed 12 days postimplantation. Tumor-infiltrating lymphocytes (TIL) were isolated by dissection of tumor tissue into small fragments in a 50-cc conical tube followed by digestion at room temperature in a bacterial shaker at 180 rpm for 30 minutes in 1 mg/mL collagenase type IV (Worthington Biochemicals) and 20 mg/mL DNase (Roche) in PBS. Cells were then further disrupted with a 1-cc syringe plunger through a 70-μm nylon cell strainer (BD Biosciences) and filtered to obtain a single-cell suspension. TILs were incubated on ice for 20 minutes with e506 fixable viability dye (eBioscience), *Spas1* tetramer (peptide sequence STHVNHLHC, NIH tetramer core), and the following antibodies: CD8 (53-6.7, RRID:AB_11124344), TCRb (H57-597, RRID:AB_1272173), and CD44 (IM7, RRID:AB_494011). For intracellular cytokine staining, TILs were plated at 1 × 10^6 cells/well in 96-well plates and stimulated for 5 hours with PMA (80 nmol/L) and ionomycin (1.3 μmol/L) for restimulation, in the presence of brefeldin A (BFA). Cells were then stained for surface markers, fixed and permeabilized using the BD Cytofix/CytoPerm kit, and stained with IFNγ (XMG1.2, RRID:AB_466193) antibody. All the antibodies were purchased through BioLegend or eBioscience. Data were collected with a Fortessa Flow Cytometer (BD Biosciences) and analyzed using FlowJo software (Tree Star; RRID:SCR_008520). For long-term tumor growth assessment, tumors were measured using a caliper from day 8 until day 29.

Analysis of Previously Published Single-Cell RNA-seq Data

The recently published human PCa scRNA-seq dataset (30) was obtained from https://doi.org/10.17632/5nnw8xrh5m.1. We reanalyzed this dataset using the Seurat pipeline (RRID:SCR_016341; v4.1.0). The BBKNN algorithm (59) was employed to mitigate potential batch effects. Clustering and single-cell distribution were visualized using Uniform Manifold Approximation and Projection (UMAP) with the Leiden algorithm. Subsequently, cell clusters were annotated based on previously reported cell-type marker genes of human PCa (60) and the combined automatic annotation method CellTypist (61). *AR* activity was calculated using the VIPER analysis (62), an algorithm that employs the transcriptional gene regulatory network targeted by AR to infer its activity. Pathway activity of MHCI (3) or IFNγ was calculated using AUCell algorithm (v1.16.0). The preprocessed matrix of gene counts versus cells contained 40,270 cells from 19 individual biopsies from a total of 11 patients. Of patients published, our initial analysis included patients 1, 3, 5, 6, 7, 9, 10, 11, and 12. Patient 11 was not included in the published table but was included in the shared dataset. After clustering all cells, luminal cells were subset for further analysis. Patient 3 was excluded for subsequent analysis due to less than 1 luminal epithelial cell with ADT and/or upon recurrence.

Activity Analysis of WCDT Biopsy Samples

To measure *AR* regulon activity of each sample in the WCDT cohort, we used the VIPER R package (version 1.26.0; ref. 62). A log1p-transformed TPM gene expression matrix and a regulatory network were used as inputs for VIPER analysis. The *viper* function was employed to calculate *AR* activities. The regulatory network used in the VIPER analysis was the same as described above. To quantify the activity of the MHCI signature (*HLA-A*, *HLA-B*, *HLA-C*, *IRF2*, *TAP1*, *TAPBP*, and *B2M* genes) in each sample, we used the single-sample gene set enrichment analysis (ssGSEA; ref. 63) implemented in the GSVA (64) R package (version 1.44.5). The ssGSEA algorithm is a rank-based method to assess the expression levels of genes of a gene signature against all other genes in each sample within a given dataset. Log-transformed gene expression profiles and the MHCI signature were used as input to ssGSEA. FDR q values were used to determine statistical significance.

Master Regulator and GSEA Analysis

RNA-seq data of pembrolizumab-treated patient samples were used to evaluate differential transcription factor activities and to perform GSEA analysis (RRID:SCR_003199). Differential gene expression analysis between responders and nonresponders was first performed using DESeq2 (version 1.32.0; ref. 47). Gene expression differences were considered significant when the adjusted P value is <0.05. Transcription factor activity was inferred by msVIPER algorithms provided in the VIPER R package (version 1.26.0). The Wald test statistic results from DESeq2 output served as a gene list input data for the VIPER analysis. The transcriptional regulatory network used in this study was curated from four databases as previously described (65). GSEA version 3.0 (66) was used to identify gene sets that were significantly activated in pembrolizumab nonresponders compared with responders from the Hallmark database [version 7.4 of the Molecular Signatures Database (MSigDB; https://www.gsea-msigdb.org/gsea/msigdb/)]. The expression data normalized by variance-stabilizing transformation in DESeq2 were used as the input of GSEA, and the default metric Signal2Noise in GSEA was applied to calculate the differential expression with respect to nonresponders and responders. The gene sets were considered to be activated if their FDR q value was less than 0.05.

Statistical Analysis

Significance of expression level differences in primary prostate cancer pre- and posttreatment samples was determined using either a Mann–Whitney U test or a prespecified FDR significance level of 0.05 as indicated above. Unpaired t tests were used to determine the statistical significance for the column plots, denoted by asterisk (*). *, $P < 0.05$; **, $P < 0.01$; ***, $P < 0.001$. For mCRPC RNA-seq analysis, we calculated the correlation between two continuous variables using Pearson's correlation coefficients. The threshold of $P < 0.05$ indicates the significance of correlation.

Data Availability

RNA-seq data generated from the DARANA study are available in the European Genome-Phenome Archive (EGA) under the accession number EGAS00001006016. RNA-seq data from patient prostate tumors before and after 6 months of neoadjuvant ADT plus enzalutamide were downloaded from GEO (GSE183100). RNA-seq data and corresponding clinical annotations of tumor samples in WCDT cohort were downloaded from previously published studies (29). Single-cell RNA-seq data from patients with mHSPC were obtained from the authors (30). Newly generated RNA-seq data from 91 days of enzalutamide treatment in the C42B cells are available from GEO (GSE277299).

Authors' Disclosures

L.N. Chesner reports grants from Prostate Cancer Foundation and the Department of Defense during the conduct of the study. J.E. Hawley reports other support from GSK, Immunity Bio, Daichi Sankyo, and Seagen, grants from DOD, and other support from Prostate Cancer Foundation, AstraZeneca, BMS/Celgene, Barinthus, Crescendo Biologics, MacroGenics, PromiCell, Amgen, and Janssen outside the submitted work. M. Sjöström reports grants from the Prostate Cancer Foundation and the Swedish Cancer Society during the conduct of the study and personal fees from Astellas and Veracyte/Adelphi Targis outside the submitted work. X. Zhu reports grants from Conquer Cancer, the ASCO Foundation, Prostate Cancer Foundation, and the Department of Defense outside the submitted work. D. Kuzuoglu-Ozturk reports grants from the Department of Defense PCRP during the conduct of the study. D. Ruggero reports personal fees from eFFECTOR Therapeutics, Inc. outside the submitted work. C.G. Drake reports other support from Johnson and Johnson Innovative Medicine outside the submitted work. A.G. Sowalsky reports other support from Astellas during the conduct of the study. L. Fong reports grants and personal fees from AbbVie, Dendreon, and Roche/Genentech, grants from Amgen, BMS, Janssen, Merck, Nektar, and personal fees from Daiichi Sankyo, Sutro, and Innovent outside the submitted work. M.R. Cooperberg reports personal fees from Veracyte, Tempus, Bayer, Janssen, Merck, Pfizer, AstraZeneca, Astellas, ExactVu, Biomarker, and LynxDx outside the submitted work. A. Ashworth reports personal fees from Azkarra Therapeutics, Kytarro, Ovibio Corporation, Tango Therapeutics, Tiller tx, Cambridge Science Corporation, CytomX, Ambagon, Bluestar/ClearNote Health, Circle, Genentech, GLAdiator, HAP10, Earli, ORIC, Phoenix Molecular Designs, Trial Library, Yingli/280Bio, Next RNA, Novartis, and Prolynx outside the submitted work, as well as patents on the use of PARP inhibitors, held jointly with AstraZeneca, from which he has benefited financially (and may do so in the future). F.Y. Feng reports nonfinancial support from Artera, Astellas, Bayer, Blue Earth Diagnostics, Bristol Meyers Squibb, ClearNote, Myovant, Roivant, Sanofi, Serimmune, and Amgen and personal fees and nonfinancial support from Janssen, Point Biopharma, and Novartis outside the submitted work. A.E. Moran reports grants from the NIH/NCI, Prostate Cancer Foundation, Kuni Foundation, Collins Medical Trust, and UCSF during the conduct of the study, as well as a patent for WO 2023/049860 issued. No disclosures were reported by the other authors.

Authors' Contributions

L.N. Chesner: Conceptualization, data curation, formal analysis, supervision, funding acquisition, validation, investigation, visualization, methodology, writing–original draft, project administration, writing–review and editing. **F. Polesso:** Data curation, formal analysis, validation, investigation, visualization, methodology, writing–original draft, project administration, writing–review and editing. **J.N. Graff:** Resources, supervision. **J.E. Hawley:** Resources, supervision. **A.K. Smith:** Data curation, formal analysis, validation, investigation, visualization, methodology. **A. Lundberg:** Data curation, software, formal analysis, validation, investigation, visualization, methodology, writing–original draft. **R. Das:** Conceptualization, data curation, formal analysis, validation, investigation, methodology. **T. Shenoy:** Conceptualization, resources, data curation, formal analysis, validation, investigation, methodology, writing–original draft. **M. Sjöström:** Conceptualization, data curation, software, formal analysis, validation, investigation, visualization, methodology, writing–original draft, writing–review and editing. **F. Zhao:** Data curation, formal analysis, investigation, visualization, methodology. **Y.-M. Hu:** Data curation, formal analysis, investigation, visualization, methodology. **S. Linder:** Data curation, software, formal analysis, validation, investigation, visualization, methodology, writing–original draft. **W.S. Chen:** Conceptualization, data curation, software, formal analysis, validation, investigation, visualization, methodology, writing–original draft. **R.M. Hawkins:** Data curation, formal analysis, writing–review and editing. **R. Shrestha:** Investigation. **X. Zhu:** Data curation, formal analysis, visualization. **A. Foye:** Data curation, validation, investigation. **H. Li:** Conceptualization, data curation, validation, investigation, methodology. **L.M. Kim:** Data curation, formal analysis, validation, investigation, visualization, methodology. **M. Bhalla:** Data curation, formal analysis, validation, investigation. **T. O'loughlin:** Data curation, formal analysis, validation, investigation, methodology. **D. Kuzuoglu-Ozturk:** Resources, methodology, writing–original draft. **J.T. Hua:** Conceptualization, resources, data curation, formal analysis, investigation, visualization, methodology. **M.L. Badura:** Data curation, formal analysis. **S. Wilkinson:** Data curation, formal analysis, investigation, writing–review and editing. **S.Y. Trostel:** Data curation, formal analysis, investigation. **A.M. Bergman:** Resources, supervision. **D. Ruggero:** Resources, supervision. **C.G. Drake:** Resources, supervision, writing–review and editing. **A.G. Sowalsky:** Resources, data curation, formal analysis, supervision, investigation, writing–review and editing. **L. Fong:** Supervision. **M.R. Cooperberg:** Supervision. **W. Zwart:** Resources, supervision. **X. Guan:** Resources, data curation, formal analysis, supervision, writing–review and editing. **A. Ashworth:** Conceptualization, resources, data curation, software, formal analysis, supervision, validation, investigation, visualization, methodology, writing–original draft, writing–review and editing. **Z. Xia:** Conceptualization, resources, data curation, software, formal analysis, supervision, validation, investigation, visualization, methodology, writing–original draft, writing–review and editing. **D.A. Quigley:** Conceptualization, resources, data curation, software, formal analysis, supervision, validation, investigation, methodology. **L.A. Gilbert:** Conceptualization, resources, data curation, software, formal analysis, supervision, funding acquisition, validation, investigation, visualization, methodology, writing–original draft, project administration, writing–review and editing. **F.Y. Feng:** Conceptualization, resources, data curation, software, formal analysis, supervision, funding acquisition, validation, investigation, visualization, methodology, writing–original draft, project administration, writing–review and editing. **A.E. Moran:** Conceptualization, resources, data curation, formal analysis, supervision, funding acquisition, validation, investigation, visualization, methodology, writing–original draft, project administration, writing–review and editing.

Acknowledgments

We would like to thank all the members of the Feng, Moran, and Gilbert labs for their helpful suggestions and technical advice, as well as Nicholas Larocque and Tina Yu for their administrative support. We thank Drs. Arul Chinnaiyan and Shaomeng Wang for the AR degrader. This study was supported in part by HDFCCC Laboratory for Cell Analysis Shared Resource Facility through the NIH grant (P30CA082103). L.N. Chesner is supported by the Prostate Cancer Foundation Young Investigator award and Department of Defense Early Investigator award (W81XWH2110046). J.E. Hawley is supported by grants from the Conquer Cancer Foundation (2019YIA to J.E. Hawley), the Prostate Cancer Foundation (2020YIA to J.E. Hawley), NCI SPORE P50 CA097186, and the NIH (T32CA203703 to J.E. Hawley, UL1TR001873 to J.E. Hawley). Z. Xia is supported by the Department of Defense Idea Development Award (W81XWH2110539) and NIH R01GM147365. Y.-M. Hu is supported by a postdoctoral fellowship of Portland Oral Health Research Training (PORT) T90 program (NIH T90 DE030859). M. Sjöström, R. Shrestha, and H. Li are supported by the Prostate Cancer Foundation Young Investigator award. X. Zhu is supported by the Prostate Cancer Foundation Young Investigator award and Department of Defense Physician Research Award through the Prostate Cancer Research Program (HT9425-24-1-0506). D. Kuzuoglu-Ozturk is supported by the UCSF Prostate Cancer Program Pilot Award. A.G. Sowalsky and S. Trostel are supported by The Intramural Research Program of the National Cancer Institute, National Institutes of Health. S. Wilkinson is supported by the Prostate Cancer Foundation Young Investigator award and Department of Defense Early Investigator award (W81XWH1910712) D. Ruggero is supported by NIH R35CA242986 and the American Cancer Society (RP-19-181-01-RMC). L. Fong is supported by a Prostate Cancer Foundation Challenge Award and NIH R35CA253175. D.A. Quigley is supported by funding from the Benioff Initiative for Prostate Cancer Research, the Prostate Cancer Foundation, NCI SPORE 1P50CA275741, and Department of Defense awards W81XWH-22-1-0833 and HT94252410252. L.A. Gilbert is funded by a Prostate Cancer Foundation Challenge Award (21CHAL06), a NIH New Innovator Award (DP2 CA239597), a Pew-Stewart Scholars for Cancer Research award, a CRUK/NIH Cancer Grand Challenges award (OT2CA278665; CGCATF-2021/100006), and the Goldberg-Benioff Endowed Professorship in Prostate Cancer Translational Biology. A.E. Moran is supported by a Prostate Cancer Foundation Young Investigator award, NCI SPORE P50 CA097186, and NIH/NCI R37CD263592. F.Y. Feng is supported by NIH/NCI 5R01CA227025 and Prostate Cancer Foundation Challenge Award. Additional funding was provided by a UCSF Benioff Initiative for Prostate Cancer Research award.

Note

Supplementary data for this article are available at Cancer Discovery Online (http://cancerdiscovery.aacrjournals.org/).

Received April 23, 2024; revised September 10, 2024; accepted December 3, 2024; published first December 5, 2024.

REFERENCES

1. Blades RA, Keating PJ, McWilliam LJ, George NJ, Stern PL. Loss of HLA class I expression in prostate cancer: implications for immunotherapy. Urology 1995;46:681–6.
2. Chen X, Lu Q, Zhou H, Liu J, Nadorp B, Lasry A, et al. A membrane-associated MHC-I inhibitory axis for cancer immune evasion. Cell 2023;186:3903–20.e21.
3. Bagaev A, Kotlov N, Nomie K, Svekolkin V, Gafurov A, Isaeva O, et al. Conserved pan-cancer microenvironment subtypes predict response to immunotherapy. Cancer Cell 2021;39:845–65.e7.
4. Lee JH, Shklovskaya E, Lim SY, Carlino MS, Menzies AM, Stewart A, et al. Transcriptional downregulation of MHC class I and melanoma de- differentiation in resistance to PD-1 inhibition. Nat Commun 2020;11:1897.
5. Sade-Feldman M, Jiao YJ, Chen JH, Rooney MS, Barzily-Rokni M, Eliane J-P, et al. Resistance to checkpoint blockade therapy through inactivation of antigen presentation. Nat Commun 2017;8:1136.
6. Zaretsky JM, Garcia-Diaz A, Shin DS, Escuin-Ordinas H, Hugo W, Hu-Lieskovan S, et al. Mutations associated with acquired resistance to PD-1 blockade in melanoma. N Engl J Med 2016;375:819–29.
7. Gao J, Shi LZ, Zhao H, Chen J, Xiong L, He Q, et al. Loss of IFN-γ pathway genes in tumor cells as a mechanism of resistance to anti-CTLA-4 therapy. Cell 2016;167:397–404.e9.
8. McGranahan N, Rosenthal R, Hiley CT, Rowan AJ, Watkins TBK, Wilson GA, et al. Allele-specific HLA loss and immune escape in lung cancer evolution. Cell 2017;171:1259–71.e11.
9. Goldman MJ, Craft B, Hastie M, Repečka K, McDade F, Kamath A, et al. Visualizing and interpreting cancer genomics data via the Xena platform. Nat Biotechnol 2020;38:675–8.
10. Bander NH, Yao D, Liu H, Chen YT, Steiner M, Zuccaro W, et al. MHC class I and II expression in prostate carcinoma and modulation by interferon-alpha and -gamma. Prostate 1997;33:233–9.

11. Mercader M, Bodner BK, Moser MT, Kwon PS, Park ES, Manecke RG, et al. T cell infiltration of the prostate induced by androgen withdrawal in patients with prostate cancer. Proc Natl Acad Sci U S A 2001;98:14565–70.
12. Obradovic AZ, Dallos MC, Zahurak ML, Partin AW, Schaeffer EM, Ross AE, et al. T-cell infiltration and adaptive Treg resistance in response to androgen deprivation with or without vaccination in localized prostate cancer. Clin Cancer Res 2020;26:3182–92.
13. Mercader M, Sengupta S, Bodner BK, Manecke RG, Cosar EF, Moser MT, et al. Early effects of pharmacological androgen deprivation in human prostate cancer. BJU Int 2007;99:60–7.
14. Guan X, Polesso F, Wang C, Sehrawat A, Hawkins RM, Murray SE, et al. Androgen receptor activity in T cells limits checkpoint blockade efficacy. Nature 2022;606:791–6.
15. Gilbert LA, Horlbeck MA, Adamson B, Villalta JE, Chen Y, Whitehead EH, et al. Genome-scale CRISPR-mediated control of gene repression and activation. Cell 2014;159:647–61.
16. Jin H-J, Zhao JC, Wu L, Kim J, Yu J. Cooperativity and equilibrium with FOXA1 define the androgen receptor transcriptional program. Nat Commun 2014;5:3972.
17. Paltoglou S, Das R, Townley SL, Hickey TE, Tarulli GA, Coutinho I, et al. Novel androgen receptor coregulator GRHL2 exerts both oncogenic and antimetastatic functions in prostate cancer. Cancer Res 2017;77:3417–30.
18. Zhao L, Han X, Lu J, McEachern D, Wang S. A highly potent PROTAC androgen receptor (AR) degrader ARD-61 effectively inhibits AR-positive breast cancer cell growth in vitro and tumor growth in vivo. Neoplasia 2020;22:522–32.
19. Kregel S, Wang C, Han X, Xiao L, Fernandez-Salas E, Bawa P, et al. Androgen receptor degraders overcome common resistance mechanisms developed during prostate cancer treatment. Neoplasia 2020; 22:111–9.
20. Bettoun DJ, Scafonas A, Rutledge SJ, Hodor P, Chen O, Gambone C, et al. Interaction between the androgen receptor and RNase L mediates a cross-talk between the interferon and androgen signaling pathways. J Biol Chem 2005;280:38898–901.
21. Baratchian M, Tiwari R, Khalighi S, Chakravarthy A, Yuan W, Berk M, et al. H3K9 methylation drives resistance to androgen receptor-antagonist therapy in prostate cancer. Proc Natl Acad Sci U S A 2022;119:e2114324119.
22. Hwang JH, Seo JH, Beshiri ML, Wankowicz S, Liu D, Cheung A, et al. CREB5 promotes resistance to androgen-receptor antagonists and androgen deprivation in prostate cancer. Cell Rep 2019;29:2355–70.e6.
23. Fassò M, Waitz R, Hou Y, Rim T, Greenberg NM, Shastri N, et al. SPAS-1 (stimulator of prostatic adenocarcinoma-specific T cells)/SH3GLB2: a prostate tumor antigen identified by CTLA-4 blockade. Proc Natl Acad Sci U S A 2008;105:3509–14.
24. Lu X, Horner JW, Paul E, Shang X, Troncoso P, Deng P, et al. Effective combinatorial immunotherapy for castration-resistant prostate cancer. Nature 2017;543:728–32.
25. Moran AE, Holzapfel KL, Xing Y, Cunningham NR, Maltzman JS, Punt J, et al. T cell receptor signal strength in Treg and iNKT cell development demonstrated by a novel fluorescent reporter mouse. J Exp Med 2011;208:1279–89.
26. Moran AE, Polesso F, Weinberg AD. Immunotherapy expands and maintains the function of high-affinity tumor-infiltrating CD8 T cells in situ. J Immunol 2016;197:2509–21.
27. Linder S, Hoogstraat M, Stelloo S, Eickhoff N, Schuurman K, de Barros H, et al. Drug-induced epigenomic plasticity reprograms circadian rhythm regulation to drive prostate cancer toward androgen independence. Cancer Discov 2022;12:2074–97.
28. Wilkinson S, Ye H, Karzai F, Harmon SA, Terrigino NT, VanderWeele DJ, et al. Nascent prostate cancer heterogeneity drives evolution and resistance to intense hormonal therapy. Eur Urol 2021;80:746–57.
29. Quigley DA, Dang HX, Zhao SG, Lloyd P, Aggarwal R, Alumkal JJ, et al. Genomic hallmarks and structural variation in metastatic prostate cancer. Cell 2018;174:758–69.e9.
30. Hawley JE, Obradovic AZ, Dallos MC, Lim EA, Runcie K, Ager CR, et al. Anti-PD-1 immunotherapy with androgen deprivation therapy induces robust immune infiltration in metastatic castration-sensitive prostate cancer. Cancer Cell 2023;41:1972–88.e5.
31. Obradovic A, Chowdhury N, Haake SM, Ager C, Wang V, Vlahos L, et al. Single-cell protein activity analysis identifies recurrence-associated renal tumor macrophages. Cell 2021;184:2988–3005.e16.
32. Ben-Batalla I, Vargas-Delgado ME, von Amsberg G, Janning M, Loges S. Influence of androgens on immunity to self and foreign: effects on immunity and cancer. Front Immunol 2020;11:1184.
33. Irelli A, Sirufo MM, D'Ugo C, Ginaldi L, De Martinis M. Sex and gender influences on cancer immunotherapy response. Biomedicines 2020;8:232.
34. Kwon H, Schafer JM, Song N-J, Kaneko S, Li A, Xiao T, et al. Androgen conspires with the CD8$^+$ T cell exhaustion program and contributes to sex bias in cancer. Sci Immunol 2022;7:eabq2630.
35. Gratzke C, Kwiatkowski M, De Giorgi U, Martins da Trindade K, De Santis M, Armstrong AJ, et al. KEYNOTE-991: pembrolizumab plus enzalutamide and androgen deprivation for metastatic hormone-sensitive prostate cancer. Future Oncol 2023;37:4079–87.
36. Zhang X, Cheng L, Gao C, Chen J, Liao S, Zheng Y, et al. Androgen signaling contributes to sex differences in cancer by inhibiting NF-κB activation in T cells and suppressing antitumor immunity. Cancer Res 2023;83:906–21.
37. Lakshmikanth T, Consiglio C, Sardh F, Forlin R, Wang J, Tan Z, et al. Immune system adaptation during gender-affirming testosterone treatment. Nature 2024;633:155–64.
38. Li F, Xing X, Jin Q, Wang XM, Dai P, Han M, et al. Sex differences orchestrated by androgens at single-cell resolution. Nature 2024 May;629:193–200.
39. Robert C, Lebbé C, Lesimple T, Lundström E, Nicolas V, Gavillet B, et al. Phase I study of androgen deprivation therapy in combination with anti-PD-1 in melanoma patients pretreated with anti-PD-1. Clin Cancer Res 2023;29:858–65.
40. Deng Y, Xia X, Zhao Y, Zhao Z, Martinez C, Yin W, et al. Glucocorticoid receptor regulates PD-L1 and MHC-I in pancreatic cancer cells to promote immune evasion and immunotherapy resistance. Nat Commun 2021;12:7041.
41. Arora VK, Schenkein E, Murali R, Subudhi SK, Wongvipat J, Balbas MD, et al. Glucocorticoid receptor confers resistance to antiandrogens by bypassing androgen receptor blockade. Cell 2013;155:1309–22.
42. Das R, Sjöström M, Shrestha R, Yogodzinski C, Egusa EA, Chesner LN, et al. An integrated functional and clinical genomics approach reveals genes driving aggressive metastatic prostate cancer. Nat Commun 2021;12:4601.
43. Horlbeck MA, Gilbert LA, Villalta JE, Adamson B, Pak RA, Chen Y, et al. Compact and highly active next-generation libraries for CRISPR-mediated gene repression and activation. Elife 2016;5:e19760.
44. Gilbert LA, Larson MH, Morsut L, Liu Z, Brar GA, Torres SE, et al. CRISPR-mediated modular RNA-guided regulation of transcription in eukaryotes. Cell 2013;154:442–51.
45. Kim D, Paggi JM, Park C, Bennett C, Salzberg SL. Graph-based genome alignment and genotyping with HISAT2 and HISAT-genotype. Nat Biotechnol 2019;37:907–15.
46. Anders S, Pyl PT, Huber W. HTSeq–a Python framework to work with high-throughput sequencing data. Bioinformatics 2015;31:166–9.
47. Love MI, Huber W, Anders S. Moderated estimation of fold change and dispersion for RNA-seq data with DESeq2. Genome Biol 2014;15:550.
48. Karzai F, Walker SM, Wilkinson S, Madan RA, Shih JH, Merino MJ, et al. Sequential prostate magnetic resonance imaging in newly diagnosed high-risk prostate cancer treated with neoadjuvant enzalutamide is predictive of therapeutic response. Clin Cancer Res 2021;27:429–37.
49. Bray NL, Pimentel H, Melsted P, Pachter L. Near-optimal probabilistic RNA-seq quantification. Nat Biotechnol 2016;34:525–7.
50. Li W, Xu H, Xiao T, Cong L, Love MI, Zhang F, et al. MAGeCK enables robust identification of essential genes from genome-scale CRISPR/Cas9 knockout screens. Genome Biol 2014;15:554.
51. Soneson C, Love MI, Robinson MD. Differential analyses for RNA-seq: transcript-level estimates improve gene-level inferences. F1000Res 2015;4:1521.

52. Li H, Durbin R. Fast and accurate short read alignment with Burrows-Wheeler transform. Bioinformatics 2009;25:1754–60.
53. Zhang Y, Liu T, Meyer CA, Eeckhoute J, Johnson DS, Bernstein BE, et al. Model-based analysis of ChIP-seq (MACS). Genome Biol 2008;9:R137.
54. Li H. A statistical framework for SNP calling, mutation discovery, association mapping and population genetical parameter estimation from sequencing data. Bioinformatics 2011;27:2987–93.
55. Wilson S, Qi J, Filipp FV. Refinement of the androgen response element based on ChIP-Seq in androgen-insensitive and androgen-responsive prostate cancer cell lines. Sci Rep 2016;6:32611.
56. Castro-Mondragon JA, Riudavets-Puig R, Rauluseviciute I, Lemma RB, Turchi L, Blanc-Mathieu R, et al. JASPAR 2022: the 9th release of the open-access database of transcription factor binding profiles. Nucleic Acids Res 2022;50:D165–73.
57. Grant CE, Bailey TL, Noble WS. FIMO: scanning for occurrences of a given motif. Bioinformatics 2011;27:1017–8.
58. Nüssing S, House IG, Kearney CJ, Chen AXY, Vervoort SJ, Beavis PA, et al. Efficient CRISPR/Cas9 gene editing in uncultured naive mouse T cells for in vivo studies. J Immunol 2020;204:2308–15.
59. Polański K, Young MD, Miao Z, Meyer KB, Teichmann SA, Park JE. BBKNN: fast batch alignment of single cell transcriptomes. Bioinformatics 2020;36:964–5.
60. Zhang T, Zhao F, Lin Y, Liu M, Zhou H, Cui F, et al. Integrated analysis of single-cell and bulk transcriptomics develops a robust neuroendocrine cell-intrinsic signature to predict prostate cancer progression. Theranostics 2024;14:1065–80.
61. Domínguez Conde C, Xu C, Jarvis LB, Rainbow DB, Wells SB, Gomes T, et al. Cross-tissue immune cell analysis reveals tissue-specific features in humans. Science 2022;376:eabl5197.
62. Alvarez MJ, Shen Y, Giorgi FM, Lachmann A, Ding BB, Ye BH, et al. Functional characterization of somatic mutations in cancer using network-based inference of protein activity. Nat Genet 2016;48:838–47.
63. Barbie DA, Tamayo P, Boehm JS, Kim SY, Moody SE, Dunn IF, et al. Systematic RNA interference reveals that oncogenic KRAS-driven cancers require TBK1. Nature 2009;462:108–12.
64. Hänzelmann S, Castelo R, Guinney J. GSVA: gene set variation analysis for microarray and RNA-Seq data. BMC Bioinformatics 2013;14:7.
65. Robertson AG, Shih J, Yau C, Gibb EA, Oba J, Mungall KL, et al. Integrative analysis identifies four molecular and clinical subsets in uveal melanoma. Cancer Cell 2017;32:204–20.e15.
66. Subramanian A, Tamayo P, Mootha VK, Mukherjee S, Ebert BL, Gillette MA, et al. Gene set enrichment analysis: a knowledge-based approach for interpreting genome-wide expression profiles. Proc Natl Acad Sci U S A 2005;102:15545–50.

Appendix IV: Curriculum Vitae

Reed M. Hawkins

Overview:

- A PhD candidate and immunologist with over 9 years of experience in biomedical research
- Extensive experience and formal training in coordinating and implementing research involving mouse models and human clinical trials, utilizing a combination of wet bench and computational approaches to characterize immune responses and mechanisms of immunotherapy efficacy
- An accomplished scientific communicator with experience writing successful grant applications, contributing authorship to scientific journal articles, and teaching and mentoring students and trainees in the classroom and lab setting

Skills:

- High-parameter flow cytometry (18+ colors)
- Mouse colony management and studying mouse models of disease
- Preparation of protein, DNA, and RNA for -omics sequencing and analysis
- Computational analysis of RNA sequencing data (R, Linux, Bioconductor packages)

Education:

PhD Candidate; Cancer Biology
Oregon Health & Science University (OHSU), Portland, OR
Expected completion: Spring 2025

BS Cellular and Molecular Biology; BS Biochemistry, *Summa Cum Laude*
Seattle Pacific University (SPU), *Seattle, WA* 2015, GPA 3.94

Bonney Lake High School, *Bonney Lake, WA* 2011, GPA 4.0, *Valedictorian*

Research Experience:

Graduate Research Assistant, Moran Lab, *Cell, Developmental and Cancer Biology Department*: *OHSU, Portland, OR* 2020-Present

- Developed an independent dissertation project investigating the role of androgen receptor (AR) in regulating CD8+ T cell responses in both mouse and human models, leveraging a combination of wet bench and computational approaches.
- Characterized the role of AR in epigenetically and transcriptionally controlling the acquisition of CD8+ T cell effector phenotype and function in response to acute infection, with implications AR activity in CD8+ T cells as a driver of sex differences in CD8+ T cell responses to disease, a critical finding to contribute to our understanding of the causes of sex differences in disease susceptibility.

- Led a scRNAseq project on over 40 prostate cancer patient tumor biopsies to characterize the tumor microenvironment and the changes in vascularization and immune cell infiltration/activation that occur in response to neoadjuvant pembrolizumab plus androgen deprivation therapy (NCT03753243).
- Contributed to a body of work published in *Nature* in March 2022 and *Cancer Discovery* in 2024 and currently preparing two first-author manuscripts for publication.

Research Technician II, Turtle Lab, *Clinical Research Division/Program in Immunology*: *Fred Hutchinson Cancer Research Center, Seattle, WA* 2015-2019

- Coordinated three phase I/II CD19 Chimeric Antigen receptor (CAR) T-cell and combination therapy clinical trials for patients with relapsed/refractory B-cell malignancies in collaboration with principal investigators, research staff, nurses, and hospital personnel.
- Assisted with functional, transcriptomic, and epigenetic correlative studies regarding efficacy of the CAR T cell treatments; pre-clinical studies of new CAR designs; and studies investigating immune reconstitution following allogeneic hematopoietic stem cell transplantation.
- Gained extensive experience in T-cell transduction, T cell functional assays, high-parameter flow cytometry panel design and optimization, RNA sequencing, human biospecimen handling and processing, and meticulous clinical trial data management in compliance with FDA regulations.

Volunteer Research Intern, Jensen Lab, *Ben Towne Center for Childhood Cancer Research: Seattle Children's Research Institute, Seattle* 2014

- Contributed to the "Transgene X" project with the goal of increasing efficacy of transgenic T-cells as therapy for pediatric cancer.

Research Assistant, Ridgway Lab, *SPU, Seattle* 2014-2015

- Investigated the cellular production, localization, and release of DMSP toxins by the marine alga, *Ulva lactuca,* an important organism in Pacific marine ecosystems.

Publications:

- Chesner LN, Polesso F, Graff JN, ..., **Hawkins RM**, ..., Feng FY, Moran AE. Androgen receptor inhibition increases MHC class I expression and improves immune response in prostate cancer. Cancer Discovery. 2025 Mar 3. doi: https://doi.org/10.1158/2159-8290.CD-24-0559
- Guan X, Polesso F, ..., **Hawkins RM**, ..., Graff JN, Xia Z, Moran AE. Androgen receptor activity in T cells limits checkpoint blockade efficacy. Nature. 2021 Mar 23. doi: https://doi.org/10.1038/s41586-022-04522-6, PMID: 35322234
- Hirayama AV, Chou CK, ..., **Hawkins RM**, ..., Riddell SR, Marcondes MQ, Turtle CJ. A novel polyer-conjugated human IL-15 improves efficacy of CD19-targeted CAR-T cell immunotherapy. Blood Advances. 2022 Nov 5. doi: https://doi.org/10.1182/bloodadvances.2022008697
- Gauthier J, Bezerra ED, ..., **Hawkins RM**, ..., Riddell SR, Maloney DG, Turtle CJ. Factors associated with outcomes after a second CD19-targeted CAR T-cell

infusion for refractory B-cell malignancies. Blood. 2021 Jan 21;137(3):323-335. doi: 10.1182/blood.2020006770. PMID: 32967009; PMCID: PMC7819764.

- Gauthier J, Hirayama AV, ..., **Hawkins RM**, ..., Riddell SR, Maloney DG, Turtle CJ. Feasibility and efficacy of CD19-targeted CAR T cells with concurrent ibrutinib for CLL after ibrutinib failure. *Blood*. 2020 May 7;135(19):1650-1660. doi: 10.1182/blood.2019002936. PMID: 32076701; PMCID: PMC7205814.
- Sheih A, Voillet V, ..., **Hawkins R**, ..., Turtle CJ. Clonal kinetics and single-cell transcriptional profiling of CAR-T cells in patients undergoing CD19 CAR-T immunotherapy. *Nat Commun*. 2020 Jan 10;11(1):219. doi: 10.1038/s41467-019-13880-1. PMID: 31924795; PMCID: PMC6954177.
- Hirayama AV, Gauthier J, ..., **Hawkins RM**, ..., Riddell SR, Maloney DG, Turtle CJ. High rate of durable complete remission in follicular lymphoma after CD19 CAR-T cell immunotherapy. *Blood*. 2019 Aug 15;134(7):636-640. doi: 10.1182/blood.2019000905. PMID: 31648294; PMCID: PMC6695558.
- Hirayama AV, Gauthier J, ..., **Hawkins RM**, ..., Riddell SR, Maloney DG, Turtle CJ. The response to lymphodepletion impacts PFS in patients with aggressive non-Hodgkin lymphoma treated with CD19 CAR T cells. *Blood*. 2019 Apr 25;133(17):1876-1887. doi: 10.1182/blood-2018-11-887067. Epub 2019 Feb 19. PMID: 30782611; PMCID: PMC6484391.
- Hay KA, Gauthier J, ..., **Hawkins RM**, ..., Riddell SR, Maloney DG, Turtle CJ. Factors associated with durable EFS in adult B-cell ALL patients achieving MRD-negative CR after CD19 CAR T-cell therapy. *Blood*. 2019 Apr 11;133(15):1652-1663. doi: 10.1182/blood-2018-11-883710. Epub 2019 Feb 6. PMID: 30728140; PMCID: PMC6460418.
- Turtle, CJ, Hanafi LA, ..., **Hawkins RM**, ..., Riddell SR, Maloney DG. (2016). Immunotherapy of non-Hodgkin's lymphoma with a defined ratio of CD8+ and CD4+ CD19-specific chimeric antigen receptor-modified T cells. *Sci Transl Med* 8(355): 355ra116.

Funding Awards:

- NRSA T32: OHSU Program in Enhanced Research Training (Award # 5T32GM71338-15); 2020-2021
- NRSA T32: OHSU Program in Biomedical Sciences Training Grant (Award #1T32GM142619-01); 2021-2022
- NRSA T32: Integrated Cancer Systems Biology Training Grant (Award #[]); 2023-Present

Teaching and Mentoring Experience:

OHSU Wy'east Postbaccalaureate Program, *OSHU, 2022-2025*

- The Wy'east program at OHSU serves as a post-baccalaureate path for Alaska Native and American Indian students into medical school. I had the privilege to teach these students for two sessions titled "Introduction to Innate Immunity" and "Innate Immune Sensors: Host-Pathogen Interactions". I received very positive feedback on my teaching method from the program coordinators and staff and faculty observers from the OHSU Teaching and Learning Center and Portland State University.

Training Future Faculty, *OHSU,* 2021-2022

- The Training Future Faculty program is organized by the Teaching and Learning Center at OHSU, and is aimed at providing teaching experience, enhanced training in pedagogy, and guidance through teaching observation and workshops.

Research Rotation Student Mentorship, Moran Lab *OHSU,* 2022-2024

- Involved in planning rotation projects for 5 research rotation students from the OHSU PBMS program, including training, teaching and mentoring the students during their 4-week rotations.

Introduction to Biostatistics Teaching Assistant, *OHSU,* 2022

- Served as a teaching assistant for the graduate-level Introduction to Biostatistics class, including answering student questions, hosting study sessions, hosting office hours, and grading homework and exams.

Cell Biology Teaching Assistant, *OSHU,* 2020

- Organized and led weekly study sessions and literature discussions for graduate students enrolled in the Cell Biology class.

Student Learning Center, *OHSU,* 2020

- Organized and hosted review sessions for students entering the OHSU Program in Biomedical Sciences and beginning their core competency classes.

Peer Mentor Program, *OHSU,* 2020

- Mentored a first-year graduate student in the Program in Biomedical Sciences at OHSU and met with them regularly to help the make decisions and navigate their first year.

Seattle Pacific University Mentor Program, *SPU,* 2018-2019

- Mentored SPU undergraduate students who were interested in entering academic research careers by sharing my experiences with them, helping to connect them with other researchers, and advising them on how to prepare for a career as an academic researcher.

Cell Biology, Biochemistry, Organic Chemistry, and Gen. Chemistry Teaching Assistant, *SPU,* 2013-2015

- Provided procedural and writing guidance to the students, prepared/maintained biological samples, maintained lab reagent stocks, and graded research reports, quizzes, and examinations

Presentations:

- **Oral: Hawkins R,** Polesso F, Ko A, Cheney J, Huynh R, Moran AM. Androgen receptor activity tunes CD8 T cell effector responses. *AAI Immunology 2025. Honolulu, HI* (May 2025)

- **Poster: Hawkins R,** Ko A, Polesso F, Moran AE, Androgen receptor activity tunes CD8 T cell effector responses. *Sex Differences in the Immune System, Trinity College Dublin* (June 2024)
- **Poster: Hawkins R,** Weeder B, Kumar S, Kopp R, Garzotto M, Thompson R, Moran AE. Leveraging a neoadjuvant clinical trial in high risk localized prostate cancer to unveil mechanisms of androgen-mediated immune suppression. *PNW Prostate SPORE Conference, UCLA, CA* (March 2024)
- **Poster: Hawkins R,** Polesso F, Ko A, Moran AE. Androgen receptor regulation of CD8 T cell immune responses. *GRC Sex Differences in Immunity 2023, Pacific Grove, CA* (April 2023)
- **Oral and Poster: Hawkins R,** Sehrawat A, Polesso F, Moran AE. Androgen receptor regulation of CD8 T cell immune responses. *Immunology 2022, AAI, Portland, OR* (May 2022)
- **Poster: Hawkins R**, Guan X, Polesso F, Wang C, Sehrawat A, Murray SE, Thomas GV, Caruso B, Graff JN, Xia Z, Moran AE. Suppressing androgen receptor activity in T cells promotes effective checkpoint blockade. *Midwinter Conference of Immunologists, Pacific Grove, CA* (January 22, 2022)
- **Poster: Hawkins R.** Androgen Receptor Regulation of T Cell Immune Responses. *OHSU Research Week, Portland, OR* (May 3, 2021).
- **Oral: Hawkins R**, Kenyon R, Anderson M, Wood D. Suspect genes involved in Wnt pathway signaling and intestinal cell fate in C. elegans. *Erickson Undergraduate Research Conference, Seattle, WA* (May 16, 2014).
- **Poster: Hawkins R**, Kenyon R, Nelson TA, Ridgway RL. DMSP localization in the macroalga, *Ulva lactuca*, by immunofluorescence microscopy. *Murdock Undergraduate Research Conference, Vancouver, WA* (November 14, 2014)

Leadership and Volunteer Experience:

- OHSU Recruitment 2020, *OHSU* – Assisted in welcoming, orienting, and recruiting prospective students for the OHSU Program in Biomedical Sciences (PBMS)
- Seattle Pacific University Mentor Program, *SPU,* 2018-Present – Mentoring aspiring undergraduate scientists as they begin to transition from undergrad to research jobs or graduate school.
- Executive Board Member and Co-founder of MEDLIFE (Medicine, Education, and Development for Low Income Families Everywhere) – SPU Chapter, *Associated Students of SPU*, 2013-2015
- Ivy Honorary, SPU's Mortar Board National Honor Society Chapter, 2014-2015
- Student Leadership Development Committee, *Associated Students of SPU*, 2014-2015
- Executive Member of SPU American Chemical Society Club, *Associated Students of SPU*, 2014-2015
- Chief Justice, Constitutional Advisory Board, *Associated Students of SPU*, 2013-2015
- Elections Task Force, *Associated Students of SPU*, 2013
- Moyer Hall Senator, *Associated Students of SPU*, 2012-2013
- Moyer Executive Hall Council, *SPU*, 2012-2013

Awards and Honors:

- Student Mentor Award, OHSU Graduate Student Organization, 2021-2022
- Dean's List throughout enrollment, *SPU*
- Trustees' Scholar Award, *SPU,* The highest academic scholarship offered at SPU
- Alpha Kappa Sigma, *SPU*, Honors society for students in the top ten percent
- Certificate of Excellence in Cellular and Molecular Biology 2015, *SPU*, Awarded to one student with exceptional performance in and support of the major
- Valedictorian, *Bonney Lake High School*, Awarded for ranking first in the class of 2011
- Advanced Placement Scholar with Distinction, *The College Board*, 2010-2011